

Advances in heterogeneous catalysts for the synthesis of polyoxymethylene dimethyl ethers

Présentée le 20 février 2020

à la Faculté des sciences de base
Groupe Kröcher
Programme doctoral en chimie et génie chimique

pour l'obtention du grade de Docteur ès Sciences

par

Christophe Jean BARANOWSKI

Acceptée sur proposition du jury

Dr A.-S. Chauvin, présidente du jury
Prof. O. Kröcher, directeur de thèse
Prof. J. Sauer, rapporteur
Dr A. Heel, rapporteur
Prof. A. Renken, rapporteur

“Nothing in life is to be feared, it is only to be understood. Now is the time to understand more, so that we may fear less.”

Marie Skłodowska Curie

Abstract

Driven by threats such as air pollution or global warming, our society is engaged in a major shift towards more sustainable industries. The required transition from fossils to renewable resources with low greenhouse gas emission is specifically challenging in the transportation sector where high thermal efficiency and energy density are key requirements. Due to their appealing properties, polyoxymethylene dimethyl ethers (OME) have recently received increasing attention as a new type of Diesel additive or substitute. When blended with Diesel fuel, they reduce the level of soot emission with a concomitant increase in combustion efficiency. OME are compatible with Diesel-powered vehicles and with the current fuel distribution infrastructure. When produced from renewable sources such as biomass, their usage results in a reduced carbon footprint compared to fossil fuels.

Due to its ability to significantly increase reaction kinetics, an effective catalyst is an essential element involved in most large-scale chemical transformations and this also holds for OME synthesis. However, the OME technology being only at an early stage of research, there is limited understanding of the catalyst structure-activity relationships for OME synthesis. Due to the thermodynamics of the reaction, currently used catalysts suffer from a low selectivity towards OME with 3 to 5 oxymethylene units (OME₃₋₅), which are the most desirable products as diesel substitute. Furthermore, current OME synthesis routes involve the usage of costly intermediate compounds, which increases the production cost and reduces the overall process efficiency.

The aim of this thesis is to progress in the development of knowledge in heterogeneous catalysis for the sustainable production of OME. We focused on rational catalysts synthesis and in-depth characterization to understand how their properties influenced OME synthesis. The acquired knowledge on the structure-activity relationship enabled the design of more performant catalysts. Lastly, we investigated water-free catalytic dehydrogenation of methanol to formaldehyde as a potential oxymethylene source to avoid the usage of the costly intermediates.

Zeolites have demonstrated a high catalytic potential for the synthesis of OME due to the required acidity for this reaction. By modifying accessibility to the active sites in an H-ZSM-5 zeolite, we demonstrated that the reaction suffered from severe internal diffusion limitations of the reactants and products in the zeolite micropores. Controlled introduction of an intercrystalline network of mesopores significantly enhanced the zeolite's activity by allowing a more significant part of the reaction to occur within the micropores. By optimizing the desilication process, we achieved a two-fold increase in the initial reaction rate and a 10 % increase of the initial selectivity towards the more desirable products (OME₃₋₅).

Subsequently, we introduced tin in montmorillonite clay as a cheap and eco-friendly alternative to zeolites. This resulted in a hierarchical material composed of tin oxide inserted between the clay layers, with Brønsted and Lewis acidity. Its advantageous textural and acidic properties resulted in an active catalyst for OME synthesis from trioxane (TRI) and dimethoxymethane (OME₁). Based on characterization and catalytic tests, we attributed the nature of its acidity to a combination of bridging hydroxyl groups resulting from the crystallization of SnO₂, and undercoordinated Sn surface sites.

To investigate the role of Lewis and Brønsted acidity for this reaction, a series of Beta zeolites with varying amounts of Brønsted and Lewis acid sites were synthesized. Brønsted acidity was varied by means of dealumination and the controlled grafting of Sn on silanol nests was performed to introduce Lewis acid sites in the zeolite framework. A synergy between these two types of acid sites resulted in a large turnover frequency increase accompanied with a reduction in by-product formation. Formaldehyde was produced *in situ* by the decomposition of TRI on Brønsted acid sites and subsequently inserted into OME upon activation of the carbonyl bond on tetrahedral Sn.

Then, we studied the causes of inhibition of the reaction kinetics by water for the synthesis of OME from TRI and OME₁ over an H-Beta zeolite, which is an efficient catalyst for OME production. The presence of water as an impurity in OME₁ at concentrations as low as 0.21 wt % severely affected the reaction kinetics. The main OME growth mechanism shifted from direct TRI insertion to formaldehyde incorporation in OME, as the level of water in OME₁ increased. The main cause of deactivation was the hampered adsorption of TRI on the zeolite active sites by the presence of water. As TRI was unable to bind to bridging

hydroxyl groups, OME growth reaction could not occur without an available oxymethylene source.

The water free, non-oxidative catalytic dehydrogenation of methanol to formaldehyde (FA) is an appealing substitute to TRI utilization. This reaction was thus investigated as a source of oxymethylene groups, to reduce the costs linked to the usage of TRI for OME synthesis. Grafting on amorphous silica in methanol was selected as the method of choice to study the activity of alkali metals for methanol catalytic dehydrogenation. The resulting catalysts displayed an increased activity for the catalytic dehydrogenation of methanol. A large gap in selectivity towards FA between ions with a high- (i.e. Li, Na) and low charge density (i.e. K, Rb, Cs) was observed. Also, an increased metal loading was detrimental to the selectivity towards FA and resulted in a larger production of CO. Na grafted on silica yielded the best combination of moderate conversion and high selectivity. But the grafting method could not be optimized further.

As a result of the work presented in this thesis, important catalyst features can now be considered when developing catalysts or designing production processes for OME synthesis. We managed to increase slightly the selectivity towards OME₃₋₅, but it is still to an unsatisfactory level. More energy-efficient processes will require alternatives to the usage of TRI as the oxymethylene source. Alkali metals grafting on silica has the potential to catalyze this reaction and this method could pave the way for future research on water-free formaldehyde production.

Keywords

Oxymethylene dimethyl ethers, OME, Zeolites, Montmorillonite clay, Hierarchical materials, SiO₂, Brønsted acidity, Lewis acidity, Methanol dehydrogenation, Alkali metals, Infrared spectroscopy.

Résumé

Notre société se doit de se transformer radicalement dans un avenir proche pour faire face à des défis majeurs tels que la pollution de l'air ou le réchauffement climatique. La transition nécessaire de sources d'énergies fossiles vers des sources d'énergies durables, dans l'objectif d'un bilan carbone neutre, représente un réel challenge. En particulier, le secteur des transports sera un des segments les plus compliqués à aborder dû aux propriétés essentielles des carburants : une efficacité thermique élevée et une densité énergétique importante. En raison de ses propriétés attrayantes, le carburant synthétique polyoxyméthylène diméthyléthers (OME) a récemment fait l'objet d'une attention croissante en tant que nouveau type d'additif ou de substitut au carburant Diesel. Lorsqu'il est mélangé avec du carburant Diesel, il réduit le niveau d'émission de suie tout en augmentant parallèlement l'efficacité de combustion. Les OME sont compatibles avec les véhicules fonctionnant avec un moteur Diesel et avec l'infrastructure de distribution de carburant actuellement établie. Produits à partir de sources renouvelables, leur utilisation entraîne une réduction de l'empreinte carbone par rapport aux combustibles fossiles.

Accéléralant la cinétique de réaction de façon notable, un catalyseur efficace est un élément essentiel pour la plupart des transformations chimiques à grande échelle. Cependant, étant à un stade précoce de recherche, il n'existe qu'une compréhension limitée des relations entre la structure d'un catalyseur et son activité pour la synthèse d'OME. En raison de la thermodynamique de la réaction, les catalyseurs actuellement utilisés souffrent d'une sélectivité faible pour les molécules d'OME ciblées, constituées de 3 à 5 unités d'oxyméthylène (OME₃₋₅), qui sont les produits les plus recherchés. De plus, les voies de synthèse OME actuelles impliquent l'utilisation d'intermédiaires coûteux, qui augmente le coût de production et réduit l'efficacité globale du procédé.

L'objectif de cette thèse est d'élargir le champ de connaissances en catalyse hétérogène pour la production durable d'OME. Pour ce faire, nous nous sommes concentrés sur la synthèse

de catalyseurs et leur caractérisation approfondie afin de comprendre comment leurs propriétés influencent la synthèse d'OME. Nous avons ensuite tenté de concevoir des catalyseurs plus performants sur la base des connaissances acquises. Enfin, nous avons étudié la déshydrogénation catalytique sans eau du méthanol en formaldéhyde en tant que source de groupement oxyméthylène, comme possible alternative à l'utilisation d'intermédiaires coûteux.

Les zéolites ont démontré un potentiel catalytique élevé pour la synthèse d'OME en raison de l'acidité requise pour cette réaction. En modifiant l'accessibilité des sites actifs dans une zéolite H-ZSM-5, nous avons démontré que la réaction souffrait de limitations sévères liées à la diffusion interne des réactifs et des produits dans les micropores de la zéolite. L'introduction contrôlée d'un réseau inter cristallin de mésopores a considérablement amélioré l'activité de la zéolite en permettant qu'une partie plus importante de la réaction se produise à l'intérieur des micropores. En optimisant l'étape de désilication, nous avons multiplié par deux la vitesse initiale de réaction et réalisé une augmentation de 10 % de la sélectivité initiale pour OME₃₋₅. Nous avons ensuite introduit Sn dans l'argile montmorillonite comme alternative économique et écologique à l'utilisation de zéolites. Cela a donné un matériau hiérarchique composé d'oxyde d'étain inséré entre les couches d'argile, possédant des sites acides de Brønsted et de Lewis. Ses propriétés texturales et acidiqes avantageuses ont permis de créer un catalyseur actif pour la synthèse d'OME à partir de trioxane (TRI) et de diméthoxyméthane (OME₁). En s'appuyant sur une combinaison d'analyses de caractérisation et de tests catalytiques, nous avons attribué la nature de son acidité à une combinaison de groupes hydroxyle pontants, résultant de la cristallisation de SnO₂, et de sites Sn sous-coordonnés en surface.

La synergie entre l'acidité de Brønsted et de Lewis au sein du catalyseur a été explorée à l'aide d'une série de zéolites Beta comportant une quantité variable de sites acides de Brønsted et de Lewis. L'acidité de Brønsted a été modifiée par désalumination et la greffe contrôlée de Sn sur les nids de silanols a permis d'introduire des sites acides de Lewis au sein de la structure de la zéolite. La synergie s'est traduite par une augmentation importante de la fréquence de cycles accomplis, accompagnée d'une réduction de la formation de sous-produits. L'activation de la liaison carbonyle sur le Sn^{IV} a permis une insertion efficace dans

l'OME du formaldéhyde, produit *in situ* via la décomposition du TRI grâce aux sites acides de Brønsted.

La zéolite H-Beta étant un des catalyseurs les plus efficaces pour la synthèse d'OME, nous avons ensuite étudié les causes d'inhibition de la cinétique de réaction par l'eau, pour la synthèse d'OME à partir de TRI et d'OME₁ sur une zéolite H-Beta. La présence d'eau en tant qu'impureté dans OME₁ à une concentration aussi faible que 0.21 % en poids a gravement affecté la cinétique de la réaction. À partir d'un certain degré d'eau dans OME₁, le principal mécanisme de croissance des OME est passé de l'insertion directe du TRI à l'incorporation de formaldéhyde dans les OME. La principale cause de désactivation était l'adsorption perturbée du TRI sur les sites actifs de la zéolite par la présence d'eau. Le TRI étant dans l'incapacité de se lier aux groupes hydroxyle pontants, les mécanismes de croissance des OME ne pouvaient plus se produire sans une source d'oxyméthylène disponible.

Étant une alternative attrayante à l'utilisation du TRI, la déshydrogénation catalytique sans eau du méthanol en formaldéhyde a été étudiée pour permettre de fournir des groupes oxyméthylène. La greffe dans du méthanol de métaux alcalins sur de la silice a été utilisée pour étudier l'activité des métaux alcalins envers la déshydrogénation catalytique du méthanol. Un large intervalle de sélectivité pour le formaldéhyde entre les ions ayant une densité de charge élevée (i.e. H, Li, Na) et faible (i.e. K, Rb, Cs) a été observé. Na greffé sur de la silice a conduit à la meilleure combinaison en matière de conversion de méthanol modérée et de sélectivité pour le formaldéhyde élevée. Cependant, la méthode de greffe n'a pas pu être optimisée.

Cette thèse a contribué à faire progresser les connaissances sur la catalyse hétérogène pour la production d'OME. Certaines caractéristiques importantes des catalyseurs ont été mises en évidence et peuvent maintenant être prises en compte lors de la mise au point de catalyseurs ou lors de la conception de procédés de production. Nous avons réussi à augmenter légèrement la sélectivité pour OME₃₋₅, mais à un niveau encore insatisfaisant. Des procédés plus économes en énergie nécessiteront de trouver des alternatives à l'utilisation du TRI comme source d'oxyméthylène. La déshydrogénation catalytique non oxydative du méthanol est un substitut attrayant à l'utilisation du TRI. La greffe de métaux alcalins sur la silice peut potentiellement catalyser cette réaction et cette méthode pourrait ouvrir la voie à de futures recherches sur la déshydrogénation catalytique du méthanol.

Mots-clés

Oxyméthylène diméthyléthers, OME, Zéolites, Argile montmorillonite, Matériaux hiérarchiques, SiO₂, Acidité de Brønsted, Acidité de Lewis, Déshydrogénation du méthanol, Métaux alcalins, Spectroscopie infrarouge.

Acknowledgements

First of all, I would like to express my deepest gratitude to Prof. Dr. Oliver Kröcher for his supervision and the boundless freedom I enjoyed during these past four years of doctoral studies. His wisdom, scientific expertise, availability and transparency were always very much appreciated. The first time we met in Brussels, I shared my vision of building a pilot plant for the production of OME by the end of my PhD, to which he replied that it was “probably” too ambitious. Four years later, I understand better what he meant. Beside teaching me how to become an independent and pragmatic researcher, I also very much appreciated all the discussions on various topics such as tennis, the rush hours of life or mountain biking.

I am deeply grateful to the two post-docs I have had the opportunity to work with during my PhD. First, Dr. Ali Bahmanpour, thank you for having been my daily science sparring partner and for always having been available for any type of advices. We shared the same office during more than three years and were the (bi)core of the GCB group, so I am deeply thankful. Second, thank you to Dr. Florent Héroguel for helping me out during the first years of my PhD. You have been a significant scientific asset and a genuine friend.

I would also like to thank Prof. Dr. Ing. Jörg Sauer, Dr. Andre Heel and Prof. Dr. Albert Renken for kindly accepting to be the co-examiners of this thesis, and Dr. Anne-Sophie Chauvin for acting as the jury president.

Due to the limited size of our laboratory, I collaborated with different groups during my PhD. I am therefore very grateful to Prof. Dr. Jeremy Luterbacher and his team for giving me the opportunity to work in their laboratories. Dr. Davide Ferri, thank you very much for letting me perform experiments in your group. I really enjoyed spending time at PSI and always felt warmly welcomed. Thank you to Prof. Dr. Sandrine Gerber, who supervises the neighboring laboratory, for inviting me to some of your group outings. Thank you to Prof. Dr. Kevin Sivula for being my PhD mentor. I would also like to thank Martin Elsener,

for teaching me the ABC's of Swagelok and helping me with various analysis. Thank you to everyone who helped with various aspects of my work: the CH magasin team, the workshop team, Yoann Dind, Benjamin Le Geyt, Emilie Baudat, Pascal Schouwink, Thomas Lagrange, Pierre Mettraux, Ducan Alexander, and Snaedis Bjoergvinsdottir. I am also thankful for all the administrative help I received from Fara Raharisolo, Anne Lene Odegaard and Madeleine Steffen.

None of this work would have been possible without the tremendous assistance that I received from the three master students who joined the lab to do their master thesis within our group. All three were very talented, and I owe them my deepest gratitude. They came as students but left as true friends. Joe, you were the first I had the opportunity to supervise, thank you for your amazing work that helped me start my PhD. Maneka, the work you did with me was pivotal for the completion of this work, so thank you! I am glad we are colleagues now. Jack, thank you for listening to the Friday life lessons but also for killing my PhD student statistics. Remember it's not too late to start one, because you did a great job! I am convinced I have learned more from you three than what I could share with you. Thank you also to Vincent Dufoulon that did his semester project in the group.

We were a small team in the CH building, but I was lucky to meet amazing people with whom I shared great moments during these four years: Patrick, Adrian, Andrej, Raphaël, Jeremy, Laura, Adrian, Lucas, Denis, Gaël, Benjamin, Yuan-Peng, Lorenz, Jean, Rémy, Wu, Bartosz, Luciano, Radmila, Oliver, Laura, Marine and all those I may have forgotten. Our coffee breaks, nights out, barbecues, nice chats, lunches, and our (sometimes) scientific discussions made my experience here a real joy.

I owe my deepest gratitude to the people I was the closest to: To Dr. Francois "Fransis" Noverraz, my good, wise friend and tireless physical condition partner; To Thibault "Fovadowski" Fovanna, with whom I travelled to various places for work or leisure, collaborated on very interesting projects—he truly embodies the "work hard, play hard" saying; To my "2039" team, thank you so much for all these great moments we shared: Marina "Titanium" Caretti, thanks for your incredible energy and positivity, and, "Floating" Luca Szabó thank you so much for everything, especially for all the shrink sessions (it's hard to pinpoint specifics when there are so many!). Your friendship was genuinely decisive, and for that I am sincerely grateful. Thank you to all my other friends in Switzerland: Delphine,

Antonin, Elfie, Aymeric, Florent, Xavier, François, Luigi. A huge thanks to all my “international” friends, for which distance or time does not matter: “Pieto” Pierre, “Yanino” Yan, Jake, Michael “Le millionaire”, “Umby” Umberto, “Atchoum” Renaud, “Zoubiloune” Alexandre. I don’t mark my words when I say you were all key for my sanity.

Last but not least, I am deeply grateful to my family which has always provided me with love, guidance and support. To my brother Nicolas, you are a true role model. You were always there when I needed any support, so thank you. I dedicate this work to my parents for all the love and care they gave to me. Maman et papa, you always believed in me and you are the most generous, benevolent persons I know. There are no words to express my gratitude to you for everything you have done.

Lausanne, 28th October 2019

Contents

Abstractv
Résuméix
Acknowledgementsxiii
Contents xvii
List of abbreviations xix
Chapter 1	Introduction..... 1
1.1	OME properties as synthetic fuel 4
1.2	Synthesis routes for the production of OME 9
1.3	Catalysts12
1.4	Reaction mechanisms20
1.5	Challenges for OME catalysts30
1.6	Aim and scope of the thesis.....31
Chapter 2	Experimental..... 33
2.1	Preparation of catalysts33
2.2	Catalytic tests33
2.3	Characterization techniques37
2.4	Reaction network and kinetic model for OME synthesis.....42
Chapter 3	Mesoporosity introduction in an H-ZSM-5 zeolite for activity improvement..... 45
3.1	Introduction45
3.2	Experimental47
3.3	Results and discussion49
3.4	Conclusions62
Chapter 4	Nature of the active sites of tin-montmorillonite for OME synthesis 63
4.1	Introduction63
4.2	Experimental65
4.3	Results and discussion66
4.4	Conclusions81
Chapter 5	Synergy between Brønsted and Lewis acid sites in Sn-Beta zeolites for OME synthesis..... 83
5.1	Introduction83

5.2	Experimental.....	85
5.3	Results.....	86
5.4	Discussion.....	99
5.5	Conclusions.....	102
Chapter 6	Influence of water on the kinetics of OME synthesis in an H-Beta zeolite	105
6.1	Introduction.....	105
6.2	Experimental.....	107
6.3	Results and discussion.....	109
6.4	Conclusion.....	125
Chapter 7	Alkali metal grafting on silica for methanol catalytic dehydrogenation	127
7.1	Introduction.....	127
7.2	Experimental.....	130
7.3	Results and discussion.....	131
7.4	Conclusions.....	148
Chapter 8	Summary and outlook	149
8.1	Summary.....	149
8.2	Outlook.....	151
References	153
Appendices	165
Appendix A.....	167
Appendix B.....	171
Appendix C.....	172
List of publications	183
Cover Features	185
Curriculum Vitae	191

List of abbreviations

A36	Amberlyst 36
AT-MMT	Acid-treated montmorillonite
AT30	Alkaline treated
ATR	Attenuated total reflection
AW	Acid wash
BJH	Barrett-Joyner-Helenda
CPMG	Carr-Purcell-Meiboom-Gill
DME	Dimethyl ether
DRIFT	Diffuse reflectance infrared Fourier transform
DRUV	Diffuse reflectance UV-Vis
DTBPy	2,6-di-tert-butyl-pyridine
EDXS	Energy-dispersive X-ray spectroscopy
EFAL	Extra-framework aluminum
EGR	Exhaust gas recirculation
FA	Formaldehyde
FAME	Fatty acid methyl ester
FTIR	Fourier transformed infrared
FWHM	Full width at half maximum
GO	Graphene oxide
HAADF	High-angle annular dark-field
HF	Hemiformal
ICP-OES	Inductively coupled plasma optical emission spectrometry
IGT	Initiation growth termination
ILs	Ionic liquids
IPA	Isopropanol
MAS-NMR	Magic angle spinning solid-state nuclear magnetic resonance
ME	Modulation-excitation
MeOH	Methanol
MF	Methyl formate
MG	Polyoxymethylene glycol
MMT	Montmorillonite
OME	Polyoxymethylene dimethyl ether
OMEE	Polyoxymethylene diethyl ether

PD	Phase-domain
PF	Paraformaldehyde
PSD	Phase sensitive detection
Py	Pyridine
SEM	Scanning electron microscopy
SF	Schulz-Flory
STEM	Scanning transmission electron microscopy
TEM	Transmission electron microscopy
TOF	Turnover frequency
TPD	Temperature programmed desorption
TPO	Temperature programmed oxidation
TRI	Trioxane
XPS	X-ray photoemission spectroscopy
XRD	X-ray diffraction

“A pessimist sees the difficulty in every opportunity; an optimist sees the opportunity in every difficulty.”

Sir Winston Leonard Spencer-Churchill

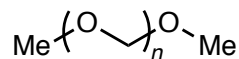
Chapter 1 Introduction

Diesel engines have a higher thermal efficiency than gasoline engines due to their higher operating pressure and temperature. Unfortunately, this advantageous feature also leads to higher levels of hazardous exhaust gas emissions, which has contributed to air pollution reaching alarming levels.^[1] These exhaust emissions were classified as carcinogenic to humans by the International Agency for Research on Cancer in 2012.^[2] Consequently, governments introduced more stringent emission limits that required the usage of sophisticated and costly emission control equipment. Some car manufacturers deceived standard emission tests and this has contributed to the current bad reputation of Diesel-powered cars. According to the World Energy Council, Diesel consumption is still expected to grow between 46 and 200 % compared to its 2010 level during the next four decades.^[3] Thus, it is expected that Diesel engines will continue to power a large share of the vehicles in the near-future. This results from their high thermal efficiency and energy density, which are the key requirements for heavy-duty transport. Meanwhile, biofuel usage will become mandatory in many areas of the world such as in the European Union with a ratio of 10 % of biofuels for transport by 2020.^[4] The current source of biodiesel is mainly first-generation biofuels such as fatty acid methyl esters (FAME) biodiesel. However, their usage was shown to increase CO₂ emissions up to 20 % compared to traditional fossil fuels when effects of indirect land use are considered.^[5]

In this context, polyoxymethylene dimethyl ethers (OME, also referred to as OMEs, POME or POMDME in the literature) have recently received increasing attention, since various studies demonstrated that a blend of OME with Diesel fuel reduced soot particles formation, unburned hydrocarbons and carbon monoxide emissions during combustion.^[6-13]

This chapter is part of a published article in Applied Catalysis B: Environmental as C. J. Baranowski, A. M. Bahmanpour, O. Kröcher, Catalytic synthesis of polyoxymethylene dimethyl ethers (OME): A review, App. Cat. B Environ. 2017, 217, 407-420.^[143] Part of the manuscript and supplementary information are reproduced here with some changes in formatting with permission from Elsevier.

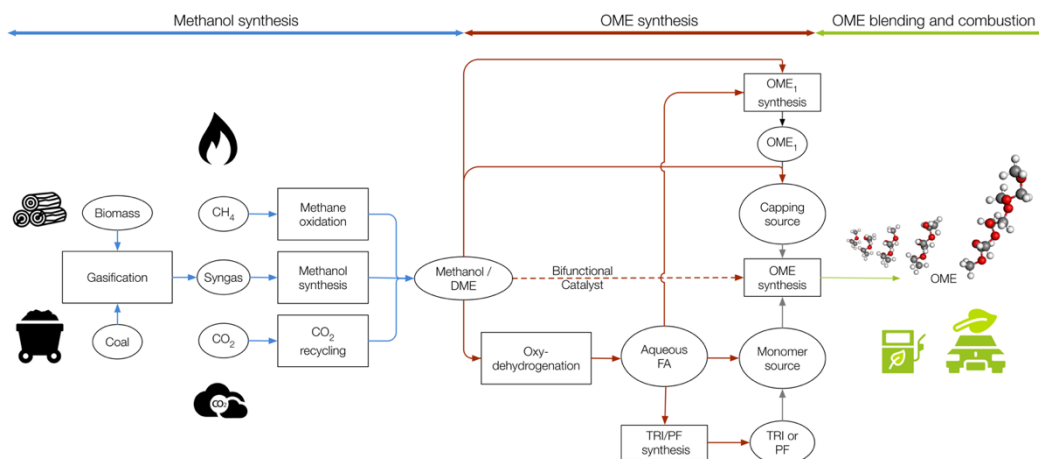
OME, shown in Scheme 1-1, are oligomers composed of CH_2O units, which are highly stable since their chains are capped with one methyl and one methoxy group. The oxymethylene chain of variable length dictates the molecule properties.



Scheme 1-1. Structure of polyoxymethylene dimethyl ethers (OME). $\text{OME}_n = \text{H}_3\text{C}(\text{-O-CH}_2)_n\text{-CH}_3$.

A particularly attractive property of OME is that blends of Diesel fuel and OME with the appropriate chain length can be used in slightly modified Diesel engines.^[7] Their properties, notably boiling point, cetane number and viscosity, can be controlled via the chain length. Therefore, their large-scale usage requires no modifications to the fuel distribution infrastructure and only slight adjustment to a car injection system. If produced from renewable sources such as biomass, their usage could reduce the global CO_2 emissions compared to fossil fuels, in addition to the potential reduction in harmful exhaust emissions.^[14,15] OME can also provide a sustainable alternative to first-generation biofuels.

OME are synthesized from methanol, which can be produced via biomass gasification and subsequent syngas conversion. Methanol is a versatile chemical considered for storing renewable energy and a product of CO_2 recycling, which constitutes the basis of the methanol economy.^[16] The different ways methanol is produced and used in the OME synthesis processes are shown in Scheme 1-2. Several combinations of reactants are available to synthesize OME. Formaldehyde is produced through methanol oxy-dehydrogenation, which is then used to produce trioxane (TRI) or paraformaldehyde (PF). Dimethoxymethane (OME_1 , also referred to as DMM in the literature) is the shortest OME and is synthesized from methanol and formaldehyde by reactive distillation. Current trends highlight the shift of focus towards production processes requiring less steps and simpler reactants such as dimethyl ether (DME), methanol or aqueous formaldehyde. This will be discussed in further details below. Researchers have proposed various OME production methods using ion-exchange resins as well as ionic liquids as catalysts.^[17,18] Considering the undesirable formation of byproducts, energy intensive separation steps are required to obtain concentrated, high-quality OME of the desired chain length that can be used in a Diesel engine or blended with Diesel fuel.



Scheme 1-2. Liquid phase synthesis routes to polyoxymethylene dimethyl ethers (OME) from methanol, which is derived from various sources. The depicted routes and reactants have been reported for the production of OME_n with $n > 1$: OME_1 = dimethoxymethane, TRI = trioxane, PF = paraformaldehyde, FA = formaldehyde, DME = dimethyl ether.

The first efforts to synthesize OME were accomplished as early as 1904, when Descudé prepared OME_2 by reaction of dichlorodimethyl ether and sodium methylate.^[19] In the 1920s, Staudinger and Luthy systematically investigated their properties and synthesis.^[20] Polyoxymethylene ethers with a high molecular weight are interesting polymer materials, called POM. In the middle of the 20th century several companies, notably DuPont in the 1960s, invented production processes to obtain thermally stable POM polymers.^[21] Boyd determined some physico-chemical properties of OME_{2-5} .^[22] As oxygen-containing compounds demonstrated promising combustion and emission properties, interest in OME production started at the beginning of the 21th century. BP corporation^[23-30] patented various production methods from several reactant combinations from 1999 to 2003, followed from 2007 to 2011 by BASF^[31-34] and others^[35,36].

Recently, both German and Chinese scientists, from the industry or academia, have been very active in OME-related technology. China envisions this technology as a solution to use its coal feedstock and alleviate its air pollution problems, while Germany could have an economical interest in maintaining a strong Diesel-powered car industry. Germany focuses on carbon-neutral production of OME in contrast to China which targets on coal as the primary carbon source. These two countries have therefore taken the lead in terms of number of scientific publications or patents. Shandong Yuhuang Chemical Co. inaugurated an OME synthesis plant in 2015 based on a fluidized-bed reactor process.^[37,38] To the best

of our knowledge, it is the only reported OME production facility alongside with pilot plants projects in Germany.^[7,12,13,39-42]

This chapter reviews the literature on OME properties and synthesis. We begin with a brief analysis of the OME properties as fuel additives. Subsequently, the main synthesis routes are outlined and the different catalysts are described together with their performances. Next, we review the various reaction mechanisms and models that were employed to describe the synthesis of OME. Finally, the aim and scope of this thesis are presented based on the challenges linked to the OME technology.

1.1 OME properties as synthetic fuel

Numerous investigations were conducted on the usage of oxygen-containing compounds (oxygenates) as fuels or additives to conventional fuels in spark-ignition engines. They were initially of interest for their high octane numbers as anti-knocking agent to replace tetraethyl lead with oxygenates such as methyl tertiary butyl ethers.^[43] Further research on fuels containing a higher weight percentage of oxygen demonstrated their soot reduction properties during combustion in Diesel engines.^[44]

The simplest oxygenates with a higher oxygen weight percentage are dimethyl ether and methanol. The former has a high cetane number, a low autoignition temperature and combusts almost soot-free in compression-ignition engines.^[45] The latter, despite its lower energy density has an inherent higher efficiency thanks to its high cetane number.^[43] However, they both have drawbacks that requires adaptation of distribution system, fuel tanks or engines.^[45] Methanol is toxic, exhibits incompatibility to certain materials and encounter cold-start problems. DME is gaseous at ambient temperature and has a miscibility gap with Diesel fuel at temperature below 0 °C. In comparison, OME are liquid, non-toxic and demonstrate good material compatibility. Additionally, there is no miscibility gap between OME and Diesel fuel.^[46] Due to these advantageous properties, engine performance tests, combustion and emission characteristics of various mixtures of fuels and OME have been reported in the literature.

1.1.1 Physico-chemical properties

A fuel must comply with country-dependent regulations and specifications, such as EN 590 for European countries. Several studies showed that OME₃₋₅ are suitable fuel additives complying with such regulations.^[10,12,13,46,47] OME have chemical properties, summarized in Table 1-1, close to paraffinic Diesel fuel and comply thus to the EN15940 standard.^[48] OME₃₋₅ display cetane numbers of 67, 76 and 90^[10], which are all higher than the minimum required by the EN 590 for commercial Diesel.^[49] Their flash points range from 53.5 to 115.0 °C ^[10], mostly meeting the lower limit of 55 °C enforced by the EN 590. Long-chain OME with $n > 5$ precipitate at temperatures below 18 °C leading to a risk of blocking the fuel filter if used.^[10] On the other side, short-chain OME with $n < 3$ have a lower viscosity than Diesel fuel that may require injector modifications. They also have a lower vapor pressure and flash point than Diesel hence not fulfilling this safety criterion.^[7,46] However, all their other physico-chemical properties, such as viscosity or lubricity, are mostly similar to Diesel fuel allowing its usage without Diesel engine modification. Additionally, if produced from natural gas, their low sulfur content even meets the most stringent fuel requirements for sulfur content.^[7,50] Finally, OME may contain residual trioxane and formaldehyde. The maximum allowed concentration of these toxic residues will need to be standardized.^[48] Overall, OME₃₋₅ are the most valuable fractions amongst OME due to their suitability as fuel additives for usage in Diesel engines with only slight modifications of the fuel supply system.

Table 1-1. OME properties^[51]

	OME ₁	OME ₂	OME ₃	OME ₄	OME ₅	OME ₆
CAS No.	109-87-5	628-90-0	13353-03-2	13352-75-5	13352-76-6	13352-77-7
Molecular Formula	C ₃ H ₈ O ₂	C ₄ H ₁₀ O ₃	C ₅ H ₁₂ O ₄	C ₆ H ₁₄ O ₅	C ₇ H ₁₆ O ₆	C ₈ H ₁₈ O ₇
Oxygen Content (%)	42.1	45.2	47	48.1	48.9	49.5
Boiling Point (°C)	42	105	156	202	242	273
Melting Point (°C)	-105	-70	-43	-10	18	38
Cetane Number	29	63	67	76	90	NA
Lower Heating Value (MJ · kg⁻¹)	22.4	20.6	19.4	18.7	18.1	17.7
Density (kg · m³)	860	980	1030	1070	1110	1140

Lautenschütz et al. studied the physico-chemical properties of polyoxymethylene diethyl ethers (OMEE).^[10] The most distinctive characteristic is their autoignition point. OMEE exhibit lower autoignition points due to the possible peroxy radical formation that can trigger decomposing chain reactions in the presence of oxygen. OMEE₂₋₄ exhibit a flash point range of 35.3 to 94.5 °C, approximately 20 °C lower than that of OME₃₋₅. Therefore, interest in these compounds remained limited. However, it was also demonstrated that the reaction of a mixture of OME and OMEE over an acidic catalyst could lead to ethoxymethoxymethane, which is the acetal with mixed ethyl and methyl end-group.^[52] This could allow for the tuning of oligomer mixtures depending on the applications and the required properties.

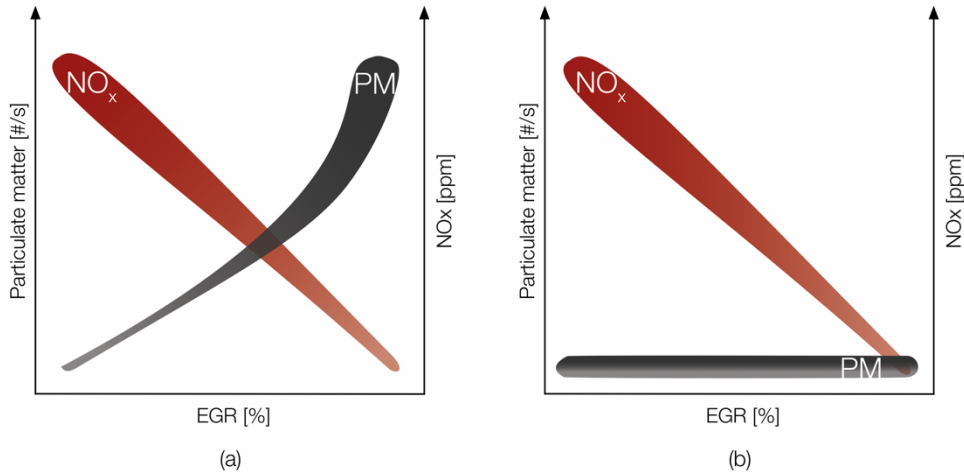
1.1.2 Combustion and emission characteristics

CO₂-neutral, infinite supply, minimum well to wheel emissions, cost-effectiveness, and functionality are the five conditions of the future sustainable energy and fuel systems.^[53] OME were shown to be compatible with these conditions in various studies.^[51,54]

OME have a lower heating value and energy content compared to conventional Diesel fuel due to their oxygen content. Their usage thus increase volumetric fuel consumption.^[7] Increasing the ratio of OME in Diesel fuel blends shortens the main combustion delay due to the increase of the mixture's cetane number. At loads higher than 6 bar indicated mean effective pressure, a longer main combustion delay has been reported.^[12] When a Diesel engine runs at high load, large amount of fuel is injected into the combustion chamber resulting in fuel-rich regions favorable for pyrolysis, which results in soot particles formation. OME do not contain carbon-to-carbon bonds, which are the most basic structural elements of soot, hence reducing the amount of soot particles emission.^[9] Besides, soot precursors are degraded by hydroxyl radicals formed during combustion of OME.^[55] The reduced soot-forming potential allows higher exhaust gas recirculation (EGR) rates which also reduces the NO_x emissions. The NO_x/particulate trade-off is thus mitigated by the addition of OME to the conventional Diesel fuel (Scheme 1-3).

Various studies confirmed the influence of OME on combustion emissions. Ianuzzi et al. observed a nearly soot-free combustion for pure OME combustion in a constant volume chamber.^[9] They also demonstrated that the addition of 5 % of OME₂ to commercial Diesel

fuel leads to 30 % reduction in soot emissions. The correlation between fuel blend oxygen content from the addition of OME and the decrease in soot particle emission was non-linear.



Scheme 1-3. Schematic representation of particulate matter (PM) and NO_x versus exhaust gas recirculation (EGR) in a compression ignition engine for the combustion of (a) Diesel and (b) pure OME.

Lumpp et al. compared combustions and emissions of Diesel fuel with a blend of 20 vol % of OME₃₋₄ to pure Diesel fuel using a six-cylinders engine.^[8] Compared to Diesel fuel emissions, soot particle emissions from the combustion of the fuel blend decreased by 60 % and 50 %, respectively, during European stationary cycle and light European transient cycle tests. The gravimetric particulate mass decreased by 40 % and 25 %, respectively. In addition, the particle number respectively decreased by 50 % and 40 %. They also compared the emissions of a blend of 10 vol % OME₂ and Diesel fuel with the emissions of the pure Diesel fuel on a single-cylinder using various engine speeds and loads. They observed a decrease of soot emissions between 30 to 40 % with an adjusted EGR to have similar NO_x emissions.

In subsequent studies, Liu et al. investigated the engine performance and emissions characteristics of blends of OME₃₋₄ with Diesel fuel and gasoline-Diesel in a single-cylinder engine.^[7,12,13] They stated that the addition of OME₃₋₄ reduced soot particles formation to a large extent. They claimed a soot-free combustion by using a 20 vol % OME₃₋₄/Diesel blend. Conversely, other studies showed that pure OME are required to prevent soot formation completely.^[11,51,56] NO_x emissions increased slightly with increasing OME ratio; they therefore identified the 20 % blend value as optimal as it minimizes NO_x and soot particles emissions. Simultaneously, CO emissions decreased drastically by 90 % at high loads (mean

effective pressure of 8 bar), but hydrocarbon emissions were only slightly reduced. Tests of a blend of OME₃₋₄/Diesel/gasoline with a 30/35/35 volume ratio showed similar emission trends. However, addition of gasoline to Diesel lowers the flash point of the blend to less than the minimum stated in the EN 590 standard.

OME₁ is commonly synthesized from methanol and its combustion properties have been investigated by various researchers.^[57] Its physico-chemical properties required modifications of the current injection system or fuel distribution infrastructure when used as a fuel or a fuel additive. To circumvent these drawbacks, blend of OME₁ with various additives have been reported in the scientific and patent literature. For example, a fuel containing OME₁ and 3-20 wt % of polyethylene glycol dimethyl ether was patented (molecular weight of 500 or 1000 g·mol⁻¹).^[58] Interestingly, the author also dissolved OME₄ or OME₆₋₁₀ in OME₁ to increase viscosity and cetane numbers in some embodiments of the patent. Feiling et al. compared emission characteristics of OME₁ with 3 wt % long-chain polyethers (OME_{1b}) and a conventional Diesel fuel (with up to 7 vol % FAME) using a single-cylinder engine at various loads.^[11] At low and high loads (respectively 3 and 7 bar pressure mean indicator), they recorded a twenty- and fortyfold particle number decrease, respectively, compared to conventional Diesel fuel. According to the authors, the high temperature in the combustion chamber at high load favored the re-oxidation of soot. Additionally, OME₁ exhibited a soot-free combustion (particulate matter concentration below the device detection limit of 0.01 to 1 mg·m⁻³).

Finally, Härtl et al. investigated various oxygenated fuels and identified OME as the most effective for soot reduction.^[51,56] Combustion and emissions of various OME blend were tested in a single-cylinder engine: OME_{3,6}, OME_{1b} and OME_{1a} (3 wt % of SYNALOX™ 40-D700 and 3 wt % of polyethylene glycol dimethyl ether with a molecular weight of 1000 g·mol⁻¹). The engine fuel system was also modified to use OME. During engine testing with a Diesel oxidation catalyst (DOC) as sole after-treatment component, they demonstrated that the soot-NO_x trade-off totally disappeared even at stoichiometric combustion. Furthermore, they verified that no formaldehyde emission occurred. However, they recorded methane emissions near stoichiometric condition that were not converted by the DOC. Methane emissions are believed to be due to an increase in methyl radical formation and

their subsequent reaction with hydrogen radicals during combustion near stoichiometric condition.

1.2 Synthesis routes for the production of OME

OME are produced by reaction of a methyl end-group provider with an oxymethylene source under acidic conditions. To a limited extent, they can also be produced using a bi-functional catalyst combining redox and acidic properties with one reactant containing both moieties. Methanol, DME and OME₁ have been reported in the literature as the sources of the methyl end-group. Different sources of monomeric formaldehyde have been reported, i.e. in liquid form as aqueous formaldehyde, in gaseous form as DME or in solid form as trioxane (TRI) and paraformaldehyde (PF). TRI, C₃H₆O₃, is a white crystalline solid with a melting point of 62 °C and boiling point of 115 °C. This cyclic ether decomposes under acidic conditions to anhydrous formaldehyde. It is produced from concentrated aqueous formaldehyde solution with low conversion by acid-catalyzed ring formation, followed by a separation step composed of several distillation columns or a combination of distillation and solvent-extraction steps.^[59]

PF or polyoxymethylene glycol, HO-(CH₂O)_n-H with $n = 8-100$, is a short polymer composed of oxymethylene moieties. It is produced by concentration of aqueous formaldehyde under vacuum. PF powder decomposes to formaldehyde upon heating at temperature from 120 to 170 °C.^[60] It depolymerizes in an acid-catalyzed reaction to formaldehyde in water according to the following reaction:



Finally, liquid and gaseous monomeric formaldehyde readily polymerizes at room temperature.^[60] Dissolved in water, it polymerizes to form a distribution of poly(oxymethylene) glycols (MGs, HO-(CH₂O)_n-H) according to reactions (1-2) and (1-3).^[61-63] It also reacts with methanol to produce hemiformals (HFs, CH₃-(O-CH₂)_n-OH) based on equations (1-4) and (1-5). These reactions do not require acid as catalyst and the equilibrium is far on the product side. Therefore, less than 0.1 % formaldehyde is found in monomeric form in aqueous solution.^[60] Due to its high reactivity, it is commercially available as formalin, an aqueous solution containing 37 to 55 wt % formaldehyde. Its methanol content is usually between 10 to 15 % which inhibits the formation of insoluble polymers.^[60]



Three routes to synthesize OME were identified and they are used to classify the combination of reactants (Table 1-2).

1.2.1 Anhydrous synthesis of OME (B2, B3, C2)

The reactants used in the anhydrous route are generally TRI with OME_1 . OME_1 reacts with CH_2O units provided *in situ* by the reversible TRI dissociation (1-6). The OME synthesis with OME_1 and TRI follows these reversible reactions:

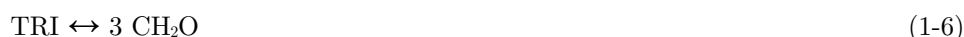
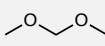
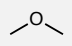
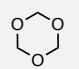
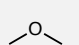


Table 1-2. Combination of reactants used for the synthesis of OME in the scientific literature.^[a]

		Capping agent		
		1 $\text{CH}_3\text{-OH}$	2 	3 
Oxymethylene source	$\text{H}_2\text{C=O}$ A	Zhang, ^[64,65] Schmitz ^[66,67]	Peter ^[68]	-
	 B	Zhao, ^[69] H. Li, ^[70] Deng, ^[71] Fang, ^[72] Wang ^[73]	Burger, ^[46,74] Wang, ^[75] Q. Wu, ^[77,78] Fu, ^[79] Li, ^[80] J. Wu, ^[81] Y. Wu ^[78]	Haltenort ^[82]
	$\text{H}-\text{C}(\text{O})_n-\text{OH}$ C	Oestreich ^[83]	Arvidson, ^[84] Zheng, ^[40,85,86] Shi ^[50]	Li, ^[87]
	 D	-	-	Zhang ^[88,89]

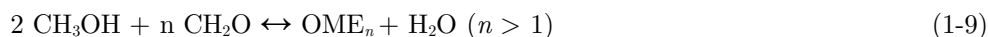
^[a] Includes studies where OME were produced with more than one oxymethylene group.

Recently, Halternort et al. demonstrated that OME could also be produced via the reaction of DME with TRI.^[82] Besides, anhydrous monomeric CH_2O should react with OME_1 in quantitative yield to OME_n . This reaction has recently been demonstrated by Peter et al., that produced OME_n by uptake of molecular formaldehyde by OME_1 at room temperature using a trimethyloxonium salt as catalyst.^[68] Usage of PF as monomeric formaldehyde provider implies generation of water according to reaction (1-1), proportionally to the average

PF chain length. It is thus formally speaking not completely anhydrous, but the concentration of water remains low compared to other routes.

1.2.2 Aqueous synthesis of OME (A1, A2, B1, C1)

Using methanol as the capping agent leads to the production of water in stoichiometric amount. Under acidic conditions, it reacts with formaldehyde from aqueous or anhydrous sources according to the reaction (1-9). A liquid-liquid equilibrium model was developed to predict the behavior of ternary system composed of water, methanol and OME.^[90] The larger number of byproducts induced by the presence of water, as well as the shorter mean chain length produced, induce a lower yield compared to the anhydrous synthesis.^[83] A larger number of separation units are thus required downstream to reach a sufficient product purity, but the number of synthesis steps is reduced compared to the anhydrous route.



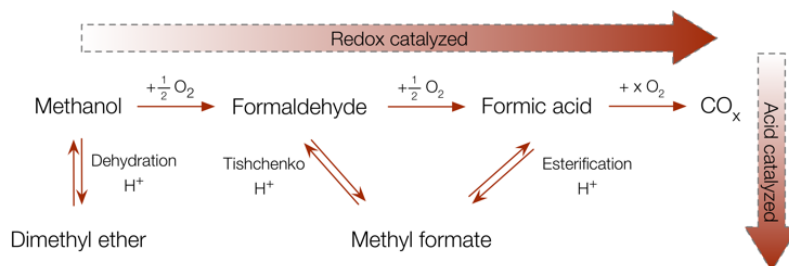
1.2.3 Selective, one-step oxidation of methanol to OME (1, D3)

OME₁ is usually produced from methanol in two consecutive steps: (i) gas-phase (oxi-)dehydrogenation over an Ag or a FeMo catalyst to produce a mixture of formaldehyde, methanol and water, followed by (ii) liquid-phase, acid-catalyzed condensation of methanol and formaldehyde. Relatively high yield can be achieved using this synthesis strategy.^[57] There has been a recent focus on the synthesis of OME, mostly OME₁, through direct, one-step selective oxidation of methanol or DME over a bi-functional catalyst combining acidic and redox properties.^[14,89,91-95] The review of Thavornprasert et al. summarizes the research conducted on the one-pot synthesis of OME₁ from methanol.^[96] An OME synthesis process from methanol using oxygen as oxidant has been published by Yu et al. in their patent application from 2010.^[36] They used a fixed bed continuous synthesis process. Zhang et al. investigated OME synthesis, notably OME₁ and OME₂, from DME on various catalysts, but only relatively low yield were achieved with this method.^[88,89,97]

1.2.4 Side reactions during OME synthesis

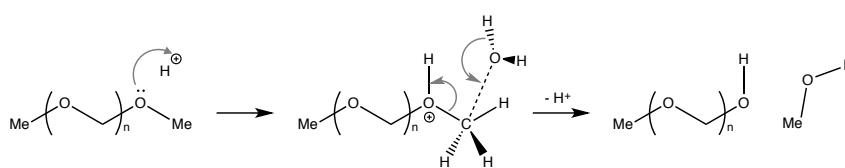
OME preparation is subjected to several side reactions, presented in Scheme 1-4, that decrease the overall yield. DME is produced via methanol dehydration in an acidic environ-

ment.^[74,98,99] Likewise, methyl formate is produced by the Tishchenko reaction from formaldehyde.^[9,73] Formaldehyde or methanol can be oxidized to formic acid and can decompose to carbon monoxide or carbon dioxide.^[98,99] Methyl formate is also produced via esterification of formic acid.



Scheme 1-4. Side reactions during OME synthesis.^[74,96,98]

The hydrolysis of OME with water is another important side reaction and is illustrated Scheme 1-5.^[40,64,74] Water presence shifts the product distribution towards shorter chains and favors the formation of HFs. It also makes the downstream separation process more tedious due to extraction with non-polar solvents such as Diesel. Various authors studied the influence of water on the reaction product distribution.^[40,66,83,100] An addition of 10 wt % water decreases the amount of OME_{>2} by 70.6 %. Wang et al. also tested the influence of water on the synthesis of OME with methanol and TRI using graphene oxide as catalyst. They reported an 85 % decrease in OME₂₋₈ selectivity when using water as a solvent compared to methanol.^[73]



Scheme 1-5. Hydrolysis of OME under acidic conditions.

1.3 Catalysts

The synthesis of OME is described as an acid-catalyzed reaction. Different catalyst categories have been investigated in the patent and scientific literatures. Two criteria are used to evaluate the performance of a catalyst: its selectivity towards a range of OME of a certain chain length and the conversion of reactants. These criteria are difficult to compare from one study to another as the reaction conditions, products of interest and the reactants vary.

References cited here have reported the synthesis of OME_n with $n > 1$ except in the case of selective, one-step synthesis of OME₁.

1.3.1 Homogeneous catalysts

Table 1-3 presents the homogeneous catalysts that were reported to catalyze the synthesis of OME. Mineral acids such as H₂SO₄, HCOOH, CF₃SO₃H have been disclosed in many patents, but fewer reports were published in the scientific literature.^[31,32,35,101] Wang et al. tested various liquid catalysts containing carboxyl, carbonyl, hydroxyl and sulfonic groups.^[73] Their results showed that the acidity of carboxyl, carbonyl and hydroxyl groups is not sufficient for efficient TRI decomposition and OME chain growth. Best results were obtained with catalysts containing a sulfonic acid functional group such as sulfuric acid, for which a TRI conversion of 72.2 % and an OME₂₋₈ selectivity of 19.3 % was achieved. Shi et al. tested several rare earth metal compounds with sulfuric acid and identified lanthanum (La³⁺/SO₄²⁻) as an efficient co-catalyst.^[50]

Table 1-3. Homogeneous catalysts used for the synthesis of OME.

Catalysts (wt %)	Reactants (molar ratio)	T (K)	Time (h)	Conv. (%) / source	Select. (%) to OME _{x-y}	Ref.
<i>Mineral acid</i>						
H₂SO₄ (0.1)	OME ₁ and PF (4:1)	373	1	68.6/PF	27.6 (3-4)	[102]
H₂SO₄ (0.27)	MeOH and TRI (2:1)	393	10	72.2/TRI	19.3 (2-8)	[73]
La³⁺/SO₄²⁻ (1)	OME ₁ and PF (1:1.6)	393	6	83.2/OME ₁	50.7 (3-8)	[50]
CF₃SO₃H (0.01)	OME ₁ and TRI (4:1)	373	40	Undisc.	22.5 (3-11)	[31]
<i>Ionic liquids</i>						
[PH-S][CF₃SO₃] (2.1)	MeOH and TRI (1.3:1)	393	4	90.3/TRI	42.6 (3-8)	[103]
[IM-S][HSO₄] (4.5)	OME ₁ and TRI (1.1:1)	388	0.66	89.1/TRI	52.4 (3-8)	[104]
[PY-BS][HSO₄] (1.61)	OME ₁ and TRI (3:1)	443	10	91.2/TRI	70.9 (3-8)	[77]

Amongst the liquid acid catalysts, ionic liquids (ILs) have several advantages. They are powerful solvents with high tunability of solvent and acidic properties. Due to their low vapor pressure and high thermal stability, they are easier to separate and recycle.^[77] They

have been used for the synthesis of OME and several were patented. Chen et al. filed several patents on methods for producing OME catalyzed by ILs using OME₁ or methanol with TRI under nitrogen pressure.^[103-105] They reached their best performance with a quaternary phosphonium salt, namely triphenyl(propyl-3-sulfonyl) phosphonium trifluoromethanesulfonate ([PH-S][CF₃SO₃-]), with a TRI conversion of 90.3 % and an OME₃₋₈ selectivity of 42.6 %, with methanol and TRI as reactants.^[103] Superior OME₃₋₈ selectivity of 52.4 % was achieved later using OME₁ as capping agent and 1-(4-sulfobutyl)-3-methylimidazolium hydrogen sulfate ([IM-S][HSO₄⁻]) as catalyst with a similar TRI conversion of 89.1 %.^[104]

Xia et al. patented a method based on the same ILs catalysts for continuously producing OME using aqueous formaldehyde (50-60 wt %) and methanol in a two-steps process.^[106,107] Formaldehyde first polymerizes to TRI, followed by an acetalization reaction to form OME. They achieved a production of 200 mL·h⁻¹ of OME₃₋₈ during 100 h from an aqueous formaldehyde solution (feed rate = 800 mL·h⁻¹), which was converted to TRI with a feed rate of 130 mL·h⁻¹ followed by reaction with 112 mL·h⁻¹ of methanol. Catalytic performance of a series of Brønsted acid ILs with different alkenesulfonic acid groups was investigated by Wu et al. for the synthesis of OME with OME₁ and TRI.^[77] They established that a stronger Brønsted acidity improves this reaction with 1-(4-sulfonic acid) butylpyridinium hydrogen sulfate ([PY-BS][HSO₄⁻]) as their best catalyst. Whereas the conversion of TRI was basically unaltered (< 90 %), the selectivity to OME₃₋₈ varied significantly. They later studied the influence of ILs hydrophobicity on their catalytic performances for the synthesis of OME with OME₁ and TRI.^[108] For this purpose, ILs with a carbon side-chain of varying length were synthesized and it showed that the hydrophobicity has only limited influence on the catalysts performance under their reaction conditions. While the conversion of TRI remained constant above 90 %, the OME₃₋₈ selectivity peaked at 57.85 % for a carbon chain length of 6 corresponding to the lowest viscosity. However, they did not consider the potential change in acidity resulting from the modification of ILs side chains.

In summary, homogeneous liquid catalysts have inherent advantages in OME synthesis such as being uniformly distributed in the reaction mixture and having all their catalytic sites available for the reaction. However, they are inherently difficult to separate. Mineral acids are inexpensive but corrosive, harmful to the environment and they only exhibit little

OME selectivity. In contrast, IIs are expensive and exhibit slow substrate diffusion, but they show better performance, especially better selectivity towards OME.

1.3.2 Heterogeneous catalysts

Table 1-4 presents the heterogeneous catalysts that were reported to catalyse the synthesis of OME. The majority of the concerned literature studies focused only on their application and not on the influence of the catalyst features. Ion-exchange resin catalysts combine some chemical benefits of homogeneous catalysis, i.e. their well-defined and uniform active sites, with the characteristic physical advantages of heterogeneous catalysis. Arvidson et al. reported the usage of Amberlite® IR120 for reacting PF with OME₁ and identified LiBr as promoting co-catalyst.^[84] Burger et al. compared Amberlyst® 36 (A36) and 46 (A46) for the production of OME.^[74] They obtained between 1 to 2 wt % of the side products DME and methyl formate using A36 compared to a completely selective reaction when using A46. They suggested that side products are catalysed by the sulfonated active sites in the catalyst micropores where formaldehyde may accumulate. A46 featured no active sites in the micropores and hence produced less side products.

Additionally, performance of several ion-exchange resins (NKC-9, D001-CC, D72) with sulfonic acid groups were investigated by Zheng et al. for the synthesis of OME from OME₁ and PF.^[85] NKC-9 exhibited the best catalytic performance with 84.6 % formaldehyde conversion and 36.6 % OME₃₋₅ selectivity. Higher surface area, higher exchange capacity and larger pore volume have led to the higher performance of NKC-9. Because all these parameters vary for NKC-9, it is difficult to study the influence of each individual parameter. However, D001-CC and D72 have similar BET surface area and exchange capacity and differ only with respect to their pore volume, which is higher for D72. It resulted in a twofold increase in formaldehyde conversion and an enhanced selectivity for D72 compared to D001-CC.

Using ion-exchange resins as catalysts involves diffusion from the bulk to the particle as well as subsequent diffusion of the molecules inside the micropores to the active sites, which depends on the characteristics of the resins. By using a series of Dowex50W resins, Oestreich et al. established that an increasing extent of crosslinking degree of the resins diminished the activity, probably due to a restricted accessibility to the active sites.^[83]

Table 1-4. Heterogeneous catalysts used for the synthesis of OME.

Catalyst (wt %)	Reactants molar ratio	T (K)	Time (h)	Conv. (%)	Select. (%) to OME _{x-y}	Ref
<i>Ion-exchange resin</i>						
A36 (4.2)	OME ₁ and TRI (2:1)	323	0.33	93.5/TRI	32 (3-6)	[46]
NKC-9 (7.0)	OME ₁ and PF (3:1) ^[a]	353	1.5	84.6/PF ^a	37 (3-5)	[85]
Dowex50Wx2 (1.0)	MeOH and PF (1:1.6)	353	0.023	Undisc.	29 (3-5)	[83]
<i>Carbon material</i>						
HS-C (undis.)	OME ₁ and TRI (undis.)	323	48	Undisc.	32 (3-7)	[109]
GO (5)	MeOH and TRI (2:1)	373	10	92.8/TRI	31 (2-8)	[73]
<i>Solid superacid</i>						
ZrO₂/γ-Al₂O₃ (0.5g)^[b]	MeOH and aqu. FA (1:3)	393	0.013 ^[c]	91.3/FA	23 (3-8) ^[d]	[64]
SO₄²⁻/TiO₂ (1.0)	OME ₁ and TRI (1:1)	353	1	89.5/TRI	55 (3-8)	[80]
SO₄²⁻/Fe₂O₃ (1.5)^[e]	MeOH and TRI (1.5:1)	403	2	81.9/TRI	23 (3-8)	[70]
<i>Zeolite</i>						
H-MCM-22 (5)	OME ₁ and TRI (1:2)	393	10	Undisc.	29 (3-8)	[69]
H-ZSM-5 (5)	OME ₁ and TRI (2:1)	393	0.75	85.3/TRI	89 (2-8)	[81]
H-Beta (1-2)^[f]	OME ₁ and TRI (3:1)	298	0.12	94.5/TRI	21 (3-5)	[110]
<i>Other</i>						
PVP-HPAs (2.3)	MeOH and TRI (2:1)	413	4	95.4/TRI	55 (2-5)	[72]
C10-AS-50 (7)	OME ₁ and TRI (3:1)	378	2	92.6/TRI	54 (3-8)	[79]
Si-ILs (4)	OME ₁ and TRI (3:1)	378	1	92/TRI	52 (3-8)	[78]
Re-PW₁₂/TiO₂ (1 mL)^[g]	DME	513	0.3ms ^[c]	15.6/DME	60 (2)	[88]

^[a] The author indicated a molar ratio of OME₁/CH₂O of 3:1 and a formaldehyde conversion of 84.6 %. The mean chain length of PF and the method to produce the formaldehyde are not mentioned. ^[b] Mass of catalyst in a fixed-bed reactor, molar ratio Zr/Al = 0.04. ^[c] Experiments conducted in a continuous setup. Indicated time = residence time. ^[d] Number taken from Figure 7 in ref [64]. ^[e] 6.4 wt % SO₄²⁻ on Fe₂O₃. ^[f] With respect to TRI. ^[g] 5 wt % Re and 20 wt % PW₁₂ on TiO₂.

Zheng et al. investigated the limitations of the internal and external mass transfer by varying the particulate diameter and stirring speed, respectively, with a NKC-9 catalyst.^[40]

They did not observe internal mass transfer limitation for particle diameters smaller than 1 mm. A stirring speed higher than 300 rpm was necessary to eliminate external mass transfer effect. The reusability of the resins was tested by various groups.^[75,85] In general, no major change in the activity of the resins was observed after several reuses. Oestreich et al. observed a 10 % decrease in reactants conversion with no change in selectivity after using the Dowex50Wx2 resin continuously for 17 days.^[83] The drawbacks of ion-exchange resins are their low thermal stability and the leaching of active species into the bulk of the solutions when using polar solvents. A continuous process that used an ion-exchange resin to produce OME was patented using PF or TRI and OME₁ as reactants.^[111] It claimed to obtain a product stream with a 53.3 wt % of OME₂₋₇.

Compared to acidic resins, solid acid carbons do not swell and exhibit higher thermal stability. Shen and co-workers developed an acidic carbon catalyst containing sulfonic acid groups (HS-C) from the carbonization and sulfonation of a phenolic-like structure.^[112] It was used for the synthesis of OME from OME₁ and TRI.^[109] The phenolic-like structure was obtained by hydrolyzation of glucose to hydroxymethylfurfural and subsequent reaction with a phenol compound. They obtained an OME₃₋₇ selectivity of 31.9 %. Wang et al. used graphene oxide (GO) with methanol and TRI, obtaining a TRI conversion of 92.8 % and an OME₂₋₈ selectivity of 30.9 %.^[73] Since GO contains various oxygen-containing functionalities such as carboxyl, hydroxyl, carbonyl and sulfonic groups, investigating the effect of each functional group on catalyst activity was important. Selective removal of carbonyl, carboxyl or hydroxyl groups resulted in 18 % less TRI and methanol conversion while removal of sulfonic groups resulted in 57 % less conversion. OME₂₋₈ selectivity decreased similarly when all functional groups were eliminated with an average decrease of 72 %. It became apparent that sulfonic, hydroxyl and carboxyl groups are all crucial for the catalytic performance of GO, especially the sulfonic group for TRI decomposition. Despite its good catalytic performance, GO reusability is limited since a decrease of 8 % and 47 % in TRI conversion and OME₂₋₈ selectivity, respectively, was observed after five cycles.

Solid superacid catalysts were also reported to be active in OME synthesis process. Zhang et al. used a zirconia supported on alumina (ZrO₂/γ-Al₂O₃) for OME synthesis from formaldehyde and methanol.^[64] Addition of ZrO₂ to unmodified alumina changes its acidity with an increment of its medium and strong acid centers. They tested the effect of the

catalyst Zr/Al molar ratio on the reaction in a fixed bed reactor. Increasing the Zr/Al ratio led to increased methanol conversion with an optimal selectivity at a 0.04 ratio. They recorded 91.3 % formaldehyde conversion and 23 % OME₃₋₈ selectivity. The catalyst proved to be stable during reaction over 500 h without decrease in conversion or selectivity. Chungu's group tested the catalytic performance of various super solid acids. Sulfated titania (SO₄²⁻/TiO₂) exhibited 89.5 % TRI conversion and 54.8 % OME₃₋₈ selectivity using OME₁ and TRI as the reactants.^[80] They also used sulfated iron silica (SO₄²⁻/Fe₂O₃-SiO₂) with various pre-treatment methods and amounts of silica.^[70] They studied the influence of number, ratio and density of Lewis and Brønsted acid sites on catalytic activity. The best sample was a sulfated iron catalyst with no silica that had the highest acidity, the highest ratio of Brønsted to Lewis acid sites, and the highest acid site density. It led to 81.9 % TRI conversion and 23.3 % OME₃₋₈ selectivity. Finally, a synergy between Brønsted and Lewis acid sites was highlighted when sulfated titania was used as a catalyst for the synthesis of OME from TRI and OME₁.

One of the interesting features of zeolites as catalysts is their tunable acidity by the adjustment of their Si/Al ratio. Their Brønsted and Lewis acidity arise from the bridged linkage of Si-(OH)-Al and Al defects, respectively. Zhao et al. investigated the activity of the zeolites H-Y, H-ZSM-5, H-MCM-22 and H-Beta on the product distribution of OME with methanol and TRI as the reactants.^[69] H-MCM-22 showed the highest OME₃₋₈ selectivity due to its larger number of acid sites compared to other tested zeolites. They determined that a Si/Al ratio of 200 in H-MCM-22 generates the highest selectivity. However, they did not control the effect of the Si/Al ratio on the conversion of reactants. Wu et al. also studied the influence of the Si/Al ratio on the conversion of TRI or OME₁ and the selectivity towards OME₂₋₈ using H-ZSM-5 as catalyst.^[81] They found 580 as the optimum Si/Al ratio. By means of pyridine adsorption and FTIR spectroscopy, they calculated that an increase of the ratio diminishes the amount of acid sites, most notably Lewis acid sites. The ratio of Brønsted to Lewis acid sites increases from 0.9 to 5.8 with an increase in the Si/Al molar ratio from 56 to 560, corresponding also to a decrease from 47.3 to 0.2 wt % of methyl formate selectivity. At too high Si/Al ratio, the catalytic activity started to deteriorate severely. Oestreich et al. compared the activity of zeolites H-Beta, H-ZSM-5 and H-MOR and CBV for the synthesis of OME from formaldehyde and methanol.^[83] The most active was H-Beta, followed by H-ZSM-5, which were both more active compared to A36, but less

than Dowex50W. CBV and H-MOR required much more time to reach the same level of conversion. Similar results were obtained by Lautenschütz et al. using TRI and OME₁, showing that H-Beta was more active than A36.^[110]

Additionally, Yu et al. impregnated an acidic molecular sieve with two metal oxides and used this catalyst in a one-step OME synthesis process from methanol using air as the oxidant.^[36] The catalyst was composed of 60-90 wt % of zeolite Y or ZSM-5, 2 to 20 wt % molybdenum oxide and 0.2 to 10 % iron oxide. They claimed that they have achieved a single-pass methanol conversion of 96-98 %, similar to the industrial formaldehyde production process.^[60] They also claimed to obtain 34 % OME_{>2} selectivity, the rest of the product being methanol, formaldehyde, OME₁, water, DME and CO_x.

Besides, other more uncommon materials were tested for OME synthesis. Super-microporous aluminosilicates (C₁₀-AS-50) were prepared by Fu et al. for the synthesis of OME using OME₁ and TRI as reactants.^[79] Super-microporous materials have a pore size range between those of microporous zeolites and ordered mesoporous materials. They achieved 92.6 % TRI conversion and 53.5 % OME₃₋₈ selectivity, and claimed that the pore size of their catalyst was more suitable to lead to a larger OME₃₋₈ selectivity. Next, nearly complete conversion of TRI and 54.9 % OME₂₋₅ selectivity was reported by Fang et al. with polyvinylpyrrolidone-stabilized phosphotungstic-acid (PVP-HPW) in a PVP/HPW molar ratio of 0.25:1.^[72] They varied the PVP/HPW ratio to tune the acidity. Finally, ILs supported on silica gel (Si-ILs) were used to combine the efficiency of ILs (3-sulfobutyl-1-(3-propyltriethoxysilane) imidazolium) with the usability of heterogeneous catalysts.^[78] Si-ILs have better catalytic activity than their unsupported counterpart with reported TRI conversion and OME₃₋₈ selectivity of 92 % and 52 %, respectively. However, they exhibited limited reusability with a loss of 22.8 % of its grafted catalytic material after six runs and one regeneration. This loss led to a decrease of 45 % and 42 % of the TRI conversion and the OME₃₋₈ selectivity, respectively.

Overall, due to their inherent advantage of being easily separated from the products, heterogeneous catalysts received the lion's share of research on OME synthesis. Among the many types of materials tested, acidic resins and zeolites demonstrated the best performance, but many options exist to improve their catalytic activities. The link between the

structure of the catalyst and its activity is often overlooked. Yet, some important parameters were highlighted such as mass-diffusion of the reactants, strength of the acid sites or type of acidity.

1.3.3 Catalyst for direct gas-phase synthesis of OME

The majority of research on the direct gas-phase synthesis of OME involves the selective oxidation of methanol over heterogeneous catalysts. Various metal oxides have been reported such as Mo-, Ru-, Re- or V-based oxides. The highest catalyst activity reported in the literature was claimed by Gornay et al. using an FeMo-based catalyst, traditionally used for formaldehyde synthesis from methanol under methanol-lean and air-rich conditions.^[113] However, using this catalyst for OME synthesis under methanol-rich conditions resulted in 56 % methanol conversion and 90 % OME₁ selectivity. Increased OME₁ yield was also obtained by Lu et al. by impregnation of V₂O₅/TiO₂ with H₂SO₄.^[92] The H₂SO₄-modified catalyst reached a methanol conversion and OME₁ selectivity of 49.0 % and 93.0 %, respectively. Additionally, a gas-phase DME conversion of 15.6 % and an OME₂ selectivity of 60.0 % was reported using rhenium oxide (Re₂O₇) modified H₃PW₁₂O₄₀ supported on TiO₂ (Re-PW₁₂/TiO₂).^[88] Re-PW₁₂ was also supported on carbon nanotubes but higher OME yields were not achieved. Recently, Grünert et al. demonstrated that OME could be produced in the gas-phase from a MeOH and FA using Si-rich zeolite (ZSM-5 and MOR) at reaction temperatures ranging from 130 to 220 °C. They achieved conversion to OME₁ but OME of larger chain length were scarcely produced.

In summary, oxidizing and acidic properties of active sites are of crucial importance for OME₁ one-step synthesis to maximize the yield, but deriving general conclusions is difficult. However, the provided data suggest that redox and acid sites of the right strength should likewise be in close vicinity.

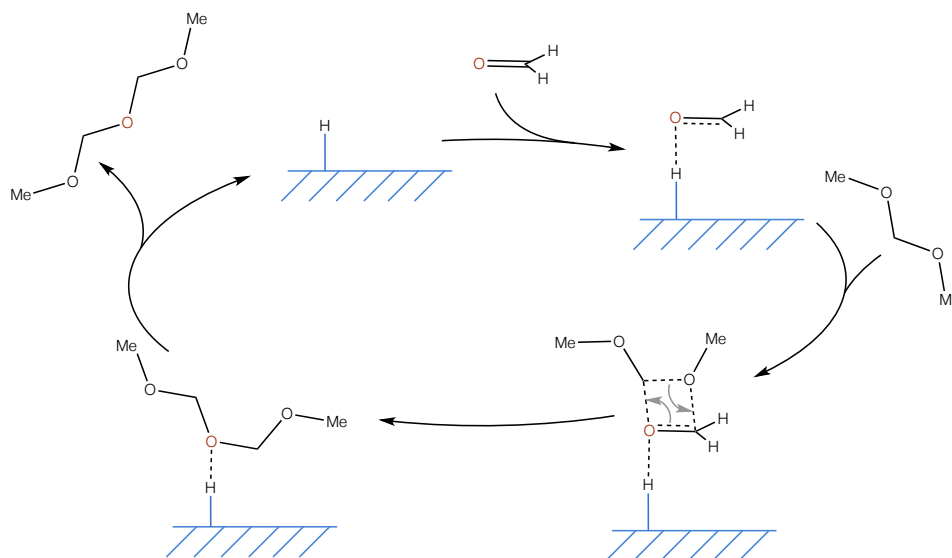
1.4 Reaction mechanisms

1.4.1 Chain growth mechanisms

Two reaction mechanisms have been reported in the literature to describe the chain growth of OME: (i) a sequential addition mechanism^[40,71,81,85,108] and (ii) an initiation, growth and termination (IGT) mechanism^[67,70,72,78,85,114]. The reaction mechanism followed

seems to depend on the phase, reactants and catalyst, but no general agreement has been reached in the literature.

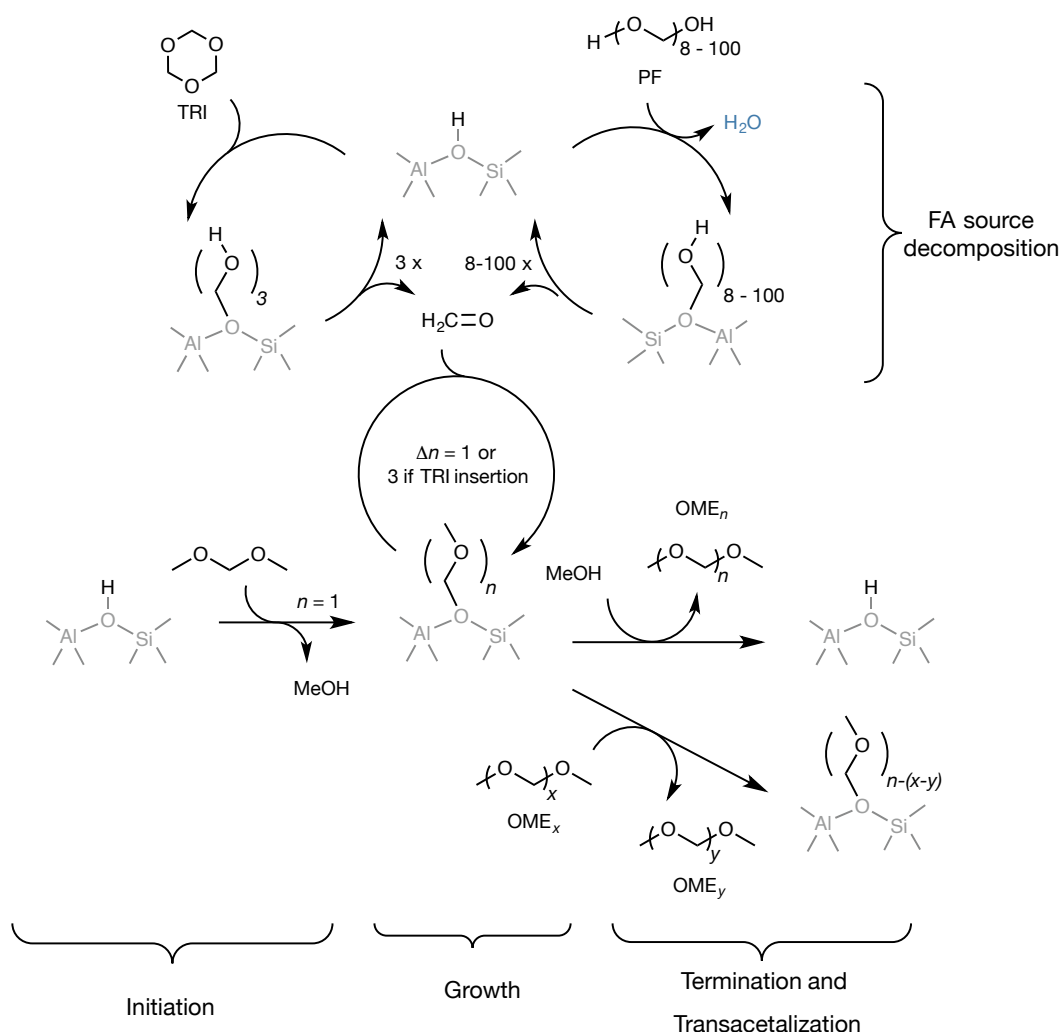
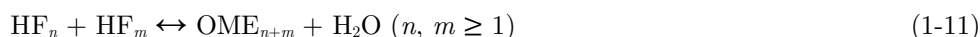
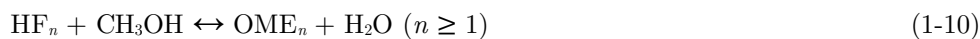
During sequential addition, formaldehyde monomers are inserted into OME_1 according to equations (1-7) and (1-8). Monomeric formaldehyde is provided by TRI or PF decomposition. Various elementary steps were reported in the literature. Arvidson et al. first suggested that protonated formaldehyde is inserted into OME with lithium bromide as a promoter using an Amberlite IR120 ion-exchange resin catalyst.^[84] Burger et al. subsequently built a model based on a customized Langmuir–Hinshelwood–Hogan–Watson mechanism in which monomeric formaldehyde and OME chemisorb before a surface addition reaction occurs.^[74] More recently, various authors suggested an Eley-Rideal mechanism where chemisorbed, monomeric formaldehyde reacts with OME in the liquid phase on sulfated active sites in an NKC-9 ion-exchange resin and on Brønsted acid sites of an H-ZSM-5 zeolite.^[40,81,85] Scheme 1-6 depicts the proposed reaction mechanism.^[81]



Scheme 1-6. Eley-Rideal reaction scheme representing the sequential addition mechanism for the synthesis of OME_2 from OME_1 and formaldehyde on an acidic surface where H represent an acidic active site on a surface based on Wu et al.^[81]

On the other hand, OME synthesis follows an initiation, growth and termination (IGT) chain growth mechanism in aqueous phase or when using catalysts able to stabilize carbocations such as ILs or zeolites. The main difference compared to the sequential addition mechanism is that the IGT mechanism involves an intermediate during the growth phase. Two reaction intermediates have been reported in the literature: carbocations and hemiformals. Hemiformals (HFs, $\text{CH}_3-(\text{O}-\text{CH}_2)_n-\text{OH}$) are intermediates produced from methanol

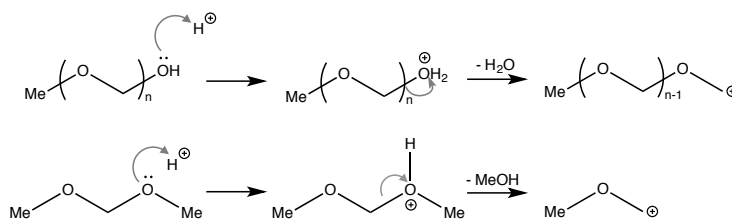
reacting with formaldehyde according to equations (1-4) and (1-5), which describe the initiation and chain growth reactions. They can react under acidic conditions with methanol to produce OME through acetalization (1-10) and a combination reaction (1-11), which are the termination reactions for HF's chain growth. Scheme 1-7 provides an overview of the IGT reaction mechanisms over a bridging hydroxyl group in a zeolite.^[115]



Scheme 1-7. Overview of the initiation-growth-termination mechanism for the anhydrous synthesis of OME from OME_1 and TRI/PF over a bridging hydroxyl group.^[115]

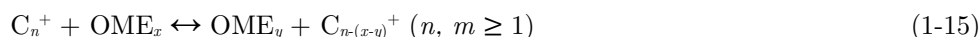
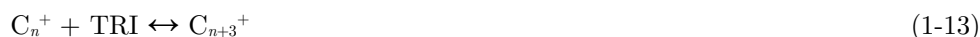
Carbocations (C_n^+ , $\text{CH}_3\text{-(O-CH}_2\text{)}_{n-1}\text{-O-CH}_2^+$, $n \geq 1$) are produced as shown in Scheme 1-8, through dehydration of HF's or the loss of a methanol group upon OME protonation. They require stabilization that can be provided by the solvent or the catalyst. Their presence in other polar, protic solvent, i.e. water, methanol has not been confirmed. Two mechanisms

contribute to OME growth: FA incorporation or direct TRI insertion, according to equations (1-12) and (1-13), respectively. Both require the OME to be in an intermediate state. According to two DFT studies that investigated the reaction of TRI and OME₁ over an H-Beta zeolite and a trimethyloxonium salt, both mechanisms contribute simultaneously to OME growth due to their similar activation energy.^[115,116] Direct TRI insertion should be slightly more favored as its required energy of activation is smaller (55 kJ · mol⁻¹) compared to FA incorporation (63 kJ · mol⁻¹) in zeolite H-Beta.



Scheme 1-8. Carbocation initiation from HF's and OME₁

Equation (1-14) describes the termination reaction as well as the initiation reaction in the backward direction. Finally, an OME being in an intermediate form can exchange a certain number of formaldehyde units with another OME during transacetalization (1-14). All OME activation energies differ only by 10 kJ · mol⁻¹, which explains why OME synthesis from OME₁ and TRI is unselective to OME₄ and lead to a Schulz-Flory distribution after a prolonged reaction time. The formation of a preferential chain length is an intricate challenge, due to this rapid transacetalization as illustrated in Scheme 1-7. With SO₃H-ILs as catalysts, DFT calculations suggested a carbocation mechanism for OME₁, and a hemiformal-carbocation pathway for methanol.^[114] Monomeric formaldehyde was provided by TRI or PF decomposition.



Hitherto, most OME syntheses routes required a methyl-end group provider and an oxymethylene source. PF or TRI are often used as *in situ* sources of the oxymethylene group, which implies two conceivable reaction pathways in OME syntheses. The first is a reaction

without prior TRI decomposition or with PF partial decomposition. The second is a complete decomposition of PF or TRI before the reaction. Wang et al. calculated by DFT that TRI observes a two-step decomposition mechanism on SO_3H -ILs prior to reaction with methanol or OME_1 .^[114] First, TRI is protonated causing ring opening and formation of a linear trioxymethylene intermediate. Subsequently, the intermediate form decomposes to produce three formaldehyde monomers. In contrast to TRI, PF containing three oxymethylene moieties decompose in a one-step mechanism before reaction with methanol or OME_1 . PF simultaneously gets protonated, releases a water molecule and decomposes. For longer PF molecules, however, an unzipping mechanism is reported in which formaldehyde monomers are produced one by one.^[21,50,85] The availability of monomeric formaldehyde from the decomposition of its precursor compounds probably plays a significant role on the product distribution, side product formation and reaction kinetics.

1.4.2 Simultaneous vs. sequential OME synthesis

The OME synthesis follows two different types of reaction pathways: a sequential or a simultaneous. In one type of reaction pathway, longer chains are not detected at the start of the reaction whereas in the other type, chains of all lengths are observed right from the beginning. This difference can be observed in the shape of the product distributions plotted in Figure 1-1.

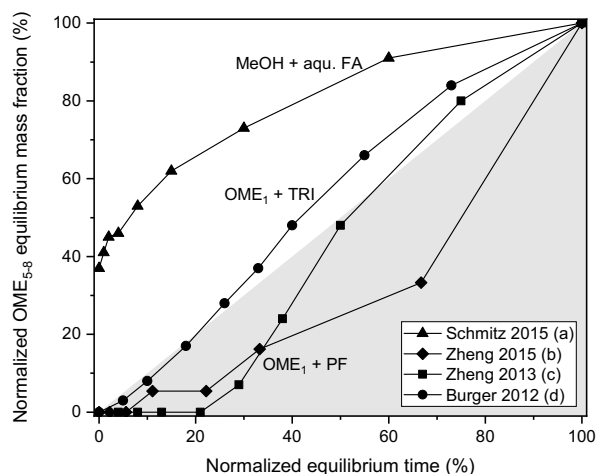


Figure 1-1. Normalized OME_{5-8} product weight fraction as a function of normalized reaction time to equilibrium. The reactions conditions are: (a) Schmitz 2015, $T = 90\text{ }^\circ\text{C}$, $\text{MeOH}/\text{FA} = 1:1.16$, 12.73 g A46. (b) Zheng 2015, $T = 60\text{ }^\circ\text{C}$, $\text{OME}_1/\text{PF} = 2:1$, 5 wt % NKC-9. (c) Zheng 2013, $T = 80\text{ }^\circ\text{C}$, $\text{OME}_1/\text{PF} = 3:1$, 1.0 wt % NKC-9. (d) Burger 2012, $T = 50\text{ }^\circ\text{C}$, $\text{OME}_1/\text{TRI} = 2.42:1$, 0.91 wt % A46. Data points were connected for the sake of clarity.

Schmitz et al. obtained simultaneous OME formation with methanol and aqueous formaldehyde.^[66,67] According to them, the reactions for the formation of HFs (1-4) and their growth (1-5) are fast compared to termination reactions—acetalization (1-10) or combination (1-11). HFs would thus have a product distribution in pre-equilibrium and would form OME of various chain lengths when the termination reactions start. In comparison, various authors who worked with OME₁ and TRI or PF, i.e. the anhydrous synthesis route, have reported sequential formation that corroborates with the sequential addition or IGT mechanisms for the synthesis of OME.^[40,74,85] Additionally, Figure 1-1 suggests that longer OME are more readily obtained when using TRI as the source of monomeric formaldehyde instead of PF. Two possibilities could explain this observation. First, the slower release of monomeric formaldehyde due to PF depolymerization mechanism could explain this observation since monomeric formaldehyde is not available to react during OME synthesis. Second, direct addition of TRI into OME followed by transacetalization could account for this increased amount of larger OME produced in the beginning of the reaction.

1.4.3 Reaction mechanisms for the direct, one-step selective synthesis of OME

Reaction mechanisms involved in the direct, one-step selective synthesis of OME differs from chain growth reactions. According to Tatibouët et al., OME₁ one-pot synthesis from methanol over metal oxide catalysts occurs according to the following mechanism.^[93] First, methanol is strongly adsorbed on the catalyst surface or forms a methoxy surface group, which is further oxidized to an adsorbed formaldehyde or dioxomethylene specie. These intermediates then react with methanol to form surface-bound hemimethylal species (CH₃OCH₂O-). Finally, another methanol molecule reacts with the hemimethylal specie to form OME₁. The authors suggested that on the surface of unsupported V₂O₅, methanol could be activated through homolytic C-H bond breaking to form highly reactive radical species •CH₂OH. The latter would then react with adsorbed methanol or methoxy species to form HF₁ adsorbed via the oxygen atom of the oxymethyl group. The redox and acid properties of the catalyst are thus key to guide the reaction towards the desired pathway.

Another study on OME₁ and methyl formate formation was conducted by Liu et al. over RuO₂ on various supports.^[94] According to them, methanol oxy-dehydrogenation to formaldehyde requires C-H activation during which lattice oxygen abstracts the hydrogen atom to subsequently form water. Dissociative chemisorption of oxygen from the feed completes the Mars-van Krevelen redox cycle by filling the oxygen vacancies. OME₁ is produced via secondary reactions on the acid sites of Al₂O₃ or SiO₂. Methyl formate will be preferentially formed if SnO₂, ZrO₂ or TiO₂ containing redox and amphoteric sites are used as supports instead.

The direct, selective OME₁ synthesis from DME was suggested to start with the irreversible DME dissociation via concerted reactions with lattice oxygen and a metal center to form two methoxy species.^[95,117] The latter undergoes subsequent reaction with hydroxyl groups to form methanol. They also form formaldehyde by hydrogen transfer that regenerates the hydroxyl groups. The mechanism of subsequent OME₁ formation has not been described but can be assumed similar to what has been explained before. No mechanism was yet proposed for the synthesis of larger OME in the gas phase except by Zhang et al. They suggested a C-H bond cleavage of OME₁ to form a CH₃OCH₂OCH₂- group that reacts with a methoxy group to form OME₂.^[88]

1.4.4 Molecular size distribution

Studies with different catalysts and reactant types reported that the molecular size distribution of OME under equilibrium conditions follows the Schulz-Flory (SF) distribution.^[40,81,109,114] It was also reported to describe the transient product distribution.^[86] SF distribution is generally used in polymer chemistry. It entails that the product distribution is purely statistical and that the reactivity of OME is independent of the chain length. It is determined by the probability of chain growth on a catalyst^[118]:

$$x_n = (1-\alpha) \cdot \alpha^{(n-1)} \text{ with } (n > 0) \quad (1-16)$$

Where n , x_n and α are the chain length, the molar fraction of products with a chain length of n and the probability of chain growth, respectively. Larger α refers to the larger average molecular weight of the produced OME. Compared to polymer chemistry, relatively low values of α have been reported, which translates into a OME product distribution containing mainly low molecular weight molecules. Similarly, the SF distribution can predict the

product distribution resulting from the Fischer-Tropsch (FT) reactions.^[118] However, some deviations for FT reactions exist, notably a higher and lower selectivity for C_1 and C_2 , respectively. No study has hitherto reported deviations from the SF distribution for the synthesis of OME, due to the small difference in activation energy between the OME of various sizes ($10 \text{ kJ} \cdot \text{mol}^{-1}$).^[115]

A first attempt to influence the OME selectivity was reported, in which the authors used different porous catalysts to investigate the effect of pore size on selectivity using the catalysts USY-1, USY-3 (60) (micropores), C_{10} -AS-50 (supermicropores = between micropores and mesopores) and C_{16} -Al-SBA-1 (mesopores) for OME synthesis.^[79] With C_{10} -AS-50, they managed to increase the OME_{3-8} selectivity by 4.6 % and 2.9 % compared to microporous and mesoporous materials, respectively. The catalyst had a similar number of acid sites and comparable acid strength. They reasoned that the selectivity achieved is matching between the pore dimension and the calculated size of the different OME leading to a partially restricted diffusion into the super-microporous materials.

1.4.5 Kinetic models

Kinetic investigation is a necessary step for reactor design and a tool for determining or confirming the reaction mechanism. Several kinetic investigations of OME synthesis have been reported in the literature as shown in Table 1-5. These kinetic models were built using reaction data from different catalysts, reactant types and reaction conditions. Each of them also have different underlying assumptions. It is therefore difficult to compare the calculated parameters, e.g. activation energies and pre-exponential factors.

Table 1-5. Available kinetic models for the synthesis of OME.

Model	Catalyst	Reactants	Reactor type	Ref.
Modified LHHW ^[a]	Ion-exchange resin A46	OME_1 & TRI	Batch	[74]
Pseudo-homogeneous	Ion-exchange resin A46	MeOH & FA	Batch	[67]
Power law	Ion-exchange resin	MeOH & FA	Plug Flow	[65]
Power law	Ion-exchange resins NKC-9	OME_1 & PF	Batch	[40]
Power law	ZrO_2/TiO_2	MeOH & FA	Plug Flow	[64]

^[a] LHHW = Langmuir–Hinshelwood–Hougen–Watson

Burger et al. first modelled the reaction of TRI and OME_1 over the acidic ion-exchange resin A46.^[74] They used a modified Langmuir–Hinshelwood–Hougen–Watson reaction

mechanism in which they assumed fast, at-equilibrium reactions of adsorbed species on the catalyst surface and rate-limiting sorption processes. They also assumed, based on the similar properties of OME of different chain length, that the adsorption and desorption rate constants are independent of the chain length. Furthermore, they assumed that all surface reaction equilibrium constants are independent of the length.

Their kinetic model describes closely the recorded concentrations of products, from different starting reactant concentrations. However, they considered that the decomposition of TRI requires three active sites to hold the protonated formaldehyde. Hence, they did not consider that any monomeric formaldehyde was in the reaction mixture. This is contrary to the DFT calculations that highlighted a TRI decomposition into three formaldehyde monomers, which subsequently interact with the sulfonic group of the ILs.^[114]

Zheng et al. built a kinetic model based on a sequential, reversible addition mechanism using OME₁ and PF with 5 wt % of NKC-9 ion-exchange resin.^[40] They assumed a first-order kinetics with respect to each reactant. They thus obtained second-order kinetics for the forward addition and a first-order kinetic for the reverse reaction. The model globally follows concentration trends but was not able to describe the transient period. This can be particularly observed from the differences between the model predictions and the experimental data for OME₂₋₃ concentrations. The following assumptions were made in their study: (i) the concentration of formaldehyde was considered constant during the reaction, (ii) the forward and reverse sequential addition constants were considered independent of the chain length, (iii) chain lengths of maximum 6 formaldehyde unit were considered, (iv) a constant volume with average density of 1.0 g·cm⁻³ was assumed. Water and methanol were not considered in the model, since the maximum calculated amount of water in the mixture was 0.7 wt % and the measured amount of methanol was less than 1 wt %.

Zhang et al. modelled OME synthesis in a continuous setup.^[64,65] Using methanol and aqueous formaldehyde with an ion-exchange resin as catalyst, they built a model based on a sequential addition mechanism even though their reaction was in aqueous conditions. They considered that OME₁ was first produced by reaction (1-10) and grew through subsequent sequential addition of monomeric formaldehyde. However, only fair agreement between model prediction and experimental data could be achieved. They also built a second model of OME synthesis from methanol and aqueous formaldehyde using ZrO₂/TiO₂ as catalyst.^[64]

In contrast to their other model, they applied an IGT chain growth mechanism with HFs as intermediates. They considered: (i) initiation by reaction (1-4) and the reverse of reaction (1-10); (ii) termination of HF_s only through combination reaction (1-11) of HFs with HF₁. Although they did not include reactions between monomeric formaldehyde and HFs, a good data-model fit was achieved, with a coefficient of determination larger than 0.99.

Schmitz et al. used a pseudo-homogeneous approach to model the reactions of methanol and aqueous formaldehyde with an A46 ion-exchange resin.^[67] They assumed that the active sites of the resin are homogeneously distributed and freely accessible in the reaction mixture. Their kinetic model accounted for formaldehyde forming MGs and HFs in fast pre-equilibrium reactions. OME formation was considered to proceed via sequential growth addition and IGT chain growth mechanism. It was found that when the reaction was conducted in the absence of OME₁, the model without the sequential addition correctly predicts the experimental data. When OME₁ was fed along with methanol and aqueous formaldehyde, only the combined model described properly the experimental data. They assumed that acetalization and sequential addition reaction rates as well as the growth constant were independent of the chain length. They accounted for limited chain length of 10 for HFs and MGs.

A reliable model for the synthesis of OME must predict the evolution of the concentrations inside the reactor when recycled products are being fed together with reactants. Burger et al. tried a pseudo-homogeneous model which fitted the experimental data except when OME₂ and OME₁ were fed into the reactor.^[74] Schmitz et al. faced similar issues and changed their model by including a growth reaction to accurately predict product and reactant compositions.^[67] The model presented by Zheng et al. seems to accurately predict the results when OME₅₋₆ are fed into the reacting mixture.^[40] However, the test experiments with OME₅ and OME₆ were conducted with an unrealistically high concentration of approximately 1 mol·L⁻¹ and 0.25 mol·L⁻¹, respectively, compared to the expected concentration of these components during OME synthesis after 100 min. It would be of high interest to test the model-data fit with a feed of OME₂. Other models did not confirm their calculations when recycling was considered.^[64,65]

1.5 Challenges for OME catalysts

In a context of increasingly stringent regulations related to exhaust emissions and with the lack of alternatives to traditional liquid fuels for long-distance transport, OME are a promising fuel for the future of mobility. Adoption of this new technology as an alternative to Diesel fuel only makes sense if its production has a global, positive impact on the environment. Throughout Chapter 1, we have identified various key challenges that need to be addressed by means of research on heterogeneous catalysis before the OME technology can potentially reach consumers' cars.

The first challenge identified is that despite preliminary research on selecting suitable catalysts for OME synthesis, there is a significant lack of understanding of their structure-relationships. Various catalysts demonstrated promising performance for OME synthesis, but comparison of their activity is arduous due to different reaction conditions, reactants and important differences in the catalyst features. Consequently, little is known about the reaction mechanisms and the elementary steps involved during OME synthesis. Understanding structure-activity relationships is an essential step to design catalysts and processes that efficiently produce OME at a large scale.

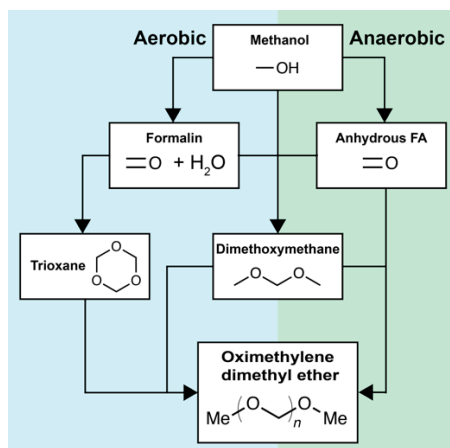
The second issue is that any OME synthesis routes generates a mixture of OME with various chain sizes, whose distribution is dictated by thermodynamics and characterized by the Schulz-Flory distribution. The largest fraction of the reaction products is comprised of OME₁₋₂ limiting the selectivity towards the products of interest (OME₃₋₅). Significant separation and stream recycling efforts are subsequently required to obtain high purity OME₃₋₅ which satisfy commercial fuel regulations. An ambitious goal is to increase the selectivity to OME₃₋₅, despite the thermodynamic limitations of this approach.

The last challenge is that current synthesis routes for the production of OME involve production of costly intermediates such as OME₁ or trioxane (TRI). Synthesis of these compounds is either expensive or energetically inefficient, leading to uneconomical production or modest reduction of CO₂ footprints. A recent study done by Schmitz et al. assessed the production costs of large-scale OME synthesis.^[119] The major costs were predicted to be of around 60 % for raw materials and 20 % for energy consumption. Price and availability were highlighted as the most important criteria by German drivers for the adoption of

alternative fuels, including OME.^[120] Therefore, design of simpler reaction pathways is essential to increase the OME production efficiency and reduce production costs in order to become price competitive with conventional fossil fuels.^[121] Current research efforts focus on simplifying the existing processes by using fewer steps and simpler reactants such as formaldehyde and methanol.

1.6 Aim and scope of the thesis

The goal of this work is to advance knowledge in the field of heterogeneous catalysis to make the OME production technology more sustainable. Based on the identified key challenges, our research focus is three-fold. The first aspect of this work is to find structure-activity relationships for OME synthesis using TRI and OME₁, being the predominant reaction pathway suggested in the literature. The second is to improve the performance of the current catalysts and to develop new active catalysts with optimized yields towards OME₃₋₅. Lastly, we aim to investigate water-free catalytic dehydrogenation of methanol to formaldehyde as the oxymethylene source, as a possible alternative to the usage of TRI (Scheme 1-9).



Scheme 1-9. Usage of anhydrous formaldehyde from methanol catalytic dehydrogenation reduces the number of steps for OME production.

The thesis is divided in three parts. The first part focuses on the improvement of catalysts performance based on modification of the catalysts structure for the synthesis of OME from TRI and OME₁ (Chapter 3 - Chapter 4). First, the accessibility to the active sites of an H-ZMS-5 zeolite is modified by various means to assess how it impacts the zeolite activity. Then, tin-montmorillonite clay is investigated as a cheaper and eco-friendly alternative

catalyst to the usage of zeolites and acidic resins. The two chapters are based on publications in “Catalysis Science & Technology”^[122] and “ChemCatChem”^[123].

In the second part of this work, the influence of the acidity and water on both reaction kinetics and mechanisms was assessed using Beta zeolites (Chapter 5 - Chapter 6). A series of Beta zeolites was used to study the synergy between Brønsted and Lewis acidity. Next, the inhibiting effect of water on the reaction kinetics was investigated by means of a combination of catalytic tests and *in situ* experiments using infrared spectroscopy. The two chapters are based on a publication in “ChemSusChem”^[124] as well as one manuscript in preparation^[125].

The last part summarizes our attempts to use catalytic dehydrogenation of methanol as a water-free source of oxymethylene for the production of OME (Chapter 7).^[126] Finally, Chapter 8 presents an overview of the thesis and suggests future opportunities in this field of research.

Chapter 2 Experimental

2.1 Preparation of catalysts

Various types of catalysts were used to catalyze the synthesis of OME and the dehydrogenation of methanol. Zeolites NH₄-ZSM-5 and NH₄-Beta were purchased from ABCR, sodium-exchanged montmorillonite clay was obtained from Fluorochem and Aerosil® 200 (fumed silica) was received from Evonik industries. All post-synthetic treatments performed on the various materials are described in the corresponding chapters. Unless mentioned otherwise, powder calcination was performed under static conditions at 550 °C with a ramp rate of 5 °C · min⁻¹.

2.2 Catalytic tests

2.2.1 Set-up for the synthesis of OME

As described in section 1.2, various reactants can be used for the production of OME. In this thesis, the anhydrous OME synthesis route, which involves OME₁ and TRI, was investigated in details. Two other OME synthesis reactions were also performed: the reactions of OME₁ with PF, as well as FA with MeOH (methanol). Besides, OME₂ equilibration to a Schulz-Flory distribution of OME, and TRI decomposition in dichloromethane (CH₂Cl₂) were also studied. TRI (99 %) and PF were purchased from Sigma-Aldrich. Unless mentioned otherwise, OME₁ (99.0 %) was obtained from Sigma-Aldrich. OME₂ to OME₆ (99.0 %) were purchased from ASG Analytics. A methanolic formaldehyde solution was prepared from PF and MeOH. PF was dissolved in MeOH and heated overnight at 60 °C under magnetic stirring with the addition of a few drops of base (sodium methoxide), followed by filtration of the undissolved PF.

Synthesis of OME were performed in two setups described in Figure 2-1. The first is a 450 mL stirred batch reactor manufactured in 316 stainless steel under a pressure of 5 bar of Ar. Typically, 30.83 g of TRI and 85.93 g of OME₁ were loaded, followed by three purges of Ar prior to mixing and heating the mixture to the reaction temperature (Figure 2-1a).

The temperature and pressure were measured respectively with a J-type thermocouple and a membrane pressure gauge. The reactor was thermostated with an electrically heated jacket. A stirring speed of 450 rpm was used, above the limit value of 300 rpm suggest by Zheng et al., to ensure that no external mass-diffusion limitation was detected.^[40] Samples (0.3 mL) were taken from the bottom of the reactor using a sample valve composed of a dip tube and a heat exchanger to cool the samples at 30 °C. Injection of the catalyst in the reactor was considered as the start of the reaction and was performed using a pressurized solid charging system.

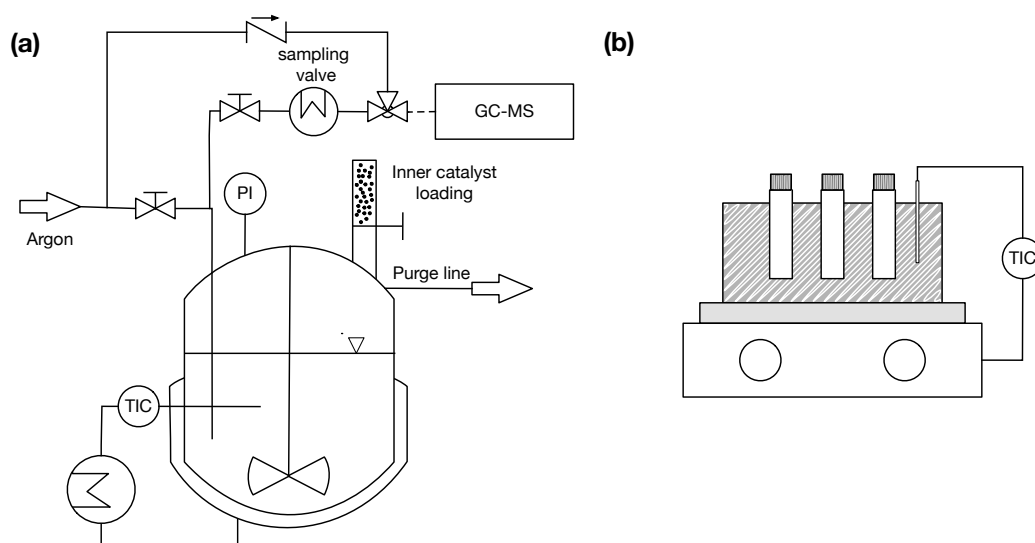


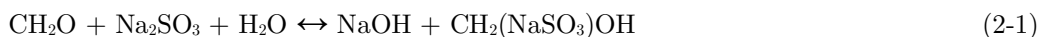
Figure 2-1. (a) The 450 mL stirred batch reactor and (b) 10 mL glass reactors immersed in a thermostated medium on a stirring plate. PI: pressure indicator. TIC: temperature indicator and control.

The second set-up used for OME synthesis (Figure 2-1b) was operated with 10 mL pressure resistant glass reactors (Grace GmbH). Typically, the catalyst powder was weighted, inserted in the reactors before the reaction, and dried overnight in the oven at 110 °C. To ensure minimal exposition to water, reactors were capped immediately after being removed from the oven and allowed to cool down to RT. Then, the reactants were added and the reactors were subsequently immersed in thermostated water or silicon oil, depending on the reaction temperature. The time of immersion of the reactors was considered as the start of the reaction.

Unless mentioned otherwise, all OME synthesis experiments were conducted with a OME₁/TRI molar ratio of 3.3 and 0.5 wt % of catalyst. A catalyst loading of 1.0 wt % was used for the reusability test with a reaction time of 60 min. TRI decomposition in CH₂Cl₂

was done using a similar method, using a 10 wt % TRI solution of DCM, previously dried over molecular sieve. Reactors were loaded with 2 wt % catalyst, relative to TRI.

An Agilent 7890B/5977A series gas chromatography mass spectrometer (GC-MS) was used for the analysis of the liquid samples. It was equipped with an HP-5 capillary column (length 30 m, outer diameter 0.32 mm, film 1.05 μm) and an automated liquid sampler. A dean switch was used to send the eluent to a flame ionization detector (FID) or to the mass spectrometer. OME₁₋₆, MeOH and methyl formate were quantified using a calibration curve. OME₇₋₈ calibration curves were constructed based on the effective carbon number method and an extrapolation of the detector response from OME₁₋₆.^[127] Formaldehyde concentration was determined by three successive titrations using the sodium sulfite method. Formaldehyde reacts with sodium sulfite in equimolar quantity to produce NaOH according to reaction (2-1), which can be then titrated.^[60]



Conversion of trioxane (X_{TRI}), selectivity to OME₃₋₅ ($S(\text{OME}_{3-5})$) and growth probability (α) were used to quantify the performance of the catalysts for the synthesis of OME and were defined as:

$$X_{\text{TRI}} = \frac{[\text{TRI}]_0 - [\text{TRI}]}{[\text{TRI}]_0} \quad (2-2)$$

$$S(\text{OME}_{3-5}) = \frac{\sum_{i=3}^5 [\text{OME}]_i}{\sum_{i=2}^8 [\text{OME}]_i} \quad (2-3)$$

$$\log \alpha = \frac{\log[\text{OME}]_{n+1} - \log[\text{OME}]_n}{n} \quad (2-4)$$

2.2.2 Set-up for the catalytic dehydrogenation of methanol

Dehydrogenation of methanol (MeOH) was performed using the experimental set-up shown in Figure 2-2. Argon was used as the carrier gas and MeOH was introduced in the feed via a MeOH bubbler (a). The reaction was performed in a 10 mm quartz-tube, fixed bed reactor (b) with a heating element allowing the temperature to reach 800 °C. Quartz wool was used to support the catalyst and to ensure proper gas mixing. The gas flows were calibrated using a bubble flowmeter (c). Gas compositions were analyzed using an online Fourier transform infrared spectrometer (FTIR) Bruker Matrix MG-01 FTIR (d),

equipped with a 10 cm gas cell heated at 120 °C. Infrared spectroscopy was chosen because it was more advantageous for analysis of transient effluent compositions compared to gas chromatography, which has a poor time resolution. The FTIR instrument had a spectral resolution set at 1 cm⁻¹. The OPUS GA software was used for quantification of the gas composition based on the collected IR spectra.

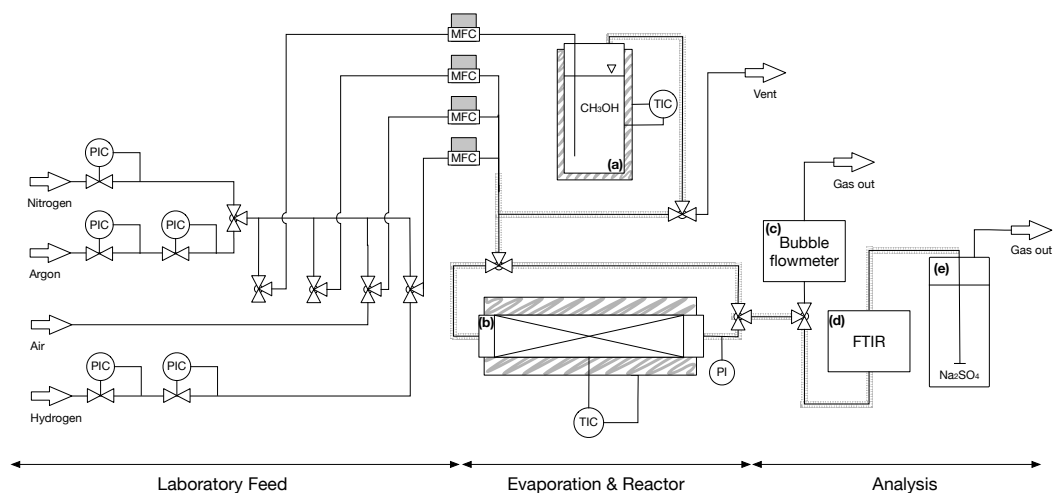


Figure 2-2. Set-up used for the catalytic dehydrogenation of MeOH in the gas-phase. (a) MeOH bubbler; (b) reactor; (c) bubble flowmeter; (d) Fourier transform infrared spectrometer (e) formaldehyde scrubber. PIC, pressure indicator and control; MFC, mass flow controller; TIC, temperature indicator and control; PI, pressure indicator. Heated lines are shown thicker.

The catalytic tests were conducted in a 10 mm tubular, fixed-bed reactor. For each test, the desired amount of catalyst was weighted, loaded in the reactor and fixed in place using quartz wool. Each catalyst was first dried under a 50 mL · min⁻¹ Ar flow at 650 °C using a ramp rate of 10 °C · min⁻¹, until no more water was detected. The Ar flow was then switch to bypass the reactor and MeOH was introduced via a bubbler thermostated at 30 °C to reach a total Ar flow of 100 mL · min⁻¹ (1.5 % MeOH). The flow was introduced to the reactor when the MeOH concentration was stable. The reactor was working at atmospheric pressure for all catalytic tests.

The following performance indicators were used to compare the performance of each catalyst sample: MeOH conversion (X_{MeOH}), selectivity towards formaldehyde (S_{FA}), yield of formaldehyde (Y_{FA}). They are defined as follows:

$$X_{\text{MeOH}} = \frac{[\text{MeOH}]_{\text{in}} - [\text{MeOH}]_{\text{out}}}{[\text{MeOH}]_{\text{in}}} \quad (2-5)$$

$$S_{FA} = \frac{[FA]_{out}}{[MeOH]_{in} - [MeOH]_{out}} \quad (2-6)$$

$$Y_{FA} = \frac{[FA]_{out}}{[MeOH]_{in}} \quad (2-7)$$

To ensure that all reaction products were monitored, a carbon balance across the system was conducted for each experiment and was defined as follow:

$$C_{balance} = [MeOH]_{out} + [FA]_{out} + 2 * [DME]_{out} + [CO_2]_{out} + [CO]_{out} + [CH_4]_{out} \quad (2-8)$$

To regenerate the catalyst activity after coking, temperature programmed oxidation (TPO) procedures were performed *in situ* using the following method. Under a 50 mL · min⁻¹ Ar flow, the sample temperature was first decreased to 300 °C. Next, synthetic air (40 mL · min⁻¹) was introduced to the reactor. When no more desorption products were detected at 300 °C, the sample temperature was raised to 700 °C using a 10 °C · min⁻¹ ramp rate. Following the TPO and before the next catalytic test, the sample was purged at 650 °C with a 50 mL · min⁻¹ Ar flow.

2.3 Characterization techniques

2.3.1 X-ray diffraction (XRD)

X-ray diffraction (XRD) patterns were recorded using a D8 advance Bruker instrument equipped with a 1D-LynxEye detector (Cu K α radiation, no monochromator, Ni filter) with a step size of 0.01°.

2.3.2 Inductively coupled plasma optical emission spectrometry (ICP-OES)

Elemental analyses were performed using inductively coupled plasma optical emission spectrometry (ICP-OES) on a Vista pro AX Varian instrument. Two methods were used to dissolve the powders. 50 mg of zeolite or Aerosil silica was digested in a 10 mL aqueous solution containing 0.5 mL of 65 % nitric acid, 0.5 mL of 40 % hydrofluoric acid and 0.25 mL of 30 % hydrochloric acid for 2 h at 95 °C. Clays were dissolved using a 1:2:2:2 mixture of HCl (30 wt %), HNO₃ (65 wt %), H₂SO₄ (96 wt %) and HF (40 wt %).

2.3.3 N₂ physisorption

N₂ physisorption experiments were performed on a Micrometrics 3Flex apparatus at liquid nitrogen temperature and N₂ relative pressures between 10⁻⁵ and 0.99. Typically, samples (ca. 150 mg) were dried at 120 °C (temperature ramp 5 °C · min⁻¹) for 5 h under vacuum. A leak test was performed before the analysis. Brunauer-Emmett-Teller (BET), Barrett-Joyner-Helenda (BJH) and t-plot methods were used to calculate the specific surface area, the mesoporous and microporous volume, respectively.

2.3.4 X-ray photoemission spectroscopy (XPS)

XPS spectra were measured on a PHI VersaProbe II scanning XPS microprobe (Physical Instruments AG, Germany) with a monochromatic Al K α X-ray source of 24.8 W power and a 100 μ m beam size. The measurement accuracy of the instrument was of 0.1 eV.

2.3.5 Magic angle spinning solid-state nuclear magnetic resonance (MAS-NMR)

Magic angle spinning nuclear magnetic resonance (MAS-NMR) was used to study the coordination and chemical environment of Al, Si and Sn. ²⁷Al and ²⁹Si spectra were collected on a 400 MHz Bruker Avance III HD spectrometer with a spinning rate of 35 and 15 kHz, respectively. ¹¹⁹Sn spectra were recorded at room temperature on a 500 MHz Bruker instrument equipped with a 11.7 T magnet (proton frequency) with a spinning rate of 20 kHz. The Carr-Purcell-Meiboom-Gill (CPMG) pulse sequence was performed on a 900 MHz Bruker Avance instrument to increase the sensitivity due to the low natural abundance of the ¹¹⁹Sn isotope. All other spectra were recorded at 298 K with a single-pulse and the typical acquisition was 1024 scans.

2.3.6 Electron Microscopy

Structure of the sample was observed by transmission electron microscopy (TEM) or high-angle annular dark-field scanning transmission electron microscopy (STEM) on a FEI Tecnai Osiris with 200 kV acceleration voltage. Grids were prepared by deposition of a drop of ethanol suspension (99.8 %, Fisher Chemical) containing the sample on a Lacey carbon grid. Energy-dispersive X-ray spectroscopy (EDXS) analysis was performed on the Bruker Esprit Software.

Scanning Electron Microscopy (SEM) was performed on a Zeiss Gemini SEM 300 electron microscope with acceleration voltage of 3 kV and with Everhart-Thornley secondary electron detector to study the morphology of the clay particles. For SEM-EDX analysis, the microscope was equipped with an Oxford detector X-max^N and EDX measurements were performed by means of AZtec software. To acquire X-rays signal from all elements present in the sample, an e-beam acceleration voltage of 6 kV was applied.

2.3.7 NH₃- and di-tert-butyl-pyridine-temperature programmed desorption

The concentration of acid sites was calculated from NH₃ temperature programmed desorption (NH₃-TPD) experiments using a Micromeritics Autochem 2920 II instrument. Typically, the sample (ca. 100 mg) was loaded in a U-shaped quartz cell and dried with a He flow (50 mL · min⁻¹) at 550 °C (2 °C · min⁻¹; hold time of 120 min). Saturation of the sample with NH₃ was done using a 1:99 NH₃:He (volumetric ratio) flow during 1 h at 50 °C. Physisorbed NH₃ was then removed with He (50 mL · min⁻¹). The temperature was then increased to 600 °C (10 °C · min⁻¹) and NH₃ was monitored using a calibrated thermal conductivity detector. For clays, a temperature of 200 °C was used for drying due to their sensitive structure and NH₃ desorption was monitored using a calibrated MKS Cirrus II mass spectrometer (mass 16).

Acidity of the external surfaces was characterized by temperature programmed desorption of 2,6-di-tert-butyl-pyridine (DTBPy). The same method as the NH₃-TPD technique was used except that the saturation of the samples was done using 50 loops of 0.1 mL of saturated vapor of DTBPy at 150 °C instead of NH₃:He mixture. An MKS Cirrus II mass spectrometer monitored the desorption (mass 149 corresponding to 2-tert-butyl-6-methylpyridine). As no calibration was performed, the measurements were only qualitative.

2.3.8 Methanol-temperature programmed desorption

The temperature programmed desorption of MeOH (MeOH-TPD) was performed using the set-up described in section 2.2.2. During the procedure, 150 mg of catalyst was dried under a 50 mL · min⁻¹ flow of Ar at 650 °C (10 °C · min⁻¹), until no more water was detected in the reactor outlet. The reactor temperature was then lowered at 350 °C and the sample was saturated with MeOH for 60 min with a 100 mL · min⁻¹ Ar flow (1.5 %

MeOH). While maintaining the MeOH flow, the temperature was lowered to 50 °C and the saturation continued for 1 h once 50 °C were reached. Afterward, the sample was purged with a 50 mL · min⁻¹ flow of Ar to remove physisorbed MeOH. The sample temperature was then raised to 800 °C (10 °C · min⁻¹) and the desorption profiles of MeOH, FA and CO were monitored with the online FTIR.

2.3.9 CO₂-temperature programmed desorption

The CO₂-temperature programmed desorption (CO₂-TPD) experiments were performed on a Micromeritics Autochem 2920 II instrument. The sample (0.15 g) was first dried during 2 h at 550 °C using a 50 mL · min⁻¹ flow of He (10 °C · min⁻¹ ramp rate). Then, the sample was saturated with CO₂ at 50 °C by a continuous flow (50 mL · min⁻¹), followed by a purge step using a He flow (50 mL · min⁻¹) for one hour at the same temperature to remove physisorbed CO₂. Afterwards, the desorption of CO₂ was monitored by an MKS Cirrus II mass spectrometer (mass 44) between 50 and 700 °C. Finally, three injections of a known volume of CO₂ were performed and used as a calibration for the MS signal.

2.3.10 Diffuse reflectance infrared Fourier transform (DRIFT) spectroscopy

Diffuse reflectance infrared Fourier transform spectroscopy (DRIFTS) was performed on a high temperature Harrick DRIFT cell mounted on a Perkin Elmer Frontier spectrometer equipped with a mercury cadmium telluride detector. Ex-situ spectra were recorded with 32 scans at a resolution of 4 cm⁻¹ after being dried 2 h under a He flow of 20 mL · min⁻¹. A drying temperature of 400 °C was used for zeolites and silica powders while a temperature of 200 °C was chosen for clays due to their sensitive nature. Pyridine adsorption experiments were performed using the following procedure: first, the sample was dried and consequently saturated with pyridine vapor at 50 °C for 30 min under a He flow of 20 mL · min⁻¹ bubbling through pyridine at room temperature. Physisorbed pyridine was then removed by flowing pure He (20 mL · min⁻¹) for 30 min. Finally, the temperature was raised to 150 and 300 °C with a ramp rate of 5 °C · min⁻¹.

2.3.11 Diffuse reflectance ultraviolet-visible (DRUV) spectroscopy

Diffuse reflectance UV-Vis spectroscopy (DRUVS) spectra were recorded on a Varian spectrometer equipped with an in-situ Harrick Praying Mantis cell. In-situ measurements were done under a N₂ flow of ca. 20 mL · min⁻¹.

2.3.12 *In-situ* attenuated total reflection Fourier transform infrared (ATR-FTIR) spectroscopy

The nature of the adsorbates on a zeolite H-Beta was investigated using attenuated total reflection infrared spectroscopy (ATR-IR). A homogeneous suspension of the catalyst sample in 2-propanol (8 mg in 1.5 ml) was dried for two hours on the ZnSe internal reflection element (IRE, 52 x 20 x 2 mm, 45°, Crystran). This resulted in the deposition of a homogeneous layer of catalyst on the IRE, which was then mounted in an in-house developed cell.^[128] The cell was placed in a four-mirror ATR-IR assembly (Specac) in the sample chamber of the spectrophotometer (Vertex 70, Bruker). The flow rate was set to 0.3 mL · min⁻¹ using a peristaltic pump (Reglo 100, Ismatec SA). At the inlet of the cell a 4-ports switching valve (Cheminert, VICI) was connected for fast switching between two solutions. The solution switch was synchronized with the acquisition of the IR spectra using the spectrometer software (OPUS, Bruker). Spectra were recorded with an 80 kHz scanner velocity by averaging 12 scans at a spectral resolution of 4 cm⁻¹ using a liquid nitrogen cooled MCT detector. During a typical experiment, the catalyst layer was equilibrated at room temperature in neat cyclohexane for an hour, prior to background collection. Cyclohexane solvent was selected because of its simple IR spectrum.

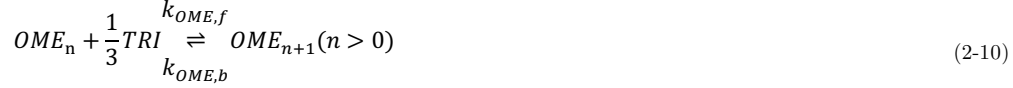
A standard experiment consisted of fifteen periods. Only the last ten periods were averaged for improvement of the S/N ratio, while signal enhancement was obtained by phase sensitive detection (PSD), using a MATLAB script. The phase domain spectra were obtained by mathematical treatment of the time-domain spectra according to the equation:

$$A_k(\varphi_k^{PSD}) = \frac{2}{T} \int_0^T A(t, \nu) \sin(k\omega t + \varphi_k^{PSD}) dt \quad (2-9)$$

where T is the length of a period, ω is the stimulation frequency, k is the demodulation index, φ_k^{PSD} is the demodulation phase angle for $k\omega$ and A(t) and A(φ_k^{PSD}) are the active species response in time- and phase-domain, respectively.^[129]

2.4 Reaction network and kinetic model for OME synthesis

A simplified pseudo-homogeneous kinetic model for the synthesis of OME was derived from a study done by Burger et al.^[74] The model considered that OME are formed from OME₁ and TRI according to:



Where $k_{OME,f}$ and $k_{OME,b}$ are the forward and backward rate constants, respectively. The equilibrium constant of reaction (2-10) was demonstrated to be independent of OME chain length^[74,80] and is defined by:

$$K_{OME}^* = \frac{[OME_{n+1}]}{[OME_n][TRI]^{1/3}} \quad (n > 0) \quad (2-11)$$

Its value can be modelled using the van 't Hoff equation:

$$\ln(K_{OME}^*) = a + \frac{b}{T/K} \quad (2-12)$$

The values of a and b were determined by fitting the experimentally obtained K_{OME}^* value at various temperatures. $k_{OME,f}$ and $k_{OME,b}$ are also assumed to be independent of OME chain length. For reaction (2-10), the reaction rate is:

$$r_{OME_n} = k_{OME,f}([OME_n][TRI]^{1/3} - \frac{1}{K_{OME}^*}[OME_{n+1}]) \quad (2-13)$$

$$\text{where } k_{OME,b} = \frac{k_{OME,f}}{K_{OME}^*}$$

Finally, the evolution of the concentration of component A over time is calculated based on:

$$\frac{d[A]}{dt} = m_{cat} \cdot c_{cat} \cdot \sum_j \nu_j r_j \quad (2-14)$$

where ν is the stoichiometric coefficient of component A in reaction r_j . The model-data fit was calculated based on the root mean square error (RMSE):

$$RMSE = 1 - \frac{1}{n} \sum_i \sum_j \sqrt{([A_{i,j,exp}] - [A_{i,j,model}])^2} \quad (2-15)$$

where n is the number of components and $A_{i,j}$ is the concentration of the i th component of the mixture at time j . The decomposition of TRI to formaldehyde was not considered in the model for two reasons. First, the simplified reaction (2-10) was considered to be adequate to simplify the complexity of the system. Secondly, including TRI dissociation did not significantly improve the model fit.

Chapter 3 Mesoporosity introduction in an H-ZSM-5 zeolite for activity improvement

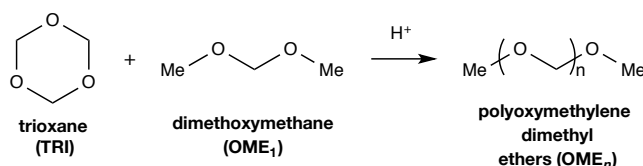
3.1 Introduction

Due to their high surface area and adjustable Si/Al ratio, zeolites are attractive for a wide range of applications ranging from catalytic cracking to water softening.^[130,131] These aluminosilicate materials are structured to provide ordered, uniform channels of molecular dimensions. Their Ångstrom-level channel sizes result in pronounced shape-selectivity widely applied in various processes including alkylation of toluene and isomerization of *n*-butene.^[132,133] However, these small channels often induce mass transport limitations, lowering the effective active zeolite volume.^[134] This limitation reduces their performance as catalysts for reactions involving bulky molecules, especially in the liquid-phase.^[135–137] Recently, this drawback was circumvented by the addition of an auxiliary network of mesopores leading to a hierarchical material.^[138,139] Amongst several possible treatment strategies, desilication by alkaline treatment prevails as an affordable and scalable post-synthetic treatment.^[140] Besides accelerating the reaction by improving access to the zeolite crystals, mesoporosity can also influence the selectivity.^[141] Notably, using supported ruthenium nanoparticles on mesoporous zeolites, Cheng et al. reported a deviation from the Schulz-Flory distribution during the Fischer-Tropsch synthesis.^[142]

OME recently demonstrated remarkable properties as green alternatives to Diesel fuel.^[8,11,46,51,143] Their synthesis process is acid-catalyzed and requires both a methyl- and an

This chapter is part of a published article in *Catalysis Science & Technology* as C. J. Baranowski, A. M. Bahmanpour, F. Héroguel, J. S. Luterbacher, O. Kröcher, Prominent role of mesopore surface area and external acid sites for the synthesis of polyoxymethylene dimethyl ethers (OME) on a hierarchical H-ZSM-5 zeolite, *Catal. Sci. Technol.* **2019**, *9*, 366–376.^[122] Part of the manuscript and supplementary information are reproduced here with some changes in formatting with permission from the Royal Society of Chemistry. C. Baranowski performed the experiments, analysed the data together with the co-authors and wrote the manuscript.

oxymethylene group provider. Various synthesis paths exist but the anhydrous route (Scheme 3-1), involving trioxane (TRI) and dimethoxymethane (OME₁), was shown to achieve the maximal yield of OME₃₋₅ with the highest reaction rate.^[66] The reaction mechanism of OME synthesis from TRI and OME₁ still remains elusive. It is believed that OME growth occurs via TRI direct insertion or incorporation of formaldehyde units, generated by TRI decomposition, into OME₁.^[114] Studies have demonstrated that OME₁ is activated to form a carbocation or a hemiformal.^[114] According to Goncalves et al., TRI insertion into OME₁ on H-Beta is more favorable than insertion of formaldehyde units formed from TRI decomposition.^[115] However, a statistical ASF distribution is still observed, since the transfer of oxymethylene units between two OME molecules (i.e. transacetalization) occurs faster than TRI insertion. The high rate of transacetalization prevents a preferential OME chain length distribution (i.e. a higher concentration of OME₄ or OME₇ compared to other OME).

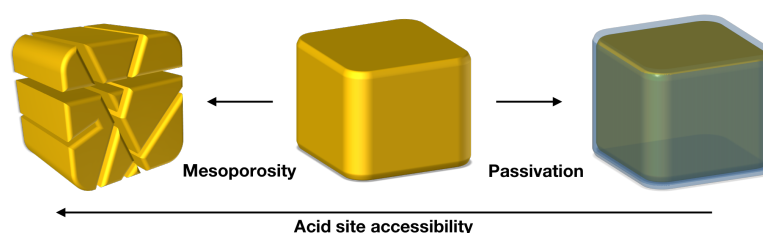


Scheme 3-1. Synthesis of OME from dimethoxymethane (OME₁) and trioxane (TRI).

Various types of aluminosilicates were found to be active for OME synthesis. H-Y, H-ZSM-5, H-Beta and H-MCM-22 were proposed as active catalysts for the OME synthesis process.^[69] Wu et al. identified H-ZSM-5 with a high Si/Al ratio as an efficient catalyst.^[81] Fu et al. achieved a superior performance using super-microporous aluminosilicates.^[79] Al-SBA-15, an ordered mesoporous material containing mainly aluminum, also catalyzed the reaction demonstrating the activity of Lewis acidity in this reaction.^[144] Despite having a superior surface area and a high concentration of acidic sites, zeolites typically have lower activities compared to acidic resins for OME synthesis.^[83] One of the reasons might be that OME are bulky molecules having a *gauche* preferential conformation due to anomeric stabilization, hampering diffusion into a zeolite's micropores.^[145,146]

Therefore, in this study we focused on the following two unaddressed questions on the synthesis of OME. Firstly, how does mass-transfer limitation affect the performance of the catalyst? Secondly, do external sites have a more prominent role compared to the internal sites in the catalytic reaction? We addressed these questions by varying the active sites accessibility on an H-ZSM-5 zeolite using two strategies in order to change the internal

diffusion limitations (Scheme 3-2). On the one hand, we introduced a secondary network of mesopores by desilication and subsequent acid wash to decrease the effect of internal diffusion limitations in the zeolite crystals. On the other hand, we passivated the external surface of the zeolite by selective silanation and epitaxial growth of a silicate-1 layer to block all the sites that are unaffected by internal diffusion. Precise quantification of mass transfer limitations within the zeolite crystal is out of the scope of this study. Nevertheless, it aims to investigate the overall, qualitative effect of internal mass transfer in an H-ZSM-5 zeolite for OME synthesis.



Scheme 3-2. Treatments applied on H-ZSM-5 to create intracrystalline mesoporosity or passivate its external surface.

3.2 Experimental

3.2.1 Introduction of mesoporosity in H-ZSM-5 zeolites

Mesoporous H-ZSM-5 zeolites were synthesized by 30 min of alkaline treatment (AT30) as described by Verboekend et al.^[147] Typically, the H-ZSM-5 zeolite (3.3 g) was stirred in a NaOH solution (100 mL, 0.2-1.0 M, Roth) for 30 min at 65 °C. After quenching the solution with ice, the powder was filtered and washed with deionized water (samples are denoted H-ZSM-5-AT30). If the alkaline concentration is not mentioned, a 0.2 M NaOH solution was used for the treatment. Some samples were subsequently dealuminated with an acid wash (AW) during which the powder was stirred in a 0.02 M HCl solution (100 mL · g⁻¹ zeolite, Fluka) at 65 °C (samples are denoted H-ZSM-5-AT30-AW). The powder was recovered by filtration. The protonic form of the sample was then obtained by three successive ion-exchange treatments with NH₄NO₃ (Sigma Aldrich, 100 mL · g⁻¹ zeolite, 65 °C). Finally, the sample was calcined under static air for 5 h at 550 °C with a 5 °C · min⁻¹ heating ramp. A mean particle size of H-ZSM-5 of 5.74 μm was determined, using a Horiba LA-950 laser diffraction particle size distribution analyzer.

3.2.2 Passivation of H-ZSM-5 crystals

Passivation of external Brønsted acid sites was carried out by two methods: selective silanation and epitaxial growth of silicalite-1. Selective silanation of the external sites was performed according to the protocol presented by Ding et al.^[148] H-ZSM-5 (3.3 g) was stirred with an ethanol solution (33 mL) containing 0.49 g of 3-aminopropyl-triethoxysilane. After 2 min of sonication to break agglomerates, the solvent was evaporated at 60 °C. The sample (H-ZSM-5@SiO₂) was then calcined under static air for 5 h at 550 °C with a 5 °C · min⁻¹ heating ramp. The bulky organosilane molecule only reacts with external acidic hydroxyl groups to form SiO_x species after calcination.

The second passivation method was performed by epitaxial growth of silicalite-1 according to the method of Ghorbanpour et al.^[149] A growth solution (225 g) was prepared with a molar ratio of 17 tetraethyl orthosilicate (TEOS, 99.999%, Sigma Aldrich): 14 tetrapropylammonium hydroxide (TPAOH, Sigma Aldrich): 9500 H₂O by adding TEOS dropwise in a TPAOH solution. After stirring overnight, 2.25 g of untreated H-ZSM-5 was added and the solution was sonicated for 5 min. The solution was transferred in a Teflon-lined Parr reactor and hydrothermally treated at 100 °C for 24 h. Then, the solution was filtered and washed with deionized water. Finally, the zeolite was obtained in its protonic form (H-ZSM-5@S-1) by three successive ion-exchange treatments for 16 h in a 0.2 M NH₄NO₃ solution at 65 °C.

3.2.3 Catalytic tests and kinetic modelling

Syntheses of OME were performed from TRI and OME₁ in a 450 mL stirred batch reactor following a protocol described in Chapter 2.2.1. Experimental data were fitted with the ExpAssoc function using ORIGIN software. Initial reaction rates (mol · min⁻¹ · g_{cat}⁻¹) were then calculated based on the value of the derivative at t=0 of [OME₂₋₈] vs. time divided by the catalyst concentration. A simplified pseudo-homogeneous kinetic model, described in section 2.4, was used to model the synthesis of OME from TRI and OME₁. The parameters of the van 't Hoff equations were determined by fitting the experimentally obtained K^{*}_{OME} value at various temperatures (Figure A8-1 in Appendix A).

3.3 Results and discussion

3.3.1 Physico-chemical properties of the catalysts

The XRD patterns (Figure 3-1) of the untreated, mesoporous and passivated H-ZSM-5 all have similar reflections, which are representative of the MFI structure. Thus, desilication and dealumination as well as both passivation methods did not alter the zeolite structure. Textural properties were investigated by N₂ physisorption with clear differences visible in the isotherms (Table 3-1, Figure 3-2a). All zeolites possessed a type II isotherm with a hysteresis loop of various size, which highlighted the presence of mesoporosity. The initial mesoporosity of the untreated H-ZSM-5, evidenced by a H4 loop in the isotherm, was generated from intercrystallite space between aggregates.^[150]

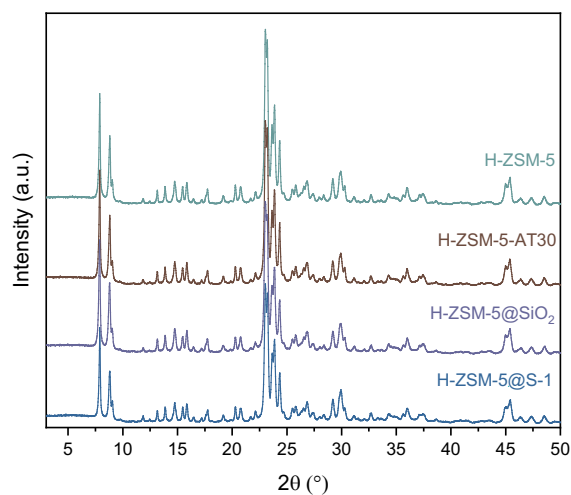


Figure 3-1. XRD diffractograms of the H-ZSM-5 zeolites.

Table 3-1. Textural parameters of untreated, mesoporous and passivated H-ZSM-5 zeolites.

Sample	Surface Area (m ² · g ⁻¹)			Volume (cm ³ · g ⁻¹)		
	BET	Micro ^[a]	Meso ^[b]	Ext.	Micro ^[a]	Meso ^[b]
H-ZSM-5	379	294	54	85	0.124	0.052
H-ZSM-5-AT30	388	280	80	108	0.116	0.110
H-ZSM-5-AT30 _{0.4M}	389	273	94	116	0.118	0.168
H-ZSM-5-AT30 _{0.6M}	329	177	131	152	0.076	0.512
H-ZSM-5-AT30 _{0.8M}	376	173	179	203	0.075	0.545
H-ZSM-5-AT30 _{1.0M}	43	25	14	17	0.011	0.032
H-ZSM-5-AT30-AW	414	287	99	127	0.122	0.127
H-ZSM-5-AT30 _{0.4M} -AW	445	311	104	134	0.129	0.165
H-ZSM-5-AT30 _{0.5M} -AW	468	320	111	147	0.136	0.208
H-ZSM-5-AT30 _{0.6M} -AW	450	294	119	156	0.125	0.237
H-ZSM-5@SiO ₂	336	272	47	64	0.116	0.050
H-ZSM-5@S1	414	345	43	69	0.144	0.060

^[a] Calculated based on the t-plot method. ^[b] Calculated based on the BJH method using the adsorption branch.

Alkaline treatment increased the total N_2 uptake and mesopore surface area (S_{meso}) from 54 to 80 $\text{m}^2 \cdot \text{g}^{-1}$ with a concomitant, slight decrease in micropore surface area (S_{micro}) from 294 to 280 $\text{m}^2 \cdot \text{g}^{-1}$. This decrease in S_{micro} can be attributed to the formation of aluminum-rich debris formed upon desilication on Al-rich H-ZSM-5 ($\text{Si}/\text{Al} < 20$). Al species can re-deposit, causing micropores blockage.^[147] Adding a subsequent acid wash step after desilication can remove these amorphous species. H-ZSM-5-AT30-AW exhibited an increased S_{meso} (99 $\text{m}^2 \cdot \text{g}^{-1}$) with a S_{micro} (287 $\text{m}^2 \cdot \text{g}^{-1}$) close to the initial value of the parent zeolite. Subsequent dealumination was thus successful in partially restoring the initial S_{micro} .

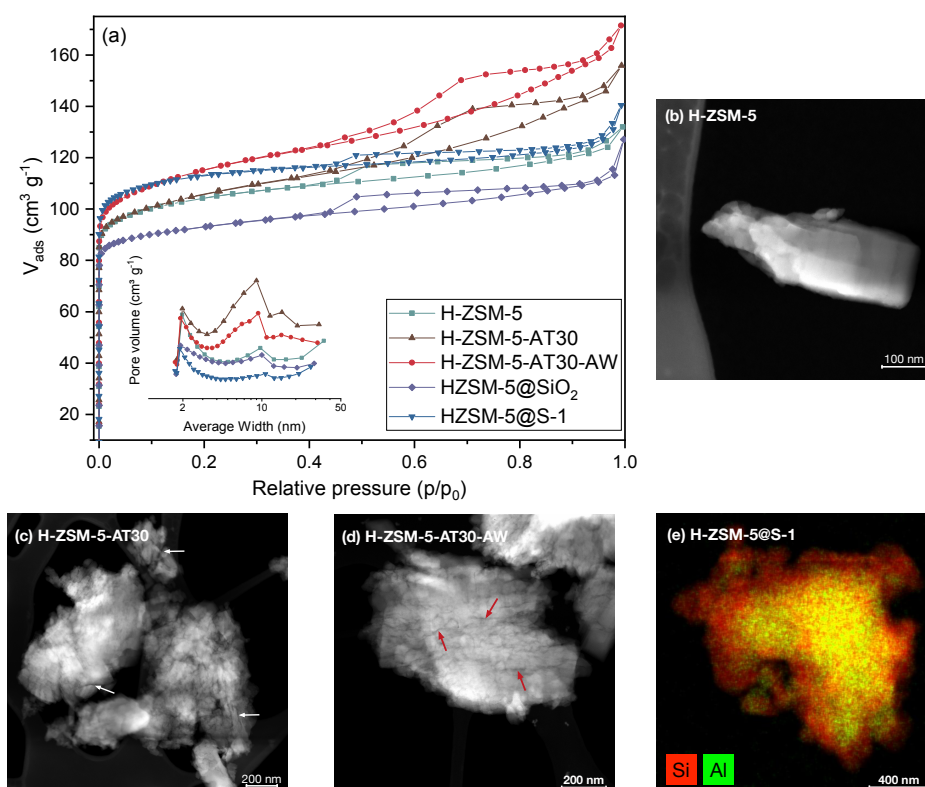


Figure 3-2. N_2 physisorption of untreated, mesoporous and passivated H-ZSM-5 with (a) N_2 isotherms and BJH pore size distribution as inset and STEM images of (b) H-ZSM-5, (c) H-ZSM-5-AT30, (d) H-ZSM-5-AT30-AW and (e) STEM-EDXS of H-ZSM-5@S-1 (Si: red; Al: green). Arrows are pointing to examples of mesopores caused by the alkaline treatment.

Both samples which were desilicated exhibited a broad peak in the pore size distribution around 9 nm indicating the presence of mesopores (Figure 3-2a, inset), as indicated by the increased S_{meso} . Scanning transmission electron microscopy (STEM) confirmed the presence of intracrystalline mesopores within the entire crystal for alkaline-treated H-ZSM-5 (Figure 3-2c and d), which were not detected for the untreated zeolite (Figure 3-2b). Overall, desilication with NaOH successfully created mesopores within the zeolite crystal by silicon

extraction with hydroxyl ions. Mild dealumination was necessary to remove aluminum debris.

The effect of desilication and dealumination treatments on the coordination of aluminum was investigated by magic angle spinning-NMR (Figure 3-3a). Signals from tetrahedral Al^{IV} , pentahedral Al^{V} and octahedral Al^{VI} have chemical shifts at 50 ppm, 30 ppm and 0 ppm, respectively.^[151-153] Alkaline treatment led to an increase in the Al^{V} and Al^{VI} signal at the expense of the Al^{IV} signal. Tetrahedral aluminum was thus partially converted upon desilication into extra-framework aluminum (EFAI) and aluminum-rich debris, which can be responsible for partial micropores blockage.^[147] The addition of an acid wash step decreased EFAI signals but also slightly decreased the Al^{IV} signal. Dealumination was thus required to regenerate the initial crystallinity.

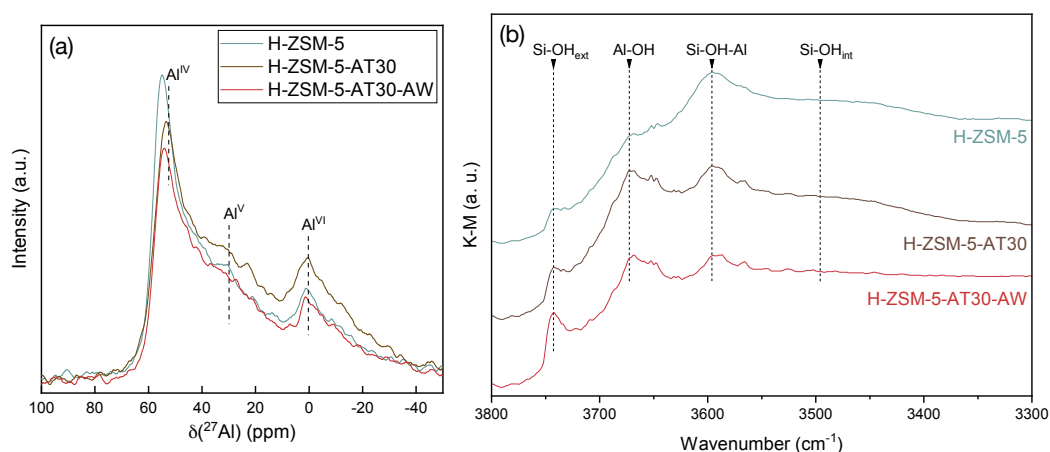


Figure 3-3. (a) ^{27}Al MAS-NMR of untreated and mesoporous H-ZSM-5 and (b) DRIFT spectra in the silanol region of untreated and mesoporous H-ZSM-5.

The FTIR spectra (Figure 3-3b) of the silanol region showed peaks assigned to isolated Si-OH (3740 cm^{-1}), Al-OH (3660 cm^{-1}), bridging hydroxyl (3590 cm^{-1}) and internal Si-OH (3495 cm^{-1}).^[154] Overall, the bridging hydroxyl signals remained constant for the three samples but higher Al-OH signals were observed for the alkaline-treated zeolites, which confirmed the presence of Al^{V} species. Dealumination also increased the signal of terminal Si-OH bonds, due to the removal of Al from the zeolite framework. ICP-OES was used to study the effect of the various treatments on the zeolites compositions (Table 3-2). The initial Si/Al ratio decreased with the alkaline treatment (from 11.3 to 10.9) and reached a value above its initial level with the additional acid wash (12.7). The influence of the extent of desilication was studied by using NaOH solutions with various concentration (0.2 to

1.0 M) for the alkaline-treatment with and without a subsequent acid wash. The textural properties of the resulting samples were characterized by N_2 physisorption and the results are quantified in Table 3-1.

As observed in Figure 3-4a, increasing the extent of desilication by increasing the concentration of NaOH during alkaline treatment led to an increase in mesopore surface area at the expense of the micropore surface area. Severe pore blocking occurred at concentrations higher than 0.4 M, highlighted by the loss of more than 40 % of S_{micro} . Adding an additional step of mild dealumination after desilication regenerated the access to the micropores while preserving the mesopores. A too severe alkaline treatment (i.e. 1.0 M) resulted in a severe amorphization of the sample, reflected by the sharp drop in micro- and mesopore surface area.

Table 3-2. ICP-OES results of untreated, mesoporous and passivated H-ZSM-5 zeolites.

Sample	Si (wt %)	Al (wt %)	Si/Al (mol · mol ⁻¹)
H-ZSM5	39	3.3	11.3
H-ZSM-5-AT30	39.6	3.5	10.9
H-ZSM-5-AT30-AW	39.5	3.12	12.7
H-ZSM-5@SiO ₂	39.2	2.6	14.3
H-ZSM-5@S-1	40.3	3.3	11.7

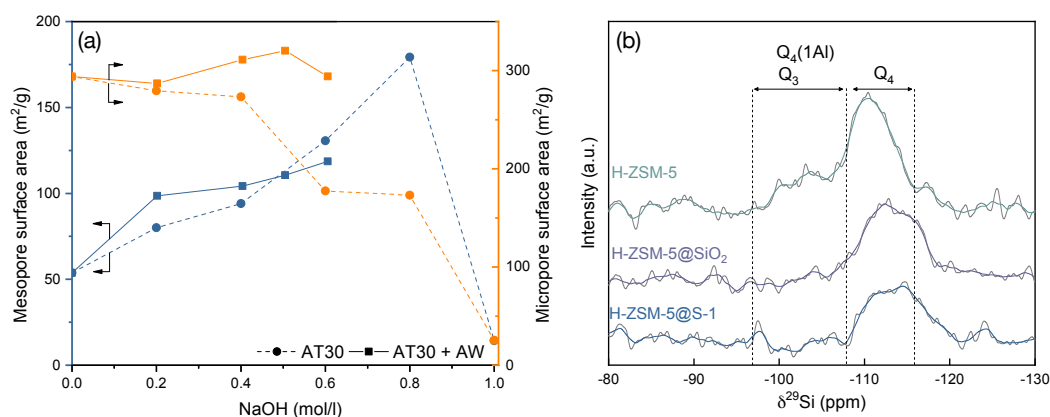


Figure 3-4. (a) Results of N_2 physisorption measurements to derive the mesopore and micropore surface area of H-ZSM-5 treated with varying concentrations of NaOH during the desilication step (AT: alkaline treatment, AW: acid wash). (b) ^{29}Si MAS-NMR of untreated and passivated H-ZSM-5. A smoothing of the signal (adjacent-averaging, 20 points) is displayed for clarity.

Zeolites samples resulting from the two passivation methods had distinctive textural properties. As shown on Figure 3-2a, silanation of H-ZSM-5 decreased the S_{micro} ($272 \text{ m}^2 \cdot \text{g}^{-1}$) while preserving the S_{meso} ($47 \text{ m}^2 \cdot \text{g}^{-1}$). However, epitaxial growth of S-1 resulted in an increase in S_{micro} ($345 \text{ m}^2 \cdot \text{g}^{-1}$) at the expense of S_{meso} ($43 \text{ m}^2 \cdot \text{g}^{-1}$). Both passivated samples

possessed a larger Si/Al ratio compared to the untreated H-ZSM-5 due to the addition of silicon from the passivation treatments. The coordination of Si was investigated by MAS-NMR (Figure 3-4b). H-ZSM-5 possessed a prominent peak at -110 ppm corresponding to framework tetrahedral silicon (Q_4).^[155] Overall, both passivated zeolites exhibited a signal shift from Q_3 and $Q_4(Al)$ (between -97 and -108 ppm) to Q_4 (between 108 and -116 ppm) indicating a larger proportion of tetrahedral silicon present in the passivated zeolites compared to the untreated zeolite.^[156] The presence of an outer layer of S-1 was confirmed by STEM-EDXS (Figure 3-2e).

Next, the acidity of the mesoporous and passivated zeolites was studied by NH_3 -temperature programmed desorption (NH_3 -TPD), pyridine adsorption FTIR spectroscopy (Py-FTIR) and di-tert-butyl-pyridine - temperature programmed desorption (DTBPy-TPD). NH_3 -TPD typically showed low- and high temperature peaks for the protonic form of zeolites (Figure 3-5a) and the results of the peak area quantification are summarized in Table 3-3. Alkaline treatment increased the acidity with H-ZSM-5-AT30 ($1.07 \text{ mmol} \cdot \text{g}^{-1}$) having 9 % additional acidity compared to the untreated H-ZSM-5 ($0.98 \text{ mmol} \cdot \text{g}^{-1}$). EFAI located on the crystal surface resulting from silicon extraction likely accounted for this increase.^[157]

The additional acid wash step diminished the acidity to a level below that of the untreated H-ZSM-5 (4 % decrease). However, their strength was enhanced as reflected by the shift towards higher desorption temperature during NH_3 -TPD. Augmenting the extent of desilication was detrimental to the acidity of the zeolite, despite the acid wash step to restore the micropore surface area. H-ZSM-5-AT30_{0.6M}-AW possessed the lowest acidity of all prepared mesoporous zeolites even though it displayed one of the highest BET surface area. There was thus a limit to the introduction of an auxiliary network of mesopores without damaging the acidic properties of the zeolites. Meanwhile, the two different methods of passivation had different effects on acidity. Despite having the same total acidity as H-ZSM-5@SiO₂ ($0.86 \text{ mmol} \cdot \text{g}^{-1}$), H-ZSM5@S-1 had a larger portion of weak acid sites, which is due to the addition of the S-1 layer that does not contain bridging hydroxyl groups.

Py-FTIR was applied to study the nature and strength of the catalyst's acidic sites (Figure 3-5b). After exposure of H-ZSM-5 to an excess of pyridine vapor at 50 °C, the characteristic bands of pyridine adsorbed on Brønsted acid sites (1530 cm^{-1}) and Lewis acid sites (1445

and 1580 cm^{-1}) were observed.^[158] The signal corresponding to Brønsted acid sites remained constant with the increase in temperature, while the signal corresponding to Lewis acid sites disappeared at temperature above 150 °C . It was thus concluded that the untreated H-ZSM-5 possessed strong Brønsted and mild Lewis acid sites. A similar trend was observed for the spectra of H-ZSM-5-AT30 and H-ZSM-5-AT30-AW obtained by Py-FTIR. Therefore, neither the alkaline treatment nor the acid wash affected the type of acidity.

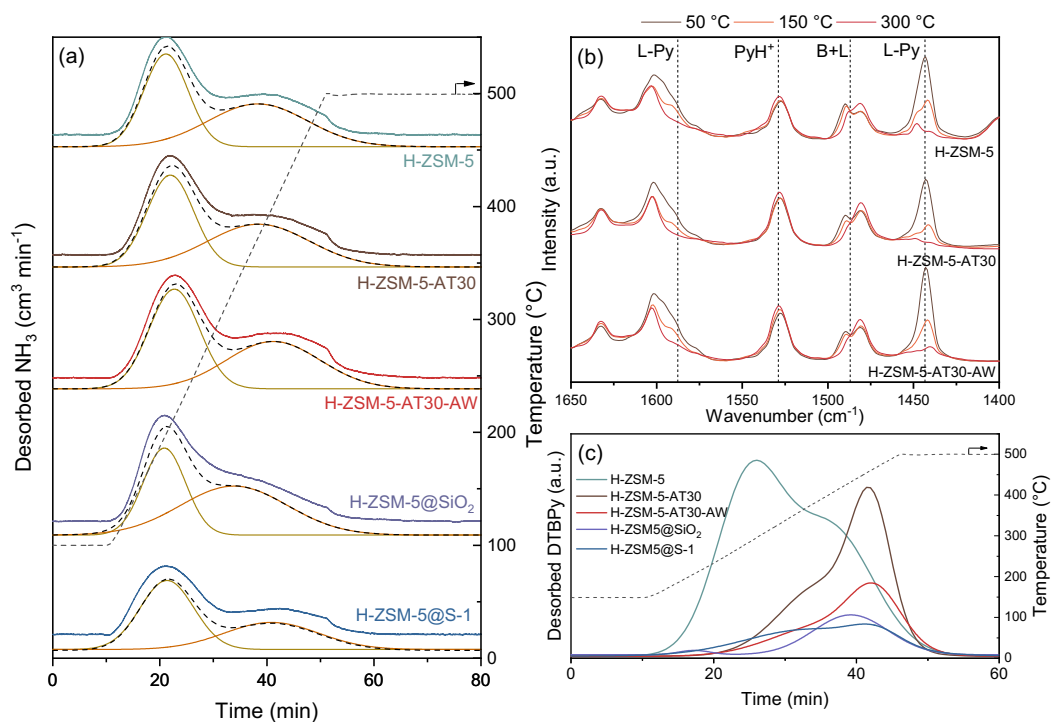


Figure 3-5. Acidity characterization of mesoporous and passivated H-ZSM-5 zeolites by (a) NH_3 -TPD, (b) Py-FTIR spectroscopy (PyH⁺ and L-Py indicate pyridinium ion and pyridine bonded to a Lewis site, respectively), and (c) DTBPy-TPD (only the cumulative peaks from Gaussian peak deconvolution is displayed for clarity and the measured spectra are in Figure A8-2).

Table 3-3. NH_3 -TPD of untreated, mesoporous and passivated H-ZSM-5 zeolites.

Sample	Total acidity (mmol · g ⁻¹)	Weak (100-200 °C) (mmol · g ⁻¹)	Strong (200-500 °C) (mmol · g ⁻¹)
H-ZSM-5	0.98	0.48	0.50
H-ZSM-5-AT30	1.07	0.53	0.54
H-ZSM-5-AT30-AW	0.94	0.50	0.44
H-ZSM-5-AT30_{0.4M}-AW	0.95	0.56	0.39
H-ZSM-5-AT30_{0.6M}-AW	0.82	0.41	0.41
H-ZSM-5@SiO₂	0.86	0.35	0.50
H-ZSM-5@S-1	0.86	0.51	0.35

The external acidity of the samples was probed by DTBPy-TPD (Figure 3-5c, Figure A8-2). DTBPy is a bulky base that cannot enter the micropores and is selective to Brønsted acid

sites due to steric constraints preventing its coordination to Lewis sites.^[159] It is thus a suitable probe for quantification of external Brønsted acidity. All treatments on H-ZSM-5 showed a significant effect on its external acidity. Desilication lowered the signal by 24 % and shifted it towards higher temperatures. This change in acidity can arise from two concomitant effects. First, as NaOH preferentially attacks Si-OH, there is a decrease in the number of external silanol groups. Second, silicon extraction can expose bridging hydroxyl groups and produce EFAl on the surface, leading to an increase of surface acidity.^[160]

The addition of an acid wash particularly affected the external acidity with a 73 % decrease compared to the untreated H-ZSM-5 signal. This treatment dealuminated the external surface thereby removing strong acid sites. As a consequence, the external acidity was more severely affected than the overall acidity. This observation is in line with Fernandez et al., who found that EFAl present on the external surface are more disposed to be extracted during dealumination than tetrahedrally coordinated Al.^[161] Lastly, both methods of passivation efficiently reduced external acidity based on a signal drop of 86 % and 81 % for H-ZSM-5@SiO₂ and H-ZSM-5@S-1, respectively. The overall acidity was found to be the same for the two samples but H-ZSM-5@SiO₂ had a higher number of strong acid sites.

3.3.2 Catalytic activity for OME synthesis

The performance of the synthesized catalysts was tested for the synthesis of OME from TRI and OME₁ in a batch reactor (Figure 3-6). All catalysts were able to synthesize OME but with major differences in the observed kinetics. Their performance followed the trend: mesoporous > untreated > passivated. Compared to H-ZSM-5, H-ZSM-5-AT30 and H-ZSM5-AT30-AW were more active catalysts. The initial reaction rate using H-ZSM-5-AT30-AW almost doubled compared to the untreated H-ZSM-5 from 0.015 to 0.028 mol.min⁻¹.g_{cat}⁻¹.

Using H-ZSM-5-AT30-AW as the catalyst, the reaction reached equilibrium between 120 and 180 min while by using H-ZSM-5 and H-ZSM-5-AT30, it required more than 180 min to reach the equilibrium. The opposite effect occurred with the passivation of the external surface where a significant decrease in performance was observed. Initial reaction rates diminished to 0.009 and 0.007 mol.g⁻¹.min⁻¹, for H-ZSM-5@SiO₂ and H-ZSM-5@S-1, respectively. Furthermore, the order of the reaction seemed to change from a first order

reaction to a zeroth-order reaction. This suggests that the reaction rate does not depend on the reactants' concentrations and that the rate-limiting step may be internal diffusion within the zeolite micropores. The equilibrium composition was not reached under 240 min using the two passivated samples.

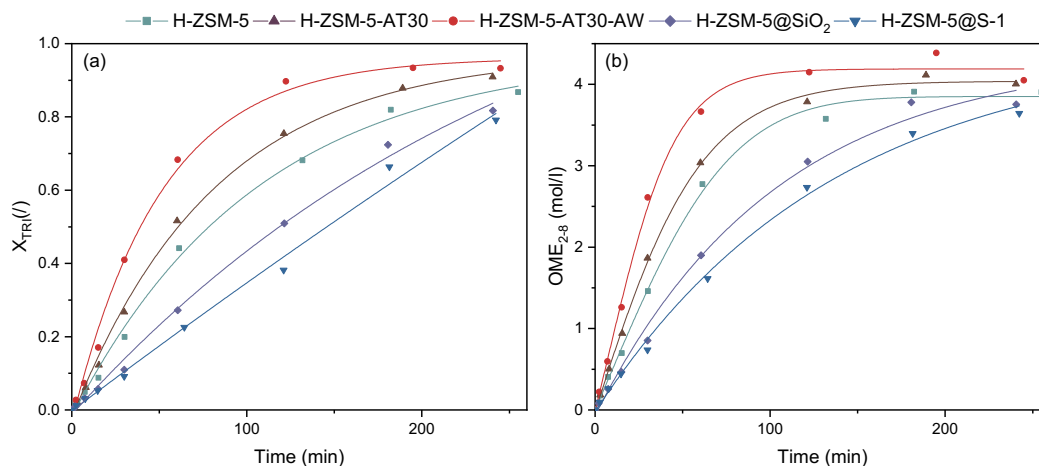


Figure 3-6. (a) TRI conversion X_{TRI} and (b) concentration of OME_{2-8} in the batch reactor (OME_1/TRI : 3.3; 0.5 wt % catalyst; 70 °C) obtained with untreated, mesoporous and passivated H-ZSM-5 zeolites.

Methyl formate (MF) is formed through the condensation of two formaldehyde units and is a by-product of OME synthesis. The production of MF (Figure 3-7a) was higher for mesoporous and passivated zeolites than for untreated H-ZSM-5. Since a higher proportion of the reaction took place in the micropores, there was a higher probability of MF formation.^[74] Reusability of H-ZSM-5-AT30-AW was also assessed by performing four consecutive runs (Figure 3-7b). The conversion of TRI and the OME size distribution remained constant, which showed that no deactivation of the catalyst occurred. The OME size distribution was calculated using the growth probability (α), which is a parameter representative of this distribution (see definition in Chapter 2.2.1); a larger value implies that larger OME are produced.

Alkaline-treated and acid-washed H-ZSM-5 zeolites exhibited the most suitable textural properties for OME synthesis. They possessed a high mesoporous surface area and their crystallinity was preserved as a result of the acid wash. The catalytic performance of zeolite candidates with varying degrees of desilication was thus also tested to better understand the effects and benefits of mesopores for OME synthesis (Figure 3-8a and b).

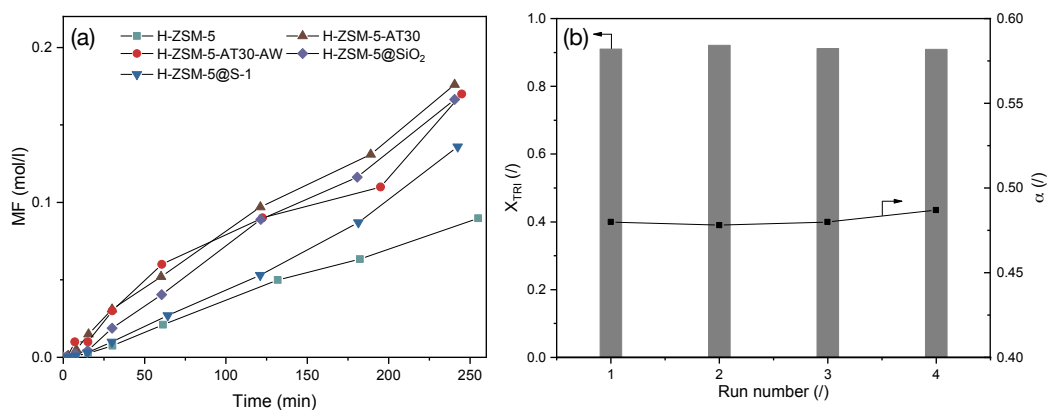


Figure 3-7. (a) Production of methyl formate (MF) versus time in the batch reactor (OME_1/TRI : 3.3; 0.5 wt % catalyst; 70 °C) obtained with untreated, mesoporous and passivated H-ZSM-5 zeolites. (b) Reusability test of H-ZSM-5-AT30-AW with TRI conversion X_{TRI} and α (OME_1/TRI : 3.3; 1.0 wt % catalyst; 70 °C; 120 min reaction time).

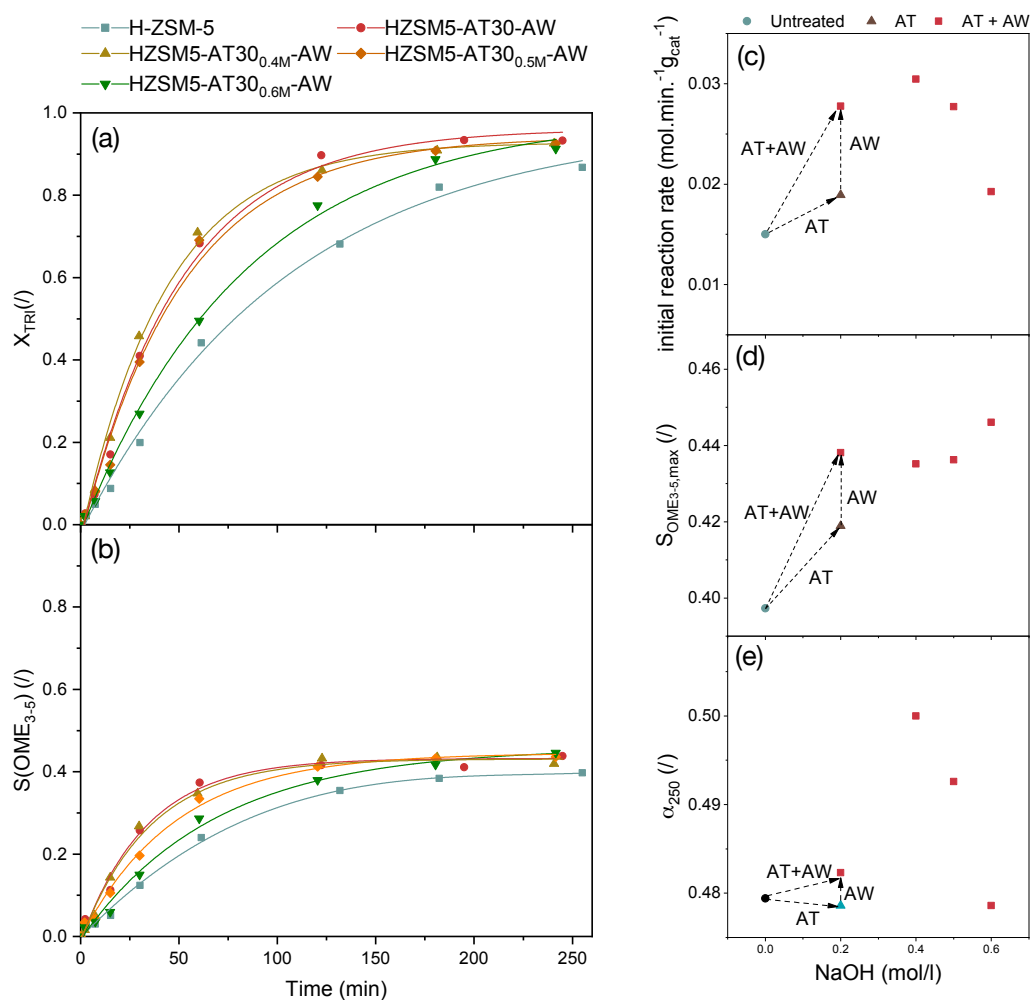


Figure 3-8. Performance comparison of untreated, mesoporous and passivated H-ZSM-5 zeolites with (a) TRI conversion X_{TRI} and (b) $S(OME_{3-5})$ (OME_1/TRI : 3.3; 0.5 wt % catalyst; 70 °C). Influence of pre-treatment of H-ZSM-5 on the catalytic performance during OME synthesis (OME_1/TRI : 3.3; 0.5 wt % catalyst; 70 °C). (c) initial reaction rate, (d) maximum selectivity $S(OME_{3-5, max})$ reached during the run, and (e) growth probability after 250 min.

The relationship between the initial reaction rate and the extent of alkaline treatment displays a maximum value reached with H-ZSM-5-AT30_{0.4M}-AW (Figure 3-8c). This catalyst showed a two-fold increase from 0.015 to 0.031 mol.min⁻¹.g_{cat}⁻¹ in the initial reaction rate compared to untreated H-ZSM-5. Alkaline treatment with a concentration above 0.4 M resulted in a more modest increase in activity despite having the highest mesopores surface area. Moreover, all mesoporous zeolites displayed an increase in S(OME₃₋₅) before the equilibrium was reached during the experiments. The maximum value S(OME_{3-5, max}) was around 10 % higher for alkaline-treated and acid-washed H-ZSM-5 zeolites (Figure 3-8d). Despite a modest increase, it seems that mesopores supported the formation of OME₃₋₅ at the expense of larger OME. We suggest that mesopores facilitate the diffusion of OME₃₋₅. Finally, we investigated the effect of the treatments on α . A small influence of mesopores was also observed on α with a maximum value of α at 250 min obtained for H-ZSM-5-AT30_{0.4M}-AW (Figure 3-8e). All catalysts led to an OME product distribution at equilibrium following the ASF distribution.

3.3.3 Structure-activity relationship

The intracrystalline network of mesopores showed to improve the activity of H-ZSM-5 for the synthesis of OME. However, it is not the only important aspect: there is a trade-off between overall acidity and accessibility. At a certain extent of alkaline treatment (i.e. using a 0.6 M NaOH solution for desilication), the concentration of acid sites decreased, which caused a decrease in the catalyst activity despite the presence of mesopores in the zeolite crystal. A correlation was found between the initial reaction rate at 70 °C and the product of S_{meso} and the acid sites concentrations (Figure 3-9), which highlights the importance of both factors for OME synthesis.

Another important aspect is the obstruction of the zeolite's micropores. H-ZSM-5-AT30 or H-ZSM-5-AT30_{0.6M}-AW are both less active, which could be due to the presence of Al-rich debris causing micropore blockage. The acid-wash step is crucial to restore the crystallinity and access to micropores but could be insufficient to remove all Al-rich debris produced when performing a desilication step using the more concentrated alkaline treatment (i.e. 0.6 M). The higher amount of Al-rich debris produced upon a stronger alkaline treatment requires in turn acid wash with a more concentrated HCl solution. However, this could also remove Brønsted acidity and thus be detrimental to the overall zeolite acidity. The acid

site strength could also be playing an important role. H-ZSM-5-AT30 and H-ZSM-5-AT30-AW both displayed enhanced acid strength that could also contribute to their overall increased performance.

Finally, considering the characterization data showing that the passivated samples lost most of their external acidity with a small decrease in the overall acidity, it becomes obvious that the external acid sites must play a more prominent role in OME synthesis than the sites within the micropores. These external sites are more easily accessible to the bulky OME₁ and TRI molecules. However, it is difficult to exactly quantify this difference as both passivation treatments also induced some changes to the bulk of the material. The least active catalyst was H-ZSM-5@S-1 for three reasons. First, the original intercrystalline volume was filled with newly generated S-1 phase, decreasing the mesoporous volume. Second, the internal acid sites of the H-ZSM-5 crystals were only accessible after diffusion through the pores of the S-1 external layer. Finally, as the S-1 layer does not contain any bridging hydroxyl group, an increasing thickness of S-1 layer also progressively lowered the fraction of strong Brønsted sites in the zeolite.

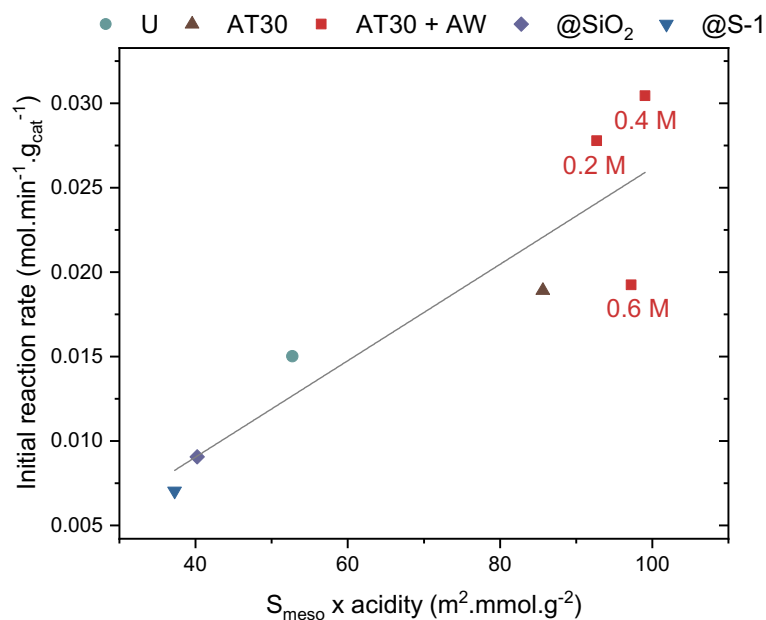


Figure 3-9. Correlation between the initial reaction rate and the product of mesopore surface area and acidity (U: untreated, AT: alkaline treatment, AW: acid wash, @SiO₂: silanated zeolite, @S-1: epitaxial growth of S-1).

To investigate further the effect of passivation and introduction of mesoporosity on the synthesis of OME, a kinetic study was performed on the untreated and passivated (H-ZSM-5@S-1) zeolites as well as on the best mesoporous candidate

(H-ZSM-5-AT30_{0.4M}-AW). They were tested at three different temperatures and each run with a specific catalyst at a certain temperature was fitted to our kinetic model to yield a value of the effective kinetic constant $k_{OME,f}$ (Table 3-4, Figure A8-3 to Figure A8-5). The value of E_{app} was then calculated for each catalyst using the linearized Arrhenius equation (Figure 3-10):

$$\ln(k_{OME,f}) = -\frac{E_a}{RT} + \ln(A) \quad (16)$$

Table 3-4. Results of the kinetic model for the kinetic study on the various catalysts.

RUN	CATALYST	TEMPERATURE (°C)	RMSE ^[A]	$K_{OME,F}$ (L·MOL ⁻¹ ·MIN ⁻¹)
K1	H-ZSM-5	70	0.60	0.0304
K2	H-ZSM-5	80	0.65	0.110
K3	H-ZSM-5	90	0.64	0.292
K4	H-ZSM-5@S-1	70	0.57	0.00695
K5	H-ZSM-5@S-1	80	0.58	0.0148
K6	H-ZSM-5@S-1	90	0.62	0.0318
K7	H-ZSM-5-AT30 _{0.4M} - AW	70	0.65	0.0659
K8	H-ZSM-5-AT30 _{0.4M} - AW	80	0.61	0.142
K9	H-ZSM-5-AT30 _{0.4M} - AW	90	0.51	0.424

^[a] RMSE = Root Mean Square Error

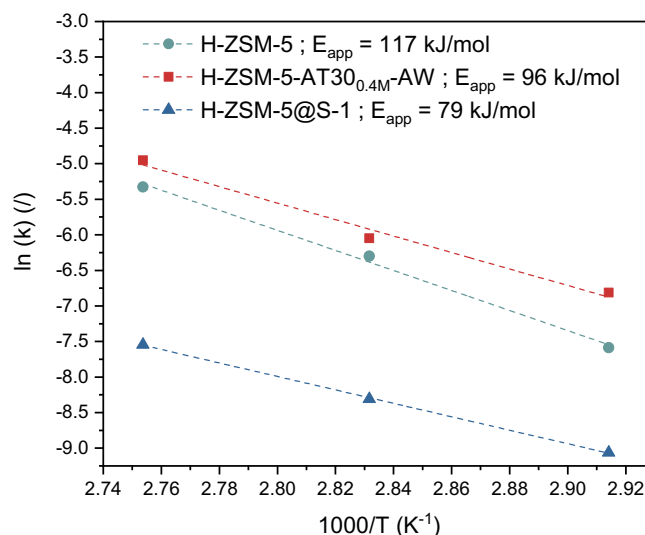


Figure 3-10. Arrhenius plot for various catalysts based on the kinetic constants extracted from the kinetic model with the apparent energy of activation.

H-ZSM-5 showed the highest E_{app} of 117 kJ · mol⁻¹, which is within the range of values (117 to 126 kJ · mol⁻¹) calculated by Wang et al. for the activation energy required for insertion

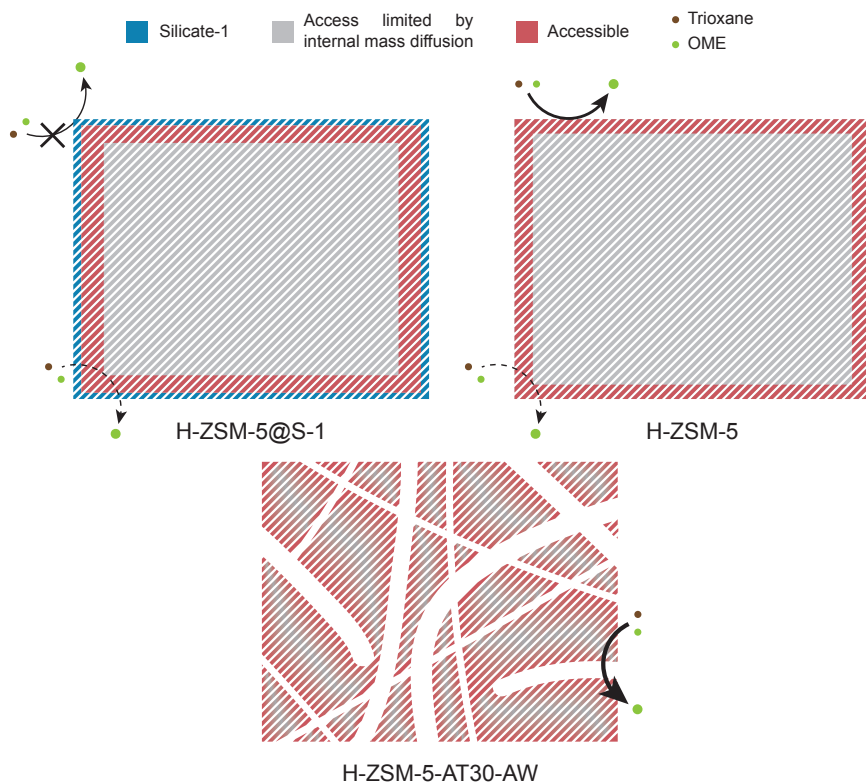
of a formaldehyde unit into an OME molecule.^[114] The lower dependency of the reaction rate on temperature for H-ZSM-5@S-1 was confirmed by its relatively low E_{app} ($79 \text{ kJ} \cdot \text{mol}^{-1}$). When the intraparticle diffusion is the rate-determining step, the slope of the Arrhenius plot changes from $-E_a/R$ to $-(E_d+E_a)/2R$ where E_d is the activation energy for the effective diffusion.^[162] The activation energy for molecular diffusion in the H-ZSM-5 channels is in the range of $5\text{-}20 \text{ kJ} \cdot \text{mol}^{-1}$.^[163]

Comparing these two values thus shows that the overall reaction rate using H-ZSM-5 is dictated by reaction taking place solely on the surface. Acid sites located inside the micropores were subjected to such severe diffusion limitations that they participated only minimally in the reaction. In the case of the passivated catalyst, the inactive external surface led the reaction to be solely dependent on internal sites, which revealed their mass transfer diffusion limitation. E_{app} for H-ZSM-5-AT30_{0.4M}-AW was found to be $96 \text{ kJ} \cdot \text{mol}^{-1}$, which reflected that both mass transfer and kinetics were controlling the observed reaction rate. Counterintuitively, this catalyst was more influenced by internal diffusion compared to H-ZSM-5 despite having higher overall performance. In this case, the external sites probably possessed similar activity to the external acid sites of H-ZSM-5 but were largely removed by the acid wash. Also, introduction of mesopores into the zeolite structure likely caused a higher proportion of the internal zeolite acid sites to participate in the reaction. The overall reaction rate was thus partly governed by internal diffusion, resulting in a lower E_{app} .

Alternatively, the reaction could take place mostly on the acid sites located inside the mesopores where moderate mass diffusion limitation occurs. A mesoporous diffusion limited regime could explain an intermediate value of E_{app} . However, this explanation is rather unlikely due to the much higher reactants' diffusivity in the mesopores compared to the micropores. This consideration is supported by the fact that mesoporous diffusion limitation has not been reported in the literature to the best of our knowledge.

Scheme 3-3 summarizes the findings of our study. The reaction mostly took place on the surface and edges of the H-ZSM-5 zeolite crystal while the bulk of the crystal was almost completely unutilized. Therefore, the resulting E_{app} was closer to the real activation energy of the reaction. Due to the addition of an external S-1 layer for H-ZSM-5@S-1, the reaction was forced to occur within the micropores, leading to a lower E_{app} . Finally, the effect of

internal diffusion was observed more severely on the hierarchical candidate compared to the untreated one with an intermediate E_{app} value. Owing to its intracrystalline network of mesopores, the bulk of the crystal was more accessible and a larger proportion of the reaction likely took place within the micropores.



Scheme 3-3. Synthesis of OME from TRI and OME₁ on the passivated, untreated and mesoporous zeolites.

3.4 Conclusions

We demonstrated that controlled insertion of intracrystalline mesopores in H-ZSM-5 led to the formation of a hierarchical material that exhibited superior catalytic performance for the synthesis of OME from trioxane and dimethoxymethane. A two-fold enhancement in initial reaction rate alongside a 10 % increase in the selectivity towards the OME with 3 to 5 oxymethylene units (OME₃₋₅) was achieved with the best catalyst (H-ZSM-5-AT30_{0.4M}-AW). Treatments to passivate the external surface of the H-ZSM-5 crystal highlighted the more prominent role of external acid sites. Access to the active sites in H-ZSM-5 micropores was found to be of high importance since large OME molecules experienced internal diffusion limitation in the zeolite's micropores. The kinetic study confirmed that the inner volume of the untreated zeolite was less accessible compared to the hierarchical zeolites that have advantageous diffusion properties.

Chapter 4 Nature of the active sites of tin-montmorillonite for OME synthesis

4.1 Introduction

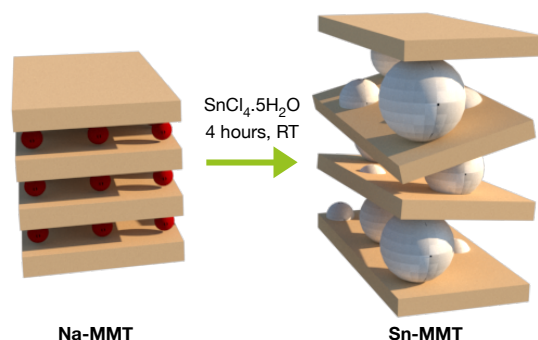
The anhydrous synthesis route, with trioxane (TRI) and dimethoxymethane (OME₁), is known to generate the highest yield of OME.^[164] Various catalysts such as zeolites, acidic resins or ionic liquids have been used for this synthesis route.^[69,74,75,143] Solid acids have the intrinsic advantage of offering an easy separation compared to ionic liquids or mineral acids. It was found that both Brønsted^[70,85] and Lewis^[144,165] acidity catalyze OME synthesis. Currently, acidic resins and zeolite H-Beta have demonstrated the highest potential as catalyst for OME synthesis.^[83,110] However, acidic resins can deactivate due to thermal instability.^[166] In Chapter 3, we demonstrated that an H-ZSM-5 zeolite suffered from severe internal mass diffusion limitation, which could be circumvented by the addition of an auxiliary network of mesopores.^[122] Development of catalysts displaying a high number of acidic sites accessible without internal diffusion limitations is thus required for an efficient OME synthesis. These findings were used to develop an eco-friendly catalyst based on clay.

Over the past decades, clay has emerged as a new type of cheap, tunable and eco-friendly material with versatile, high-end applications ranging from adsorbents to drilling fluids.^[167,168] It is capable of catalyzing a wide range of reactions such as addition, oxidation or dehydration.^[169,170] Its structure possesses advantageous features: it is composed of stacked

This chapter is part of a published article in ChemCatChem as C. J. Baranowski, A. M. Bahmanpour, F. Héroguel, J. S. Luterbacher, O. Kröcher, Insights into the nature of the active sites of tin-montmorillonite for the synthesis of polyoxymethylene dimethyl ethers (OME), *ChemCatChem* **2019**, 3010-3021.^[123] Part of the manuscript and supplementary information are reproduced here with some changes in formatting with permission from Wiley-VCH. C. Baranowski performed the experiments, analysed the data together with the co-authors and wrote the manuscript.

aluminosilicate layers with intrinsic ion-exchange properties. Montmorillonite (MMT) is a 2:1 phyllosilicate clay with each layer composed of an octahedral alumina sheet sandwiched between two tetrahedral silica sheets.^[171] Isomorphous substitution by lower valence atoms such as Ca^{II} , Al^{III} or Mg^{II} in the aluminosilicate lattice generates a net negative charge counterbalanced by cations between the layers. These properties were leveraged to generate new types of structures such as delaminated clay or pillared layered clay (PILC), which are routinely used to catalyze various organic reactions. Notably, PILC can attain high accessible surface area with pore sizes larger than conventional zeolites.^[172]

Introduction of tin by ion-exchange in MMT was recently shown to lead to a new catalytic material (Sn-MMT) following a simple procedure illustrated in Scheme 4-1.^[173,174] Its advantageous textural and acidic properties, as well as its ease of preparation compared to other tin-containing heterogeneous catalysts, lead to its application in various organic reactions. Wang et al. reported that Sn-MMT displayed a highly superior activity than Sn-grafted MCM-41 for the cyanosilylation of ketones.^[175] They later found that its high specific surface area was formed by the intercalation of SnO_2 nanoparticles between clay layers, resulting in strong Brønsted and Lewis acidity.^[176-178] Sn-MMT was also found to display a disorganized “house-of-cards” structure.^[173] The coexistence of acid sites was leveraged for various hemicellulose upgrading reactions: conversion of carbohydrates to 5-(hydroxymethyl)furfural (HMF),^[179] HMF self-etherification,^[174] synthesis of alkyl lactates from triose^[180] and the production of furfural from xylose^[181]. Sn-MMT was also applied for the Baeyer-Villiger oxidation.^[182]



Scheme 4-1. Insertion of tin between montmorillonite (MMT) clay layers.

Despite this extensive research, the nature of Sn-MMT's acidity remains unclear. A reaction mechanism involving chain-like polymers of SnO_2 in between the clay layers was suggested by Wang et al.^[178] Masui et al. proposed that the contact domain between clay layers and

hydroxylated SnO₂ nanoparticles was responsible for the material's catalytic activity.^[173] Finally, an isolated Sn species was also referred to by Hara et al.^[182] Therefore, the aim of this study was two-fold. First, we aimed at evaluating the activity of modified MMT clay for the synthesis of OME. Acid-treatment and insertion of tin were performed to introduce acidity in MMT. Activity of both catalysts was subsequently assessed and compared with Amberlyst 36 (A36), a common acidic resin. Second, we seek to elucidate the source of activity of Sn-MMT. From the results of the catalytic tests together with characterization data and control experiments, conclusions were drawn about the nature of the active sites in Sn-MMT.

4.2 Experimental

4.2.1 Acid- and tin chloride treatment

The acid-treated montmorillonite (AT-MMT) was prepared as described in a protocol given by Beloufa et al.^[183] Crushed MMT clay (30 g, Fluorochem) was dispersed in 120 mL of deionized water and the mixture was stirred for 2 h at room temperature in an Erlenmeyer flask. Then, 100 mL of a 0.5 M sulfuric acid aqueous solution was added. The solution was maintained for two days under stirring at room temperature. The mixture was then filtered and washed with distilled water until pH 7 was reached. Finally, the product was dried for 24 h at 110 °C and crushed in a mortar.

Sn-MMT was prepared as described in a protocol given by Shinde et al.^[174] Na-MMT (5.0 g) was stirred for 4 h at room temperature in 80 mL of a 0.3 M aqueous SnCl₄ solution (Sigma Aldrich). The clay was then collected by filtration and washed with distilled water until a pH of 7 was reached. The product was then dried for 24 h at 110 °C and crushed in a mortar. Sn-MMT-TT400 was obtained by thermal treatment of Sn-MMT at 400 °C for 3 h under static air with a temperature ramp of 5 °C · min⁻¹. Hydroxylated SnO₂ nanoparticles (denoted as Sn(OH)₄) were prepared by hydrolysis of Sn⁴⁺ in a basic aqueous solution, by mixing a SnCl₄ aqueous solution (0.3 M, 100 mL) with 30 % aqueous ammonia (26 mL) at room temperature.^[184] The white precipitate was filtered and dried at 110 °C overnight.

4.2.2 Catalytic tests

Syntheses of OME were performed in two setups according to a protocol described in section 2.2.1. The first setup is a 450 mL stirred batch reactor and the second is composed

of 10 mL glass reactors with PTFE screw caps and a silicon sealing disk. Unless mentioned otherwise, all experiments were conducted at 70 °C with an OME₁/TRI molar ratio of 3.3 and 0.5 wt % of catalyst. A catalyst loading of 1.0 wt % was used for the reusability test with a reaction time of 60 min. Tests that required to reach equilibrium were performed during 240 min with a 0.5 wt % catalyst loading. Amberlyst 36 (A36) was obtained from Sigma Aldrich.

4.3 Results and discussion

First, the effects of tin insertion and acid-treatment on Na-MMT's structure and morphology are presented and discussed. Next, the activities of the synthesized catalysts for the production of OME are presented and compared to A36. The influence of reaction parameters is also analyzed for Sn-MMT, our best clay-based candidate. In order to clarify the nature of the active sites, we subsequently compare the activity of Sn-MMT to two similar materials, Sn-MMT-TT400 and tin hydroxide (Sn(OH)₄), which were similarly characterized. Finally, structure-activity relationships are discussed.

4.3.1 Structure and morphology of Na-MMT, AT-MMT and Sn-MMT

MMT possesses ordered units at different dimensions.^[185] The layer is the first unit with a thickness of around 1 nm and a lateral dimension between 1-2 μm. The second unit consists of tactoids, which are several layers stacked onto each other in a turbostratic structure. Aggregates constitute the third unit and are composed of several tactoids with various arrangements that depend on different factors, including the nature of the interlayer cation. Micropores can be present between layers (e.g. slit-shaped pores, lenticular-shaped) and mesopores generally arise from the presence of intertactoid pores. Clusters of aggregates may form interaggregates pores which are large mesopores to macropores. N₂ physisorption was used to investigate the textural properties of the samples resulting from tin insertion and acid-treatment (Table 4-1, Figure 4-1a). It is important to note that N₂ does not penetrate the interlayer space of unmodified MMT.^[186]

Table 4-1. Textural and acidic parameters of Na-MMT, AT-MMT and Sn-MMT, Sn-MMT-TT400 and Sn(OH)₄.

Sample	Surface (m ² · g ⁻¹)			Volume (cm ³ · g ⁻¹)		Acidity (mmol · g ⁻¹)			
	BET	Micro ^[a]	Meso ^[b]	Micro ^[a]	Meso ^[b]	Total	Weak	Medium	Strong
Na-MMT	69	24	38	0.012	0.10	0.17	0.12	0.00	0.05
AT-MMT	119	32	70	0.016	0.14	0.31	0.20	0.11	0.00

Sn-MMT	269	54	149	0.026	0.13	0.71	0.30	0.21	0.20
Sn-MMT-TT400	263	39	142	0.017	0.14	0.51	0.38	0.07	0.06
Sn(OH) ₄	165	75	46	0.037	0.030	0.61	0.29	0.26	0.06

^a Calculated based on the t-plot method. ^b Calculated based on the BJH method using the adsorption branch.

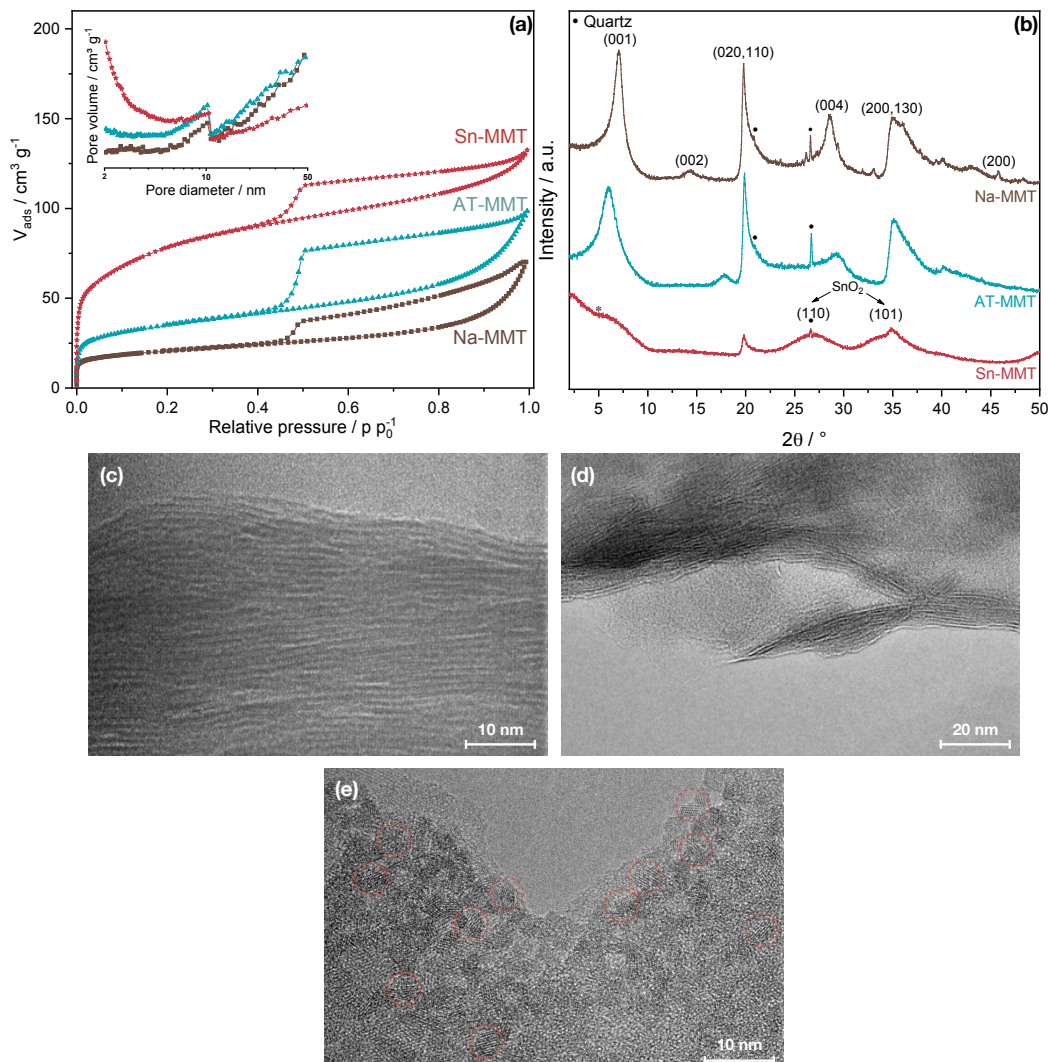


Figure 4-1. (a) N₂ isotherms of the catalyst samples and incremental pore volume determined using the BJH method (inset), (b) powder X-ray diffraction patterns of the catalyst samples (* indicates peak related to the sample holder) and TEM images of (c) Na-MMT, (d) AT-MMT, (e) Sn-MMT. Dotted circles are highlighting examples of lattice fringes observed for Sn-MMT.

All clays possessed a type II isotherm with an H2 hysteresis loop closing vertically at p/p^0 of 0.44, which is typical for clay. Acid-treatment and insertion of tin increased the specific surface area from 69 to 119 and 269 $\text{m}^2 \cdot \text{g}^{-1}$, respectively (Table 4-1). At low relative pressure, increased N₂ uptake for AT-MMT and Sn-MMT indicated an increase in the microporous surface area (S_{micro}). The mesoporous surface area (S_{meso}) increased from 38 to 70 and 149 $\text{m}^2 \cdot \text{g}^{-1}$ for AT-MMT and Sn-MMT, respectively. Acid-treatment of Na-MMT led to layer delamination (Figure 4-1d), and to almost 90 % replacement of interlayer Na⁺ by

H⁺ (Table 4-2). Other cations present in the interlamellar space were also partly removed (e.g. K⁺, Ca²⁺). Mild clay dealumination was also observed, with its Si/Al molar ratio going up from 2.98 to 3.13. Furthermore, other substituting atoms (i.e. Mg²⁺ and Fe²⁺) were also partly removed by the acid treatment, as the Si/Mg and Si/Fe molar ratios increased from 17.13 to 20.61 and from 24.05 to 25.94, respectively.

Table 4-2. ICP-OES results for Na-MMT, AT-MMT and Sn-MMT.

	Na-MMT (wt %)	AT-MMT (wt %)	Sn-MMT (wt %)
Si	25.4	27.4	17.8
Al	8.2	8.4	5.7
Mg	2.9	2.6	1.8
Na	2.9	0.26	660 ppm
Sn	0.0	0.0	27.8
Fe	2.1	2.1	1.4
Ca	1.1	0.55	0.13
Si/Al (mol)	2.98	3.13	3.00
Si/Mg (mol)	17.13	20.61	19.34
Si/Fe (mol)	24.05	25.94	25.28

Meanwhile, despite Sn-MMT having a larger S_{meso} compared to AT-MMT, it possessed a similar mesoporous volume, which could indicate the presence of interlayer tin. Sn-MMT possessed a broader distribution of small mesopores as well as fewer large mesopores (Figure 4-1a, inset). ICP-OES analysis (Table 4-2) revealed that upon ion-exchange with SnCl₄, Sn-MMT reached 27.8 wt % of tin with only 660 ppm of sodium. SEM-EDXS confirmed that tin was homogeneously distributed in the clay particles as no tin aggregation was detected (Figure 4-2d). The Si/Al molar ratio remained constant after tin insertion which indicates that no composition modifications occurred to the aluminosilicate sheets.

X-ray diffraction (Figure 4-1b) was used to investigate the clay structure and the nature of the tin phase. Na-MMT was identified with the (00 l) reflection at 7.0°, 14.2° and 28.6° as well as with the (020,110) and (200,130) reflections with maxima located at 19.9° and 34.9°, respectively.^[187,188] The (001), (002) and (004) reflections of Sn-MMT almost disappeared showing a complete loss of the layered structure (confirming delamination) as well as a shift to lower diffraction angle, implying an increase in the mean interlayer distance from 1.24 nm to 1.31 nm (calculated using Bragg's law).^[173,189] A broad (001) basal reflection is observed for AT-MMT which hence only suffered from partial layer stacking loss and an

increase in the mean interlayer distance to 1.45 nm. Retention of the (020,110) and (200,130) reflections intensity suggested preservation of the two-dimensional structure (i.e. the clay sheets) for both Sn-MMT and AT-MMT.^[190]

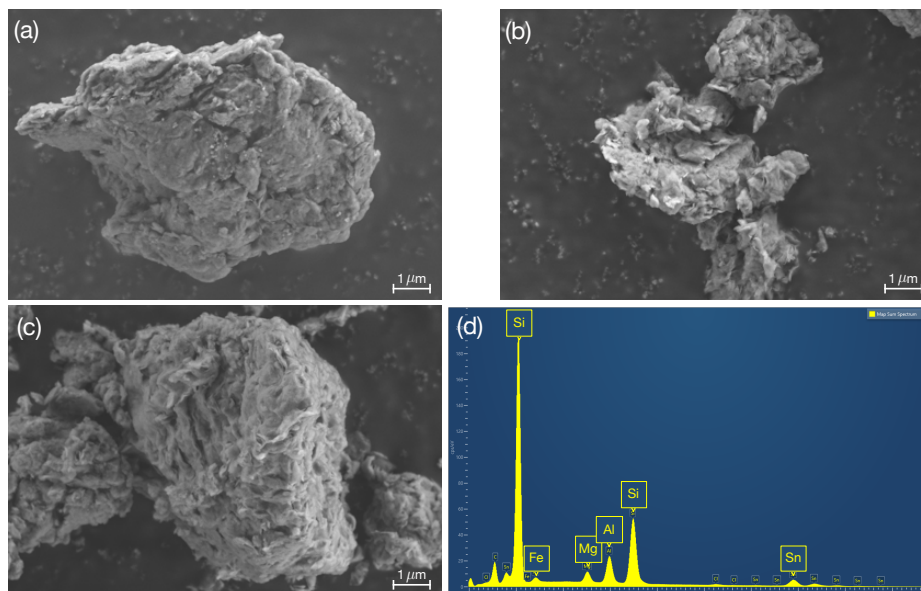


Figure 4-2. SEM images of (a) MMT (b), AT-MMT and (c) Sn-MMT and (d) EDXS spectrum of Sn-MMT.

Sn-MMT displayed diffraction peaks characteristic of a rutile-type SnO_2 structure with broad peaks at 26.7° and 34.8° , corresponding to the (110) and (101) reflections, respectively.^[173] The presence of broad peaks points to the formation of small, well-dispersed nanocrystals (below 5 nm). Combined with the porosity results, we deduced that these crystals were inserted between the clay layers. Our results are thus in agreement with the report from Masui et al., stating that the presence of a nanocrystalline SnO_2 phase changed the stacking arrangement of tactoids into a disordered ‘house-of-card’ structure.^[173] Sn-MMT displayed the largest S_{micro} , as the presence of SnO_2 nanocrystals likely induced the formation of additional interlayer microporous volume. The presence of interlayer SnO_2 was confirmed by bright field transmission electron microscopy, where lattice fringe contrasts were observed (Figure 4-1e). Due to the sensitive nature of the interlayer SnO_2 particles, no elemental analysis study was performed, as prolonged exposure to the electron beam led to aggregation of the SnO_2 crystals. The presence of (110) and (101) SnO_2 planes was confirmed by selected area electron diffraction (Figure 4-3a and b).

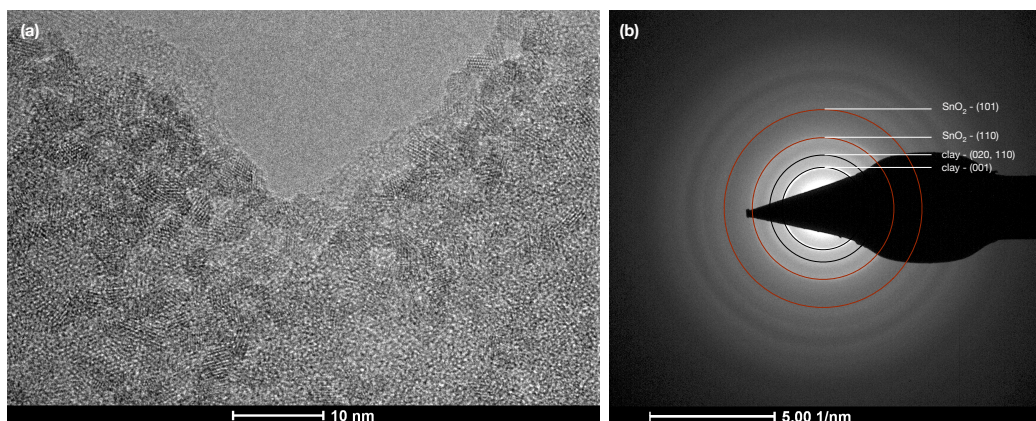


Figure 4-3. (a) TEM image and (b) selected area electron diffraction pattern of Sn-MMT.

Diffuse reflectance infrared Fourier transform spectroscopy (DRIFTS) was carried out to gather additional information on the modifications of the clay (Figure 4-4). Due to the diversity of structural groups present, interpretation of the curves can sometimes be intricate due to peak overlapping. Samples containing MMT displayed two peaks corresponding to structural hydroxyl groups bounded to octahedral Al in the OH stretching and bending regions, at 3623 and 917 cm^{-1} , respectively.^[191] Acid-treatment resulted in decrease of the peaks at 917, 875 and 836 cm^{-1} , assigned to bending vibrations of the hydroxyl groups (Al_2OH), (AlFeOH) and (AlMgOH), respectively.^[190] Mg^{2+} was more prone to leaching upon acid-treatment than Fe^{3+} .^[192]

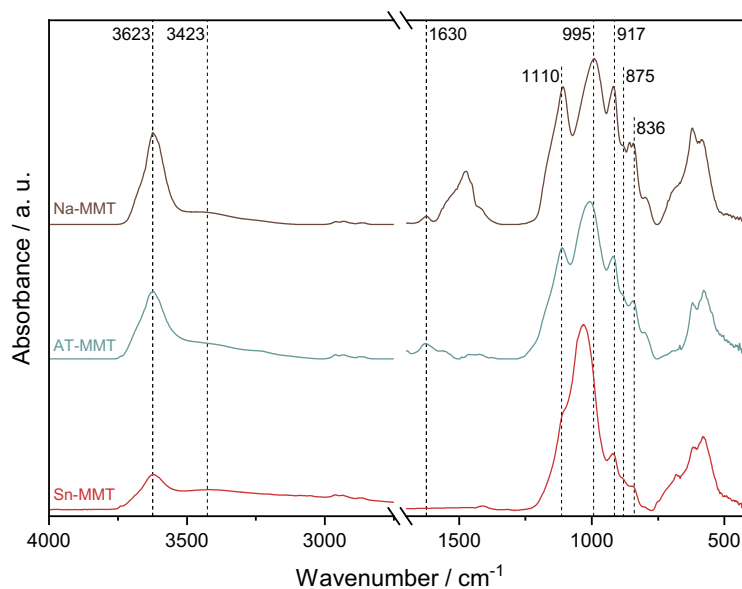


Figure 4-4. Ex-situ DRIFT spectra of Na-MMT, AT-MMT and Sn-MMT.

The presence of chemisorbed and physisorbed water, most probably due to the hydration layer of the cations, was detected at 1630 cm^{-1} and 3423 cm^{-1} . Additionally, The Si-O out-

of-plane and in-plane stretching peaks were identified at 1110 and 995 cm^{-1} , respectively. We observed a shift in both signals with the various treatments, which could be due to the change in the interlayer water content. These vibrations were independent of the nature or the concentration of the interlayer cation.^[193] A detailed analysis of Sn-MMT spectrum is provided later.

Natural MMT contains paramagnetic and/or ferromagnetic species that make MAS-NMR analysis difficult.^[194] Substitution of Si^{4+} by Al^{3+} in the tetrahedral sheet and substitution of Al^{3+} by Mg^{2+} in the octahedral sheet also induced broader peaks. ^{27}Al MAS-NMR (Figure 4-5a) shows two resonance peaks at ca. 70 and 5 ppm, which are attributed to four-fold Al^{IV} (tetrahedral sheet) and six-fold Al^{VI} (octahedral sheet), respectively.^[194-196] Overall, the proportion of Al^{VI} to Al^{IV} did not change significantly, indicating that the sheet structure stayed intact during acid-treatment or SnCl_4 ion-exchange.

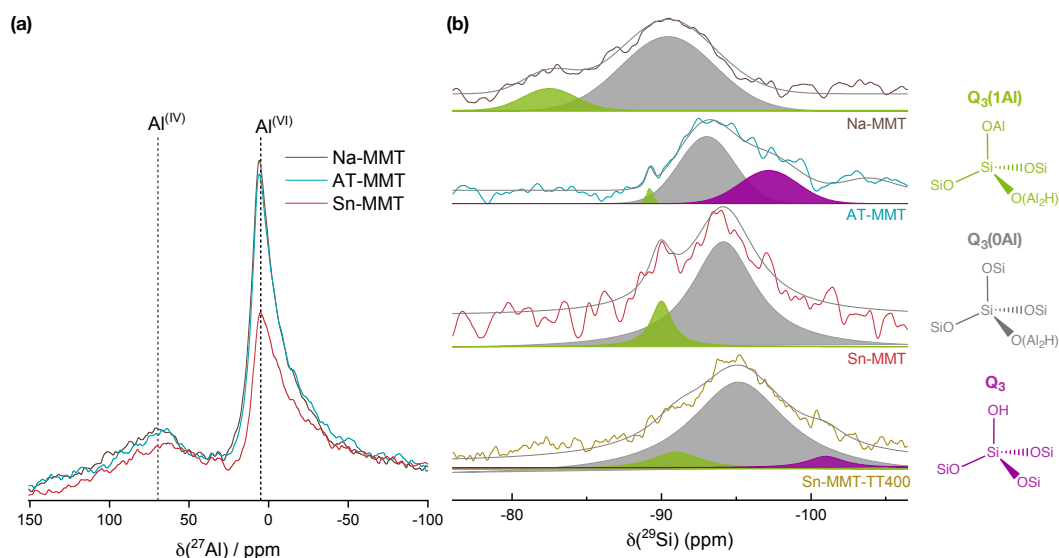


Figure 4-5. (a) ^{27}Al MAS-NMR spectra of Na-MMT, AT-MMT and Sn-MMT and (b) ^{29}Si MAS-NMR spectra of Na-MMT, AT-MMT, Sn-MMT and Sn-MMT-TT400.

Magic angle spinning nuclear magnetic resonance (MAS-NMR) was used to investigate the local structure of Si and Al atoms. The ^{29}Si MAS-NMR spectrum of Na-MMT shows a broad peak corresponding to $\text{Q}_3(0\text{Al})$ (silicon atom connected to three silicon atoms via a basal oxygen and to the octahedral layer via an apical tricoordinated oxygen) (Figure 4-5b). The chemical shift of $\text{Q}_3(0\text{Al})$ depends on the nature of the interlayer cation and shifts towards higher frequencies with a lower amount of Na^+ cations in the interlamellar space.^[197] Specifically, this peak appears at -90.5, -93.0 or -93.8 ppm for Na-MMT, AT-MMT and Sn-MMT, respectively. A shoulder centered at ca. -83, -89 or -90 ppm for Na-MMT, AT-MMT

and Sn-MMT, respectively, corresponds to a $Q_3(1Al)$ moiety (silicon atom connected to two silicon and one aluminum atoms via bridging oxygens and to the octahedral sheet via an apical oxygen).^[197] Finally, the acid-treatment results in the appearance of a peak for Q_3 ($SiO=Si-OH$) due to dealumination.

4.3.2 Catalytic properties for OME synthesis

Next, we assessed the activities of the various clays for OME synthesis from TRI and OME_1 and compared it to the activity of A36. TRI conversion, selectivity towards OME_{3-5} as well as chain growth probability vs. time are displayed in Figure 4-6. Their activities followed the trend: $A36 > Sn-MMT > AT-MMT > Na-MMT$. Na-MMT showed almost no TRI conversion but both treatments applied on the clay significantly improved its activity. AT-MMT possessed a modest activity while Sn-MMT performance was close to A36, our reference material. The latter reached equilibrium after 120 min of reaction while 180 min were necessary for Sn-MMT to achieve the same results. AT-MMT did not reach equilibrium during the experimental run time. Sn-MMT led to a higher selectivity of 0.44 to OME_{3-5} at the end of the run compared to 0.41 using A36 (Figure 4-6b). Both catalysts led to an equal value of α , which reflects a chain length distribution that followed the SF distribution (Figure 4-6c).

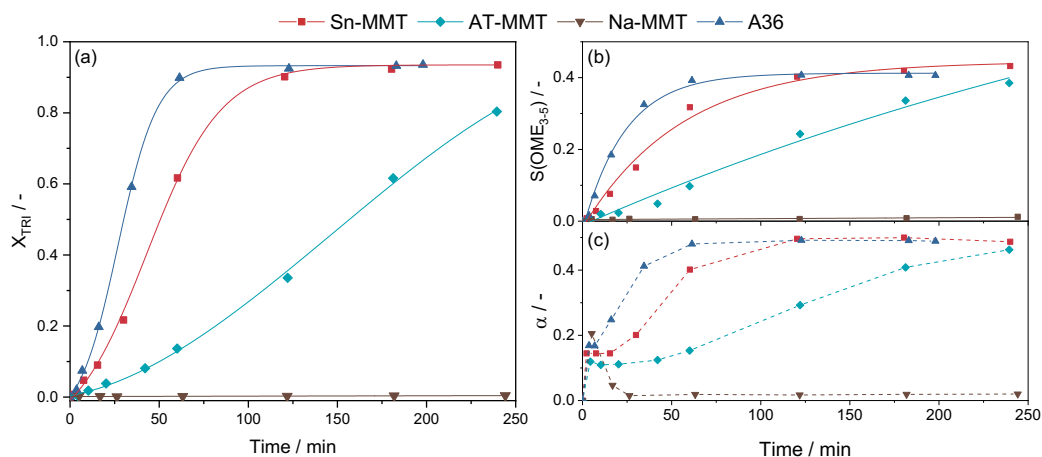


Figure 4-6. (a) TRI conversion X_{TRI} , (b) selectivity to OME_{3-5} $S(OME_{3-5})$ and (c) chain growth probability α for the production of OME.

A more detailed study on the influence of reaction parameters was performed using Sn-MMT as the most active MMT-based candidate for the synthesis of OME (Figure 4-7). Increase of the reaction temperature resulted in a lower TRI conversion and α value at

equilibrium as expected for an exothermic reaction (Figure 4-7a). Additionally, TRI conversion and α increased linearly with catalyst concentration (Figure 4-7b). As expected, changing the molar ratio of OME₁/TRI affected both TRI conversion and α at equilibrium (Figure 4-7c): decreasing the ratio diminished the TRI conversion but increased α , while an increase in the ratio resulted in higher TRI conversion with smaller α . Indeed, increasing the proportion of TRI increases the OME chain length distribution at the expense of TRI conversion at equilibrium; this parameter thus needs to be optimized to maximize the production of OME₃₋₅. Stability of Sn-MMT and A36 was also assessed during four successive runs (Figure 4-7d) where comparable activities and no deactivation were observed.

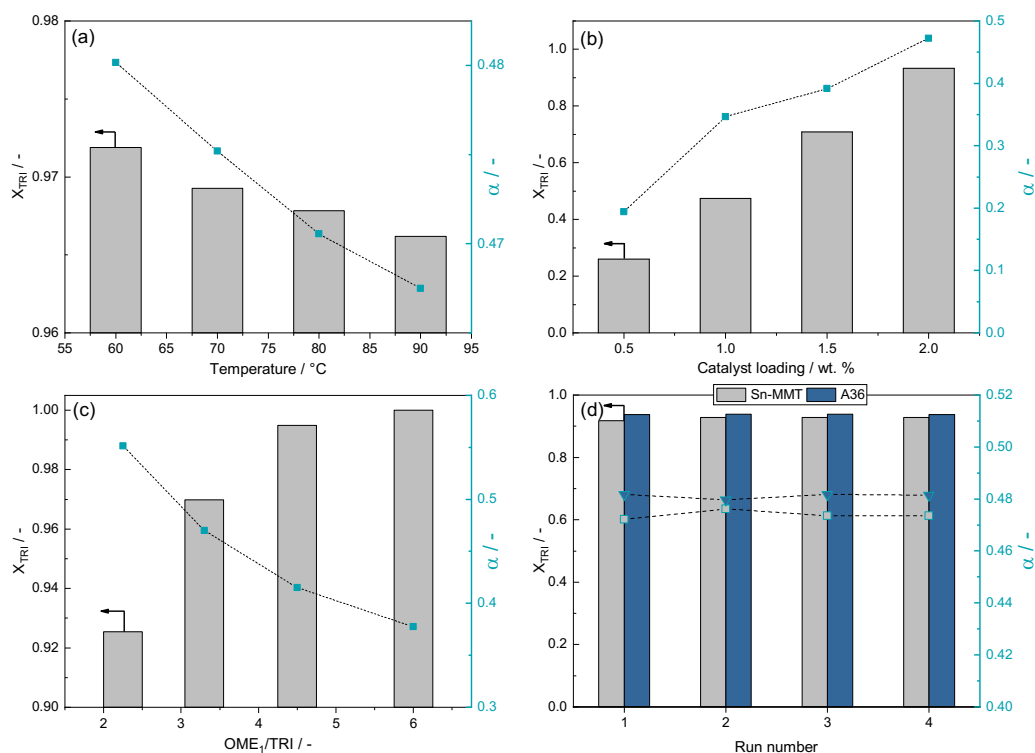


Figure 4-7. OME synthesis from OME₁ and TRI. TRI conversion X_{TRI} and chain growth probability α (a) at equilibrium for various temperature (0.5 wt % Sn-MMT, reaction time 240 min), (b) at various Sn-MMT wt % (reaction time 30 min), (c) at equilibrium for different OME₁/ TRI molar ratio (0.5 wt % Sn-MMT, reaction time 240 min) and (d) in a reusability test with A36 and Sn-MMT (1.0 wt %, reaction time 60 min).

4.3.3 Catalytic properties and characterization of SnO₂ catalysts

In order to shed more light on the source of acidity of Sn-MMT, we studied the activity of two similar materials: Sn-MMT-TT400 (obtained after calcination at 400 °C for 3 h of Sn-MMT) and tin hydroxide (Sn(OH)₄, synthesized by reduction of SnCl₄). They help to understand the effect of calcination on the performance of Sn-MMT, and the inter-

action between clay and tin. Previous studies already used a similar comparison for a different reaction but failed to provide a detailed explanation on their lack of activity in comparison with Sn-MMT.^[173,174] As expected, both catalysts displayed much lower activity compared to Sn-MMT for the synthesis of OME from TRI and OME₁ (Figure 4-8). Thermal treatment showed a drastic effect on the TRI conversion with a drop of 92 % while a TRI conversion of only 2.3 % was reached using Sn(OH)₄.

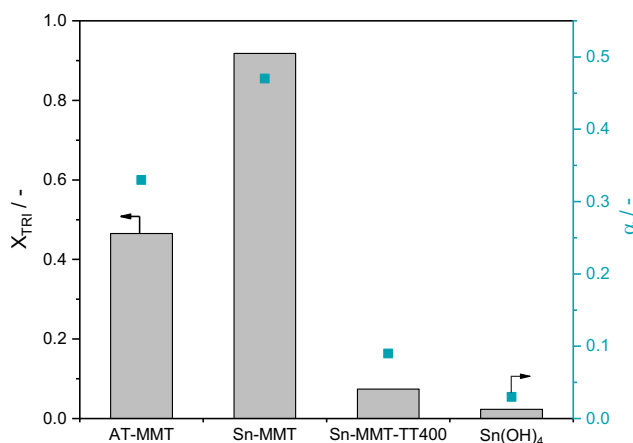


Figure 4-8. TRI conversion X_{TRI} and chain growth probability α for AT-MMT, Sn-MMT, Sn-MMT-TT400 and Sn(OH)₄ (1.0 wt % catalyst, reaction time 60 min).

A careful characterization of Sn-MMT-TT400 and Sn(OH)₄ has been performed in order to build structure-activity relationships. Sn-MMT, Sn-MMT-TT400 and Sn(OH)₄ displayed diffraction peaks characteristic of SnO₂ structure (Figure 4-9b) with average crystallite sizes of 2.74, 4.82 and 3.04 nm, respectively (calculated based on the (001) reflection using Scherrer's equation). The thermal treatment of Sn-MMT slightly affected the (020,110) and (200,130) reflections, which could indicate a change in the clay layer crystal lattice. Additionally, N₂ physisorption suggests sintering of SnO₂ nanocrystals upon thermal treatment with a decrease in S_{micro} , while S_{meso} remained rather constant (Table 4-1, Figure 4-9a). Sn(OH)₄ displayed a type I isotherm (S_{micro} of 75 m² · g⁻¹ and S_{meso} of 46 m² · g⁻¹) and confirms the high microporosity of the tin hydroxide phase.

In order to get more insight into the deactivation mechanism of Sn-MMT during the thermal treatment, we performed in-situ DRIFTS of Sn-MMT at 400 °C (Figure 4-10). An increase in vibrations related to symmetric O-Sn-O and antisymmetric Sn-O-Sn stretching mode of a surface bridging oxide was observed at 669 and 737 cm⁻¹, respectively, which is

attributed to sintering of SnO_2 nanocrystals.^[198] The peaks at 1327 and 1415 cm^{-1} are overtones of these two vibrations.

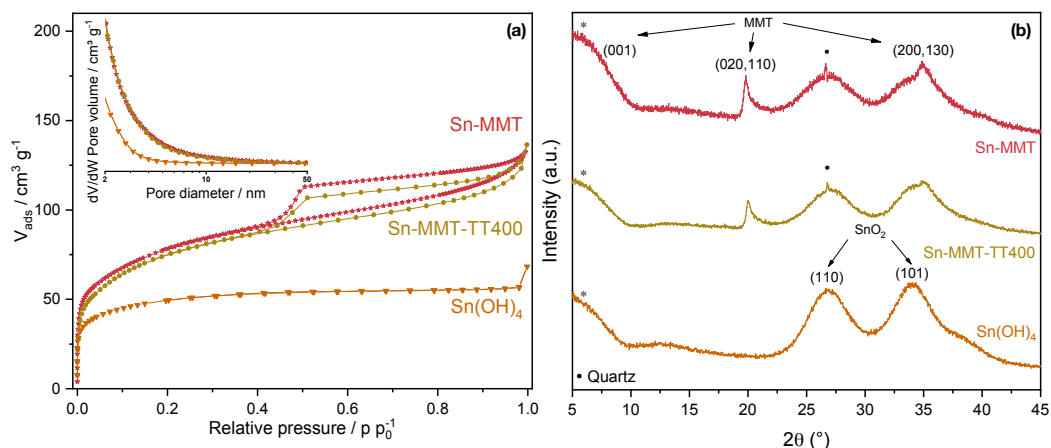


Figure 4-9. (a) N_2 isotherms and dV/dW pore volume BJH adsorption branches as inset of the catalyst samples and (b) powder X-ray diffraction patterns of Sn-MMT, Sn-MMT-TT400 and $\text{Sn}(\text{OH})_4$. * Peaks related to the sample holder.

Furthermore, we also observed a decrease of the signal between 850 and 950 cm^{-1} that corresponds to the hydroxyl bending region. This phenomenon was ascribed by Alvero et al. to the migration of cations in vacant hexagonal holes of the silica sheet where they interact with structural hydroxyl groups.^[199] Meanwhile, analysis of the hydroxyl stretching region showed a decrease of a broad peak between 3300 and 3500 cm^{-1} , which can be attributed to the dehydration of the clay and/or the condensation of Sn-OH groups. No change was identified in the Si-OH (ca. 3740 cm^{-1}) and Al-OH regions (3640 cm^{-1}).

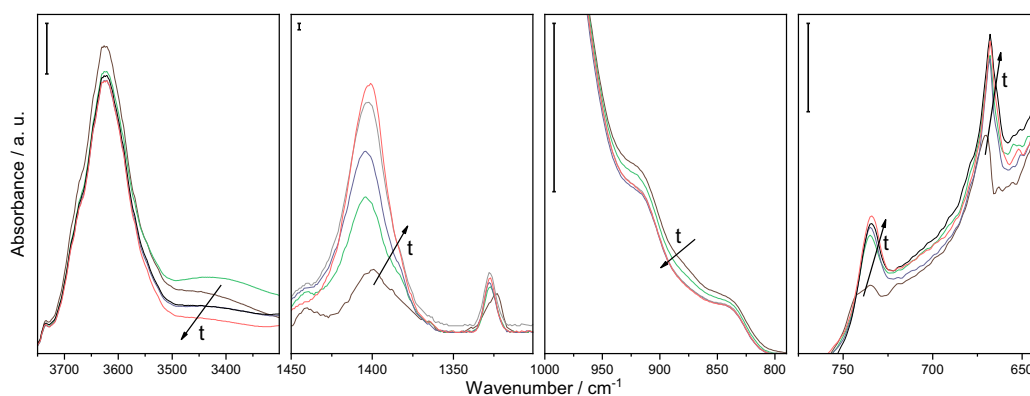


Figure 4-10. In-situ DRIFT spectra of Sn-MMT treated at 400 °C under 20 mL · min⁻¹ of He at various times (the scale bar on the top left of each frame indicates the relative intensity).

Comparison between ex-situ DRIFT spectra of Sn-MMT and Sn-MMT-TT400 shows a large difference in the intensity of the OH stretching region between 3500 and 3300 cm^{-1}

due to irreversible desorption of both chemisorbed water and hydroxyl surface groups (Figure 4-11). When the hydration shell of the proton is removed at high temperature, H^+ migrates in the clay sheet, thereby neutralizing its net charge, a phenomenon known as the Hofmann-Klemen effect. This was confirmed by a slight shift in the Si-O-Si stretching vibration which could result from lattice distortion of the Si-O framework due to the presence of the proton.^[199] This corroborates with the XRD patterns showing a weakening of the (020,110) reflection. Furthermore, a similar decrease of the signal intensity between 850 to 950 cm^{-1} was observed compared to the in-situ DRIFTS measurements. The effect of the thermal treatment of the clay was also observed with ^{27}Si MAS-NMR spectroscopy showing a shift of the Q3(0Al) peak from -93.8 to -95.1 ppm, which is attributed to the formation of a neutral structure (Figure 4-5b).^[200] Overall, it appeared that during the thermal treatment, the interlayer water was removed, dehydroxylated SnO_2 nanocrystals sintered, and protons migrated inside the clay layers.

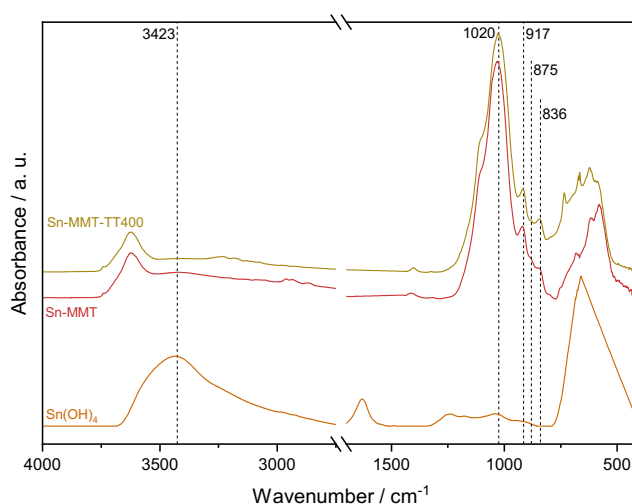


Figure 4-11. Ex-situ DRIFT spectra of Sn-MMT, Sn-MMT-TT400 and $Sn(OH)_4$.

Meanwhile, analysis of $Sn(OH)_4$ DRIFT spectrum shows a broad peak around 3440 cm^{-1} corresponding to the O-H stretching vibration from the hydroxylated surface and molecular water, also responsible for the peak at 1630 cm^{-1} (Figure 4-11). Saturation of the signal occurred at wavenumbers below 680 cm^{-1} due to the strong signal from Sn-O-Sn stretching vibration.^[198]

The local structure of Sn was also investigated by ^{119}Sn MAS-NMR (Figure 4-12a). All samples have similar signals with a main peak centered around -604 ppm, which can be ascribed to octahedral tin in bulk SnO_2 .^[201] No tetrahedral tin was detected. Variation of

the main peak can be the result of hydroxylation of SnO₂ surface and its crystalline size.^[202] Peak broadening indicates the presence of SnO₂ nanocrystals as surface atoms have different chemical shifts compared to bulk atoms. Hydroxylation of the tin surface was indicated by signals of the first and second tin layer which have chemical shifts of -590 and -615 ppm, respectively (Figure 4-12a, inset).^[173,203] Sn-MMT-TT400 and Sn-MMT appear to have a slight signal shift towards lower values compared to Sn(OH)₄. We suggest that this is caused by covalent anchoring of Sn atoms to the clay sheet to one or two silicon atoms via an oxygen bridge.^[204] Thermal treatment would thus also increase the number of covalent bonds between SnO₂ and the tetrahedral silica sheet. A similar anchoring mechanism was observed for Al-pillared MMT upon thermal treatment.^[172]

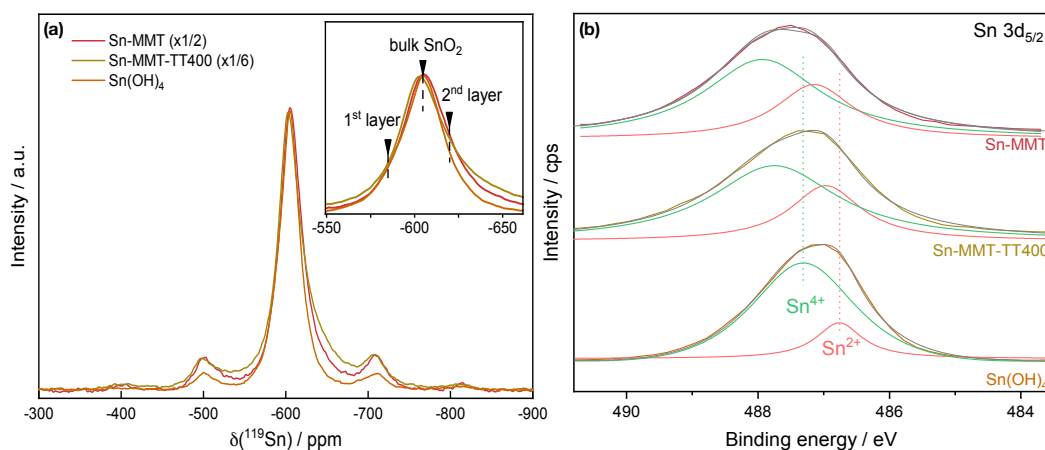


Figure 4-12. (a) ¹¹⁹Sn MAS-NMR spectra and enlarged view of the main peak (inset). (b) Deconvolution of the main XPS peak of Sn-MMT, Sn-MMT-TT400 and Sn(OH)₄

For further analysis of the oxidation states of the surface SnO₂ species, we employed XPS which provides small probing depth in contrast to MAS-NMR (Figure 4-12b). The high-resolution Sn 3d_{5/2} XPS spectra of Sn(OH)₄ were deconvoluted into two peaks attributed to Sn²⁺ and Sn⁴⁺, respectively centered at 486.8 and 487.3 eV.^[205] Figure 4-12b demonstrates that the tin prevalently existed as Sn⁴⁺ compared to Sn²⁺, which is an aliovalent substitution that require a charge compensation mechanism (i.e. an oxygen vacancy). In comparison, tin species residing between the clay exhibited two differences: a higher proportion of Sn²⁺ and a shift of both peaks towards higher binding energies (Table 4-3). According to Yang et al., a shift towards higher binding energies reflects a surface with a higher amount of oxygen vacancies.^[206] Being positively charged, they cause a decrease in the electron density of nearby Sn, and thus an increase in their binding energies. We suggest that the negative charge of the aluminosilicate layers induced a higher number of structural defects

during crystallization of SnO₂ in the interlamellar space (i.e. Sn²⁺ and adjacent oxygen vacancies). Therefore, the activity of Sn-MMT could be due to a higher number of oxygen vacancies and adjacent undercoordinated Sn²⁺ atoms on the surface, which were also demonstrated to be more active in NO₂ sensing.^[207] Thermal treatment of Sn-MMT resulted in a shift towards lower binding energy but did not affect the proportion of Sn²⁺/Sn⁴⁺. Compared to Sn-MMT, Sn-MMT-TT400 displayed thus a lower amount of undercoordinated surface Sn. Analysis of the O1s peak would not provide more information since it would also contain a large contribution from oxygen moieties present in the clay layer.

Table 4-3. Deconvolution of the Sn 3d_{5/2} peak for Sn-MMT, Sn-MMT-TT400 and Sn(OH)₄.

	Binding energy (eV)		
	Sn ⁴⁺	Sn ²⁺	Area Sn ⁴⁺ /Area Sn ²⁺ (-)
Sn-MMT	487.9	487.1	2.2
Sn-MMT-TT400	487.7	486.9	2.4
Sn(OH)₄	487.3	486.8	3.0

4.3.4 Acidic properties of the catalysts

Sample acidity was studied by NH₃-TPD (Figure 4-13a) and py-FTIR (Figure 4-13b). The NH₃-TPD profiles may not be perfectly reliable at temperatures above 400 °C as structural changes may occur above this temperature. Acidity was measured by deconvolution of the NH₃-TPD profiles and these values are presented in Table 4-1. While Na-MMT had a very low acidity (0.17 mmol · g⁻¹), exchanging interlamellar Na⁺ cations with H⁺ (AT-MMT) increased its acidity to 0.31 mmol · g⁻¹. Thermal treatment of Sn-MMT decreased acid site concentration from 0.71 to 0.51 mmol · g⁻¹ but did not alter the nature and strength of the acid sites with no difference observed by FTIR spectroscopy after saturation with pyridine vapor at 50 °C.^[158] The typical bands for Brønsted (1530 and 1365 cm⁻¹), Lewis (1451 and 1609 cm⁻¹) and H-bonded pyridine (1444 and 1596 cm⁻¹) acidity were observed for Sn-MMT and Sn-MMT-TT400. The signal corresponding to Lewis acid sites remained constant with increasing temperatures, while the signal corresponding to Brønsted acid sites slightly diminished. Thus, both catalysts displayed strong Lewis acid sites and moderate Brønsted acidity. Meanwhile, weak and moderate Brønsted acidity were identified for Na-MMT and AT-MMT, respectively. Finally, Sn(OH)₄ mostly displayed Lewis acid sites of moderate strength (0.61 mmol · g⁻¹).

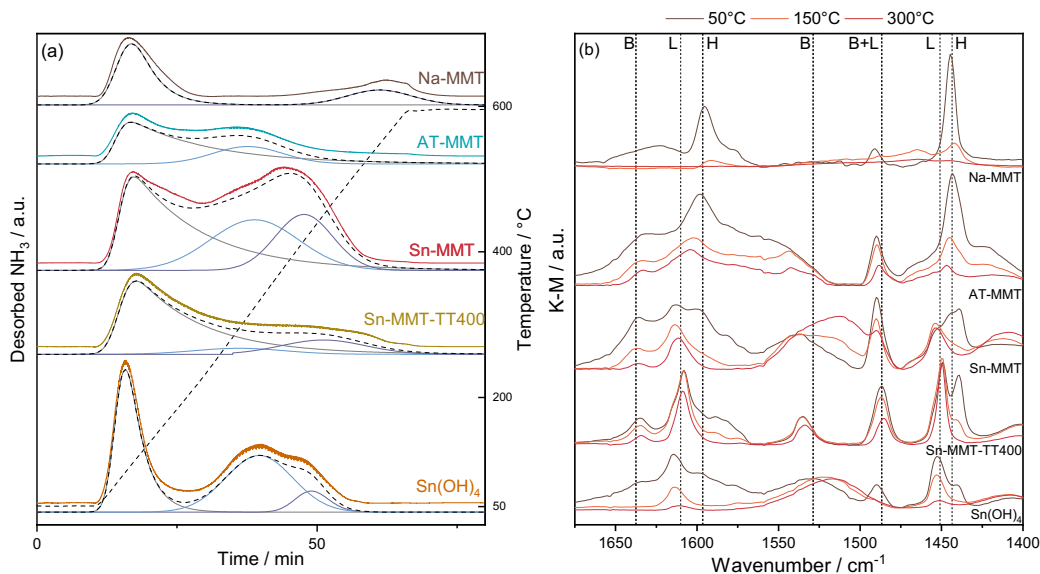
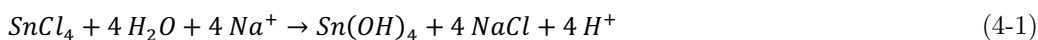


Figure 4-13. Characterization of the acidity of the catalysts by (a) NH_3 -TPD and (b) pyridine-FTIR spectroscopy at various temperatures (B and L indicate pyridine bonded to Brønsted and Lewis sites, respectively, while H indicates H-bonded pyridine).

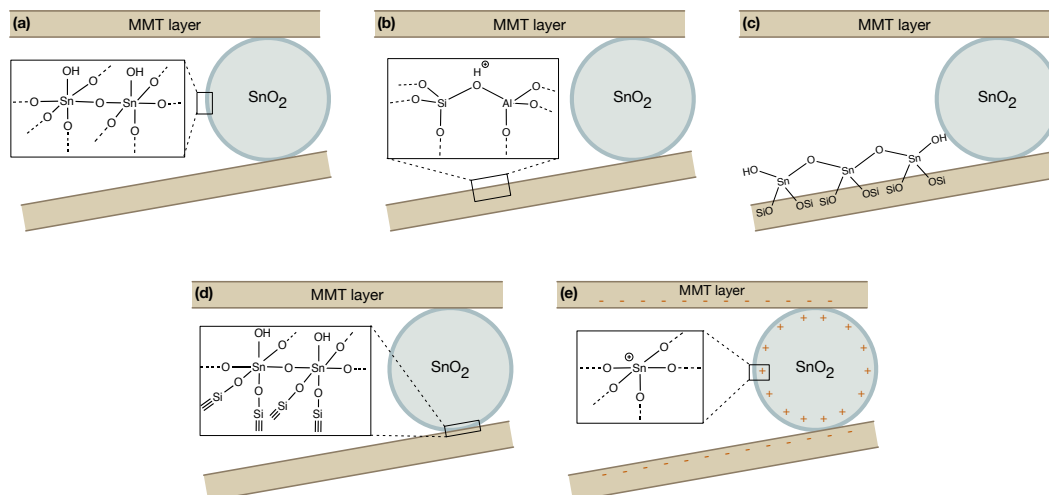
4.3.5 Discussion on the nature of the active sites

The characterization data obtained in this study helped to shed light on Sn-MMT structure and active sites. Upon ion-exchange with tin chloride, SnO_2 nanocrystals were formed in between MMT layers by Sn^{4+} hydrolysis according to Equation (4-1). As a result, clay layers were opened and exposed. Sn-MMT displayed a high surface area, as well as higher accessibility to strong acid sites due to the presence of micro- and mesopores.



Comparison of the catalytic activity of Sn-MMT, Sn-MMT-TT400 and $\text{Sn}(\text{OH})_4$ in OME synthesis, combined with the catalysts' characterization data allowed us to clarify the nature of the acid sites present in Sn-MMT (Scheme 4-2). The first question to answer is whether the acidity comes from the clay layer, the SnO_2 nanocrystals, or both. First, since the activity of $\text{Sn}(\text{OH})_4$ was the lowest among these three catalysts, it is clear that the SnO_2 nanocrystals have to be within the clay layers to efficiently catalyze OME synthesis. Surface Sn atoms acting as moderate Lewis acid and hydroxyl groups on the surface of the nanocrystals are insufficient to catalyze OME synthesis (Scheme 4-2a). Therefore, the proposal of Shinde et al. that hydroxylated SnO_2 nanocrystals act as a source of Brønsted acidity is invalid.^[174]

Second, the clay layer is known to expose only weak Brønsted-acidic silanols and weak Lewis acid sites (i.e. undercoordinated Al^{3+} or Mg^{2+} at the edge of the clay sheet). Acidic protons could be produced during Sn^{4+} hydrolysis (Equation (4-1)) and stabilized by the clay layer (Scheme 4-2b). These protons migrated into the clay layer during the thermal treatment, neutralizing the clay positive charge and reducing its acidity. However, these acidic protons are known to be of moderate strength.^[208]



Scheme 4-2. Schematic representation of the possible acid sites of Sn-MMT.

Similar to pillaring of MMT with aluminum, we thus suggest that acidity is most probably linked to the combination of SnO_2 and the clay layers. Depending on the coordination and environment of Sn, several scenarios are possible. First, isolated, fourfold-coordinated Sn bound to three O-Si and one hydroxyl group could be the source of its acidity where SnO_2 nanocrystals would only serve as pillars to increase the surface area of MMT (Scheme 4-2c). Thermal treatment would cause them to migrate and coalesce with the SnO_2 nanocrystals and hence to lose their activity. However, fourfold-coordinated tin atoms were not detected by ^{119}Sn MAS-NMR.

Third, interfacial Sn atoms, anchored to the clay layer, could act as the source of Brønsted acidity (Scheme 4-2d). However, it would be rather unlikely that surface Sn could act both as cross-linking point to the clay layers as well as acid sites. Only four-fold coordinated Sn, present on high energy facets such as the (111) and the (221) facets, could simultaneously coordinate to the clay layer and a hydroxyl group. Furthermore, access to these sites to OME molecules would be rather difficult.

Considering ^{119}Sn MAS-NMR and XPS data, showing that clay stabilized the formation of defective SnO_2 nanocrystals displaying a higher number of undercoordinated surface Sn^{2+} atoms, we believe that these defects act as strong Lewis acid sites (Scheme 4-2e). Undercoordinated surface sites of nanocrystals are electron deficient and are known to display a Lewis-acidic character.^[209] Thermal treatment of Sn-MMT would cause sintering of the SnO_2 nanocrystals and migration of H^+ inside the clay. The resulting catalyst would contain neutral SnO_2 nanocrystal devoid of its acidity.

Acidity characterization showed that strong Lewis and moderate Brønsted acid sites were present. Furthermore, it demonstrated that thermal treatment affected mostly the acid site concentration. Therefore, we suggest that the source of Sn-MMT acidity is a combination of: (1) Si-OH-Al groups, produced during the crystallization of SnO_2 by the release of H^+ (Scheme 4-2b) and (2) strong Lewis acid sites at the SnO_2 surface formed by undercoordinated Sn^{2+} surface atoms stabilized by the negative charge of the clay layer (Scheme 4-2e). The presence of both Lewis and Brønsted acid sites explains the observed high activity of Sn-MMT for OME synthesis. Liu et al. suggested a synergistic effect of Brønsted and Lewis acid sites for the synthesis of OME from paraformaldehyde and OME_1 .^[210] The Lewis acidity in $\text{Sn}(\text{OH})_4$ alone was insufficient to catalyze OME synthesis, while the Brønsted acidity in AT-MMT resulted in only moderate activity. Besides acidity, the presence of both micro- and mesopores in Sn-MMT also allowed enhanced mass transport for bulky OME molecules.

4.4 Conclusions

We reported that tin incorporation into clay-based materials boosted the catalytic activity for OME synthesis to reach similar performances compared to that of the reference acidic resin. Based on a detailed characterization, we gained insights into Sn-MMT active sites nature: upon ion-exchange with SnCl_4 , SnO_2 nanocrystals were formed and expanded the MMT layers to produce accessible Brønsted and Lewis acid sites, leading to a disorganized house-of-cards structure. Control experiments revealed that hydroxylated tin oxide alone is a poor catalyst for OME synthesis. Moreover, Sn-MMT deactivates by losing its acidity upon thermal treatment, which occurs via successive dehydration, sintering of the SnO_2 phase and migration of protons within the clay layers. Sn-MMT acidity is attributed to Si-OH-Al group, formed as a by-product of SnO_2 crystallization, and undercoordinated, defective SnO_2 surface sites. The negative charge generated by the MMT layers is key in

stabilizing these surface defects, which act as strong Lewis acid sites. In conclusion, our work identifies the active sites present in Sn-MMT and provides a first instance of clay-based catalysts for the synthesis of OME.

Chapter 5 Synergy between Brønsted and Lewis acid sites in Sn-Beta zeolites for OME synthesis

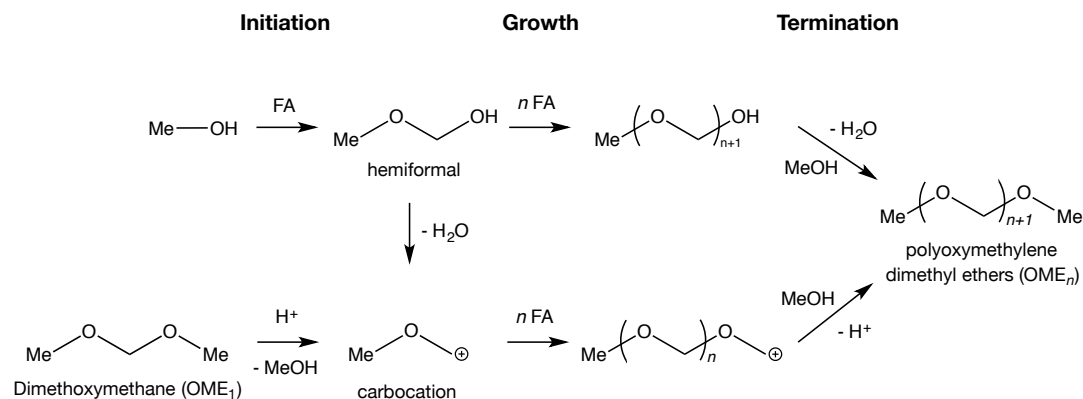
5.1 Introduction

Different synthesis routes exist depending on the oxymethylene and oxymethyl sources:^[143] dimethoxymethane (OME₁), methanol or dimethyl ether, reacts with trioxane (TRI), formaldehyde (FA) or paraformaldehyde (PF) to form a Schulz-Flory (SF) distribution of OME. The anhydrous route demonstrated the highest OME yield and diminishes downstream separation effort, but synthesis from methanol and FA reduces the number of reaction steps required to produce OME.^[83,110]

Two reaction mechanisms were reported in the literature for OME synthesis: initiation, growth and termination (IGT) or sequential addition.^[67,114,115,143] The reactants and catalyst used determine which mechanism will prevail. The IGT mechanism is illustrated in Scheme 5-1. Initiation happens through the generation of a carbocation or a hemiformal intermediate. In the anhydrous route, OME₁ forms a carbocation on a Brønsted site, whereupon methanol is released. Alternatively, methanol reacts rapidly with FA to generate a hemiformal. Growth occurs then by insertion of FA units into the above mentioned intermediates, but insertion of TRI into OME has also been reported.^[115] FA units can be generated from the decomposition of TRI or PF. In their intermediate carbocation form, two OME can also exchange FA units (transacetalization reaction). Finally, termination occurs when methanol reacts with a hemiformal to produce OME and water (acetalization reaction). In

This chapter is part of a published article in ChemSusChem as C. J. Baranowski, M. Roger, A. M. Bahmanpour, O. Kröcher, Nature of the synergy between Brønsted and Lewis acid sites in Sn-Beta zeolites for polyoxymethylene dimethyl ethers synthesis, *ChemSusChem* **2019**, 4421-4431.^[124] Part of the manuscript and supplementary information are reproduced here with some changes in formatting with permission from Wiley-VCH. C. Baranowski performed the experiments, analysed the data together with the co-authors and wrote the manuscript.

the anhydrous route, the termination reaction is the reverse reaction of the initiation. The other reaction mechanism proposed is the sequential addition, which is similar to the growth step of IGT, except that OME are not in an intermediate form.^[81]

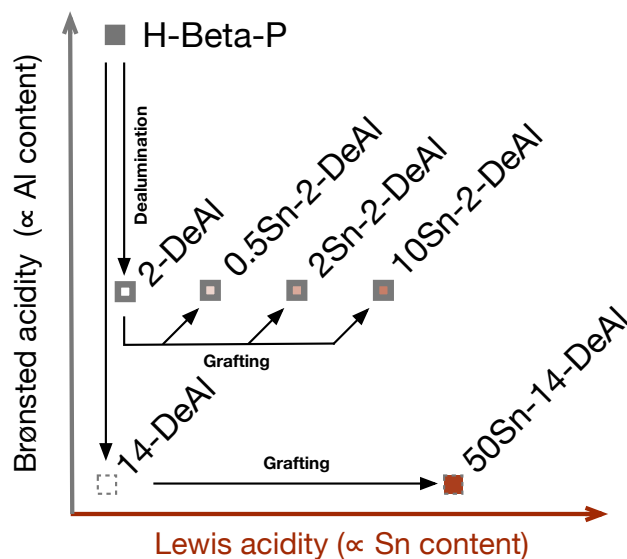


Scheme 5-1. OME synthesis following the IGT mechanism from methanol or OME₁.

Various studies demonstrated that strong Brønsted acidity was required for OME synthesis.^[70,85] Others showed that Lewis acidity could also catalyze OME production.^[144,165] However, these studies implied a wide range of reactants and catalysts, which prevents general conclusions to be drawn. Liu et al. reported the existence of a synergy between Lewis and Brønsted acid sites for the synthesis of OME from PF and OME₁.^[210] However, their suggested reaction mechanism does not explain the nature of this synergistic effect. Thus, the precise role of Brønsted and Lewis acid sites, and their potential synergy remains ambiguous. Considering these uncertainties, the goals of this chapter were twofold. First, we sought to acquire a deeper understanding of the type of acidity involved in the different OME synthesis steps. Second, we aimed at investigating the nature of the synergy between Lewis and Brønsted acid sites.

The results from Chapter 4 demonstrated that Sn-MMT, which displayed Brønsted and Lewis acidity, was an active catalyst for OME synthesis from TRI and OME₁. But the nature of clay and the synthesis method of tin-montmorillonite complicate the precise control over the concentration of Brønsted and Lewis acid sites. The objectives of this chapter were pursued by synthesizing a series of beta polymorph A (BEA) zeolites with various amounts of Brønsted and Lewis acid sites (Scheme 5-2). H-BEA was demonstrated as an active catalyst for OME synthesis, more performant than acidic resins under anhydrous conditions.^[110] Lewis acidity was introduced in the zeolite framework via Sn incorporation by grafting in dichloromethane, as it was shown to lead to high and controllable Sn content

with little extra-framework Sn.^[211] These catalysts were then applied in several reactions for OME synthesis. The results of this work demonstrated that Brønsted sites were active in all steps of OME synthesis while Lewis acid sites were only active in OME growth, PF decomposition and hemiacetal acetalization. Our study also confirmed the synergy between Brønsted and Lewis sites, and identified FA insertion in OME on tetrahedral Sn as the key step involving Lewis sites.



Scheme 5-2. Treatments applied to parent H-Beta zeolite (H-Beta-P) for the synthesis of a series of zeolites with varying amounts of Brønsted and Lewis acid sites.

5.2 Experimental

5.2.1 Partial and complete dealumination of zeolite Beta

Partial or complete dealumination were performed on a Beta zeolite (Si/Al = 11, ABCR). The parent H-Beta zeolite (H-Beta-P) was first obtained by calcination of NH_4 -Beta at 550 °C for 5 h with a 10 °C · min⁻¹ temperature ramp. Partial dealumination was achieved by stirring the zeolite overnight in a 2.0 M solution of nitric acid (HNO_3 , 65 %, Sigma Aldrich) at 80 °C under reflux (55 mL · g⁻¹ catalyst). Alternatively, a solution of 14.0 M HNO_3 (50 mL · g⁻¹ catalyst) stirred at 100 °C under reflux for 8 h was used for complete dealumination. The partially or completely dealuminated zeolite was then filtered and repeatedly washed with deionized water until a neutral pH was reached. The powder was then dried overnight in an oven at 110 °C. The partially and completely dealuminated zeolites were named 2-DeAl and 14-DeAl, respectively, according to the HNO_3 concentration used during the treatment.

5.2.2 Post-synthetic Sn grafting of dealuminated Beta zeolite in dichloromethane

Dealuminated Beta zeolite (2-DeAl or 14-DeAl) was first thoroughly dried under vacuum at 200 °C overnight. Anhydrous dichloromethane (CH₂Cl₂, 99.8 %, Acros) was added to the powder through a moisture-free cannula transfer (100 mL · g⁻¹ catalyst) using Schlenk techniques. A determined amount of SnCl₄ (1.0 M in CH₂Cl₂, Acros) was subsequently added with a syringe and the mixture was stirred magnetically (450 rpm) at 70 °C for 7 h under reflux in N₂.^[211] The powder was then recovered by filtration and thoroughly washed with dry isopropanol (Acros). Next, the recovered solid was dried at 110 °C overnight and calcined at 550 °C for 5 h under static air with a temperature ramp of 10 °C · min⁻¹. Each catalyst is denoted as xSn-y-DeAl, where x and y are the Sn precursor concentration in CH₂Cl₂ (mM · g⁻¹ zeolite) and the HNO₃ concentration during dealumination, respectively.

5.2.3 Catalytic testing for OME synthesis

OME₁ (99.5 %) was obtained from Acros and its H₂O content was determined by Karl-Fisher titration (0.04 wt % H₂O). Synthesis of OME was performed in 10 mL pressure resistant glass reactors dipped in a water bath thermostated at the reaction temperature, following a protocol described in Chapter 2.2.1. Experimental data from the reaction of TRI and OME₁ were fitted with the Boltzmann function using the ORIGIN software. The turnover frequencies (TOFs) were calculated using the following formula:

$$TOF_{max} = \frac{rate_{max}}{C_{ac} \cdot C_{cat}} \quad (5-1)$$

where rate_{max} is the maximum value of the derivative of [OME_{2-s}] vs. time (mol · L⁻¹ · s⁻¹), C_{ac} is the acid sites concentration of the catalyst (mol · g⁻¹) and C_{cat} is the catalyst concentration (g · L⁻¹).

5.3 Results

5.3.1 Physico-chemical characterization of the catalysts

Neither the dealumination treatments, nor Sn grafting affected the zeolite structure, as all XRD patterns were consistent with the BEA topology (Figure 5-1). Further-

more, no peak corresponding to a tin oxide phase was detected, which ruled out the possibility of the presence of extra-framework SnO_2 crystallites larger than 3 nm in the samples. The textural properties were assessed by N_2 physisorption measurements (Table 5-1). Analysis of the results confirmed that no structure amorphization was identified following the dealumination and grafting treatments applied to the zeolites. The protonated parent zeolite (H-Beta-P) displayed initial mesoporosity ($172 \text{ m}^2 \cdot \text{g}^{-1}$), which increased with the dealumination treatment to 189 and $192 \text{ m}^2 \cdot \text{g}^{-1}$ for 2-DeAl and 14-DeAl, respectively. Dealumination also induced a slight increase in H-Beta-P microporous surface area (S_{micro}) from $356 \text{ m}^2 \cdot \text{g}^{-1}$, to 379 and $400 \text{ m}^2 \cdot \text{g}^{-1}$ for 2-DeAl and 14-DeAl, respectively. Sn grafting resulted in a small decrease in S_{micro} , while the mesoporous surface area decreased with an increase in the Sn grafting concentration.

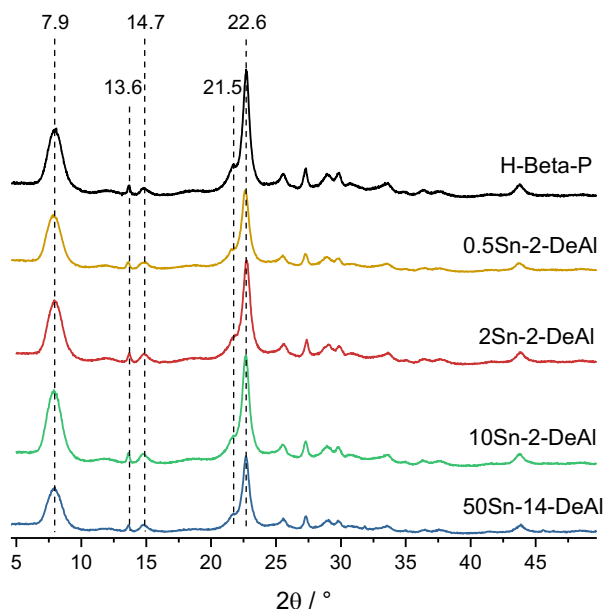


Figure 5-1. XRD patterns of H-Beta-P and the Sn-modified Beta zeolites.

ICP-OES analysis (Figure 5-2a) confirmed that the aluminum concentration decreased with an increasing dealumination extent, changing from 3.5 to 0.35 wt % with partial dealumination. Complete dealumination led to removal of almost all Al content (0.046 wt % left). Increasing Sn loadings were achieved for the partially dealuminated, Sn-modified samples with increasing SnCl_4 concentration during Sn grafting. A maximal Sn concentration of 1.09 wt % was reached for 10Sn-2-DeAl. The highest Sn content of 3.06 wt % was obtained with 50Sn-14DeAl, which thus mainly contained Sn compared to Al (Sn/Al molar ratio of 13.41).

Table 5-1. Textural parameters, composition and acidity of the catalysts.

Sample	Surface area ($\text{m}^2 \cdot \text{g}^{-1}$)			Volume ($\text{cm}^3 \cdot \text{g}^{-1}$)		Composition (wt %)			Acidity ($\text{mmol} \cdot \text{g}^{-1}$)
	BET	Micro ^[a]	Meso ^[b]	Micro ^[a]	Meso ^[b]	Al	Si	Sn	
H-Beta-P	543	356	172	0.155	0.536	3.50	41.40	0	0.880
2-DeAl	589	379	189	0.166	0.655	0.35	43.31	0	0.196
14-DeAl	609	400	192	0.174	0.638	0.05	43.41	0	0.081
0.5Sn-2-DeAl	554	348	188	0.150	0.694	0.35	43.46	0.28	0.187
2Sn-2-DeAl	567	361	184	0.158	0.655	0.35	43.78	0.63	0.193
10Sn-2-DeAl	556	357	182	0.156	0.621	0.35	43.55	1.09	0.225
50Sn-14-DeAl	558	352	183	0.152	0.610	0.05	45.00	3.06	0.230

^[a] Calculated based on the t-plot method. ^[b] Calculated based on the BJH method using the adsorption branch.

DRIFT spectroscopy confirmed that Sn was incorporated into the zeolite framework in vacant silanol nests (Figure 5-2b). Aluminum extraction led to an increase in the terminal Si-OH and internal silanol nest signals, respectively at 3740 and ca. 3500 cm^{-1} .^[212] The silanol nest signal decreased with increasing Sn loading, while the isolated silanol signal did not vary.

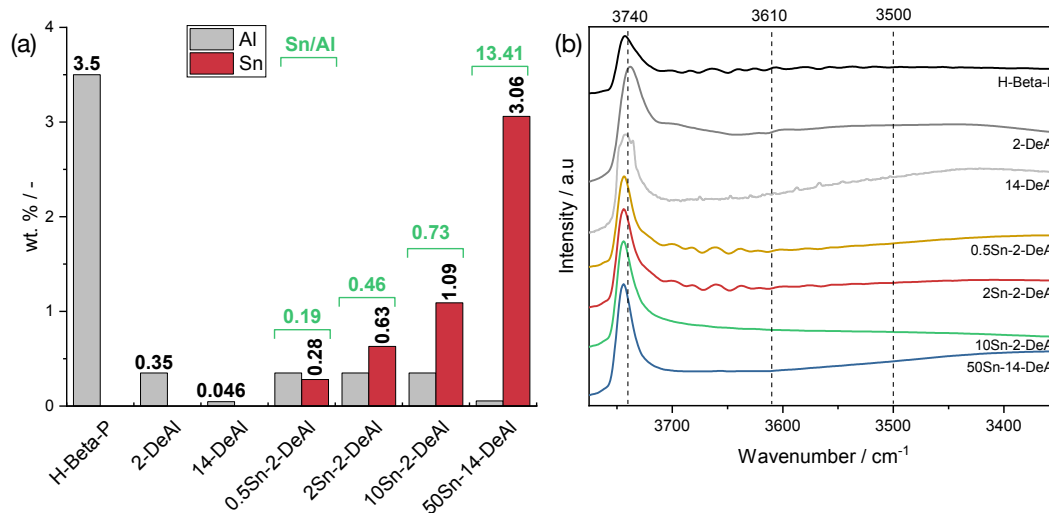


Figure 5-2. (a) ICP-OES analysis of the various catalysts. (b) DRIFT spectra of the hydroxyl stretching region of the parent, dealuminated and Sn-modified samples.

The Sn distribution in the zeolite framework was also examined by HAADF-STEM imaging with elemental mapping (Figure 5-3). Sn was well dispersed in all Sn-containing samples and no aggregates were observed.

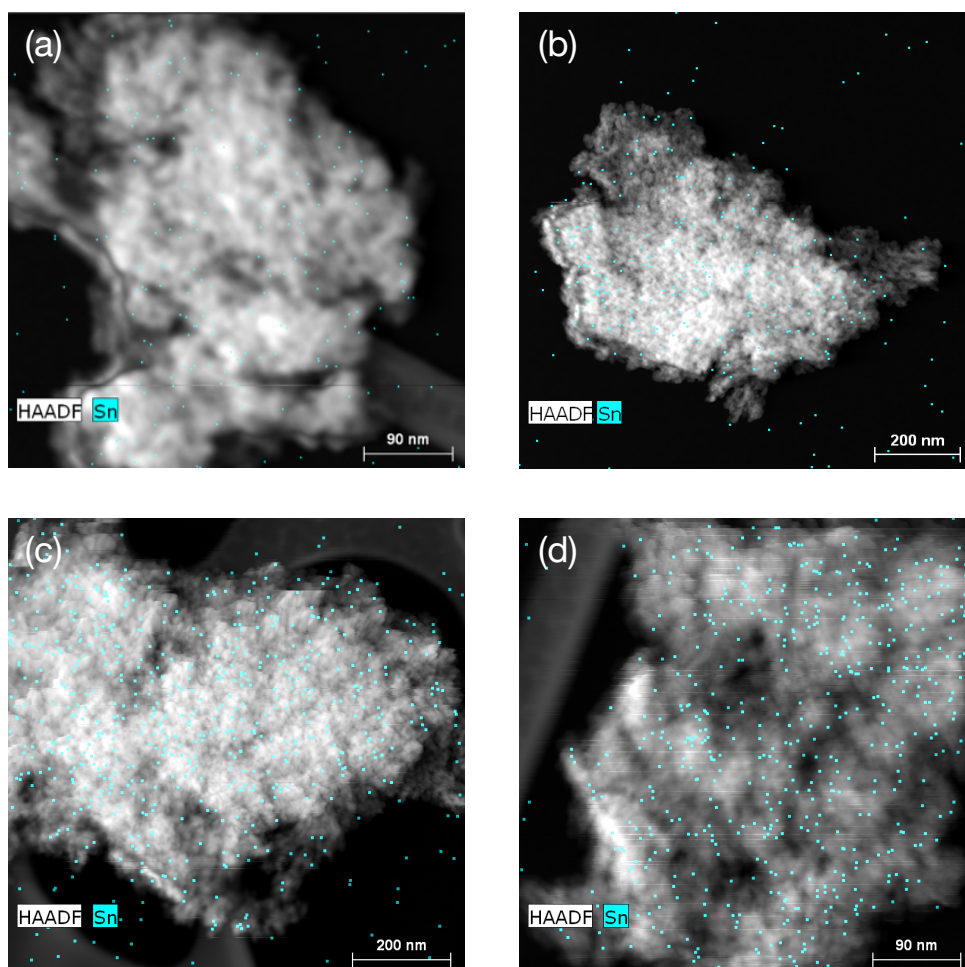


Figure 5-3. STEM-EDXS images of the Sn-containing catalysts: (a) 0.5Sn-2-DeAl, (b) 2Sn-2-DeAl, (c) 10Sn-2-DeAl and (d) 50Sn-14-DeAl.

Next, Sn coordination states in the Sn-modified samples were studied by XPS (Figure 5-4a). Overall, the two signals derived from the $3d_{5/2}$ and $3d_{3/2}$ were close to previously reported values corresponding to tetrahedrally coordinated framework Sn (487.4 and 495.8 eV).^[213] No signal caused by octahedral Sn was detected at 486.0 and 494.4 eV, which shows that no extra-framework Sn was present in these catalysts.

Diffuse reflectance UV-Vis (DRUV) spectroscopy also confirmed that no extra-framework Sn was present as no signal was obtained around 280 nm, which has been attributed to extra-framework SnO_2 (Figure 5-4b).^[204] The main signal was located between 218 and 235 nm, arising from the ligand-to-metal charge transfer from the surrounding O atoms to the unoccupied orbitals of isolated Sn^{IV} .^[214]

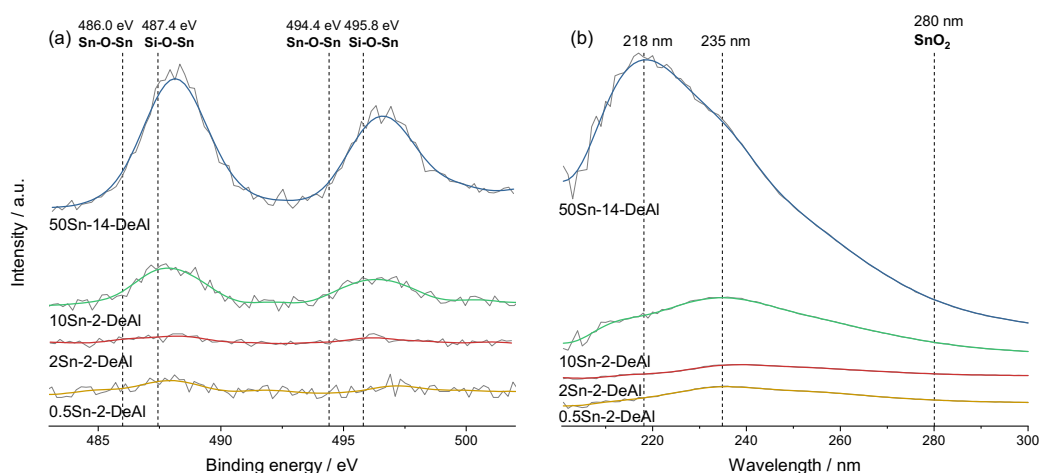


Figure 5-4. Analysis of the Sn-containing catalysts by (a) XPS and (b) in-situ DRUV spectroscopy at 400 °C under a He flow of 20 mL · min⁻¹. The gray and colored lines correspond to the original and smoothed curves, respectively. Smoothing was performed using a fast Fourier transform (FFT) filter (5 points).

The Sn-containing samples were further characterized by ¹¹⁹Sn magic angle spinning NMR (MAS-NMR) (Figure 5-5a and b). 50Sn-14-DeAl, which contained the highest Sn load, displayed a peak centered at -616 ppm, which corresponds to the hydrated form of Sn in a tetrahedral coordination in the framework lattice.^[215] Due to their smaller loadings and the low abundance of ¹¹⁹Sn, Carr–Purcell–Meiboom–Gill (CPMG) MAS-NMR analysis were performed for the partially dealuminated, Sn-modified samples. This resulted in a sharper peak located at -643 and -650 ppm for 2Sn-2-DeAl and 10Sn-2-DeAl, respectively. This signal is attributed to hydrated, hydrolyzed open Sn sites, which are expected after Sn grafting on silanol nests in a dealuminated zeolite.^[211,215] Sn concentration in 0.5Sn-2DeAl was too low to acquire an effective signal and is thus not displayed. However, due to the similarity in the grafting method, we suggest that Sn coordination to the framework is similar to the other dealuminated samples. Overall, these characterization results indicate that Sn grafting resulted in the incorporation of Sn in a tetrahedral coordination within the dealuminated BEA framework.

Samples acidity was quantified by NH₃-TPD (Figure 5-6a, Table 5-1). Overall, partial dealumination reduced the acid sites concentration from 0.880 to 0.196 mmol · g⁻¹ for H-Beta-P and 2-DeAl, respectively. 14-DeAl contained a residual acidity of 0.081 mmol · g⁻¹. Meanwhile, the acidity of the partially dealuminated, Sn-modified samples increased proportionally to the Sn loading, with a maximal concentration of 0.225 mmol · g⁻¹ reached for 10-Sn-2DeAl. Sn grafting on 14-DeAl resulted in the appearance of a peak centered around

200 °C in its NH₃-TPD profile and increased its acidity to 0.230 mmol · g⁻¹, close to the acid sites concentration of 10Sn-2-DeAl.

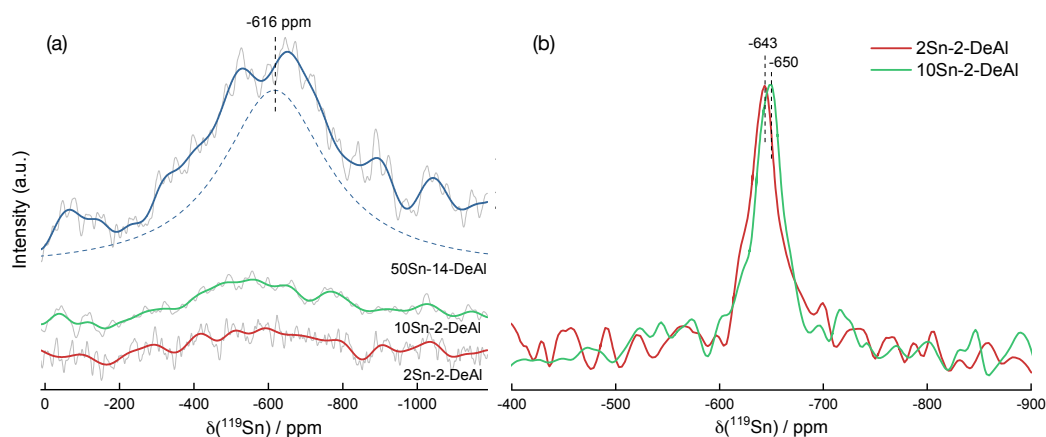


Figure 5-5. ¹¹⁹Sn MAS-NMR analysis of 50Sn-14-DeAl, 10Sn-2-DeAl and 2Sn-2-DeAl using (a) single-pulse and (b) Carr-Purcell-Meiboom-Gill (CPMG).

The nature and strength of the catalysts acid sites were studied by infrared spectroscopy of adsorbed pyridine (Figure 5-6b). Characteristic vibrational bands of H-bonded pyridine (1444 and 1596 cm⁻¹), and pyridine bonded to a Brønsted (1530 cm⁻¹) or a Lewis site (1451 and 1610 cm⁻¹) were detected.^[216] Comparison of H-Beta-P and 2-DeAl spectra shows that dealumination did not affect the strength of Brønsted acid sites as the signal intensity remained constant with increasing temperatures. Brønsted acidity was almost absent from 14-DeAl, which did not display a signal at 1530 cm⁻¹.

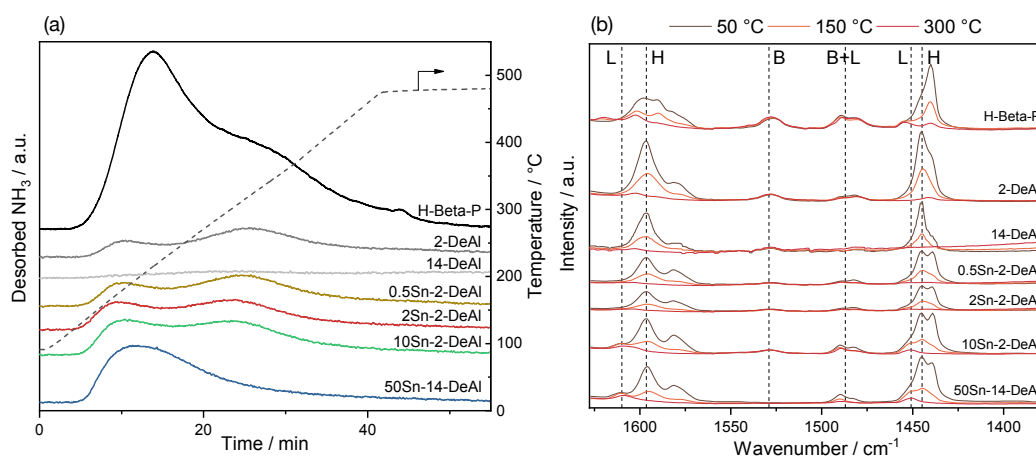


Figure 5-6. Characterization of the acidity of the various catalysts by (a) NH₃-TPD and (b) pyridine-FTIR spectroscopy at various temperature (H indicates H-bonded pyridine, while L and B respectively indicate pyridine bonded to Lewis and Brønsted sites).

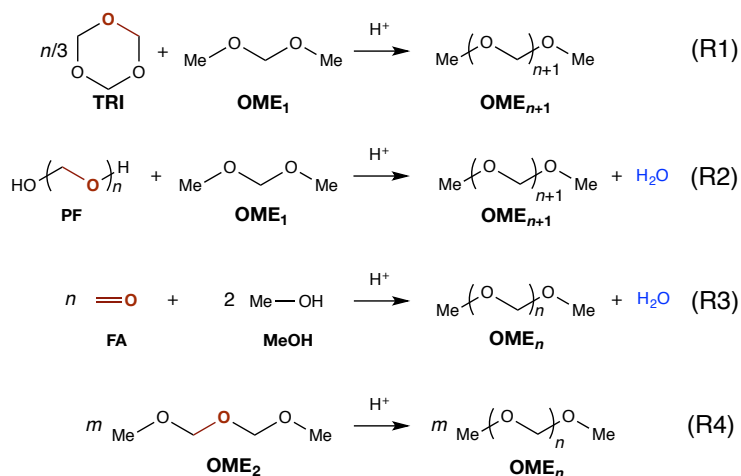
Notably, all dealuminated samples displayed a higher signal due to pyridine H-bonded to silanol groups. 0.5Sn-2-DeAl, 2Sn-2-DeAl and 10Sn-2-DeAl all displayed Brønsted and

Lewis acidity while 50Sn-14-DeAl only exhibited Lewis acidity. Signals corresponding to Lewis acid sites were more clearly observed for 50Sn-14-DeAl and 10Sn-2-DeAl due to the higher Sn content. The signals assigned to Lewis sites of Sn-modified samples slightly decreased with increasing temperatures and thus correspond to a moderate acid strength.

Overall, H-Beta-P and 2-DeAl contained strong Brønsted sites, 50Sn-14DeAl possessed moderate Lewis acidity, and the partially dealuminated, Sn-modified samples contained strong Brønsted and moderate Lewis acidity. The latter was thus generated from tetrahedral Sn incorporated in the dealuminated framework.

5.3.2 Catalytic performance screening for various OME synthesis reactions

In order to elucidate the role of Lewis and Brønsted acid sites during the various steps of OME synthesis, the synthesized catalysts were used for the reactions described in Scheme 5-3: OME₁ and TRI (R1), OME₁ and PF (R2), FA and MeOH (R3) and OME₂ equilibration (R4). First, TRI and OME₁ (R1) were used as reactants (Figure 5-7a). A decrease in activity was observed with an increase in the dealumination extent. Addition of Lewis acid sites on the completely dealuminated zeolite did not increase the sample activity as 14-DeAl and 50 Sn-14-DeAl had similar minor TRI conversion and formaldehyde concentration. Compared to 2-DeAl, catalysts displaying both Brønsted and Lewis sites had a much higher activity, comparable to H-Beta-P, despite their much lower concentration of acid sites.



Scheme 5-3. Various reactions performed for the synthesis of OME. The different sources of formaldehyde are displayed in red. Reaction R4 leads to a Schulz-Flory distribution of OME with OME₁/FA = 1.

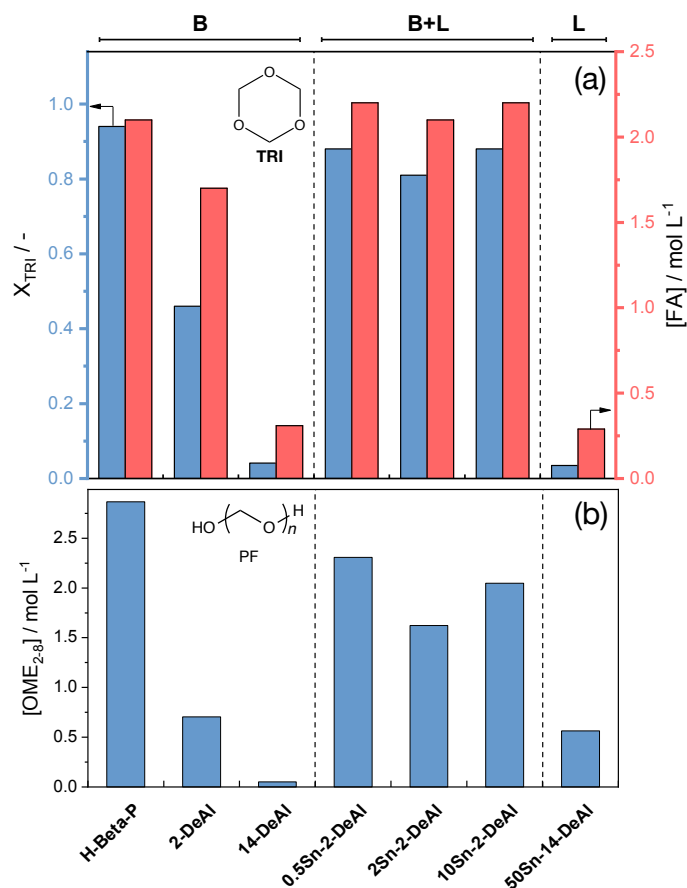


Figure 5-7 Synthesis of OME using various catalysts: (a) TRI conversion X_{TRI} and FA concentration using OME₁ and TRI ($T = 30\text{ }^{\circ}\text{C}$, 0.5 wt % catalyst, reaction time of 20 min, molar ratio OME₁:TRI = 3.3), (b) OME₂₋₈ concentration using OME₁ and PF ($T = 60\text{ }^{\circ}\text{C}$, 0.5 wt % catalyst, reaction time of 20 min, molar ratio OME₁:FA = 1.1).

The synthesis of OME using PF and OME₁ (R2) displayed results similar to R1 with a large increase in activity when both Brønsted and Lewis sites were present (Figure 5-7b). However, two differences were noticed. First, dealumination had a more severe effect on the performance; 2-DeAl reached an OME₂₋₈ concentration of only 0.70 mol · L⁻¹, compared to 2.86 mol · L⁻¹ for H-Beta-P. Second, 50Sn-14-DeAl had a notably better performance (0.56 mol · L⁻¹) compared to 14-DeAl (0.05 mol · L⁻¹), but still much lower compared to H-Beta-P. Lewis acid sites were thus active in R2, but less than Brønsted acid sites, as more OME were produced using 2-DeAl than 50Sn-14-DeAl, despite the larger acid site concentration of the latter.

Next, the synthesis of OME from FA and MeOH was performed (R3, Figure 5-8). The effect of dealumination on the performance was more severe on the catalyst performance compared to R1 and R2. After 16 h, 2-DeAl and 14-DeAl respectively reached an OME₂₋₈

concentration of 0.15 and 0.05 mol · L⁻¹, compared to 3.01 mol · L⁻¹ for H-Beta-P. Meanwhile, no clear increase in activity was observed when both Brønsted and Lewis sites were present; 0.5Sn-2-DeAl had performance comparable to 2-DeAl. However, Lewis acid sites also contributed to OME synthesis, as 2Sn-2-DeAl, 10Sn-2-DeAl and 50Sn-14-DeAl had an activity superior to the dealuminated samples.

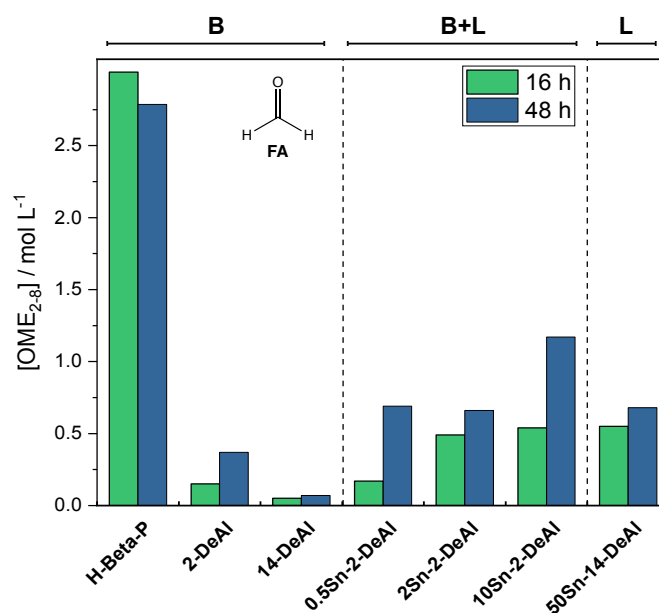


Figure 5-8. Synthesis of OME from FA and MeOH using various catalysts with OME_{2,8} concentration (T = 80 °C, 1.0 wt % catalyst, molar ratio MeOH:FA = 2.0).

Therefore, it appears that the activity was more correlated to the concentration of acid sites and less to their nature. The presence of water, produced in large amounts from reaction R3, seemed to affect Lewis acid sites more severely than Brønsted acid sites, as the results after 48 h showed a higher relative increase for all samples containing Brønsted acid sites compared to 50Sn-14DeAl bearing only Lewis acid sites.

Reactions R1 to R3 involve several reaction steps occurring at the same time. Thus, it is intricate to highlight what type of acidity is active for one specific step. From the reaction results, it was clear that Brønsted acid sites were active for all three reactions, but the role and activity of Lewis acid sites was not clear. To gain a better insight into the reaction mechanism, two additional reactions were studied, involving fewer reaction steps. First, OME₂ equilibration into a SF distribution of OME (R4) was performed. This reaction requires the activation of OME on an acid site for FA units to be transferred between different OME during transacetalization. Similarly to R1, it occurs under anhydrous conditions, but

does not involve TRI decomposition. Therefore, a SF distribution of OME was obtained from OME₂ when exposed to an active, acidic catalyst.

Figure 5-9a demonstrates this effect with H-Beta-P: OME of various chain length were obtained as OME₂ concentration decreased, reaching a SF distribution at equilibrium. The rates of OME₂ equilibration over the different catalysts followed the trend: H-Beta-P > 2-DeAl > 0.5Sn-2-DeAl > 14-DeAl > 50Sn-14-DeAl (Figure 5-9b). As Sn-modified catalysts had lower performance compared to their dealuminated counterparts, it is clear that Brønsted acidity is required to activate OME for the equilibration reaction R4, while Lewis acidity is insufficient for this purpose.

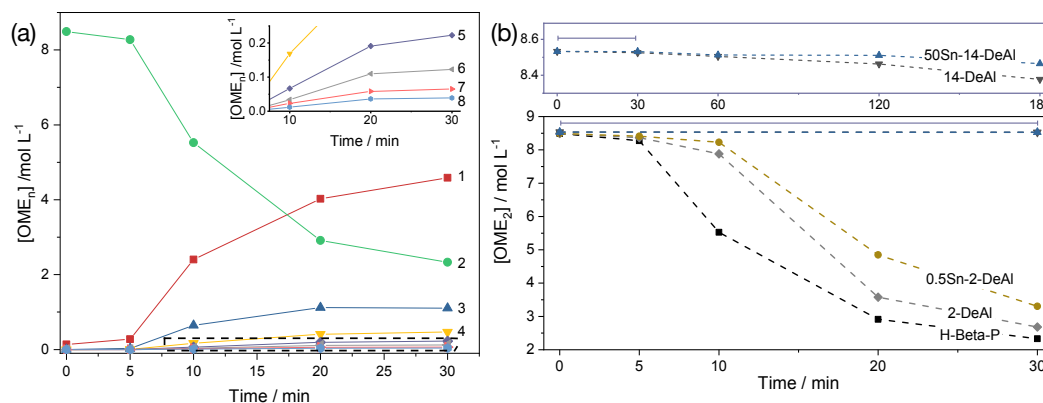


Figure 5-9. (a) Concentration of OME_n vs. time for H-Beta-P during OME₂ equilibration reaction (T = 25 °C, 1.0 wt % catalyst, OME₂ = 99.0). The inset displays the concentration inside the dashed square between 8 and 30 min. The numbers displayed refer to the OME chain length. (b) Equilibration of OME₂ (99.0 %) into OME_n using the various catalysts tested (T = 25 °C, 1.0 wt % catalyst) (bottom). The reaction was performed at a larger time-scale for 14-DeAl and 50Sn-14-DeAl (top).

The second reaction that was studied is the decomposition of TRI in CH₂Cl₂, which was performed using various catalysts in order to understand the interaction of Sn with TRI in the absence of OME₁ (Figure 5-10). TRI decomposition increased with an increasing Al content: H-Beta-P reached a TRI conversion of 0.34 compared to 0.26 and 0.13 for 2-DeAl and 14-DeAl, respectively. Addition of Sn in the zeolite framework at low concentrations did not alter the conversion significantly: 0.5Sn-2-DeAl and 2Sn-2-DeAl reached a TRI conversion of 0.26 and 0.24, respectively. However, at higher Sn concentrations, TRI conversion increased by 31 and 29 % for 50Sn-14DeAl and 10Sn-2DeAl, respectively, compared to their dealuminated counterparts. Meanwhile, methyl formate (MF) production augmented with increasing Sn content for partially dealuminated, Sn-containing zeolites. Interestingly, the combination of Brønsted and Lewis sites resulted in the highest MF production among Sn-containing zeolites. Notably, 50Sn-14-DeAl produced approximately

half the amount of MF compared to 10Sn-2-Deal despite the same total acidity and a three-fold Sn concentration in the zeolite. Thus, it appears that Brønsted acid sites were considerably more active for the TRI decomposition compared to Lewis acid sites. Presence of Sn resulted in the production of MF, especially when combined with Brønsted acid sites.

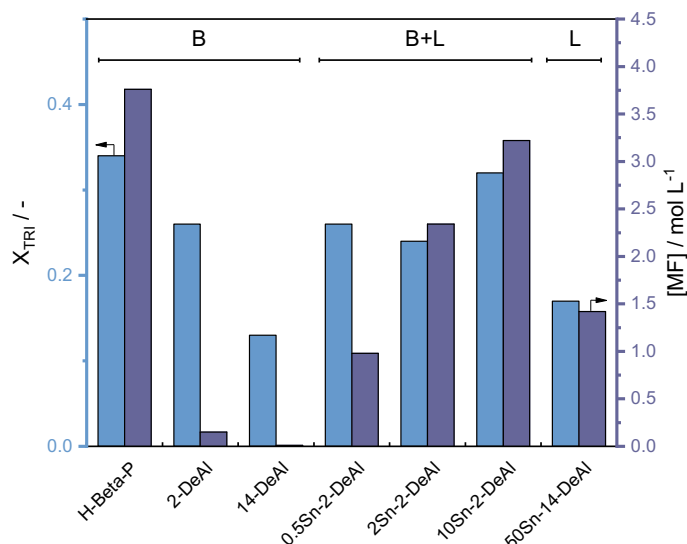


Figure 5-10. TRI conversion X_{TRI} and MF concentration for the TRI decomposition in CH_2Cl_2 using various catalysts ($T = 70^\circ\text{C}$, 2.0 wt % catalyst, reaction time of 64 h, 10 % TRI in CH_2Cl_2).

Overall, strong Brønsted acid sites resulting from bridging hydroxyl groups were active for all reactions performed. For catalysts containing only Brønsted acidity, an increasing extent of dealumination always led to a decrease in catalytic performance. In contrast, moderate Lewis acid sites resulting from tetrahedral Sn were inactive for R1 and R4, but still provided moderate activity for R2 and R3. When both Brønsted and Lewis acid sites were present, in combination with OME_1 and a source of formaldehyde, a large increase in activity was observed which is ascribed to a synergistic effect between both acid sites.

5.3.3 Synergy between Brønsted and Lewis acid sites for OME_1 synthesis from TRI and OME_1

In order to get a better insight into the nature of this synergistic effect, reaction R1 was performed with higher time resolution with H-Beta-P, 2-DeAl and the partially dealuminated, Sn-modified samples (Figure 5-11a). All catalysts exhibited a transition period in the beginning of the reaction due to an equilibration of temperature between the reactor and the thermostated bath. This resulted in an acceleration of the reaction rate observed for all catalysts during the first five minutes of the reaction. H-Beta-P first reached

the maximal TRI conversion, closely followed by the zeolites containing both Brønsted and Lewis acid sites. However, the turnover frequency (TOF) was the lowest over H-Beta-P, followed by 2-DeAl (Figure 5-11a, inset). The higher TOF value obtained with 2-DeAl compared to H-Beta-P could be due to a combination of two factors. First, dealuminated zeolites have stronger acid sites (higher Si/Al), which could accelerate the catalytic cycle due to reduced values of activation energy.^[217] Second, the dealumination treatment could have removed possible Al-rich debris present in the parent zeolite framework, thereby lowering the risk of OME internal molecular diffusion limitation.^[122]

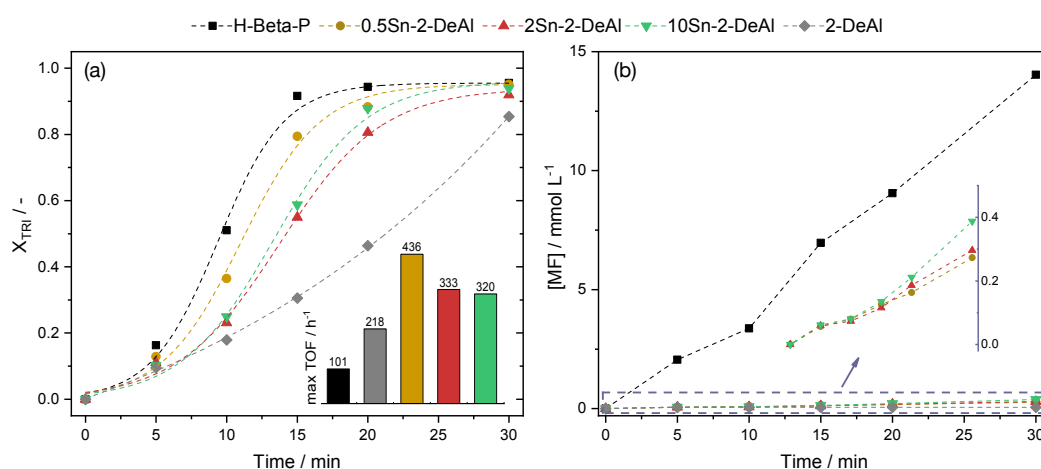


Figure 5-11. Synthesis of OME using various catalysts from OME₁ and TRI concentration ($T = 30$ °C, 0.5 wt % catalyst, molar ratio OME₁:TRI = 3.3). (a) TRI conversion X_{TRI} vs. time and (inset) max TOF. The experimental data were fitted using the Boltzmann model and the maximum rate of reaction is calculated in Figure B8-6 in Appendix B. (b) Methyl formate production vs. time.

Compared to 2-DeAl and H-Beta-P, a two- and four-fold increase of the TOFs was observed for 0.5Sn-2-DeAl, respectively, which we explain by a synergistic effect between Brønsted and Lewis acid sites. However, addition of Sn beyond the concentration in 0.5Sn-2DeAl resulted in a decrease of the TOFs. Such trend was already reported for the Sn-Beta in other catalytic reactions and means that not each Sn species is active for OME synthesis.^[218,219]

MF is a by-product of OME synthesis and results from the condensation of two FA units.^[46] MF production was notably higher for H-Beta-P, while partial dealumination suppressed MF production to values below the detection limit (Figure 5-11b). This phenomenon is probably due to the reduced acid site density and the resulting increased distance between two Brønsted sites in the zeolite framework obtained in 2-DeAl.^[74] When the average distance between two Brønsted sites exceeds the distance, which is required for condensation

of two FA units, MF formation is no longer possible. Lewis acid sites were also producing MF, proportionally to the Sn loading (Figure 5-11b, inset). However, their activity was much lower compared to Brønsted sites. After 30 min, 10Sn-2-DeAl produced $0.39 \text{ mmol} \cdot \text{L}^{-1}$ of MF compared to $14.02 \text{ mmol} \cdot \text{L}^{-1}$ for H-Beta-P.

Analysis of other reaction parameters provided additional evidences on the nature of the synergistic effect. First, all samples displayed a linear relationship between the concentration of OME_{2-8} and TRI conversion (Figure 5-12a) with only small amounts of the intermediate FA found in the reaction mixture. This suggests that TRI decomposition to formaldehyde was the rate determining step. This interpretation is in accordance with previous studies that have identified decomposition of the FA source as the rate limiting step and its large energy barrier (between $60\text{-}80 \text{ kJ} \cdot \text{mol}^{-1}$).^[114,115,165,220] Additionally, FA concentration only increased during the reaction for all catalysts and reached a stable level once a SF distribution of OME was reached (Figure 5-12b), suggesting that FA insertion is not the rate limiting step of the reaction.

Furthermore, it challenges the possibility that tetrahedral Sn assists with the decomposition of TRI into formaldehyde units. A higher TRI conversion for a specific concentration of product should have been observed if tetrahedral Sn had been active in TRI decomposition, and this effect should have increased with increasing Sn content, which was not observed. FA concentration as a function of TRI conversion was also independent of the various catalysts, which means that TRI conversion reflects the reaction progress (Figure 5-12c). This was further confirmed by the analysis of the intermediate-to-product ratio ($\text{FA}/\text{OME}_{2-8}$) as a function of TRI conversion (Figure 5-12d). Catalysts containing only Brønsted acid sites and catalysts containing both Lewis and Brønsted acid sites displayed a similar pattern, which suggests that FA concentration during the reaction was a function of the reaction progress and was not influenced by the presence of Lewis acid sites.

TRI insertion into OME_1 to form OME_4 was observed in the beginning of the reaction (Figure 5-13). However, this phenomenon was not promoted by using dealuminated, Sn-containing zeolites. The concentration of OME_4 as a function of TRI conversion displayed a similar behavior across the various catalysts tested. Therefore, the possibility that Lewis acid sites assist TRI insertion in OME_1 was ruled out.

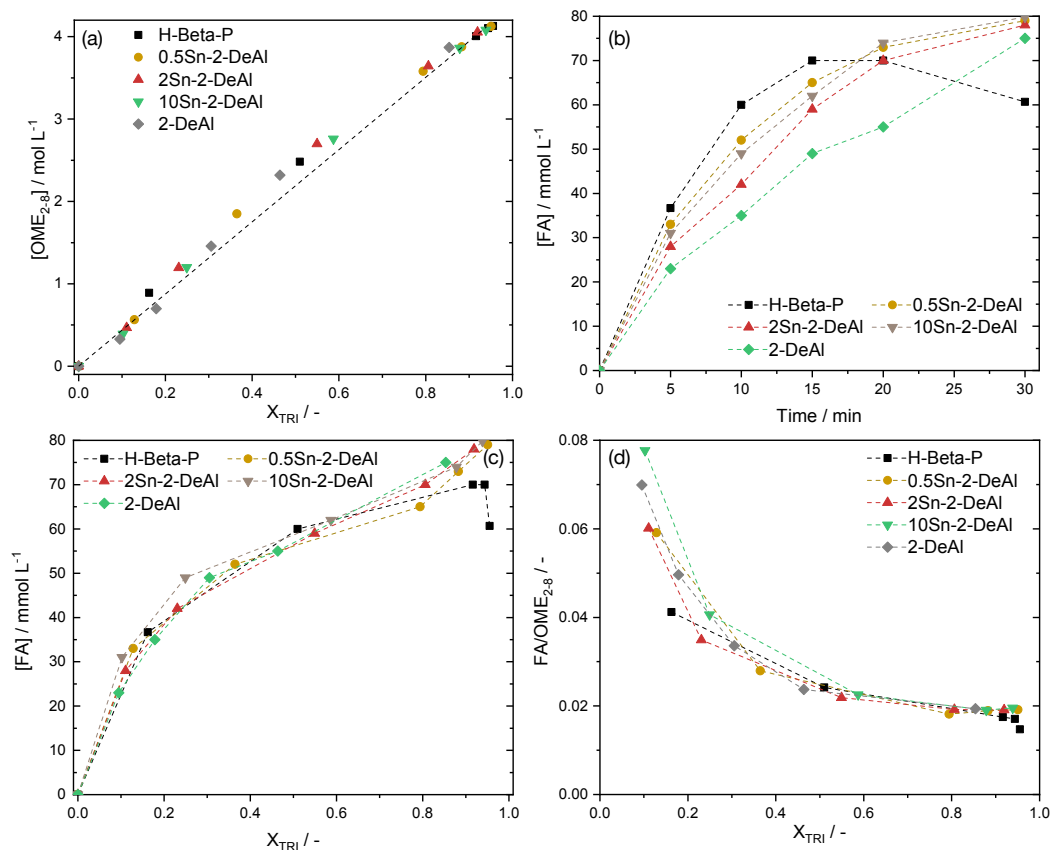


Figure 5-12. Synthesis of OME using various catalysts from OME₁ and TRI concentration (T = 30 °C, 0.5 wt % catalyst, molar ratio OME₁:TRI = 3.3). (a) OME₂₋₈ concentration vs. TRI conversion X_{TRI}, (b) FA concentration vs. time, (c) FA concentration vs. TRI conversion X_{TRI}, and (d) intermediate to product ratio vs. TRI conversion X_{TRI}.

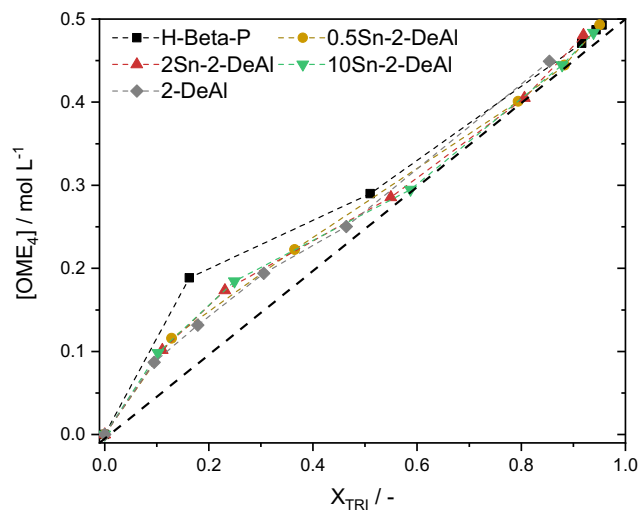


Figure 5-13. OME₄ concentration vs. TRI conversion (X_{TRI}) during OME synthesis from OME₁ and TRI using various catalysts (T = 30 °C, 0.5 wt % catalyst, molar ratio OME₁:TRI = 3.3).

5.4 Discussion

Catalyst characterization demonstrated that tetrahedrally coordinated Sn was successfully incorporated in the framework of the dealuminated zeolites. The partially

dealuminated, Sn-grafted samples presented both Brønsted and Lewis acid sites, while H-Beta-P and 2-DeAl exhibited Brønsted acid sites, and 50Sn-14-DeAl only Lewis acid sites. It has to be mentioned that H-Beta-P might contain residual Lewis acidity below the detection limit due to extra-framework Al. For 50Sn-14-DeAl, ICP-OES indicated residual aluminum, which is a potential source of Brønsted acidity. However, pyridine adsorption spectroscopy did not show signs of Brønsted acidity for this sample and only Lewis acidity could be detected. We conclude from these findings that the potential residual Lewis acidity in H-Beta-P and Brønsted acidity in 50Sn-14-DeAl can be neglected in the interpretation of the results. Please note that due to the low concentration of Sn in 0.5Sn-2-DeAl, some characterization methods such as MAS-NMR could not provide enough signal and the state of Sn was thus interpreted using samples with a larger Sn concentration.

The synthesized catalysts were used in a series of reactions to clarify the role of Lewis and Brønsted acid sites in the various synthesis steps (Table 5-2). Strong Brønsted acid sites, resulting from bridging hydroxyl groups, were active in all OME synthesis steps (i.e. initiation, growth and termination), independent of the reactants. Dealumination decreased the concentration of Brønsted acid sites, leading to an almost proportional reduction of the catalyst performance. In comparison, Lewis acid sites resulting from tetrahedrally coordinated Sn incorporated in the zeolite framework were not active in all steps involved in OME synthesis. First, Lewis acid sites could not catalyze the OME initiation/termination step. Second, they could not decompose TRI into FA units, while they could decompose PF. However, a synergy between Brønsted and Lewis acidity was observed for the reaction of OME₁ with TRI or PF. Notably, production of OME from OME₁ and TRI using 0.5Sn-14DeAl resulted in a four-fold increase in TOF compared to H-Beta. No synergy was detected when producing OME from MeOH and FA.

The first difference in activity between Lewis and Brønsted acid sites was observed during the initiation-termination step, which, unlike Brønsted acid sites, did not occur on Lewis acid sites. On the one hand, OME₂ equilibration experiments demonstrated that addition of Sn was detrimental to the catalyst performance, showing the inability of Lewis acid sites to activate OME₂ through generation of a carbocation. On the other hand, tetrahedral Sn-catalyzed OME synthesis from FA and MeOH demonstrated the activity of the Sn sites for

acetalization. The activity of 50Sn-14DeAl in R2, which involves OME₁ and PF, was probably due to the generation of water from the decomposition of PF, which should be sufficient to reverse acetalization.

Table 5-2. Activity comparison of Brønsted and Lewis acid sites for the various OME synthesis steps.

Synthesis Steps	Reactant/intermediate	Brønsted (bridging hydroxyl)	Lewis (tetrahedral Sn)
Initiation/Termination	Carbocations	Active	Inactive
	Hemiformal	Active	Active
Growth/Sequential addition		Active	Active
Decomposition of FA source	TRI	Active	Inactive
	PF	Active	Active

The second difference in activity is related to the decomposition of TRI into FA units, which did not occur on tetrahedrally coordinated Sn. 50Sn-14-DeAl exhibited an activity superior to 14-DeAl for R2, while both catalysts were inactive for R1. Thus, PF must have been decomposed on Lewis acid sites into FA units, which were subsequently used for OME growth. However, it appeared that the activity of tetrahedrally coordinated Sn for PF decomposition was not as high as Brønsted acid sites. Meanwhile, TRI decomposition in CH₂Cl₂ revealed that TRI conversion was due to the presence of Brønsted acid sites and that addition of low to moderate Sn concentration did not improve TRI conversion. Additionally, detailed investigation into the reaction of OME₁ and TRI revealed that, despite their very different activity, the intermediate-to-product ratio did not vary during the course of the reaction among the catalysts (i.e. H-Beta-P, 2-DeAl, and partially dealuminated, Sn-modified samples). The possibility that TRI was inserted into OME₁ was also discarded based on the comparison of OME₄ production versus OME₂₋₈.

The synergy between Brønsted and Lewis acidity, which resulted in a four-fold increase in TOF, was only observed for reactions involving OME₁ and a FA source (i.e. R1 and R2). No synergy was detected when OME were produced from MeOH and FA. This is in accordance with the results of Li et al., showing no synergy between Brønsted and Lewis acid sites for the reaction of MeOH with TRI.^[70] It is important to note, from our results and previous studies, that such a synergy was only reported when OME₁ was used as one of the reactants.^[70,210] The presence of water could also be an important factor to obtain such a synergy. When using MeOH or formalin, water from the reaction medium or produced

during acetalization could coordinate with Lewis acid sites to convert them to Brønsted acid sites. That could potentially explain why no synergy was observed under these conditions. The effect of water on the reaction kinetics of OME synthesis from TRI and OME₁ will be studied in Chapter 6.

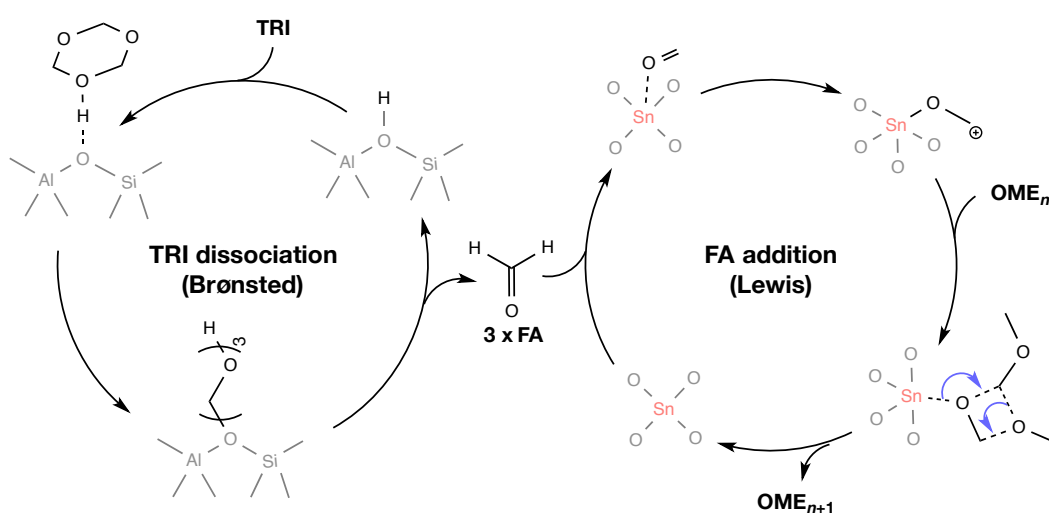
Because tetrahedral Sn was not active for TRI decomposition and OME initiation to carbocations, the synergy between Brønsted and Lewis acid sites can only be explained by a higher activity of tetrahedral Sn in the OME growth step. FA units were made available by TRI decomposition on Brønsted acid sites and growth occurred on tetrahedral Sn as Lewis acid sites, which increased the overall reaction rate. Increasing the Sn concentration further in the partially dealuminated zeolite decreased the TOF, but presence of a small amount of Lewis acid sites may have been sufficient to rapidly incorporate the produced FA into OME.

Activation of the carbonyl group of FA by interaction with tetrahedral Sn could likely be the initial step for insertion of FA into OME. This finding was supported by results from OME synthesis from TRI and OME₁, as well as TRI decomposition in CH₂Cl₂, which showed an increase in MF production with an increasing Sn content. Production of MF by condensation of two FA units is probably a result of FA activation by Sn. Furthermore, dealuminated, Sn-modified catalysts also produced much less MF compared to H-Beta-P during OME synthesis, which suggests that FA units were rapidly inserted in OME. Thus, we suggest that the synergy between Brønsted and Lewis acid sites is a consequence of TRI dissociation on Brønsted acid sites and sequential addition on Lewis acid sites, as illustrated in Scheme 5-4. It is important to underline that FA insertion can also occur on Brønsted acid sites. However, only considering TRI decomposition and FA insertion on Brønsted acid sites does not justify the nature of the synergy between Lewis and Brønsted acidity.

5.5 Conclusions

In summary, tetrahedrally coordinated Sn was successfully incorporated in the framework of dealuminated BEA zeolites via Sn grafting in dichloromethane leading to a series of BEA zeolites with varying Lewis and Brønsted acid sites. The synthesized catalysts were used for a combination of OME synthesis reactions to clarify the role of Brønsted and Lewis acid sites. Our results demonstrated that Lewis acid sites resulting from tetrahedrally

coordinated Sn were not active in all OME synthesis steps, while Brønsted acid sites were. Notably, TRI dissociation and OME₁ activation did not occur on Lewis acid sites. The presence of both sites resulted in a synergy when OME₁ was used with PF or TRI. Notably, 0.5Sn-2-Deal exhibited a significant increase in TOF and reduction in byproduct generation. This synergistic effect was explained by a more efficient FA insertion into OME on Lewis acid sites, while production of FA units by TRI or PF decomposition occurred on Brønsted acid sites. The interaction between tetrahedral Sn and the carbonyl group of FA resulted in an activated FA, likely to be inserted into OME.



Scheme 5-4. Suggested reaction mechanism for the synthesis of OME from OME₁ and TRI with Brønsted and Lewis sites. The reaction was depicted with OME₁ for readability.

Chapter 6 Influence of water on the kinetics of OME synthesis in an H-Beta zeolite

6.1 Introduction

In the context of polyoxymethylene dimethyl ether (OME) synthesis, water can be a co-product of the acetalization of methanol and hemiformals, or can be present as an impurity in the solvent used. The results from Chapter 5 showed that water could influence the reaction kinetics by potentially preventing the synergy between Brønsted and Lewis acid sites. The influence of water on the kinetics of OME synthesis remains vague but its impact on the reaction equilibrium has been studied by various authors. Zheng et al. reported that water induced hydrolysis of dimethoxymethane (OME₁) to methanol and formaldehyde (FA).^[221] Water concentration of above 5 wt % led to a significant decrease in the OME yield. They also found zeroth order dependency of water on the OME synthesis from methanol and FA using Zr-alumina as catalyst.^[64] Burger et al. reported the production of large amounts of by-products when methanol or water was present during the synthesis.^[74] Thus, the reaction route involving anhydrous reactants (i.e. trioxane (TRI) and OME₁) has been hitherto preferred. Two reaction mechanisms were proposed to describe the synthesis of OME in anhydrous conditions using zeolite H-Beta: incorporation of FA from *in situ* decomposition of TRI or direct incorporation of TRI into OME₁.^[115] Both mechanisms require similar energy barriers, and therefore, are believed to happen simultaneously.

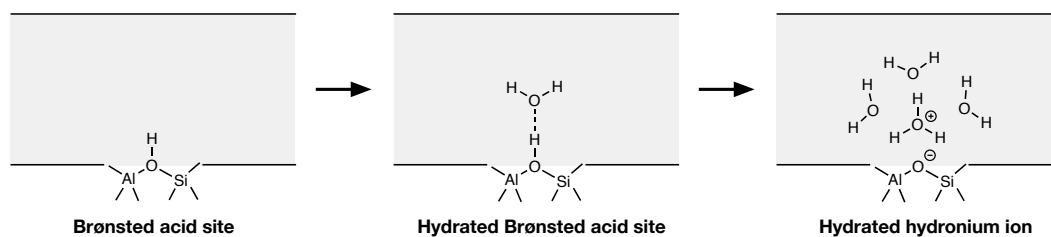
Zeolites have been extensively used for OME synthesis because of their unique and advantageous features: silicon tetrahedra combine to form frameworks with large surface areas

This chapter is based on the manuscript: Baranowski C. J., Fovanna T., Roger M., McCaig J., Signorile M., Bahmanpour A. M., Kröcher O., Water inhibition of oxymethylene dimethyl ether synthesis over an H-BEA zeolite: a combined kinetic and in situ ATR-IR study, *Manuscript in preparation* 2019.^[125] Together with the co-authors, C. Baranowski performed the experiments, analysed the data and wrote the manuscript.

and well-defined pores of molecular dimensions. Their one- to three-dimensional micropores of various sizes connected by channels and cages provide them with unique properties such as shape selectivity or activation by molecular confinement. Their acidity originates from the aliovalent substitution of a silicon framework atom by a trivalent metal cation, such as aluminum, generating a negative charge in the lattice balanced by a bridging hydroxyl group.^[222] Nowadays, the chemical industry routinely uses their catalytic properties for various reactions such as hydrogenation, alkylation or isomerization.^[223] Despite extensive investigation, their activity for various chemical reactions has not yet been fully understood. Specifically, understanding how water influences the catalytic activity of zeolites is challenging, since water can have various influences in the reaction system. This comprises the catalyst, reactants, intermediates, products or the influence of water as reaction media.

Both positive and negative influences of water during chemical reactions in zeolites have been reported. Dehydration rate of 1-propanol on a H-ZSM-5 zeolite was significantly hampered in the presence of water due to the stabilization of a reaction intermediate, which increased the activation energy.^[224] On the contrary, catalytic cracking using zeolite Beta was improved by the presence of water in the feed, due to a better dispersion of hydrocarbons.^[225] For the same reaction, the concentration of water in the zeolite can also be a parameter which can positively or negatively affect the kinetics: low amounts of water increased the reaction rates for C-H bond activation by an order of magnitude, but had deleterious effects on the kinetics at higher concentrations.^[226]

Recently, it was demonstrated that the presence of water changes the nature of the acidic sites in a zeolite from a bridging hydroxyl group to a stabilized hydronium cluster, as illustrated in Scheme 6-1.^[227,228] Hydronium ions in the zeolite channels diminish the available pore volume and can have different interactions with reactants compared to a bridging hydroxyl group.^[229] In the liquid phase, the presence of water in the zeolite channels can have an important impact on the reaction rate, and thus on the reaction mechanism. For instance, the reaction mechanism of cyclohexanol dehydration changes when the acid site changes from a bridging hydroxyl group to a hydronium ion.^[230] Similarly, protonation of olefins by hydronium ions must overcome a significantly higher energy barrier compared to a bridging hydroxyl group, leading to lower reaction rates.^[231]



Scheme 6-1. Hydration of a Brønsted acid site in a zeolite channel.

A study from Lautenschütz et al. highlighted that the presence of small amounts of water in the reaction medium significantly increased the time to reach equilibrium for OME synthesis from TRI and OME₁.^[110] They also revealed that zeolite H-Beta was more affected by water than acidic resins. However, they did not quantify, nor study the possible reasons, which explained their observation. Therefore, this study aims at elucidating the effect of water on the kinetics of OME synthesis from OME₁ and TRI using zeolite H-Beta. This objective was pursued by performing a kinetic study using various water concentrations in OME₁ as the reactant. Furthermore, we used attenuated total reflectance infrared (ATR-IR) spectroscopy, to investigate the nature of the adsorbed species *in situ*. This technique is useful for studying the solid-liquid interfaces of catalytic systems, such as those which exist within zeolites.^[232] Usage of Modulation-excitation (ME) and phase sensitive detection (PSD) allows to increase of the signal-to-noise ratio and signal enhancement by converting spectra recorded in the time domain to the phase domain (see section 2.3.12).^[233] This facilitates the investigation of low levels of species, such as transient adsorbates or intermediates. Combined with ATR-IR, these tools contributed to understand complex catalytic systems where the solid-liquid interface plays a crucial role.^[234,235] Therefore, ME-ATR-IR is here applied to probe and understand the effect of water on OME synthesis kinetics.

6.2 Experimental

6.2.1 Materials

All reagents were of analytical grade and obtained from commercial suppliers. Trioxane (99 %, Sigma-Aldrich), dimethoxymethane (99.0 % from Sigma-Aldrich and 99.5 % from Acros), 2-propanol (LiChrosolv, hypergrade LC-MS, Merck), and pyridine (>99.0 %, Sigma-Aldrich) were used without further modification. Cyclohexane (99.8 %, analytical reagent grade, Fischer Chemical) was dried over molecular sieves (3A, 1-2 mm beads, Alfa Aesar), and filtered on microfiber filter (GF/D, Whatman) before use. In order to study the influence of water on the synthesis of OME, increasing amounts of water were

added to OME₁. The water content was determined by Karl-Fisher coulometric titrations using a Metrohm Titrando 737 instrument. Depending on the water concentration, the various OME₁ sources were named OME_{1-x}-H₂O, where x is the water content in wt %.

6.2.2 Catalytic study

Syntheses of OME were performed in glass reactors (Grace, 10 mL) with PTFE screw caps and a silicon sealing disk, following a protocol described in Chapter 2.2.1. Before the reaction, the catalyst powder was weighted, inserted in the reactors, and dried overnight in the oven at 120 °C, which is sufficient to remove physisorbed water from the zeolite pores, but insufficient to remove chemisorbed water. Elimination of the latter requires temperatures above 400 °C and a high level of vacuum.^[229] To ensure minimal exposition to water, reactors were capped immediately after being removed from the oven and allowed to cool down to RT. OME_{1-x}-H₂O was then quickly inserted in the reactors to restrict the uptake of moisture from the air by the zeolite, followed by the addition of TRI. All the experiments were performed with an OME₁/TRI molar ratio of 3.3 and 0.5 wt % of catalyst.

The kinetic model used describes the synthesis of OME from TRI and OME₁ and is described in section 2.4.^[122] Briefly, we used a pseudo-homogeneous kinetic model, where the synthesis of OME proceeds according to the following simplified equation:



Where $k_{OME,f}$ and $k_{OME,b}$ are the forward and backward rate constants, respectively. The constants used in the van 't Hoff equation were determined experimentally (Figure C8-7 in Appendix C).

6.2.3 Modulation excitation attenuated total reflectance spectroscopy (ME-ATR)

The nature of adsorbates was investigated using attenuated total reflection infrared spectroscopy (ATR-IR) in combination with modulation-excitation (ME) and phase sensitive detection (PSD) according to a protocol described in section 2.3.12. The following concentration modulation-excitation set of experiments was carried out: (i) TRI (5 mM) vs neat cyclohexane; (ii) OME₁ (15 mM) vs neat cyclohexane; (iii) TRI vs TRI with H₂O (0.7 mM H₂O); (iv) OME₁ vs OME₁ with H₂O (0.7 mM H₂O, 1 wt % in OME₁); (v) OME₁

+ TRI vs OME₁; (vi) OME₁ + TRI vs TRI (vii) OME₁ + TRI vs OME₁ + TRI + H₂O. One half-cycle was 191 s while a full period was 382 s.

The interaction of OME₁ and TRI with the catalyst was also studied in the presence of pyridine. After an initial equilibration in cyclohexane for an hour and background collection, a pyridine solution (5 mM, in cyclohexane) was introduced to the catalyst layer for 30 min. Physisorbed pyridine was then removed by flowing neat cyclohexane for 30 min. After adsorption (30 min) or desorption (30 min) of OME₁ or TRI, the ME experiment was started by repeating experiment (i) and (ii), as described above. The reference spectra of OME₁ and TRI were obtained by measurement of pure OME₁ and solid TRI in the cell. Peaks were assigned based on ab initio studies (Figure C8-21 and Figure C8-22 in Appendix C).^[145,146,236,237]

6.2.4 DFT simulation

Quantum chemical calculations were performed with the Gaussian 16 (rev. C01) code.^[238] The IR spectra and the adsorption electronic energies, enthalpies and Gibbs free energies for relevant molecules, also interacting with Brønsted sites (represented with a minimal model, Figure C8-8 and Figure C8-9) were simulated with the B3LYP hybrid DFT functional,^[239,240] including dispersive forces through the Grimme D3 empirical scheme.^[241] The polarizable continuum model (PCM) was adopted to implicitly include the effect of solvent (i.e. cyclohexane), for the sake of a better comparison with ATR-IR data.^[242] All the atoms were described with the Pople 6-31+D(d,p) basis set.^[243] To obtain more accurate electronic energies, these have been extrapolated to the complete basis set (CBS) for all the considered models, according to the procedure described in Appendix C (Figure C8-10).

6.3 Results and discussion

In section 5.3.1, the physico-chemical properties of zeolite H-Beta are briefly discussed. Next, the results of the kinetic study of OME synthesis are described in section 6.3.2 and the results of ME-ATR experiments are presented in section 6.3.3. Finally, section 6.3.4 summarizes and discusses the influence of water on the catalytic activity of zeolite.

6.3.1 Physico-chemical characterization of the catalyst

The XRD pattern displayed the characteristic reflections of a zeolite BEA structure (Figure C8-11) and the Si/Al molar ratio was determined by ICP-OES analysis as 11.4. N₂ physisorption was carried out to deduce the textural properties of the zeolite (Figure C8-12). The measured isotherm shows type IV characteristics with high volume uptake at low relative pressures and a hysteresis loop at high relative pressures. The overall shape of the isotherm highlights the presence of micropores (356 m² · g⁻¹) and mesopores (172 m² · g⁻¹), for which the size distributions are displayed in a BJH adsorption plot (Figure C8-12, inset). The presence of aggregates of small crystals of around 10 nm was confirmed by STEM (Figure C8-13). The mesoporous volume is a result of the intercrystallite space between aggregates. The relatively high mesoporosity of the zeolite limited the extent of internal diffusion limitation during OME synthesis.^[122]

NH₃ temperature programmed desorption (NH₃-TPD) and pyridine ATR-IR (py-ATR-IR) spectroscopy were used to study the acidic properties of the catalyst (Figure C8-14a and b). A total acidity of 0.880 mmol · g⁻¹ was obtained by quantification of the NH₃-TPD results. The nature of the acidity was determined by py-ATR-IR. Signals ascribed to pyridine bound to the Brønsted acid sites were detected at 1490, 1545 and 1638 cm⁻¹.^[158] Overall, H-Beta displayed strong Brønsted acidity.

6.3.2 Catalytic activity of zeolite H-Beta for OME synthesis in the presence of water

The synthesis of OME using TRI and OME₁ with various water concentrations was conducted at 30 °C (Figure 6-1). Equilibrium TRI conversion was reached within 30 min using OME₁-0.03-H₂O. Higher concentrations of water in OME₁ led to a negligible activity: after 60 min, OME₁-0.21-H₂O and OME₁-0.40-H₂O reached a TRI conversion of only 1.8 % and 1.1 %, respectively. The synthesis was also performed with OME₁ from a different supplier with a water content of 0.44 wt %, which reached a TRI conversion of 0.6 % after 60 min. Thus, TRI conversion at 30 °C was almost negligible at water concentration as low as 0.21 wt %. Our observations are in agreement with the work of Lautenschütz et al., as water had a deleterious effect on the kinetics of OME synthesis from TRI and OME₁, which increased as the water concentration in OME₁ was raised.^[110]

Next, we tested the effect of catalyst pre-treatment on the performance of H-Beta. In the catalyst pre-treatment procedure (section 6.2.2), exposure to moisture from ambient air is typically minimized. When the catalyst was intentionally exposed to ambient air for 2 min prior to reaction, the time required to reach a TRI conversion close to equilibrium was quadrupled compared to the standard pre-treatment procedure (Figure 6-1).

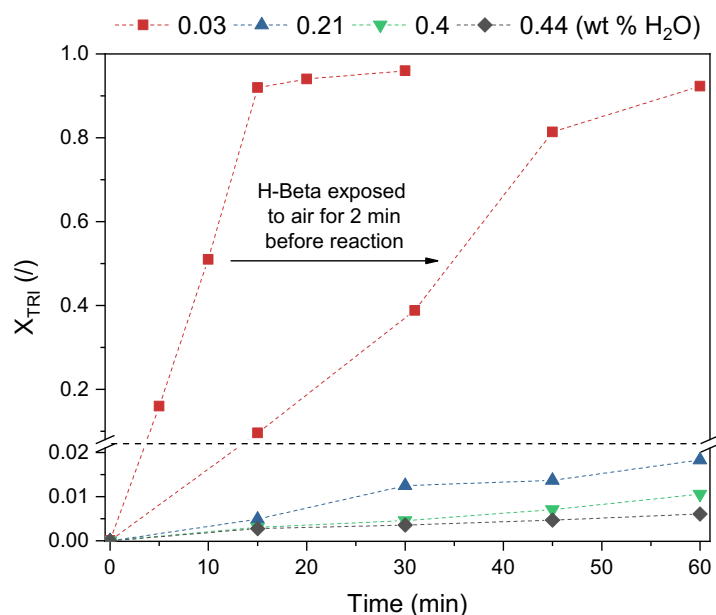


Figure 6-1. TRI conversion X_{TRI} vs. time for the synthesis of OME from OME₁ and TRI using various water concentrations in OME₁ ($T = 30$ °C, 0.5 wt % catalyst, molar ratio OME₁:TRI = 3.3). OME₁ (0.44 wt % H₂O) was obtained from a different supplier.

In order to quantify and understand how water affects the catalytic activity of zeolite Beta for OME synthesis from TRI and OME₁, we performed a kinetic study by varying the concentration of water in OME₁. For each water concentration, the reaction was performed at three different temperatures, which allowed reaching equilibrium TRI conversion within two hours. As expected, higher temperatures were required for larger water concentrations to overcome slower reaction kinetics. Each run at a certain temperature was fitted to the kinetic model to yield a value of $k_{\text{OME},f}$ (Table 6-1, Figure C8-15 to Figure C8-17). The values of the apparent activation energy ($E_{a,\text{app}}$) and the frequency factor (A) for each water concentration were then derived using the linearized Arrhenius equation (Figure 6-2a):

$$\ln(k_{\text{OME},f}) = -\frac{E_a}{RT} + \ln(A) \quad (6-2)$$

According to the Arrhenius model, which is derived from the collision theory, the activation energy is the minimum energy required for reactants to form a product and the frequency

factor A is a measure of the rate at which collisions occur. Two trends were observed from the Arrhenius parameters for water concentrations in OME₁ between 0.03 and 0.44 wt %. On the one hand, $E_{a,app}$ increased linearly with an increasing water concentration from 96.1 to 100.7 kJ · mol⁻¹ (Figure 6-2b). On the other hand, A decreased by more than an order of magnitude as the water concentration was raised (Figure 6-2c).

Table 6-1. Results of the kinetic model for the kinetic study on the various catalysts.

RUN	H ₂ O WT % OME ₁	TEMPERATURE (°C)	RMSE ^[A]	K _{OME,F} (L·MMOL ⁻¹ ·MIN ⁻¹)
K1	0.03	25	0.56	1.421
K2	0.03	30	0.55	2.733
K3	0.03	35	0.59	4.917
K4	0.21	40	0.53	0.272
K5	0.21	50	0.54	1.065
K6	0.21	60	0.65	2.586
K7	0.44	50	0.45	0.114
K8	0.44	60	0.49	0.430
K9	0.44	70	0.53	1.013

^[a] RMSE = Root Mean Square Error

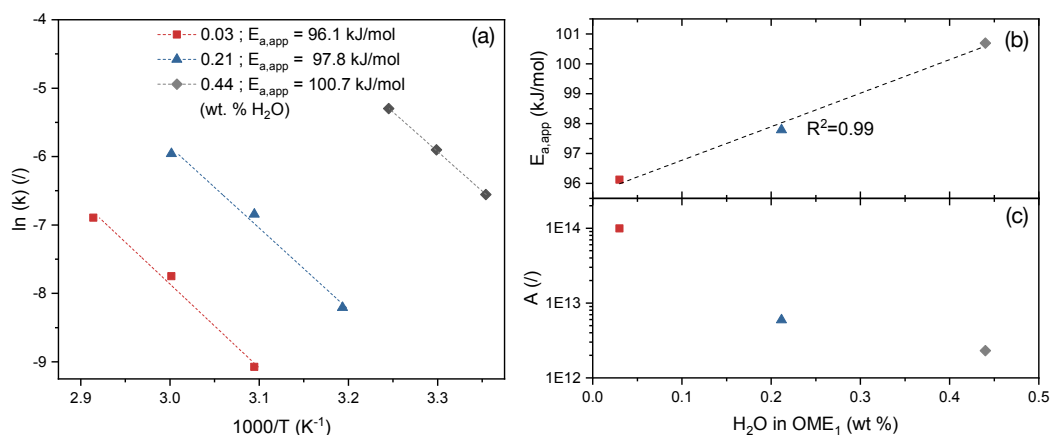


Figure 6-2. (a) Arrhenius plot for various water concentrations in OME₁ based on the kinetic constants extracted from the kinetic model. Values obtained from the Arrhenius plot for the (b) apparent activation energy and (c) pre-exponential factor vs. water concentration in OME₁.

Analysis of reaction parameters obtained from the kinetic study was performed in order to obtain additional information on the impact of water. These values cannot be compared against time across different runs due to the different time scales. Therefore, analysis of the reaction parameters against TRI conversion was performed, which reflects the reaction progress. Each run displayed a linear relationship between the concentration of OME₂₋₈ and the conversion of TRI (Figure 6-3). OME of larger sizes were produced as a function of the decomposition of TRI similarly across the water concentration range that was tested. The

achieved TRI conversions and OME_{2,8} concentrations were similar across the different temperatures and water concentrations. Therefore, the presence of water as an impurity mainly affected the reaction kinetics, but did not change the equilibrium parameters.

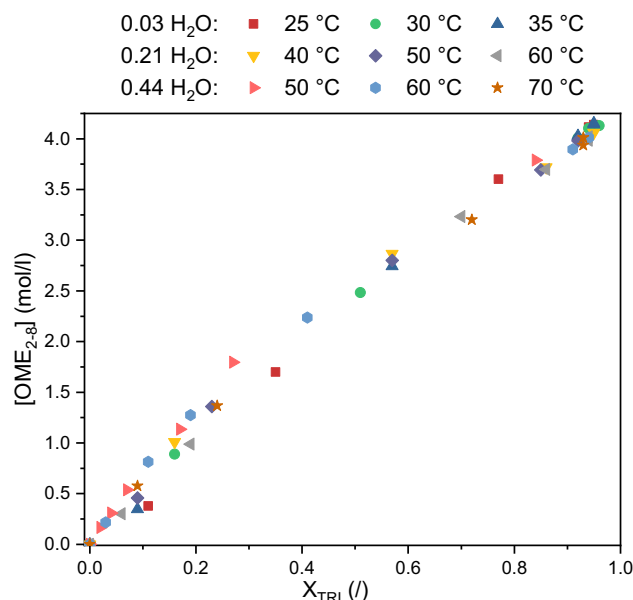


Figure 6-3. OME_{2,8} concentration vs. TRI conversion X_{TRI} for the synthesis of OME using various water concentrations in OME₁.

The conversion of TRI results from two reaction mechanisms contributing to OME growth: incorporation of FA produced *in situ* from TRI decomposition or TRI direct insertion into OME.^[115] Both reactions happen simultaneously and their contribution to OME growth could be monitored by analysis of the selectivity towards OME_{3,5} as well as the concentration of FA as a function of TRI conversion (Figure 6-4a and b). Using OME₁-0.03-H₂O, a large increase in OME_{3,5} selectivity was observed compared to the runs with a higher water content, especially at TRI conversion below 20 %. Oppositely, usage of OME₁-0.44-H₂O resulted in a smaller OME_{3,5} selectivity compared to the runs with a smaller water content. Interestingly, this trend was also observed for equilibrium TRI conversion with a difference of around 2 % in the final OME_{3,5} selectivity. This suggests that as the water concentration in OME₁ was increased, the main mechanism responsible for OME growth shifted from direct TRI insertion to TRI decomposition/FA insertion. This effect was more distinctly observed at lower TRI conversion due to the higher concentration of OME₁ and TRI, which resulted in selective OME₄ production after TRI direct insertion in OME₁, even occurring at equilibrium. The concentrations of OME₂ and OME₄ as a function of TRI conversion

reflect the trend highlighted by the analysis of the selectivity towards OME₃₋₅ (Figure C8-18a and b).

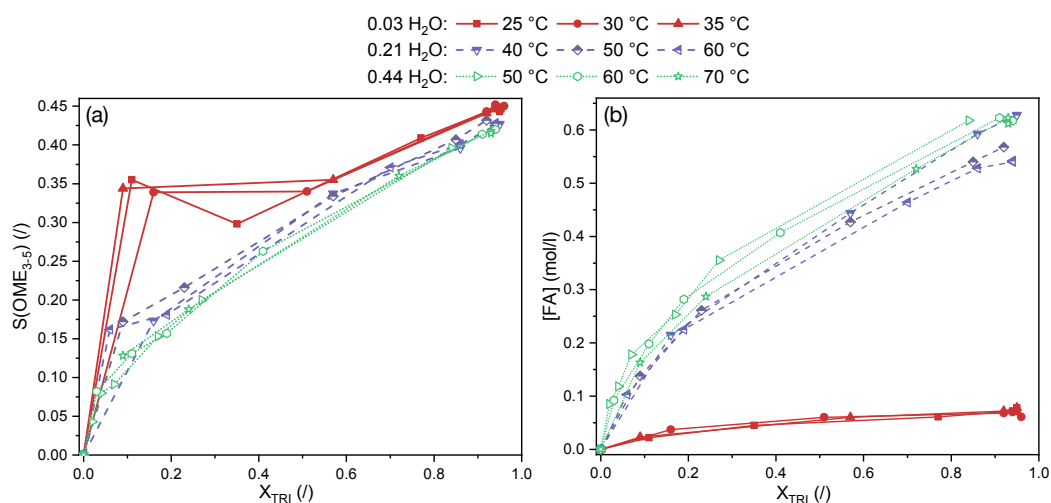


Figure 6-4. Synthesis of OME using various water concentrations in OME₁ with (a) selectivity towards OME₃₋₅ and (b) formaldehyde concentration, vs. TRI conversion X_{TRI} .

The concentration of FA exhibited different trends depending on the water concentration, which corroborated with the shift in the growth mechanism (Figure 6-4b). As the water concentration increased, the concentration of FA during the run increased, most notably between OME₁-0.03-H₂O and OME₁-0.21-H₂O. Polyoxymethylene glycols (MG) and hemiformals (HF) formation were both favored by the presence of water and increased the level of detected FA. A higher water content could lead to a higher fraction of FA existing in the form of MGs, which are formed from the combination of polymerized FA units and water. FA units can also be contained in HFs which are formed with higher levels of water by OME hydrolysis, which also produces methanol. The latter can then react with FA units leading to larger hemiformal concentrations. Molecular FA, MGs and HFs contributed to the overall FA concentration determined by the sodium sulfite method.^[60] The reaction temperature also affected the concentration of FA to a smaller extent.

Combining the results from the catalytic study (Figure 6-2) and the analysis of the reaction parameters led to two important conclusions for the synthesis of OME from TRI and OME₁. First, the difference in $E_{\text{a,app}}$ while using OME with the lowest and highest water content of ca. 4.5 kJ · mol⁻¹ obtained from the kinetic study was a result of the change in the OME growth mechanism. It was shown that direct TRI insertion has a smaller activation energy (8 kJ · mol⁻¹) compared to TRI decomposition/FA insertion.^[115] The apparent activation

energy thus increased as a larger fraction of the OME growth occurred through TRI decomposition/FA insertion. This shift could be provoked by the change in the source of Brønsted acidity from bridging hydroxyl groups to hydronium ions with larger water content in the zeolite.^[244] Multiple water molecules are able to form strong hydrogen bond networks, in which a charged specie such as a proton from a bridging hydroxyl is delocalized into a hydronium ion.^[228] Such a protonated water cluster is known to be a weaker acid compared to a zeolitic proton.^[224] It could also be argued that hydronium ions may simply be inactive for the reaction, resulting in a decrease in the number of acid sites as the concentration of water is raised. This is rather unlikely as the temperature dependence of the kinetic constant followed the Arrhenius model for the various concentrations of water in OME₁.

The second observation is that the presence of water in the zeolite pores led to a loss of accessibility to the active site. At higher water concentrations, hydronium clusters contain up to eight water molecules the zeolite channels.^[229] Eckstein et al. observed noticeable changes in the reaction rate due to different values in the pre-exponential factor, which was the result of solvation degree of zeolite Beta for the alkylation of cyclophenol.^[244] In our case, the frequency factor decreased approximately by an order of magnitude when the water concentration was doubled. As the frequency factor is the product between the frequency of collision and a steric factor, solvation of the Brønsted acid sites (BAS) could decrease the availability of the acid sites, thus decreasing the number of collisions with the proper orientation between the reactants to form an activated complex.^[245] Considering that water concentration had a larger impact on the frequency factor than on $E_{a,app}$, it is inferred that the loss in accessibility had a more severe impact on the kinetics than the change in the reaction mechanism.

6.3.3 Modulation-excitation attenuated total reflectance infrared spectroscopy

In situ attenuated total reflectance infrared (ATR-IR) spectroscopy experiments were performed to elucidate how water inhibits OME synthesis and to investigate potential competitive adsorption within the zeolite framework. This allowed to evaluate whether OME₁, TRI or H₂O was preferentially attached to the binding sites in zeolite H-beta. Experiments were performed with diluted solutions of OME₁ (15 mM), TRI (5 mM) and water

(0.7 mM) using cyclohexane as the solvent. To verify if the reaction was still proceeding under these diluted conditions, catalytic tests were first performed in batch conditions (Figure C8-19). The ME-ATR-IR experiments were carried out in a flow cell, as working under flow conditions increases control of the reactive environment and prevents accumulation of surface species, which can happen in batch conditions.^[246]

a) *Adsorption-desorption of OME₁ and TRI on H-Beta*

The adsorption-desorption of OME₁ and TRI on H-Beta was monitored in concentration modulation experiments and the collected time-resolved spectra were converted from the time-domain to the phase-domain (PD). Figure 6-5a and c show the PD spectra collected during adsorption-desorption of OME₁ or TRI against neat cyclohexane, respectively. The two peaks at 3699 and 3665 cm⁻¹ were assigned to external and internal silanol groups, respectively.^[212] These vibrational bands appear to be shifted to lower wavenumbers compared to gas phase references; the isolated silanol vibrational band is expected to be present in the spectra between 3747 and 3744 cm⁻¹.

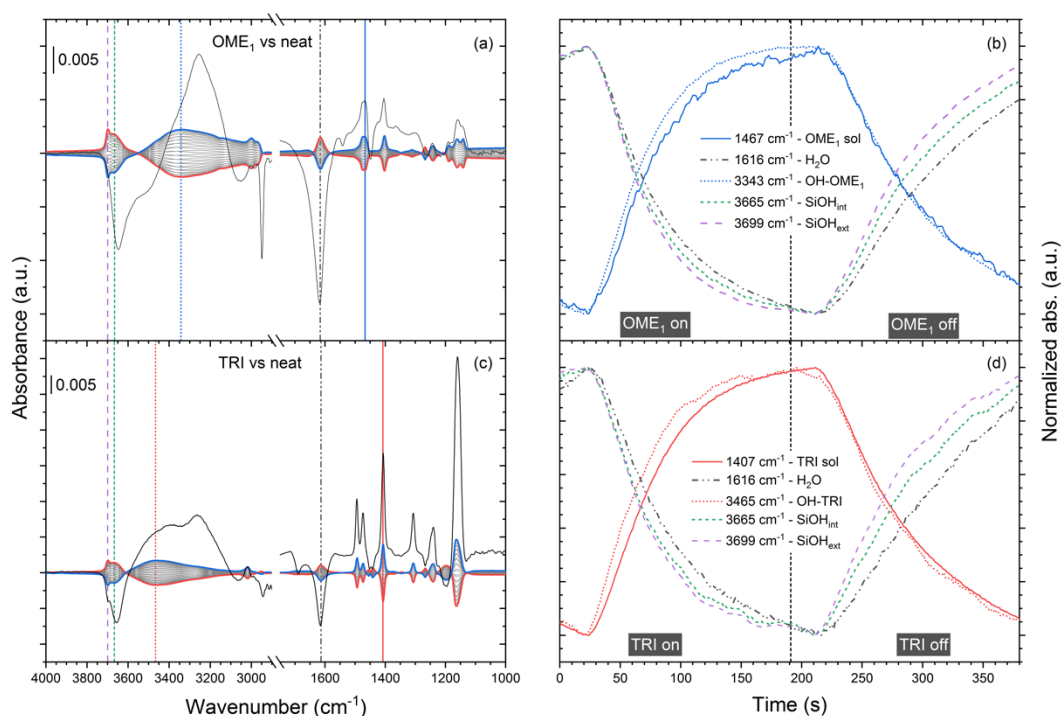
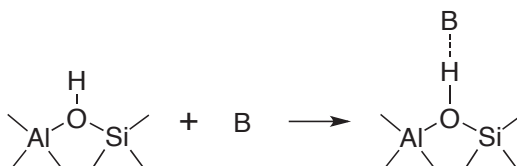


Figure 6-5. ATR-IR spectra of OME₁ vs. neat solvent (a,b) and of TRI vs. neat solvent (c,d). Selected vibrational bands in the time-domain (b,d) are displayed vertically in the phase-domain (a,c) at the corresponding wavenumber with the same line pattern and colour. A full spectrum in the time domain is shown (solid black line) in comparison with the phase domain (a,c).

A broad band centered at ca. 3400 cm⁻¹ of opposite sign with respect to the silanol peaks, can be ascribed to the adduct formation of OME₁ or TRI with both the silanol groups and

the BAS. Scheme 6-2 illustrates the interaction of a base (B) with a BAS in a zeolite to form an adduct. This will be accompanied by a downward shift (red-shift) of the O-H stretching frequency to lower numbers (0–400 cm^{-1}), with a proportional increase in integrated intensity and full width at half maximum (FWHM).^[212] This shift is proportional to the adsorption enthalpy of the base. Despite originating from various signals due to various types of adducts with silanols, only the maxima of these broad bands obtained at 110° and 290° in the PD was used to describe the adducts of OME₁ or TRI with silanol groups (Figure C8-20). Maxima of the broad bands at 3343 and 3465 cm^{-1} were assigned to OH-OME₁ and OH-TRI adducts, respectively.



Scheme 6-2. Formation of an adduct between a base and a bridging hydroxyl group in a zeolite channel.

These assignments were also based on the analysis of the maximum of each adduct band in the time-domain profile, which were directly correlated to the concentration of the analogous species in solution (Figure 6-5b and d). The bands at 1465 and 1407 cm^{-1} were selected as the tracers for dissolved OME₁ and TRI, respectively, based on the analysis of the reference spectra (Figure C8-21 and Figure C8-22). These bands were in phase with the broad OH bands and exhibited opposite sign with respect to the signals of free silanol groups. This behavior correlates the consumption of silanol groups to the formation of the OH-OME₁ and OH-TRI adducts, between 3600 and 2900 cm^{-1} .

Considering that the red-shift is proportional to the adsorption enthalpy, the comparison of the broad band maximum of the OH-OME₁ (3343 cm^{-1}) and the OH-TRI (3465 cm^{-1}) adducts reveals that the bonding of OME₁ to the silanol groups is stronger than that of TRI. When forming an adduct with the hydroxyl group, the H atom moves closer to OME₁ compared to TRI. Therefore, the affinity for the surface followed the order: OME₁ > TRI. It is worthwhile to mention that the adduct region of OME₁ is composed of at least two vibrational bands that have two different kinetic rates. This can be determined by following the maxima of selected peaks across all phase angles. In the case of TRI, all peaks in the adduct region of the PD spectra are behaving symmetrically, which means that the species residing below this envelope are all behaving with the same kinetics.

In the fingerprint region, all the signals in phase with the bands in the adduct region were assigned to dissolved OME₁ or TRI. The assignment was performed by comparison of the spectra of the reactant in cyclohexane solution with literature.^[247,248] The absence of additional bands corresponding to adsorbed species can be due to the few adsorbed species on the surface, which would be below the detection limit. Also, the C-O vibrational bands of both OME₁ and TRI could not be observed due to signal saturation by the zeolite framework in the region 1120-980 cm⁻¹. The presence of the signal at 1616 cm⁻¹ was assigned to water and reflects the affinity of water for the zeolite surface, despite its low solubility in cyclohexane.^[249] During equilibration with the neat solvent, water could not be removed entirely from the zeolite pores. It was displaced by the flow of the TRI and OME₁ solutions but the signal was slightly restored upon removal of the solutions by the solvent because of the water traces in neat cyclohexane (0.004 wt % by Karl-Fischer titration).

b) Water concentration modulation effect on OME₁ and TRI adsorption-desorption

The effect of water on the adsorption-desorption of OME₁ and TRI is presented in Figure 6-6. Interestingly, the intensities of the PD spectral features obtained in the modulation experiment of OME₁ against OME₁ + H₂O is much smaller compared to the intensities of the adsorption-desorption PD spectra in the absence of water (Figure 6-5). The modulation of water in the presence of OME₁ also resulted in a high level of noise in the temporal response of the selected signals, which indicate that the presence of water did not perturb significantly the adsorption of OME₁ on the zeolite framework (Figure 6-6b).

Inversely, the modulation of water strongly affected the adsorption of TRI (Figure 6-6c and d), revealing that bonding of TRI to the silanol groups is weaker compared to that of water. The PD spectra exhibit signals corresponding to solvated and chemisorbed TRI that are identical to those observed for the adsorption-desorption of TRI in the absence of water (Figure 6-5c). The response of these signals in the time domain mirrored the concentration of water in the feed (Figure 6-6d). Hence, the modulation of water in the presence of TRI or OME₁ suggests that the adsorption enthalpy of OME₁, TRI and water with the zeolite binding sites followed the order: OME₁ > H₂O > TRI.

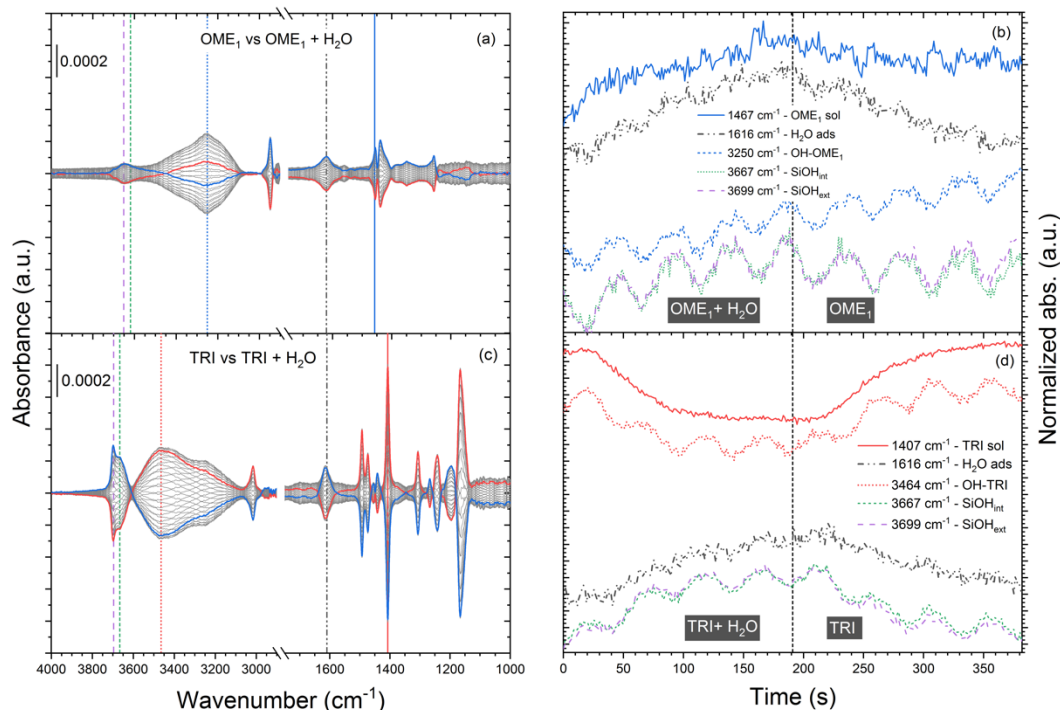


Figure 6-6. ATR-IR spectra of OME₁ vs. OME₁ + H₂O (a,b) and TRI vs. TRI + H₂O (c,d). Selected vibrational bands in the time-domain (b,d) are displayed vertically in the phase-domain (a,c) at the corresponding wavenumber with the same line pattern and colour.

c) Reactants modulation under reactive condition

The surface coverage of the catalyst under reaction condition was also investigated by concentration modulation experiments (Figure 6-7). During TRI modulation in OME₁ solution, the vibrational bands associated with the silanol groups in solution displayed a low intensity in the PD (Figure 6-7a). Thus, the modulation of the concentration of TRI did not significantly impact the occupancy of those sites. The PD spectra also resemble the spectra obtained in Figure 6-6c for the adsorption-desorption of TRI. In the adduct region, both OME₁ and TRI were slightly influenced by this modulation and this is reflected in the temporal response of the signals (Figure 6-7b). Concentrations of dissolved or coordinated OME₁ were in phase opposition with dissolved TRI and OH-TRI adducts. In parallel, external and internal silanols were also responding to the modulation of TRI. Upon introduction of TRI, the external silanol groups were first freed from the coordination with OME₁, followed by internal ones. The recovery of the silanols happened before the increase in concentration of TRI, both on the surface and in solution. Since the reaction was happening while removing TRI from the solution, the adsorbed species were consumed first to form larger OME. The silanols were freed from coordination with OME₁ compared to when the concentration of TRI is insufficient for the reaction to happen. OME₁ stopped

to be consumed, which gave rise to an increase of its concentration in solution and at the surface of the catalyst. Ultimately, the decrease of the concentration of coordinated and dissolved OME_1 implied the consumption of the reactant.

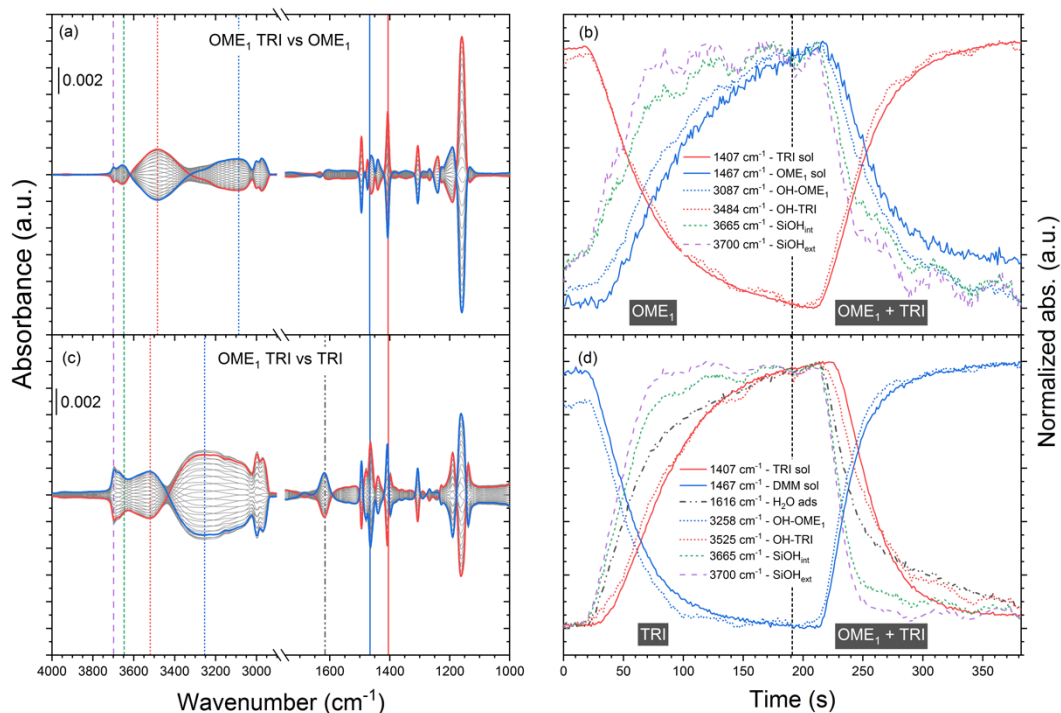


Figure 6-7. ATR-IR spectra of $\text{OME}_1 + \text{TRI}$ vs. OME_1 (a,b) and $\text{OME}_1 + \text{TRI}$ vs. TRI (c,d). Selected vibrational bands in the time-domain (b,d) are displayed vertically in the phase-domain (a,c) at the corresponding wavenumber with the same line pattern and colour.

Similar observations can be made during the modulation experiment of OME_1 in the TRI solution (Figure 6-7c and d). However, the signals corresponding to external and internal silanol groups were larger than during the modulation of TRI . Therefore, a larger amount of silanol groups in solution were consumed in the presence of OME_1 , in agreement with the higher affinity of OME_1 for the silanol groups compared to TRI that was demonstrated above. Hence, when TRI was constantly present in the reaction feed, it first reacted with OME_1 bound to the silanol groups. Furthermore, the modulation of OME_1 in the presence of TRI perturbed the adsorption of water reflected in the signal obtained at 1616 cm^{-1} . In the time domain, this signal was delayed compared to that of the silanols, which could reflect the adsorption of water to a stronger acid site. Overall, these two ME-ATR-IR experiments under reaction conditions demonstrated that the occupancy of the silanol groups was dominated by OME_1 under reaction conditions.

Finally, the modulation of water in a continuous feed of both reactants ($\text{OME}_1 + \text{TRI}$ vs $\text{OME}_1 + \text{TRI} + \text{H}_2\text{O}$) showed water mostly perturbed the tracer signal of TRI at 1407 cm^{-1} under reaction condition (Figure C8-23). As the signal corresponding to TRI in solution was in phase opposition with the modulation of water, water was able to displace TRI but not OME_1 , therefore confirming the affinity trend for the zeolite binding sites: $\text{OME}_1 > \text{H}_2\text{O} > \text{TRI}$.

d) Adsorption-desorption of OME_1 and TRI after pyridine anchoring on the BAS

To differentiate between adducts bound to the silanol groups or to the BAS, pyridine adsorption experiments were performed, during which the BAS were poisoned prior to the modulation experiments. Spectral features at 1490 , 1545 and 1638 cm^{-1} confirmed that the bonded pyridine did not desorb from BAS under continuous flow of OME_1 or TRI solutions (Figure C8-24).^[250] After the adsorption of pyridine, the modulation of TRI or OME_1 were carried out and the PD data obtained in the presence (110 to 280°) and the absence (290 to 100°) of pyridine are compared in Figure 6-8. During OME_1 modulation, blocking the BAS with pyridine changed significantly the aspect of the PD spectra in the adducts region (Figure 6-8a). Compared to the experiment without pyridine, a blue-shifted, more symmetric envelope was obtained in the presence of pyridine. An additional change occurs for the signal at 1140 cm^{-1} , which has a higher relative peak intensity to the peak at 1160 cm^{-1} in the presence of pyridine. This signal is associated with the asymmetric stretching mode of O-C-O groups ($\nu_{\text{as}}(\text{OCO})$) and might be a fingerprint of OME_1 binding to BAS.^[247]

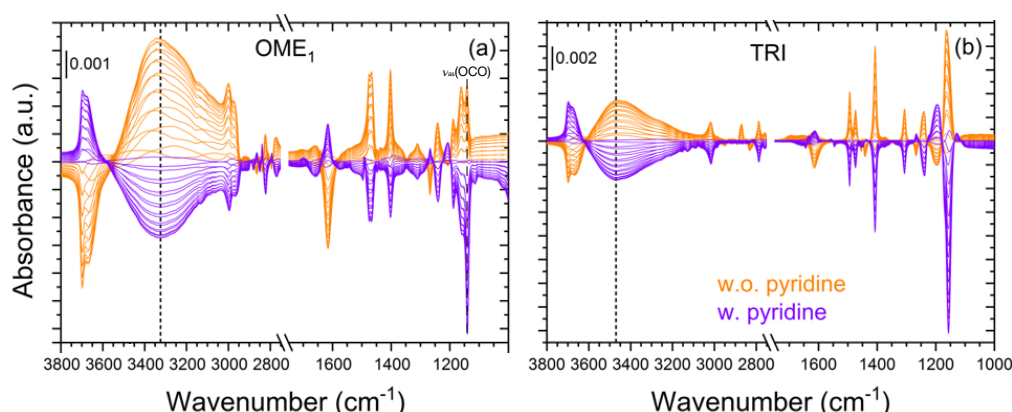


Figure 6-8. Phase-domain ATR-IR spectra on the catalyst without (orange) and with (purple) adsorbed pyridine. (a) OME_1 vs. neat solvent. (b) TRI vs. neat solvent.

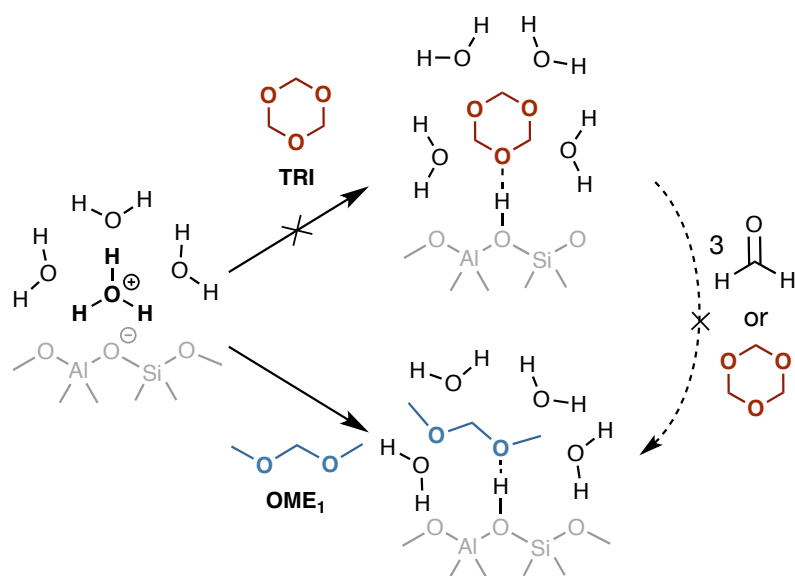
In comparison, the two sets of PD spectra obtained from the modulation experiments with TRI were very similar irrespective of pyridine poisoning (Figure 6-8b). The different impacts of pyridine on the modulation of OME₁ or TRI revealed two important trends. First, under the studied conditions, TRI did not bind to the BAS but interacted only with the silanol groups. On the contrary, the observation that poisoning with pyridine prevented the adsorption of OME₁ with BAS, proved that OME₁ interacted with BAS. Second, the lower intensity of OME₁ $\nu_{\text{as}}(\text{OCO})$ at 1142 cm⁻¹ in the absence of pyridine compared to the signal of dissolved OME₁ at 1160 cm⁻¹ could be due to coordination of OME₁ to the BAS via its oxygen atom. Such a coordination of OME₁ could prevent this vibration from occurring. Also, all the PD spectra related to OME₁ and TRI experiments reveal strong peaks associated to CH₂ and CH₃ groups, while in solution, these peaks appear very weak in comparison to the vibrational modes involving C-O bonds (see Figure C8-21 and Figure C8-22). This might be also an indication that OME₁ and TRI are binding via their oxygen atoms to the zeolite framework.

6.3.4 Causes for zeolite deactivation due to water for OME synthesis

Water severely affected the kinetics of OME synthesis using TRI and OME₁ over an H-Beta zeolite. The kinetic study revealed that the apparent energy of activation increased and the pre-exponential factor decreased with increasing water content in OME₁. The ATR-IR study demonstrated that OME₁ possesses higher affinity for the zeolite binding sites compared to water and TRI, and that water competes predominantly with TRI for adsorption on the zeolite binding sites. The combination of these two sets of experiments offer new insights into the cause of catalyst inhibition in the presence of water. Competitive adsorption of the reactants and water within the zeolite is considered the main cause for the kinetic inhibition of water. We believe that the limited adsorption of TRI to the zeolite active sites due to the presence of water resulted in slower reaction kinetics. It is worthwhile to mention that even at higher levels of water, molecular water is presumably at very low concentrations due to the formation of polyoxymethylene glycols and hemiformals.

The adsorption-desorption experiments of OME₁ and TRI demonstrated that in cyclohexane the affinity of OME₁ for the surface is stronger than TRI (Scheme 6-3). The higher adsorption enthalpy of OME₁ to the zeolite binding sites explains the higher resistance of

OME₁ against competitive adsorption with water. On the contrary, the less strongly adsorbed TRI is much more susceptible for perturbation and displacement by water. We attribute the different affinity of H₂O and TRI for the silanol groups to the greater ability of a water molecule/cluster to accommodate a proton than the C-O-C group of TRI. Under reaction conditions, modulation of TRI in the continuous presence of OME₁ did not impact silanol occupancy as much as OME₁ modulation in the presence of TRI. Finally, modulation of water affected TRI adsorption more severely in the constant presence of TRI and OME₁. Overall, the trend for the adsorption enthalpies of OME₁, TRI and H₂O with the zeolite binding sites was in the order OME₁ > H₂O > TRI.



Scheme 6-3. Suggested mechanism of the kinetic inhibition by water during OME synthesis on a H-Beta zeolite.

In order to further corroborate our proposed water inhibition mechanism, we computed the energetic descriptors for the adsorption of OME₁, TRI and H₂O over a minimal BAS model (B3LYP-D3/CBS level of theory). The simulation results show that all the considered adducts are thermodynamically stable and their formation is favored at the considered temperature-pressure conditions (Table 6-2). The optimized adduct structures are shown in Figure C8-9. As inferred from the experimental evidences, the stability for the adsorption on BAS follows the order: OME₁ > H₂O > TRI. By estimating the equilibrium constant of each adsorption process from the ΔG values, the equilibrium adducts population can also be estimated. It is dominated by OME₁-BAS species, accounting for more than 95 % of the total adducts, regardless of the H₂O concentration. Conversely, the TRI-BAS/H₂O-BAS ratio

is strongly affected by the H₂O content, being 1.4 at the highest H₂O concentration considered in this work (0.44 wt %), whereas it noticeably increases by a factor of about 15 (up to 20.8) when the H₂O concentration drops to 0.03 wt %. Such estimates confirm that the accessibility of BAS by TRI is the key step for sustaining the synthesis of OME.

Table 6-2. B3LYP-D3/CBS electronic energies (ΔE), enthalpies (ΔH) and Gibbs free energies (ΔG) for OME₁, TRI and H₂O with BAS (expressed in kJ · mol⁻¹).

Adduct	ΔE	ΔH	ΔG
OME ₁ -BAS	-59.8	-53.2	-6.3
TRI-BAS	-50.0	-43.6	-0.3
H ₂ O-BAS	-53.5	-46.6	-4.3

The spectroscopic experiments with BAS poisoning by pyridine offer novel molecular level insights into the interaction of the reactants with the hydroxyl groups of the zeolite. Blockage of the BAS by pyridine significantly perturbed the interaction of OME₁ with the catalyst surface and thus the PD spectra, revealing that OME₁ interacted with both the BAS and the silanol groups of the pristine catalyst. Conversely, no significant changes were observed in the case of TRI, suggesting that TRI does not bind to the BAS under these experimental conditions. TRI activation is required to provide oxymethylene units for OME growth, independently of the growth mechanism. The inability of TRI to bind to a BAS probably decreased the decomposition of TRI to FA units, as well as its ability to be inserted into an OME (Scheme 6-3). We suggest that the decreased frequency factor A obtained in the kinetic study was a result of the competitive adsorption of water and TRI, which ultimately reflects the accessibility of the reactants to the zeolite active sites. The presence of water also shifted the main growth mechanism from direct TRI insertion to TRI decomposition/FA incorporation, which was accompanied by a slight increase in $E_{a,app}$.

The results presented in this work also provide additional insights into previous studies about OME synthesis. Wu et al. studied the impact of the Si/Al ratio on the activity of H-ZSM-5. A Si/Al ratio of 580 led to the best performance, while the material with the lowest Si/Al ratio of 25 exhibited the lowest turnover frequency.^[81] A sufficient number of “medium-strong” acid sites was concluded to be required for this reaction. In light of the presented results demonstrating the impact of water concentration on the catalytic activity of H-Beta, we believe that the results of Wu et al. could also have been influenced by a higher water sorption capacity of low Si/Al H-ZSM-5. As zeolites with high Si/Al ratio are

hydrophobic, less water diffuses into the pores to the adsorption sites, which could have in turn influenced the reaction kinetics.

Finally, we also demonstrated that exposure to ambient moisture greatly affected the catalytic activity. Even a similar exposure to ambient moisture for a set of catalysts may not prove to be sufficient, as the hygroscopicity may vary across the tested catalysts. It is thus important that future catalytic studies on OME synthesis are performed with minimum exposure to air before reaction. Furthermore, the concentration of water in OME₁ should always be mentioned, so that catalytic activities can be compared across studies.

6.4 Conclusion

The presence of water in OME₁ at concentrations as low as 0.21 wt % affected greatly the activity of zeolite H-Beta for the synthesis of OME from TRI and OME₁. Larger water concentrations required higher temperatures to reach equilibrium due to slower kinetics. Even the short exposure of zeolite H-Beta to the humid atmosphere was sufficient to significantly hinder its performance due to the uptake of water. We performed a kinetic study that revealed that both the apparent energy of activation and the pre-exponential factor were negatively impacted by water with an increasing level of water in OME₁. We also observed a shift of the main OME growth mechanism from direct TRI insertion to TRI dissociation with subsequent FA incorporation. Through ATR-FTIR spectroscopy, we also studied TRI and OME₁ adsorption modes, offering new perspectives on the reaction. The affinity of reactants for the zeolite surface followed the order: OME₁ > H₂O > TRI. While OME₁ interacted with the silanol groups and the Brønsted acid sites (BAS), TRI exclusively bonded to the silanol groups. Combined together, these results suggest that the kinetic inhibition of water was due to the inability of TRI to interact with the BAS, which prevented its direct insertion or decomposition to FA units.

To clearly assign the binding sites of OME₁ and TRI, as well as to probe the reaction mechanisms, further studies would be required. Also, great care in catalyst pre-treatment should be considered in future studies on the catalytic synthesis of OME to ensure that water concentration is not influencing the results. Furthermore, water concentration in OME₁ should be checked and mentioned to allow for comparison of catalyst activities across studies.

Chapter 7 Alkali metal grafting on silica for methanol catalytic dehydrogenation

7.1 Introduction

Production of OME requires a source of oxymethylene units to react with methyl-end groups resulting in a Schulz-Flory distribution of OME.^[143] Presence of water has a deleterious effect on its synthesis: it affects the equilibrium parameters, requires higher reaction temperatures and yields a higher fraction of byproducts.^[40,74] Therefore, using a hydrous production route requires larger separation efforts in the downstream processing of the product stream. Production of OME from anhydrous reactants such as trioxane (TRI) or dimethoxymethane (OME₁) has been hitherto favored compared to other compounds such as formalin or methanol, which either contains water or generates it through acetalization. The results from Chapter 6 highlighted that the reaction kinetics were also severely affected by the presence of water: only 0.21 wt % of water in OME₁ severely affected the reaction kinetics while using zeolite H-Beta as the catalyst.^[125]

Production of monomeric, anhydrous formaldehyde (FA) by non-oxidative methanol dehydrogenation (here referred to as catalytic dehydrogenation) was demonstrated as a cost-efficient alternative to the energy-intensive production of TRI for OME production.^[251] The feasibility of this approach was demonstrated in a study by Peter et al., in which OME were synthesized from OME₁ by the uptake of monomeric gaseous FA.^[68] With a yearly production volume of millions of tons per year, FA is a base chemical in the chemical industry for various materials such as resins, polymers, paints or explosives, some of which also require anhydrous FA for their synthesis.^[60] Current FA production processes rely on

This chapter is based on the manuscript: Baranowski C. J., Brandon J., Bahmanpour A. M., Kröcher O., Alkali metal grafting on silica for methanol catalytic dehydrogenation, *Manuscript in preparation* **2019**.^[126] C. Baranowski performed the experiments, analysed the data together with the co-authors and wrote the manuscript.

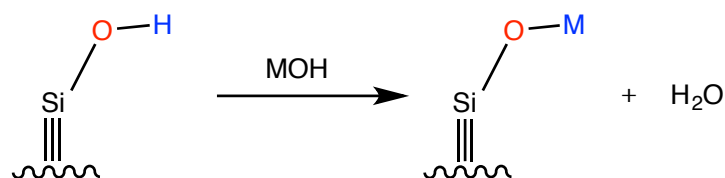
the oxi-dehydrogenation of methanol over silver or iron-molybdenum catalysts, which results in the formation of large quantities of water.^[252] By performing the reaction in anaerobic conditions, the oxidative dehydrogenation of methanol can be suppressed. However, conversion of methanol to FA and hydrogen is a challenging reaction; high temperatures are required to overcome the large positive enthalpy of reaction ($84 \text{ kJ} \cdot \text{mol}^{-1}$) and sufficient methanol conversion can only be reached at temperatures above $600 \text{ }^\circ\text{C}$.^[253,254] FA is unstable at these temperatures and several side reactions diminish the overall reaction yield (e.g. FA decomposition to CO and methanol dehydration).^[255]

A significant amount of research has been dedicated to the identification of suitable catalysts for the catalytic dehydrogenation of methanol since the 1960s. Silver-based catalysts demonstrated high activity but relied on the presence of surface oxygen, and bulk oxygen present in the silver lattice.^[256] They were shown to deactivate rapidly in the absence of oxygen and required frequent regenerations by oxidative treatments.^[257] Copper possesses a high selectivity for the dehydrogenation of alcohols but a low specific activity; research on Cu-containing catalyst has therefore focused on finding effective support and modifiers.^[258] Phosphorous was found to increase significantly the catalyst activity when it is supported on silica and the highest recorded yield was in the 40 % range at temperatures between 400 and $500 \text{ }^\circ\text{C}$ for a $\text{CuO-Cu}_3(\text{PO}_4)_2/\text{SiO}_2$.^[259] This performance could not be reproduced by other researchers and the catalyst was prone to rapid deactivation.^[260] Zinc-based catalysts were also found to be active for the catalytic dehydrogenation of methanol and were studied extensively over various supports. Under mild conditions, conversion as high as 50 % were reported with a FA selectivity of 90 % over a ZnO/SiO_2 catalyst.^[261] Yet, irreversible catalyst deactivation occurred under typical reaction conditions due to reduction of ZnO and subsequent evaporation of metallic zinc.^[262]

Another group of catalysts active in the methanol catalytic dehydrogenation reaction are alkali metals.^[253] Amongst these elements, sodium was studied in various forms (e.g. sodium carbonate, sodium aluminates) and demonstrated the highest activity compared to other studied catalysts.^[263] Its reaction mechanisms remain unclear. It was suggested that dissociative adsorption of methanol occurred on siloxane bridges of a Na-ZSM-5 zeolite.^[264] Other authors proposed that the reaction is initiated at the surface of the catalyst, and then proceeds in the gas-phase.^[255,265] It was reported that hydrogen desorption was the rate-

limiting step, which could be accelerated by hydrogen spillover on active carbon.^[266] Sauer et al. also demonstrated that these salts decompose at high temperatures leading to sodium evaporation, which then induces a homogeneous radical vapour-phase reaction.^[267,268] Alkali metals present as ions in zeolite X or Y were also used in the side-chain alkylation of toluene with methanol, which requires dehydrogenation of methanol to formaldehyde as an intermediate step.^[269,270]

Alkali metals possess an important potential to catalyze the catalytic dehydrogenation of methanol, but it remains unclear why sodium is the most active among these elements. Moreover, there is a need for the development of catalysts which can prevent sodium evaporation whilst preserving its activity towards catalytic dehydrogenation of methanol. For this purpose, we used amorphous silica as a support to graft alkali metals according to a method developed by Keller et al.^[271] During this procedure, surface sites such as silanol groups are deprotonated to silanolates under basic conditions, followed by ion-exchange with an alkali metal (Scheme 7-1). This method can reach atomic dispersion whilst preventing amorphization of the support due to the inhibition of Si-O bond hydrolysis.^[271,272]



Scheme 7-1. Grafting of alkali metals on fumed silica according to Keller et al.^[271]

Silica was chosen as a support due to its high thermal stability, inertness, and mechanical strength. Usage of other supports displaying surface acidic surface groups, such as Al_2O_3 , was not considered as their usage can result in methanol dehydration and coke formation, which are highly undesirable.^[253,260] The project goals were two-fold. First, we aimed to assess the catalytic performance of each of the synthesized catalysts. Secondly, we intended to reach a deeper understanding of the structure-activity relationship of alkali metal-grafted silica for the catalytic dehydrogenation of methanol.

7.2 Experimental

7.2.1 Preparation of alkali metal supported on fumed silica by grafting

Alkali metals grafted on silica were prepared according to a protocol developed by Keller et al.^[271] Typically, Aerosil® fumed silica was dried overnight in an oven at 150 °C. It was then transferred under inert atmosphere using Schlenk techniques. A calculated amount of the alkali metal hydroxide salt (LiOH, ABCR, 98 %; NaOH, Sigma-Aldrich, 97 %; KOH, Fisher Chemicals, 85 %; RbOH · 2H₂O, Fluka, 95 %; CsOH 50 wt % in H₂O, ABCR, 99.9 %) was inserted in a round bottom flask, in which methanol (anhydrous, Sigma-Aldrich, 60 mL · g⁻¹ of silica) was transferred by cannula transfer. Following complete salt dissolution, the methanolic solution was transferred to the round bottom flask containing the silica powder. The mixture was then stirred by magnetic stirring (450 rpm) at 25 °C for 10 min. After quenching with ice, it was filtered and washed with methanol (3 times with ca. 100 mL). The powder was then dried overnight at 110 °C. Finally, it was calcined in static air at 550 °C with a temperature ramp of 10 °C · min⁻¹.

The various catalysts were named M-SiO₂, where M is the alkali metal used during grafting. If no concentration is mentioned, a 0.1 M MOH concentration in methanol was used during grafting. A second series of catalysts were synthesized with a smaller metal loading with KOH, RbOH and CsOH and are referred to as M-SiO₂-SL. During the grafting procedure of these samples, the concentrations of KOH, RbOH and CsOH in methanol were 3.75 · 10⁻², 1.88 · 10⁻² and 9.37 · 10⁻³ M, respectively. Specifically for Na-grafted catalysts, the concentration was also varied from 0.05 to 0.15 M and the resulting samples are referred to as Na-SiO₂-xM, where x is the concentration of NaOH during grafting. Finally, grafting in isopropanol (IPA, anhydrous, Sigma-Aldrich) was also performed with a 0.1 M NaOH concentration, resulting in the sample M-SiO₂-IPA. The extent of amorphization ξ_{amorph} of a sample was defined according to Equation (7-1), where $S_{BET}(SiO_2)$ and $S_{BET}(sample)$ are the specific surface area of silica and of the sample after the grafting procedure, respectively.

$$\xi_{amorph} = \frac{S_{BET}(SiO_2) - S_{BET}(sample)}{S_{BET}(SiO_2)} \quad (7-1)$$

7.3 Results and discussion

7.3.1 Physico-chemical characterization of the catalysts

The elemental composition of each catalyst was investigated by ICP-OES (Figure 7-1, Table 7-1). The results confirmed that all alkali metals were successfully supported on silica. The metal content of the catalysts which were supported using an alkali hydroxide concentration of 0.1 M varied significantly across the various alkali metals. There was a ca. fourfold increase in the metal to silicon (M:Si) molar ratio between Li-SiO₂ (0.0021) and Na-SiO₂ (0.0087). Moving down the group 1 elements of the periodic table from Na to Cs, the M:Si ratio approximately doubled between each element with a maximal value of 0.0769 for Cs-SiO₂. Considering that the basicity of the hydroxide salts increases with the alkali metal cation size, higher molar metal loadings were obtained with larger alkali metals.^[273] Larger salt basicity resulted in a larger deprotonation of the silica surface and a larger concentration of silanolates available for ion-exchange.

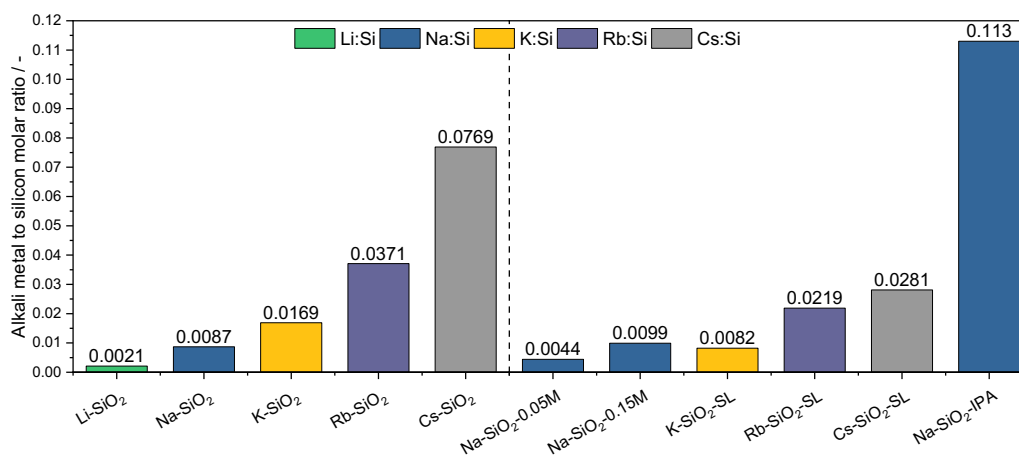


Figure 7-1. Alkali metal to silicon molar ratio (M:Si) of the various synthesized catalysts.

In the case of Na, the grafting procedure was repeated by varying the concentration of NaOH, as well as by substitution of methanol. By decreasing the NaOH concentration to 0.05 M, the Na:Si loading was reduced by a factor of 2 for Na-SiO₂-0.05M. In contrast, an increase of the NaOH concentration to 0.15 M resulted in a more modest increase in metal loading to 0.0099 for Na-SiO₂-0.15M. Substitution of methanol with isopropanol while maintaining the NaOH concentration at 0.1 M had a much larger influence on the metal loading: Na-SiO₂-IPA reached a Na:Si ratio of 0.113. For larger metal cations, another series of

catalysts was synthesized with smaller metal loadings (M-SiO₂-SL) in order to obtain comparable metal concentration with Na-SiO₂ and the M:Si ratio was reduced to a maximum of 0.0281 for Cs-SiO₂-SL.

Table 7-1. Characterization results from ICP-OES, N₂ physisorption and CO₂ chemisorption.

	M:Si molar ratio (/)	Surface area (m ² · g ⁻¹)			Basicity (μmol CO ₂ · g _{cat} ⁻¹)
		BET	Micro ^[a]	Meso ^[b]	
SiO ₂	/	218	19	179	0.90
Li-SiO ₂	0.0021	190	16	164	2.60
Na-SiO ₂	0.0087	169	15	142	13.00
K-SiO ₂	0.0169	135	13	111	25.05
Rb-SiO ₂	0.0371	121	15	97	27.48
Cs-SiO ₂	0.0769	95	14	72	23.60
Na-SiO ₂ -IPA	0.113	69	4	59	85.35
Na-SiO ₂ -0.05	0.0044	170	14	148	/
Na-SiO ₂ -0.15	0.0099	157	15	133	/
K-SiO ₂ -SL	0.0082	176	10	156	11.96
Rb-SiO ₂ -SL	0.0219	166	13	139	13.67
Cs-SiO ₂ -SL	0.0281	160	16	143	4.76

^[a] Derived from the t-plot method. ^[b] Derived from the BJH method using the adsorption branch.

Elemental mapping was performed by STEM-EDXS for Na-SiO₂ and K-SiO₂ (Figure 7-2a and b), and showed atomically dispersion on the surface without the presence of aggregates. X-ray Diffraction (XRD) was used to study the crystallinity of the samples (Figure 7-2c). All samples displayed a broad peak centered around 22° and no crystalline reflection was detected in the angle range of 5 to 35°. Therefore, the grafting treatments with the various alkali hydroxide salts in methanol did not alter the amorphous structure of silica. Furthermore, no reflections corresponding to an alkali metal or an alkali metal oxide were detected, which confirmed the absence of crystals above 5 nm in the samples and correlated with the elemental mapping done by STEM-EDXS.

The textural properties of the catalysts were determined by N₂ physisorption (Table 7-1). The isotherms and the BJH cumulative pore size distribution are displayed in Figure 7-2d. All catalysts present a type IVa isotherm characterized by N₂ uptake in the micropores at low relative pressure, an H2b hysteresis loop and an inflexion point at the saturation pressure. The total N₂ uptake and the mesoporous surface area decreased with an increasing alkali metal size. Compared to SiO₂, all grafted catalysts displayed a lower BET surface area due to surface amorphization (Figure 7-3a). The BET surface area of the samples

varied according to the alkali metal, the MOH concentration, and the solvent used. Overall, grafting with larger alkali metals in methanol resulted in lower BET surface area. Additionally, the extent of amorphization was much higher when using IPA as a solvent rather than methanol during grafting of Na, with the produced catalysts Na-SiO₂-IPA and Na-SiO₂ having a specific surface area of 69 and 169 m² · g⁻¹, respectively.

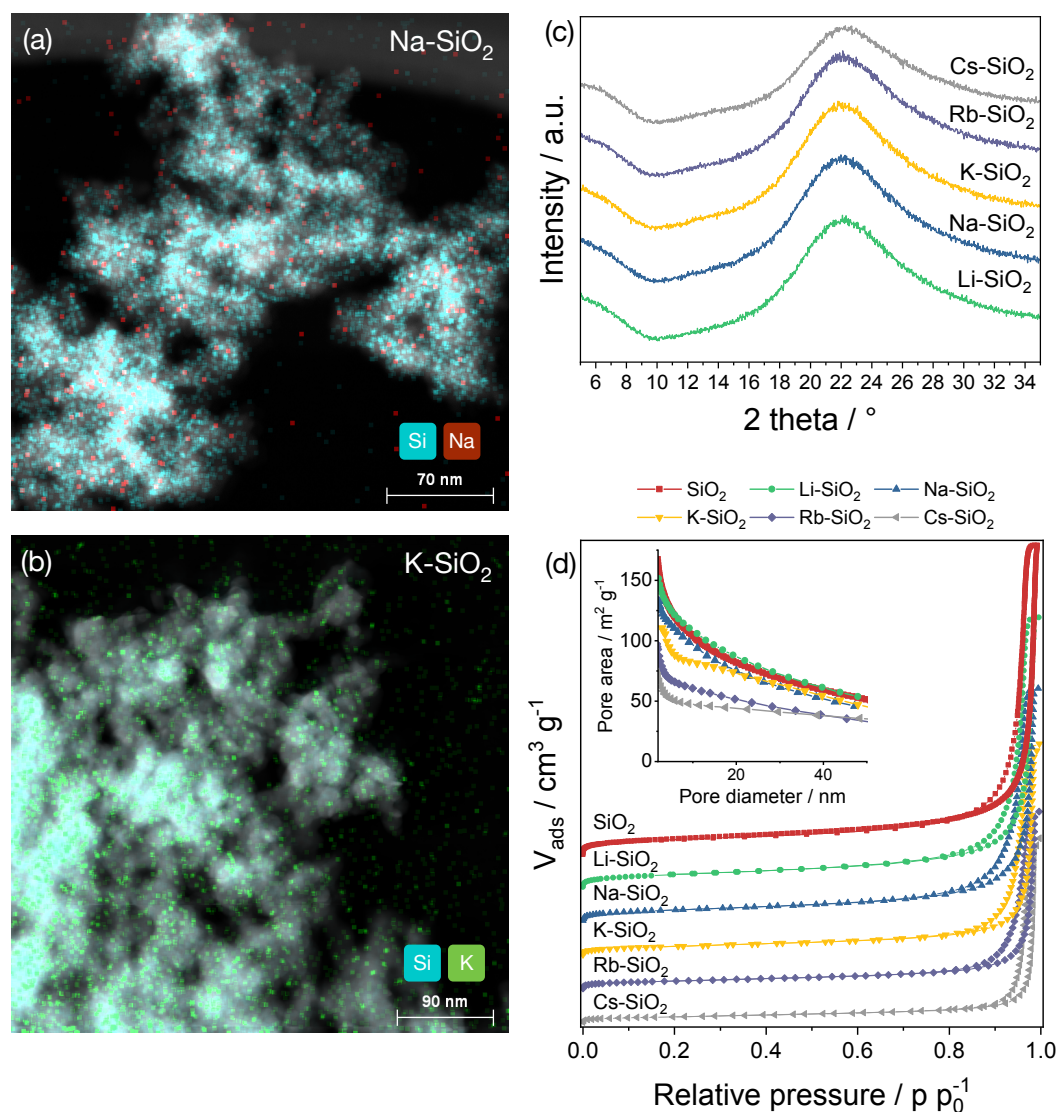


Figure 7-2. STEM-EDXS images of (a) Na-SiO₂ and (b) K-SiO₂ (Si: blue, Na: red, K: green). (c) XRD patterns of the metal grafted catalysts. (d) Isotherms of the various catalysts grafted using a 0.1 M MOH concentration and the cumulative pore area using the BJH method with the adsorption branch (inset).

The series of catalysts produced with a lower concentration of alkali hydroxide salt resulted in less surface amorphization, which can be deduced from the comparison of the BET surface area of samples M-SiO₂ with M-SiO₂-SL. Overall, a correlation was found between the

extent of amorphization of the sample and the catalyst loading (Figure 7-3b), which highlights the trade-off between deposition of alkali metals on silica and preservation of its surface area. These results are in line with the findings from Keller et al.^[271]

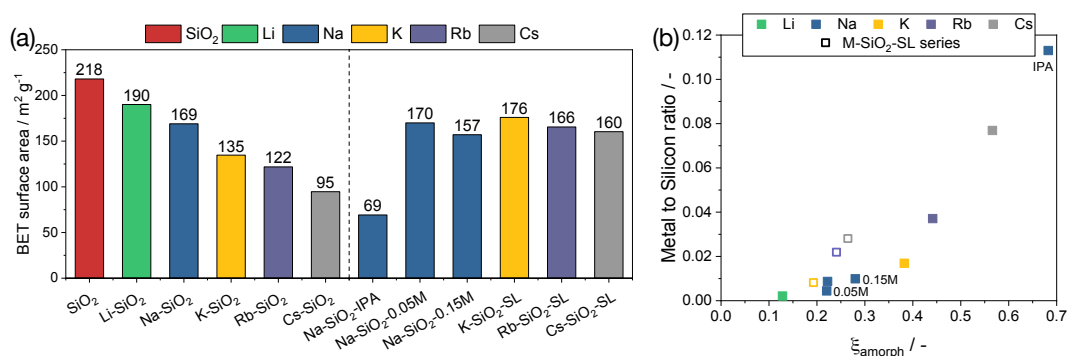


Figure 7-3. (a) BET surface area of the various synthesized catalysts. (b) Correlation between the extent of amorphization ξ_{amorph} and the M:Si molar ratio.

CO₂ temperature programmed desorption (CO₂-TPD) was performed to quantify the number and strength of the basic sites of each catalyst (Figure 7-4a). From SiO₂, the CO₂ peak area increased moving down the group 1 elements, which indicated the presence of basic sites following alkali metal grafting.^[271] The increasing concentration of the basic sites seemed to reach a plateau: moving from K-SiO₂ to Cs-SiO₂, the peak area did not vary significantly, despite the increase in the M:Si ratio identified by ICP-OES. This could indicate that the surface became saturated with alkali metals at M:Si above the one reached by K-SiO₂ (0.0169). Alternatively, the increase of the concentration of the basic sites could stop due to the combination of increasing surface loading and decreasing specific surface area. Due to their higher basicity, Rb and Cs hydroxide salts dissolved a larger fraction of silica while increasing the deposition of the respective alkali metal on the silica surface. The highest basicity was obtained for Na-SiO₂-IPA with a value of 85.35 $\mu\text{mol CO}_2 \cdot \text{g}_{\text{cat}}^{-1}$, considerably higher than Na-SiO₂ (13.00 $\mu\text{mol CO}_2 \cdot \text{g}_{\text{cat}}^{-1}$). The basicity values obtained for the M-SiO₂-SL series were similar to that of Na-SiO₂ ($\pm 13\%$), except in the case of Cs-SiO₂-SL for which 4.76 $\mu\text{mol CO}_2 \cdot \text{g}_{\text{cat}}^{-1}$ was recorded.

The nature of the alkali metal supported on silica did not appear to affect strongly the strength of the basic sites, as all the CO₂ peak maximum were comprised between 110 and 150 °C. XPS Analysis of the binding energy of oxygen (O1s) can provide information on the oxygen basicity: as the O1s binding energy decreases, the electron pair donation becomes more favorable and the basicity becomes stronger.^[274] The analysis confirmed that

the relative basic strength of each of the catalysts was similar, which was reflected by the same value of the binding energy obtained, considering the measurement accuracy of the instrument (Figure 7-4b).

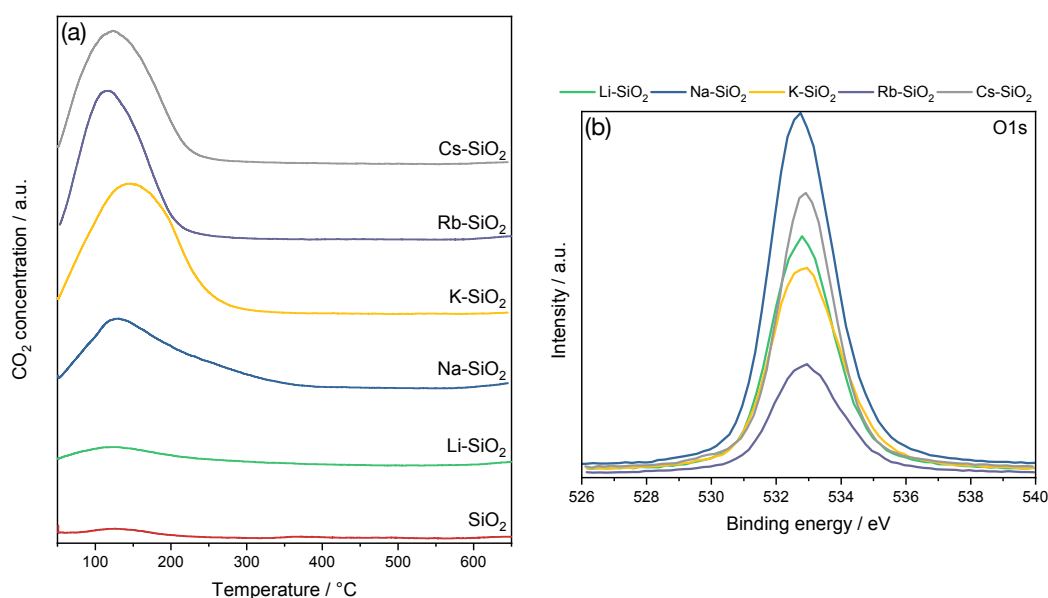


Figure 7-4. (a) CO₂-TPD and (b) high resolution O1s XPS spectra of the alkali metal grafted catalysts (M-SiO₂).

Temperature programmed desorption of MeOH (MeOH-TPD) was performed to understand the interaction between the catalyst and methanol, during which the desorption of MeOH, FA and CO were recorded (Figure 7-5). Analysis of the desorbed methanol revealed two main peaks (Figure 7-5a). The first one around 150 °C increased in area with an increase in atomic number within the alkali metal group. This peak was attributed to weakly adsorbed MeOH and its desorption peak maximum was similar for all alkali metals. The second peak at higher temperatures, attributed to strongly adsorbed MeOH, formed due to the electrostatic interaction between the lone electron pair of the oxygen atom and the grafted alkali metals.^[275] It can be observed that the position of the desorption peak maximum of the strongly adsorbed MeOH decreased with increasing alkali metal size. Li-SiO₂ did not follow the trend, probably as a result of its smaller metal loading compared to the other samples.

FA was produced at temperatures above the desorption peak of strongly adsorbed MeOH (Figure 7-5b). For all alkali grafted catalysts, the amount of desorbed FA was smaller compared to the amount of desorbed MeOH. The desorption peak maximum of FA also shifted to lower temperatures moving down the alkali metals catalysts in the periodic table,

except for Rb-SiO₂ which produced FA as from 250 °C. CO was produced in more significant amount compared to FA and the minimum desorption temperature was around 350 °C. Higher amounts of CO were produced for SiO₂ as well as Li- and Na-SiO₂, with a desorption peak maximum occurring around 750 °C (Figure 7-5c). In contrast, a decreasing desorption peak maximum was observed for K-SiO₂, Rb-SiO₂, and Cs-SiO₂. It is also interesting to mention that, as opposed to the desorption of MeOH, the presence of alkali metals was not necessary for SiO₂ to produce CO.

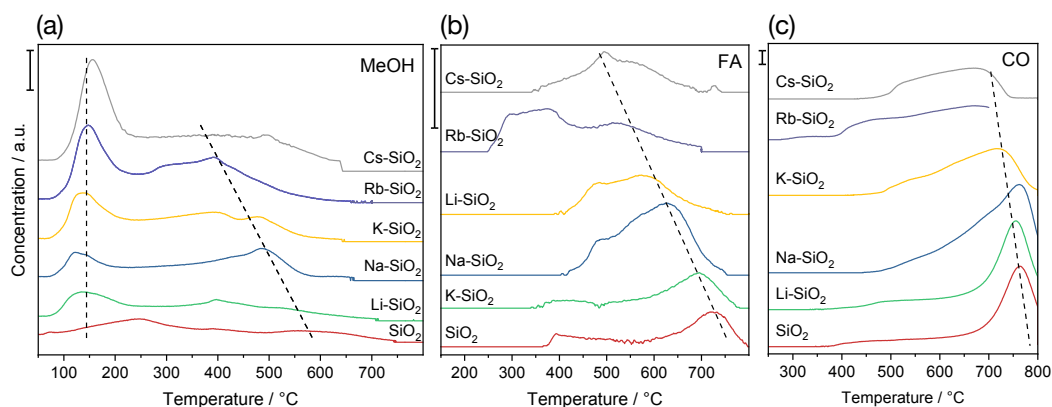


Figure 7-5. Methanol-TPD of the alkali metal grafted catalysts (M-SiO₂) with (a) MeOH, (b) FA and (c) CO. The bar on the left of each graph indicates 250 ppm.

It is difficult to attribute the cause of change in the desorbed products from the MeOH-TPD between the different catalysts in the M-SiO₂ series, as the various alkali metal hydroxide salts used with the same concentration during grafting resulted in very different M:Si ratio. Therefore, MeOH-TPD was also performed on the catalysts synthesised with a smaller metal loading for K, Rb and Cs (M-SiO₂-SL), and were compared to Na- and Li-SiO₂ (Figure 7-6). The desorption of methanol followed a similar trend, but the desorption peak for the strongly adsorbed methanol shifted less severely to lower temperature compared to the M-SiO₂ samples (Figure 7-6a). Oppositely, the desorption peaks of FA (620 °C) and CO (755 °C) were approximately the same for all samples in the M-SiO₂-SL series, unlike the M-SiO₂ series (Figure 7-6b and c). Considering that methanol was adsorbed on the alkali metals, and that partial or full dehydrogenation occurred independently of the presence of these metals, it was thus inferred that various sites appear to exist on the samples.

7.3.2 Catalytic activity

The performance of the M-SiO₂ series of catalysts was investigated for the catalytic dehydrogenation of methanol at 650 °C (Figure 7-7). Compared to the unmodified SiO₂, which

was relatively inactive, all grafted catalysts displayed an increased activity for the reaction. The conversion of methanol increased as the atomic weight and the concentration of the alkali metal increased (Figure 7-7a). The results for the selectivity towards FA displayed an opposite trend: the most selective candidates were SiO_2 and Li-SiO_2 , followed closely by Na-SiO_2 (Figure 7-7b). A large drop in FA selectivity was observed for larger alkali metals (i.e. K, Rb, Cs), falling from 0.63 to 0.04 when moving down from Na to K after 7.5 h on stream.

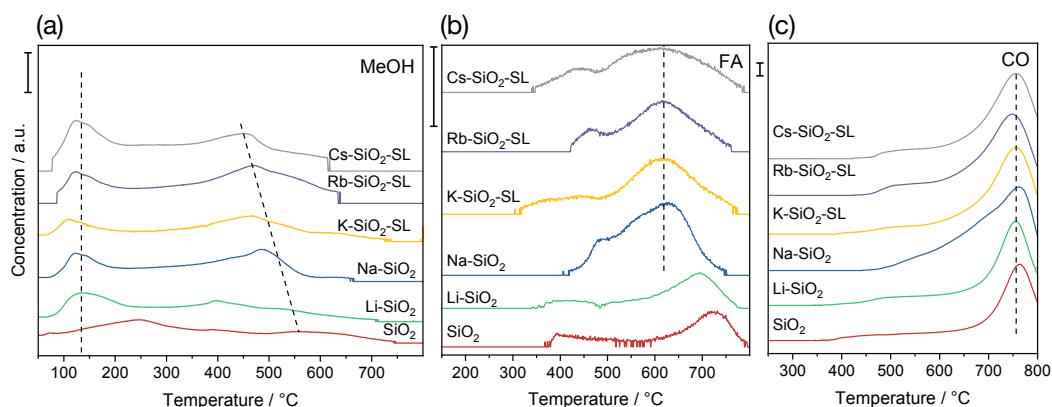


Figure 7-6. Comparison of the methanol-TPD of the alkali metal grafted catalysts ($\text{M-SiO}_2\text{-SL}$) with Na- and Li-SiO_2 , and SiO_2 . (a) MeOH, (b) FA and (c) CO. The bar on the left of each graph indicates 250 ppm.

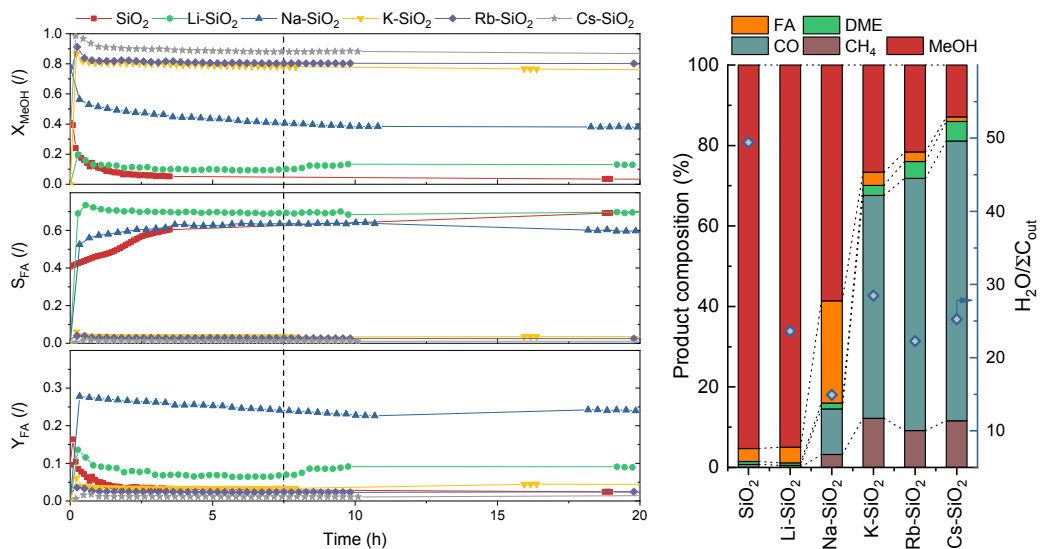


Figure 7-7. Performance of the alkali metal catalysts grafted with a 0.1 M MOH concentration (M-SiO_2) for methanol dehydrogenation at $650\text{ }^\circ\text{C}$ with (a) methanol conversion X_{MeOH} , (b) selectivity towards formaldehyde S_{FA} , (c) yield to formaldehyde Y_{FA} and (d) product stream composition following 7.5 h on stream (indicated by a dashed line).

Overall, the highest yield was obtained for Na-SiO_2 , with a value of 0.24 after 20 h on stream (Figure 7-7c). The second-best candidate was Li-SiO_2 due to its large FA selectivity, followed by the larger alkali metals grafted on silica. The composition of the product stream

after 7.5 h of reaction is displayed in Figure 7-7d. An increasing amount of methanol was converted to CO moving down the elements of group 1 of the periodic table. Complete dehydrogenation of methanol to CO was thus the main cause for the decrease in FA selectivity. Besides FA and CO, DME and CH₄ were also produced. DME production is a result of the dehydration of methanol and was thus accompanied by the production of water. At high temperature, DME experiences pyrolysis to methane, CO, and hydrocarbons as well as various coke precursors.^[276] These side-reactions, which severely diminished the selectivity towards FA, were observed to a higher extent for larger alkali metal cations grafted on silica. Na-SiO₂ yielded the lowest ratio of water per product generated, which is essential in the water-free methanol dehydrogenation.

Su et al. demonstrated that the selectivity towards FA decreases as the conversion reaches values above 80 %, which are close to the thermodynamic limit, due to the instability of FA at temperatures above 600 °C.^[253] It could be thus argued that the lower FA selectivity for K-, Rb- and Cs-SiO₂ is due to their high methanol conversions. Therefore, their performances were tested with an increased WHSV in order to reach lower conversion value and to compare the value of FA selectivity between these catalysts and Na-SiO₂, the best M-SiO₂ candidate (Figure 7-8). At 2.5 times higher WHSV, their methanol conversion was effectively reduced below 0.70 and their selectivity towards FA increased to a maximum of 0.10 for K-SiO₂, which was still much lower compared to the FA selectivity of Na-SiO₂ with a 2.5 times lower WHSV. The complete methanol dehydrogenation to CO was responsible for the decreased FA selectivity, as well as to the dehydration of methanol to DME and subsequent pyrolysis.

Considering that the metal loading and the nature of the alkali metal are changing simultaneously, it is difficult to attribute the change in activity to one or the other parameter using the catalytic test results from the M-SiO₂ catalysts series. Therefore, the same catalytic test was performed using the M-SiO₂-SL catalysts series, and the results were compared to Na-SiO₂ (Figure 7-9). The concentrations of alkali metal hydroxide used during grafting for the M-SiO₂ series were increasingly reduced going from K to Cs (see section 7.2.1). The characterization results showed that their M:Si molar ratios were comprised between 0.0082 (K-SiO₂-SL) and 0.0281 (Cs-SiO₂-SL). However, the basicity of Cs-SiO₂-SL

was considerably smaller than K-SiO₂-SL, with values of 4.76 and 11.96 $\mu\text{mol CO}_2 \cdot \text{g}_{\text{cat}}^{-1}$, respectively.

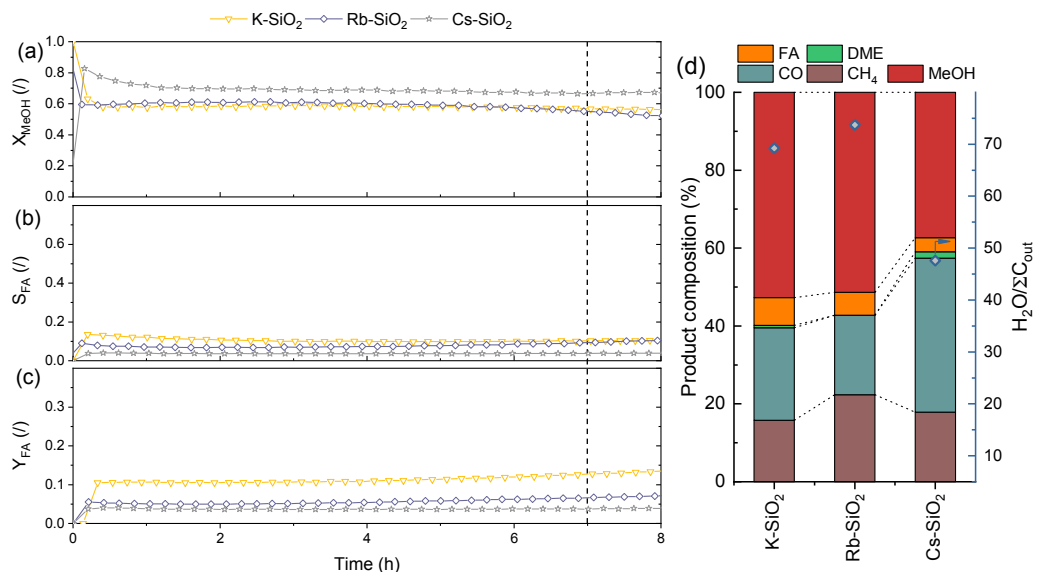


Figure 7-8. Performance of K-, Rb- and Cs-SiO₂ (WHSV: 26.75 h⁻¹) for methanol dehydrogenation at 650 °C with (a) methanol conversion X_{MeOH} , (b) selectivity towards formaldehyde S_{FA} , (c) yield to formaldehyde Y_{FA} and (d) product stream composition following 7 h on stream (indicated by a dashed line).

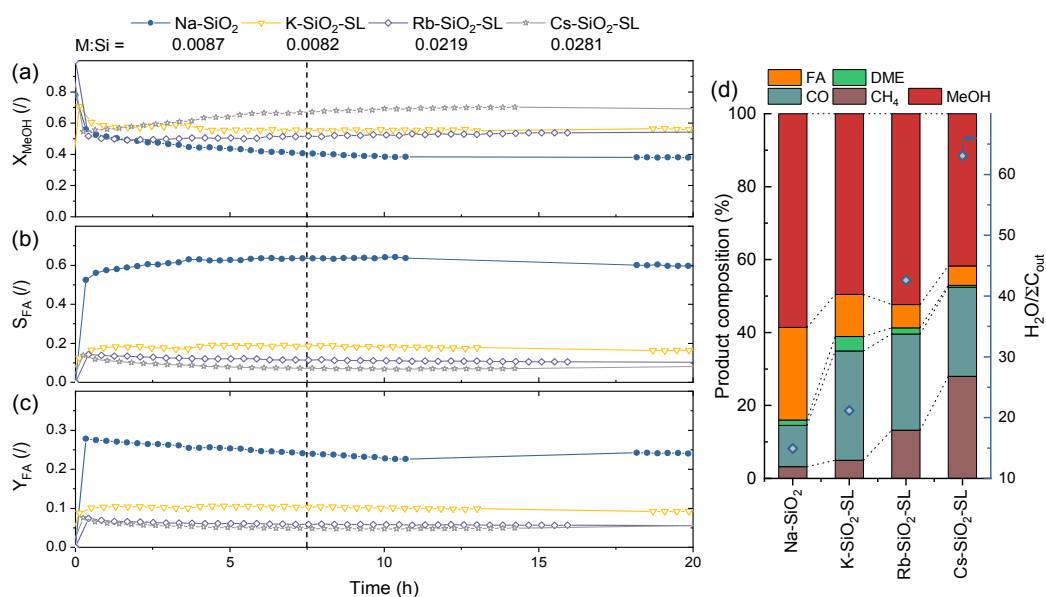


Figure 7-9. Performance of the M-SiO₂-SL series compared to Na-SiO₂. (a) Methanol conversion X_{MeOH} , (b) selectivity towards formaldehyde S_{FA} , (c) yield to formaldehyde Y_{FA} and (d) product stream composition following 3 h on stream (indicated by a dashed line).

As expected, the methanol conversion was reduced for each catalyst compared to their M-SiO₂ counterparts, and followed the following trend: Cs-SiO₂ > K-SiO₂ > Rb-SiO₂ > Na-SiO₂ (Figure 7-9a). Thus, it did not exactly respect the order of the group 1 elements. Yet, the selectivity towards FA became smaller moving down the group 1 elements (Figure

7-9b). Among the grafted alkali metals, the highest FA selectivity was reached for Na (0.64), largely above K (0.19), Rb (0.11) and Cs (0.07). Analysis of the product composition after 7.5 h revealed two trends (Figure 7-9d). First, there was a large increase in CO production at the expense of FA, moving down from Na to K, Rb and Cs. Second, increased production of CH₄ was observed with an increasing alkali metal cation size. This was also reflected in the ratio of water to product generated, which was the largest for Cs-SiO₂-SL (63), more than four times higher compared to Na-SiO₂ (15).

Considering that the deposition of Na on SiO₂ yielded the best performance among the various alkali metals, the grafting procedure was repeated using various NaOH concentrations in methanol in an attempt to optimize the performance of Na-SiO₂ (Figure 7-10). Overall, the conversion of methanol followed the order: Na-SiO₂-0.15M > Na-SiO₂-0.05M > Na-SiO₂. The reverse sequence was obtained for the selectivity towards FA. Overall, all three catalysts resulted in a very similar yield of FA, which demonstrated that the optimization potential of the catalyst with respect to metal loading was limited. The impact of the change of the solvent during grafting on the catalytic performance was also assessed by substituting methanol with isopropanol. It resulted in a much less stable catalyst, as Na-SiO₂-IPA underwent rapid deactivation to lower methanol conversion level compared to the other catalysts. Besides, during the first 3 h using this catalyst, methanol conversion was above 60 % and FA selectivity was below 0.25, which confirmed that a high metal loading preferentially leads to complete methanol dehydrogenation to CO, especially during the transition phase.

With increasing reaction time, all samples suffered from a gradual decline in FA concentrations. Catalyst deactivation was frequently reported for the catalytic dehydrogenation of methanol, and was attributed to catalyst coking or evaporation of the active phase.^[260] Depending on the cause of deactivation, the regeneration of the catalyst might be possible: evaporation of the active phase is an irreversible deactivation cause while surface coke is removable by oxidative treatments. Considering that coke was deposited, which was indicated by a change of colour of the powders from white to black after every run, the catalyst regeneration by oxidative treatment was investigated using Na-SiO₂ (Figure 7-11).

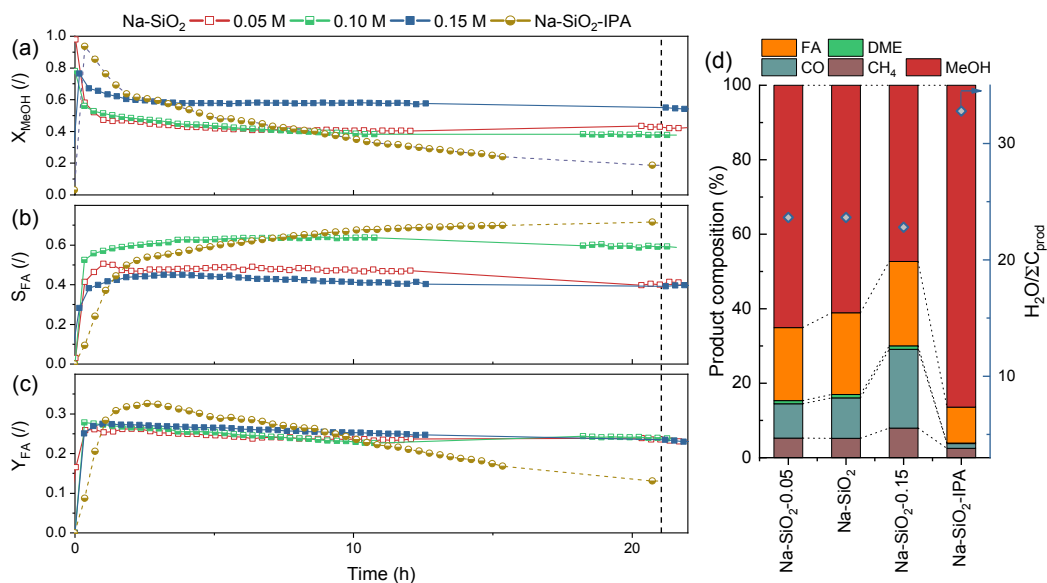


Figure 7-10. Performance of the Na-SiO₂ catalysts grafted with various concentrations of NaOH and with isopropanol (IPA) (a) methanol conversion X_{MeOH} , (b) selectivity towards FA S_{FA} , (c) yield to FA Y_{FA} and (d) product stream composition following 21 h on stream (indicated by a dashed line).

During run 1, the FA yield was reduced from a maximum of 0.26 to 0.13 after 45 h, due to a simultaneous reduction in FA selectivity and methanol conversion (Figure 7-11a). The loss in selectivity towards FA was the result of an increasing amount of CH₄ being produced at the expense of FA. Temperature-programmed oxidation (TPO) was performed to regenerate the catalyst activity, according to the protocol described in section 2.2.2 (Figure 7-11d and e). Regeneration by exposition to O₂ at high temperatures led to the release of CO₂ and CO, probably due to the removal of potential surface carbon deposit, as well as water. Similar results were obtained during the two oxidative treatments with the CO₂ peak observed at 575 °C.

After the oxidative treatments, the catalyst activity changed at the beginning of the reaction with a larger methanol conversion and a lower selectivity compared to the initial run, due to the emission of large amounts of CO (Figure 7-11b and c). The time necessary to reach the maximum FA selectivity increased from 1 to 10 h. It is likely that the exposition to O₂ at high temperatures changed the silica surface properties, which increased its activity for complete methanol dehydrogenation. However, the catalyst performance after the transition periods were similar during run 2 and 3 compared to the initial performance. The maximum FA yields reached during run 2 and 3 were slightly superior to the maximum

yield obtained during run 1, but the reason for this increase is not clear. Overall, the catalytic activity of Na-SiO₂ could be regenerated by oxidative treatments and its deactivation is linked to surface coking, which was confirmed by TPO.

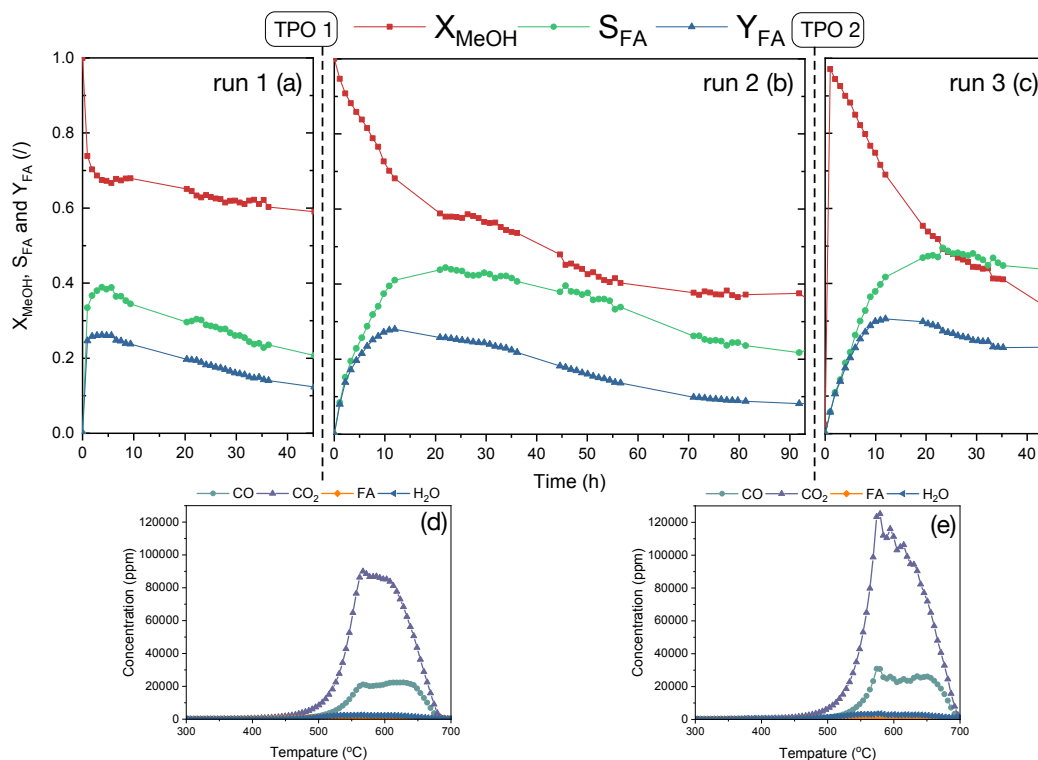


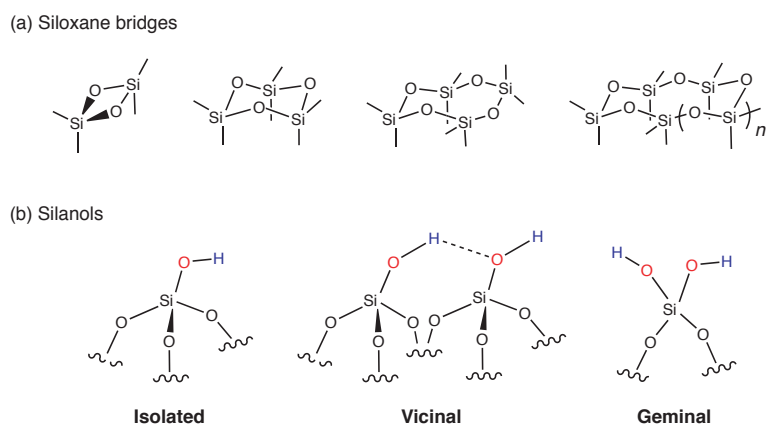
Figure 7-11. Na-SiO₂ performance at 650 °C and oxidative regenerations by O₂ treatments with methanol conversion X_{MeOH} , FA selectivity S_{FA} , and FA yield Y_{FA} . (a) Initial, (b) after the 1st O₂ treatment, (c) after the 2nd O₂ treatment, (d) 1st TPO, (e) 2nd TPO.

7.3.3 Structure-activity relationships

Grafting of alkali metals on amorphous silica radically changed the activity of the initial material for the catalytic dehydrogenation of methanol. Various catalysts were synthesized using different alkali hydroxide salts or by changing the salt concentration during the grafting procedure. In order to understand how the structure of these catalysts affected their activity, several aspects have to be discussed. First, the structure and chemistry of silica is briefly described. Then, the chemistry of alkali metals and their interaction with silica are outlined. Finally, the active sites for methanol dehydrogenation and a potential reaction mechanism are explored.

Amorphous silica is composed of tetrahedral SiO₄ units, yielding a complex surface made of rings, which comprise between six and twelve members (Scheme 7-2a).^[277] The silica surface also displays various types of hydroxyl groups, namely isolated, vicinal and germinal

silanols (Scheme 7-2b). Their concentrations vary depending on the conditions: higher temperatures lead to dehydroxylation of the surface. Vicinal hydroxyl groups condense above 150 °C, and at temperatures around 700 °C, the silica surface becomes mainly decorated with isolated silanols. Above 700 °C, the silica also restructures with a simultaneous loss of specific surface area and the formation of very reactive siloxane bridges such as the four-member ring. Considering the silica surface at a temperature of 650 °C, an oxygen atom in silica can thus essentially be present in an isolated silanol (Si-OH) or in a siloxane group (Si-O-Si).^[277]

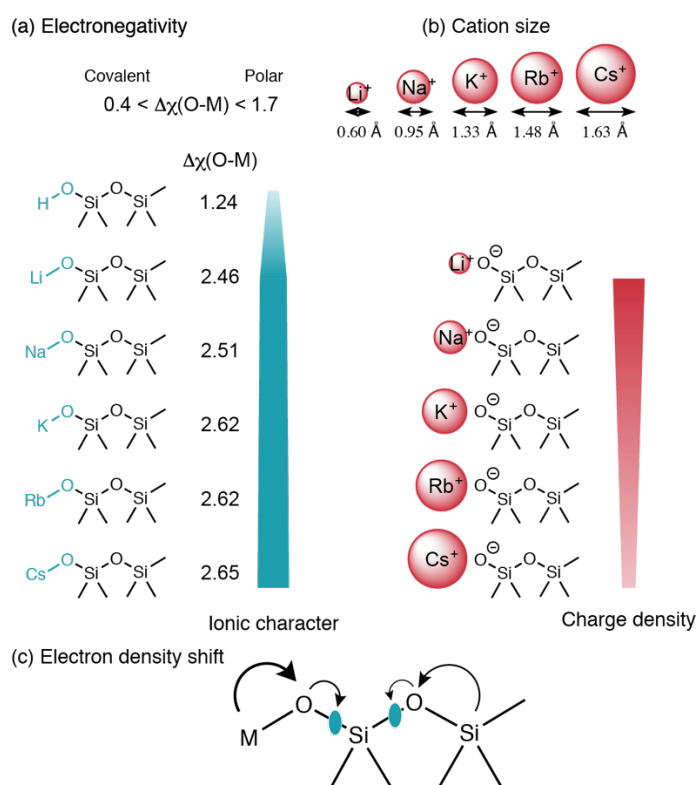


Scheme 7-2. Silica surface composed of (a) various cycle sizes of silanol bridges and (b) silanol groups.^[277]

Due to the heterogeneity of the surface of amorphous silica, other sites could result from the grafting of alkali metals. In an effort to simplify and discuss the structure-activity relationships, only the siloxane bridge and the alkali metal cations stabilized by a silanolate group are here considered as the active sites for the catalytic dehydrogenation of methanol. It is obvious that there could be other possibilities but they are beyond the scope of this study. The cation is considered to be directly coordinated with the silanolate generated by deprotonation during the grafting procedure. However, it is likely that various cation adsorption structures exist on the surface after grafting. It was reported that adsorption of Na on silica following a treatment with NaOH resulted in Na⁺ ions forming monodentate, bidentate and tridentate configurations, by coordination with silanolate, siloxane and hydroxyl groups.^[278] Likewise, the structure of the cationic sites in alkali metal-grafted USY zeolites was found to involve coordination with adjacent siloxane and silanol groups.^[272]

Assuming a successful grafting on the surface of silica by the method of Keller et al.,^[271] Scheme 7-3 illustrates how the metal-oxygen bond and the silica framework are influenced by the coordination with an alkali metal. The chemistry of alkali metals is determined by

their size and electronegativity. First, the Lewis basic character of the framework oxygen atoms augments with an increasing ionic character of the M-O bond, which changes greatly by substituting H with an alkali metal (Scheme 7-3a).^[279] The presence of an electropositive cation provokes an electron density shift on the surface of silica and increases the basicity of the adjacent oxygen bridge (Scheme 7-3c). The ionic character of the bond does not change greatly depending on the alkali metal: as the atomic weight increases, the bond polarity increases only slightly.

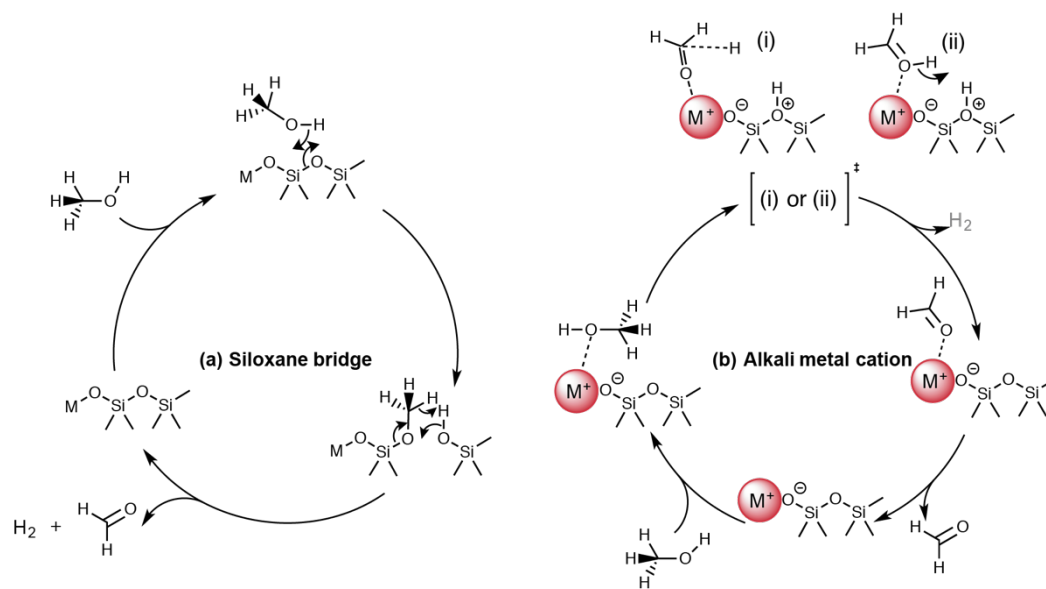


Scheme 7-3. Influence of the alkali metal cation on the M—O bond and the silica lattice by change in (a) the electronegativity, (b) the cation size, and (c) the electron density shift.

Oppositely, the metal cation size varies greatly moving down the group 1 elements of the periodic table (Scheme 7-3b): Cs^+ radius of 1.63 Å is more than twice the size of the radius of Li^+ (0.60 Å).^[280] The cation charge density varies proportionally to this change in size and the elements can thus be classified into two groups: high (Li, Na) and low (K, Rb, Cs) charge density cations.^[273] As observed during methanol-TDP, electrostatic interaction of methanol with the alkali metals is greatly affected by their charge density. The alkali metal ion can coordinate with the lone electron pair of methanol—more strongly to small ions due to their larger charge density. Generation of FA or CO was not affected by the nature of the ion. Therefore, it is more likely that they are the result of methanol bounding to

siloxane bridges adjacent to silanolates accommodating the alkali metal. The change in electronegativity moving down the group 1 elements is relatively small compared to the change in charge density.

We can suggest two reaction mechanisms that could occur on the surface of the alkali metal-grafted silica. As previously reported, the first one considers that the dehydrogenation occurs on the siloxane bridge and that the alkali metal acts as the promotor (Scheme 7-4a).^[275,281] As the electropositive alkali metal shifts the electron density closer to the adjacent oxygen, its basicity increases. It is then more likely to interact with methanol by hydrogen abstraction from the hydroxyl group. Methanol dissociative adsorption results in the opening of the oxygen bridge with the generation of a methoxy and a hydroxyl group. Then, a hydrogen from the methoxy group combines with the adsorbed H to liberate H₂ as well as FA.



Scheme 7-4. Suggested reaction mechanisms for the catalytic dehydrogenation of methanol involving (a) the siloxane bridge or (b) the alkali metal cation.

The second reaction mechanism assumes that the alkali metal cation is the active site (Scheme 7-4b). It was reported that methanol was converted to formaldehyde on alkali metal cation for the alkylation of toluene on alkali metal-exchange zeolite Y.^[282] Methanol interacts with the alkali metal cation via the lone electron pair of the oxygen and its adsorption results in the elongation of its hydroxyl bond. Two intermediates can be formed depending whether the first hydrogen is cleaved from the hydroxyl (i) or the methyl group (ii). Attempts to identify an intermediate have not yet been successful.^[282] Overall, FA is

produced following a two-step process, which could involve a carbocation: abstraction of the first hydrogen and recombination with the second to form H_2 . FA then interacts with the metal cation via its carbonyl group before desorbing.

The results of the catalysts characterization and the catalytic tests can provide additional insights into the reaction mechanism. Two parameters mainly influenced the activity of the catalysts during methanol catalytic dehydrogenation: the nature of the alkali metal and its concentration on the silica surface. First, a higher concentration of alkali metal on the silica surface resulted in a lower selectivity towards FA. When the surface displayed a higher concentration of alkali metals such as K, Rb, or Cs (M-SiO₂ series), a large fraction of methanol was converted to CO. Likewise, a lower FA selectivity was observed with Na grafted with the highest NaOH concentration (Na-SiO₂-0.015) or with isopropanol (Na-SiO₂-IPA). It can thus be inferred that the loss in selectivity towards FA with an increasing metal concentration on the silica surface occurs independently of the nature of the alkali metal.

The second parameter that severely influenced the performance of the catalysts was the nature of the alkali metal. For a range of M:Si molar ratios comprised between 0.0087 and 0.0281 (Li-SiO₂, Na-SiO₂ and the M-SiO₂-SL series), a large difference in FA selectivity was observed between high and low charge density cations and it followed the trend: Li > Na > K > Rb > Cs. These results can be compared to a study from Kang et al., who investigated the adsorption of methanol on alkali-cation-exchanged zeolite using DFT (excluding Li⁺). Despite being an amorphous network of silicon tetrahedra, silica can still be compared to a zeolite with keeping in mind the differences such as the crystallinity and the source of negative charge. Three important conclusions were derived from the results of their study (Table 7-2). First, the energy of adsorption of methanol calculated from the interaction of the lone electron pair of the O atom with the alkali metals ($E_{ads, MeOH}$) decreases from Na⁺ to Cs⁺. Second, the energy of activation to form formaldehyde and hydrogen (E_{act}) was the highest for Na⁺ and the lowest for Rb⁺. Finally, the energy of adsorption of formaldehyde via interaction of the carbonyl bond of formaldehyde with the alkali metal ($E_{ads, FA}$) was higher for larger alkali metals.

Table 7-2. Energy of adsorption of methanol ($E_{\text{ads, MeOH}}$) and formaldehyde ($E_{\text{ads, FA}}$) on an alkali-exchanged zeolite and energy of activation for methanol dehydrogenation to FA. Taken from Kang et al.^[282]

	$E_{\text{ads, MeOH}}$ ($\text{kJ} \cdot \text{mol}^{-1}$)	$E_{\text{ads, FA}}$ ($\text{kJ} \cdot \text{mol}^{-1}$)	E_{act} ($\text{kJ} \cdot \text{mol}^{-1}$)
Na	67	23	248
K	64	30	233
Rb	58	35	225
Cs	52	41	241

Parallels can be drawn between this DFT study and the results from our catalytic tests. The selectivity towards FA decreased with an increasing atomic number of the alkali metals. As FA is unstable at 650 °C, it is clear that it must desorb rapidly from the surface of the catalyst to prevent further decomposition to CO and H₂. Therefore, we suggest that the decrease in FA selectivity is due the higher energy of adsorption of FA on larger alkali metals. As a result, FA remains longer on the surface and has a higher probability to undergo complete dehydrogenation to CO. Consequently, it is more likely that the dehydrogenation of methanol occurs on the alkali metal than on the bridging hydroxyl. If the reaction were to occur on the siloxane bridge, the resulting FA would need to hop to the adjacent alkali metal, which is rather unlikely considering the $E_{\text{ads, FA}}$. If the reaction occurs on the alkali metal, the formaldehyde is already coordinated to it, which results in the observed FA selectivity.

Different parameters can be varied during the grafting methods to influence the deposition of alkali metals, and ultimately, the performance of the resulting catalyst. Increasing the metal hydroxide concentration resulted in a higher M:Si ratio but led to surface amorphization. Likewise, substituting methanol by isopropanol dramatically increased the surface loading with a simultaneous reduction of the specific surface area. Other parameters involved in the protocol should be studied more systematically in order to understand their influence on the resulting catalyst. The pre-treatment of silica is likely a key parameter that should change the interaction of the basic salt with the silica surface during the grafting procedure. Next, the time of contact as well as the temperature could probably affect the catalyst properties. Specifically, precisely controlling the flow during the cannula transfer of the basic solution to the pre-treated silica could also result in a more repeatable grafting procedure. Finally, other incorporation methods such as metal insertion or incipient wetness impregnation are also worth to be investigated.

7.4 Conclusions

Functionalization of a fumed silica surface with alkali metals was investigated for the catalytic dehydrogenation of methanol to formaldehyde (FA). Grafting in alcoholic media using alkali hydroxide salts was chosen as the method for catalysts preparation. The basicity of the salt was a crucial parameter: a higher metal loading was achieved using hydroxide salts with larger alkali metal cations. Varying the salt concentration and the solvent also affected the catalyst loading. Overall, a trade-off between metal loading and surface amorphization was observed, demonstrating the limit of alkali metal deposition on the silica surface using this method.

The resulting catalysts displayed an increased activity for the catalytic dehydrogenation of methanol. Two active sites were identified: the metal cation and the siloxane bridge adjacent to it. The varying electron density of the supported alkali metal cation severely affected the FA selectivity, which followed the trend: $\text{Li} > \text{Na} > \text{K} > \text{Rb} > \text{Cs}$. A large drop was observed between cations of high (Li, Na) and low charge density (K, Rb, Cs), which was triggered by the increasing adsorption energy of FA on a metal cation of a decreasing charge density. Considering these results, a reaction mechanism was suggested where methanol dehydrogenation occurs on the supported alkali metal through a two-step process. First, methanol interacts with the alkali metal via its oxygen lone electron pair, followed by the hydroxyl hydrogen abstraction by the adjacent oxygen bridge. Second, the hydrogen from the methoxy intermediate combines with the adsorbed H to form H_2 .

Na grafting on fumed silica resulted in a moderate metal loading, which yielded the best combination of high FA selectivity and moderate methanol conversion. Despite attempts to improve Na-SiO₂ performance, the grafting method could not yet be optimized further. However, alkali metal supported on silica are found to be promising candidates for the catalytic dehydrogenation of methanol to formaldehyde.

Chapter 8 Summary and outlook

8.1 Summary

The objective of this thesis was to advance research in the field of heterogeneous catalysis for the sustainable production of polyoxymethylene dimethyl ether (OME). The areas of focus were to establish structure-activity relationships, to develop more efficient catalysts and to explore new synthesis routes. This was accomplished through a combination of material synthesis, in-depth catalyst characterization, OME synthesis reactions and advanced spectroscopic methods.

In the first part of this work, we studied the influence of accessibility to the active sites in an H-ZSM-5 zeolite on the synthesis of OME from dimethoxymethane (OME₁) and trioxane (TRI). Introduction of an intracrystalline network of mesopores with alkaline treatments resulted in more performant catalysts, whereas surface passivation led to a severe drop in performance. By optimization of the desilication treatment, we achieved a 10 % increase of the initial selectivity for the products of interest (OME₃₋₅) and a two-fold increase in the initial reaction rate compared to the parent H-ZSM-5 zeolite. A trade-off existed between accessibility to the active sites provided by mesoporous surface area and overall acidity contained within the micropores, which restricted the possible catalytic improvement by desilication. Based on a kinetic study, we highlighted that OME synthesis on zeolites from TRI and OME₁ suffered from internal mass diffusion limitations and that introduction of mesopores increased the fraction of the reaction taking place within the micropores.

Based on these results, we explored the performance of montmorillonite clay, being a cheap and eco-friendly alternative to the usage of zeolites. After insertion of SnO₂ nanoparticles between the clay layers, the resulting material, tin-montmorillonite, possessed both micro- and mesopores, as well as a combination of Brønsted and Lewis acidity. Tin-montmorillonite showed similar catalytic performance as acidic resins for OME synthesis from OME₁ and TRI. We investigated the nature of its acidity, which was attributed to a combination

of bridging hydroxyl groups resulting from SnO₂ crystallization and undercoordinated Sn surface sites.

In the second part of this work, we systematically studied how the characteristics of both reactants and the catalysts can influence both the reaction products and the reaction kinetics. Using a series of Beta zeolites with a varying amount of Brønsted and Lewis acidity, we demonstrated that incorporation of a small concentration of tetrahedral Sn in the zeolite framework resulted in a large turnover frequency increase. This synergy between Brønsted and Lewis acidity was ascribed to a favored OME growth on Sn^{IV} sites via activation of formaldehyde (FA), produced *in situ* from the decomposition of TRI on bridging hydroxyl groups. This synergistic effect was detected using the anhydrous synthesis route, but not for the reaction of methanol and FA, which involved the production of water.

Next, we studied the inhibition of the reaction kinetics by water for the synthesis of OME from TRI and OME₁ over an H-Beta zeolite. We highlighted that water, present as an impurity in OME₁, severely affected the reaction kinetics at concentrations as low as 0.21 wt %. We demonstrated that the main OME growth mechanism shifted from direct TRI insertion to FA incorporation in OME, as the level of water in OME₁ increased. Through ATR infrared spectroscopy, we showed that the presence of water perturbed the adsorption of TRI on the zeolite active sites. Unable to bind to bridging hydroxyl groups, TRI was not available for all OME growth mechanisms.

Lastly, we investigated the water-free catalytic dehydrogenation of methanol to formaldehyde as a potential source of oxymethylene groups for OME growth. Grafting on silica in methanol was selected as the method of choice to study the activity of alkali metals for methanol catalytic dehydrogenation. Presence of alkali metals on the silica surface boosted its catalytic activity. A large gap in selectivity towards FA was observed between ions with a high (i.e. Li, Na) and low charge density (i.e. K, Rb, Cs). Na yielded the best combination of moderate conversion and high selectivity, but the grafting method was not further optimized. A reaction mechanism was suggested where methanol dehydrogenation occurs on the alkali metal supported by the silanolate group.

8.2 Outlook

The work presented in this thesis contributed to advancing knowledge on heterogeneous catalysis for the production of OME. Based on the results of this thesis, important catalyst features, such as porosity or type of acidity, have been highlighted and should be considered when developing catalysts or designing production processes for OME synthesis. However, significant improvements are still required for the OME technology to reach consumer's car sustainably and cost-effectively.

More energy-efficient processes will require alternatives to the usage of TRI as the oxymethylene source. If TRI cannot be selectively inserted into OME₁ without TRI dissociation and OME transacetalization, the production of neat OME₃₋₅ will always require large downstream separation efforts. In this work, we did not succeed at notably influencing the selectivity towards OME₃₋₅ for OME synthesis from TRI and OME₁. Usage of mesoporous H-ZSM-5 as well as almost anhydrous OME₁ increased slightly the selectivity towards the products of interest, but to a currently far too low level to justify the major exergy loss that the production of TRI implies.

Direct insertion of molecular formaldehyde into OME₁ could alleviate this problem and the non-oxidative catalytic dehydrogenation of methanol is an appealing alternative to TRI utilization. In Chapter 7, we demonstrated that alkali metals grafted on silica have the potential to catalyze this reaction. Despite having reasonable performance, the inherent challenges of the reaction taking place at such a high temperature could not be overcome by our best candidate. Methanol dehydration to dimethyl ether and the subsequent coking of the catalysts could not yet be prevented. In light with the results from Chapter 6 that highlights the kinetic inhibition of OME synthesis by water, it could be questioned whether the reaction stream from methanol catalytic dehydrogenation is an efficient source of oxymethylene groups due to the presence of water. Additional research should thus be performed on the influence of water on the kinetics of molecular FA incorporation for OME growth. Nevertheless, new methods and supports should be investigated to leverage alkali metals activity to obtain a stable catalyst and a water-free formaldehyde stream.

In conclusion, the OME technology is still in the early stages of research but answers an important need for the future of mobility. Its predicted production efficiency being still

slightly lower than Fisher-Tropsch Diesel or methanol-to-gasoline products, research should focus on exploring new catalytic routes. Among them, certain are currently being investigated, and others are still at the stage of research ideas. Selective direct gas-phase oxidation of methanol to OME₁ has demonstrated its potential to significantly reduce the separation energy and the equipment costs currently required for the anhydrous production route. Eventually, reductive synthesis from methanol, CO₂ and H₂ to OME would result in further efficiency gain. Despite promising results, these two alternatives are currently unable to produce reasonable amounts of OME larger than OME₁. Ultimately, direct synthesis of OME from syngas is an interesting concept whose feasibility could be investigated.

References

- [1] Ö. Andersson, in *Handb. Combust. Vol.3 Gaseous Liq. Fuels Ed.*, **2010**, pp. 415–440.
- [2] *IARC Monogr.* **2014**, *105*, 451–467.
- [3] World Energy Council, *Global Transport Scenarios 2050*, **2011**.
- [4] European Parliament, *Off. J. Eur. Union* **2009**, *140*, 16–62.
- [5] W. Maus, E. Jacob, R. Brück, P. Hirth, *MTZ Worldw.* **2012**, *73*, 4–11.
- [6] R.-J. Zhu, X.-B. Wang, H. Miao, Z.-H. Huang, *J. Automob. Eng.* **2010**, *224*, 521–531.
- [7] H. Liu, Z. Wang, J. Wang, X. He, Y. Zheng, Q. Tang, J. Wang, *Energy* **2015**, *88*, 793–800.
- [8] B. Lump, D. Rothen, C. Pastötter, R. Lämmermann, E. Jacob, *MTZ* **2011**, *72*, 34–39.
- [9] S. E. Iannuzzi, C. Barro, K. Boulouchos, J. Burger, *Fuel* **2016**, *167*, 49–59.
- [10] L. Lautenschütz, D. Oestreich, P. Seidenspinner, U. Arnold, E. Dinjus, J. Sauer, *Fuel* **2016**, *173*, 129–137.
- [11] A. Feiling, M. Münz, C. Beidl, *ATZextra Worldw.* **2016**, *21*, 16–21.
- [12] H. Liu, Z. Wang, J. Zhang, J. Wang, S. Shuai, *Appl. Energy* **2015**, *185*, 1393–1402.
- [13] H. Liu, Z. Wang, J. Wang, X. He, *Energy* **2016**, *97*, 105–112.
- [14] X. Zhang, A. Kumar, U. Arnold, J. Sauer, *Energy Procedia* **2014**, *61*, 1921–1924.
- [15] N. Mahbub, A. O. Oyedun, A. Kumar, D. Oestreich, U. Arnold, J. Sauer, *J. Clean. Prod.* **2017**, *165*, 1249–1262.
- [16] M. Bertau, H. Offermanns, L. Plass, F. Schmidt, H.-J. Wernicke, in *Methanol Basic Chem. Energy Feed. Futur.*, Springer Berlin Heidelberg, Berlin, Heidelberg, **2014**, pp. 51–301.
- [17] J. Burger, H. Hasse, *Chem. Eng. Sci.* **2013**, *99*, 118–126.
- [18] J. Burger, E. Ströfer, H. Hasse, *Chem. Eng. Res. Des.* **2013**, *91*, 2648–2662.
- [19] M. Descudé, *C. R. Hebd. Seances Acad. Sci.* **1904**, *138*, 1703–1705.
- [20] H. Staudinger, M. Ltithy, *Helv. Chim. Acta* **1925**, *8*, 41–64.
- [21] M. Haubs, K. Kurz, G. Sextro, *Ullmann's Encycl. Ind. Chem.* **2012**, 1–16.
- [22] R. H. Boyd, *J. Polym. Sci.* **1961**, *50*, 133–141.
- [23] G. P. Hagen, M. J. Spangler, *Preparation Of Polyoxymethylene Dimethyl Ethers By Catalytic Conversion Of Dimethyl Ether With Formaldehyde Formed By Oxy Dehydrogenation Of Dimethyl Ether*, **1999**, 5,959,156.

- [24] G. P. Hagen, M. J. Spangler, *Preparation Of Polyoxymethylene Dimethyl Ethers By Catalytic Conversion Of Methanol With Formaldehyde Formed By Oxy-Dehydrogenation Of Dimethyl Ether*, **2000**, 6,160,174.
- [25] G. P. Hagen, M. J. Spangler, *Preparation Of Polyoxymethylene Dimethyl Ethers By Catalytic Conversion Of Dimethyl Ether With Formaldehyde Formed By Oxy-Dehydrogenation Of Dimethyl Ether*, **2000**, 6,160,186.
- [26] G. P. Hagen, M. J. Spangler, *Preparation Of Polyoxymethylene Dimethyl Ethers By Catalytic Conversion Of Dimethyl Ether With Formaldehyde Formed By Oxidation Of Methanol*, **2000**, 6,166,266.
- [27] G. P. Hagen, M. J. Spangler, *Preparation Of Polyoxymethylene Dimethyl Ethers By Acid-Activated Catalytic Conversion Of Methanol With Formaldehyde Formed By Oxy-Dehydrogenation Of Dimethyl Ether*, **2001**, US 6,265,528 B1.
- [28] G. P. Hagen, M. J. Spangler, *Preparation Of Polyoxymethylene Dimethyl Ethers By Catalytic Conversion Of Formaldehyde Formed By Oxidation Of Dimethyl Ether*, **2002**, US 6,392,102 B1.
- [29] G. P. Hagen, M. J. Spangler, *Preparation Of Polyoxymethylene Dimethyl Ethers By Acid-Activated Catalytic Conversion Of Methanol With Formaldehyde Formed By Dehydrogenation Of Methanol*, **2002**, US 6 437 195 B2.
- [30] G. P. Hagen, M. J. Spangler, *Preparation Of Polyoxymethylene Dimethyl Ethers By Catalytic Conversion Of Formaldehyde Formed By Oxy-Dehydrogenation Of Dimethyl Ether*, **2003**, US 2003/0171534 A1.
- [31] H. Schelling, E. Stroefler, R. Pinkos, A. Haunert, G.-D. Tebben, H. Hasse, S. Blagov, *Method For Producing Polyoxymethylene Dimethyl Ethers*, **2007**, US 2007/0260094 A1.
- [32] E. Stroefler, H. Hasse, S. Blagov, *Process For Preparing Polyoxymethylene Dimethyl Ethers From Methanol And Formaldehyde*, **2010**, US 7,700,809 B2.
- [33] E. Stroefler, H. Hasse, S. Blagov, *Method For Producing Polyoxymethylene Dimethyl Ethers From Methanol And Formaldehyde*, **2010**, US 7,671,240 B2.
- [34] E. Stroefler, H. Hasse, S. Blagov, *Method For The Production Of Polyoxymethylene Dialkyl Ethers From Trioxan And Dialkylethers*, **2011**, US 7,999,140 B2.
- [35] R. Patrini, M. Marchionna, *A Process for the Selective Production of Dialkyl-Polyformals*, **2005**, EP 1 505 049 A1.
- [36] P. Yu, J. Liu, H. Rong, C. Shi, Q. Fu, J. Wang, W. Zhang, X. Zhou, *Process of Oxidative Conversion of Methanol*, **2010**, EP 2 228 359 A1.
- [37] J. Wang, Y. Zheng, S. Wang, T. Wang, S. Chen, C. Zhu, *Method For Producing Polyoxymethylene Dimethyl Ethers*, **2015**, US Patent US2015/0291722.
- [38] J. Wang, Q. Tang, S. Wang, T. Wang, S. Chen, Y. Wang, *Fluidized Bed Reactor and Method for Preparing Polyoxymethylene Dimethyl Ethers from Dimetroxymethane and Paraformaldehyde*, **2015**, US Patent US2015/0273426 A1.
- [39] M. Li, Y. Long, Z. Deng, H. Zhang, X. Yang, G. Wang, *Catal. Commun.* **2015**, 68, 46–48.
- [40] Y. Zheng, Q. Tang, T. Wang, J. Wang, *Chem. Eng. Sci.* **2015**, 134, 758–766.
- [41] C. Brünglinghaus, 'Projekt OME erforscht schadstoffarme Kraftstoffe', **2016**.
- [42] J. Burger, T. Dittmer, in *3rd Methanol Technol. Policy Commer. Congr.*, **2016**.

- [43] G. A. Olah, A. Goepfert, G. K. S. Prakash, *Beyond Oil and Gas: The Methanol Economy*, Wiley-VCH, **2009**.
- [44] Y. Ren, Z. Huang, H. Miao, Y. Di, D. Jiang, K. Zeng, B. Liu, X. Wang, *Fuel* **2008**, *87*, 2691–2697.
- [45] C. Arcoumanis, C. Bae, R. Crookes, E. Kinoshita, *Fuel* **2008**, *87*, 1014–1030.
- [46] J. Burger, M. Siegert, E. Ströfer, H. Hasse, *Fuel* **2010**, *89*, 3315–3319.
- [47] D. Y. Han, Z. B. Cao, W. W. Shi, X. D. Deng, T. Y. Yang, *Energy Sources, Part A Recover. Util. Environ. Eff.* **2016**, *38*, 2687–2692.
- [48] T. Wilharm, E. Jacob, in *3rd Metanol Technol. Policy Commer. Congr.*, **2016**.
- [49] Ö. Andersson, P. C. Miles, in *Encycl. Automot. Eng.* (Ed.: L. JohnWiley & Sons), John Wiley & Sons, Ltd, Chichester, UK, **2014**, pp. 1–36.
- [50] G. Shi, J. Miao, G. Wang, J. Su, H. Liu, *Asian J. Chem.* **2015**, *27*, 2149–2153.
- [51] M. Härtl, K. Gaukel, D. Pélerin, G. Wachtmeister, *MTZ Worldw.* **2017**, *2*, 52–58.
- [52] P. Haltenort, L. Lautenschütz, U. Arnold, J. Sauer, *Top. Catal.* **2019**, *62*, 551–559.
- [53] W. Maus, E. Jacob, M. Härtl, P. Seidenspinner, G. Wachtmeister, in *Internat. Wiener Mot.*, Düsseldorf, **2014**, pp. 325–347.
- [54] E. Jacob, W. Maus, *MTZ Worldw.* **2017**, *78*, 52–57.
- [55] L. Lahaye, G. Prado, *Soot in Combustion Systems and Its Toxic Properties: (Proceedings of a NATO Workshop; Le Bischenberg, Obernai, August 31-September 3, 1981)*, Springer, Obernai, **1981**.
- [56] M. Härtl, P. Seidenspinner, E. Jacob, G. Wachtmeister, *Fuel* **2015**, *153*, 328–335.
- [57] J.-O. Drunsel, M. Renner, H. Hasse, *Chem. Eng. Res. Des.* **2012**, *90*, 696–703.
- [58] E. Jacob, *Fuel For Compression-Ignition Engines Based On Monooxymethylene Dimethylether*, **2014**, US 2014/0223807 A1.
- [59] T. Grützner, H. Hasse, N. Lang, M. Siegert, E. Ströfer, *Chem. Eng. Sci.* **2007**, *62*, 5613–5620.
- [60] G. Reuss, W. Disteldorf, A. O. Gamer, A. Hilt, *Ullmann's Encycl. Ind. Chem.* **2012**, 444–487.
- [61] I. Hahnenstein, H. Hasse, C. G. Kreiter, G. Maurer, *Ind. Eng. Chem* **1994**, *33*, 1022–1029.
- [62] I. Hahnenstein, M. Albert, H. Hasse, C. G. Kreiter, G. Maurer, *Ind. Eng. Chem. Res.* **1995**, *34*, 440–450.
- [63] M. Maiwald, H. H. Fischer, M. Ott, R. Peschla, C. Kuhnert, C. G. Kreiter, G. Maurer, H. Hasse, *Ind. Eng. Chem. Res.* **2003**, *42*, 259–266.
- [64] J. Zhang, D. Fang, D. Liu, *Ind. Eng. Chem. Res.* **2014**, *53*, 13589–13597.
- [65] J. Zhang, M. Shi, D. Fang, D. Liu, *React. Kinet. Mech. Catal.* **2014**, *113*, 459–470.
- [66] N. Schmitz, F. Homborg, J. Berje, J. Burger, H. Hasse, *Ind. Eng. Chem. Res.* **2015**, *54*, 6409–6417.
- [67] N. Schmitz, J. Burger, H. Hasse, *Ind. Eng. Chem. Res.* **2015**, *54*, 12553–12560.

- [68] A. Peter, S. M. Fehr, V. Dybbert, D. Himmel, I. Lindner, E. Jacob, M. Ouda, A. Schaadt, R. J. White, H. Scherer, et al., *Angew. Chemie - Int. Ed.* **2018**, *57*, 9461–9464.
- [69] Q. Zhao, H. Wang, Z. Qin, Z. Wu, J. Wu, W. Fan, J. Wang, *J. Fuel Chem. Technol.* **2011**, *39*, 918–923.
- [70] H. Li, H. Song, L. Chen, C. Xia, *Appl. Catal. B Environ.* **2015**, *165*, 466–476.
- [71] X. Deng, Z. Cao, X. Li, D. Han, R. Zhao, Y. Li, *Synth. React. Inorganic, Met. Nano-Metal Chem.* **2015**, *46*, 1842–1847.
- [72] X. Fang, J. Chen, L. Ye, H. Lin, Y. Yuan, *Sci. China Chem.* **2015**, *58*, 131–138.
- [73] R. Wang, Z. Wu, Z. Qin, C. Chen, H. Zhu, J. Wu, G. Chen, W. Fan, J. Wang, *Catal. Sci. Technol.* **2016**, *6*, 993–997.
- [74] J. Burger, E. Ströfer, H. Hasse, *Ind. Eng. Chem. Res.* **2012**, *51*, 12751–12761.
- [75] L. Wang, W.-T. Wu, T. Chen, Q. Chen, M.-Y. He, *Chem. Eng. Commun.* **2014**, *201*, 709–717.
- [76] J. Zhang, B. Tang, D. Fang, D. Liu, *Asian J. Chem.* **2014**, *3*, 70–73.
- [77] Q. Wu, M. Wang, Y. Hao, H. Li, Y. Zhao, Q. Jiao, *Ind. Eng. Chem. Res.* **2014**, *53*, 16254–16260.
- [78] Y. Wu, Z. Li, C. Xia, *Ind. Eng. Chem. Res.* **2016**, *55*, 1859–1865.
- [79] W. H. Fu, X. M. Liang, H. Zhang, Y. M. Wang, M. Y. He, *Chem. Commun.* **2015**, *51*, 1449–1452.
- [80] H. Li, H. Song, F. Zhao, L. Chen, C. Xia, *J. Energy Chem.* **2015**, *24*, 239–244.
- [81] J. Wu, H. Zhu, Z. Wu, Z. Qin, L. Yan, B. Du, W. Fan, J. Wang, *Green Chem.* **2015**, *17*, 2353–2357.
- [82] P. Haltenort, K. Hackbarth, D. Oestreich, L. Lautenschütz, U. Arnold, J. Sauer, *Catal. Commun.* **2018**, *109*, 80–84.
- [83] D. Oestreich, L. Lautenschütz, U. Arnold, J. Sauer, *Chem. Eng. Sci.* **2017**, *163*, 92–104.
- [84] M. Arvidson, M. E. Fakley, M. S. Spencer, *J. Mol. Catal.* **1987**, *41*, 391–393.
- [85] Y. Zheng, Q. Tang, T. Wang, Y. Liao, J. Wang, *Chem. Eng. Technol.* **2013**, *36*, 1951–1956.
- [86] Y. Zheng, Q. Tang, T. Wang, J. Wang, *Chem. Eng. J.* **2015**, *278*, 183–189.
- [87] X. Y. Li, H. Bin Yu, Y. M. Sun, H. B. Wang, T. Guo, Y. Le Sui, J. Miao, X. J. Zeng, S. P. Li, *Appl. Mech. Mater.* **2013**, *448–453*, 2969–2973.
- [88] Q. Zhang, Y. Tan, G. Liu, J. Zhang, Y. Han, *Green Chem.* **2014**, *16*, 4708–4715.
- [89] Q. Zhang, W. Wang, Z. Zhang, Y. Han, Y. Tan, *Catalysts* **2016**, *6*, 43.
- [90] N. Schmitz, A. Friebel, E. von Harbou, J. Burger, H. Hasse, *Fluid Phase Equilib.* **2016**, *425*, 127–135.
- [91] H. Liu, E. Iglesia, *J. Phys. Chem. B* **2003**, *107*, 10840–10847.
- [92] X. Lu, Z. Qin, M. Dong, H. Zhu, G. Wang, Y. Zhao, W. Fan, J. G. Wang, *Fuel* **2011**, *90*, 1335–1339.

- [93] J. Tatibouët, H. Lauron-pernot, *J. Mol. Catal. A Chem.* **2001**, *171*, 205–216.
- [94] H. Liu, E. Iglesia, *J. Phys. Chem. B* **2005**, *109*, 2155–2163.
- [95] Q. Zhang, Y. Tan, C. Yang, Y. Han, *J. Mol. Catal. A Chem.* **2007**, *263*, 149–155.
- [96] K. Thavornprasert, M. Capron, L. Jalowiecki-Duhamel, F. Dumeignil, *Catal. Sci. Technol.* **2016**, *6*, 958–970.
- [97] Q. Zhang, Y. Tan, G. Liu, C. Yang, Y. Han, *J. Ind. Eng. Chem.* **2014**, *20*, 1869–1874.
- [98] J. Faye, M. Capron, A. Takahashi, S. Paul, B. Katryniok, T. Fujitani, F. Dumeignil, *Energy Sci. Eng.* **2014**, *3*, 115–125.
- [99] K. Thavornprasert, M. Capron, L. Jalowiecki-Duhamel, O. Gardoll, M. Trentesaux, A. S. Mamede, G. Fang, J. Faye, N. Touati, H. Vezin, et al., *Appl. Catal. B Environ.* **2014**, *145*, 126–135.
- [100] L. Lautenschütz, Neue Erkenntnisse in Der Syntheseoptimierung Oligomerer Oxymethylen dimethylether Aus Dimethoxymethan Und Trioxan, **2015**.
- [101] D. S. Moulton, D. W. Nageli, *Diesel Fuel Having Improved Qualities And Method Of Forming*, **1998**, 5,746,785.
- [102] W. F. Gresham, Lindamere, E. Brooks, Richard, E. Terrace, *Preparation of Polyformals*, **1948**, 2,449,469.
- [103] J. Chen, Z. Tang, C. Xia, X. Zhang, Z. Li, *Method For Preparing Polymethoxymethylal*, **2009**, US Patent US 7,560,599 B2.
- [104] J. Chen, *Method For Synthesizing Polyoxymethylene Dimethyl Ethers By Ionic Liquid Catalysis*, **2010**, US 2010/0056830 A1.
- [105] J. Chen, H. Song, C. Xia, X. Zhang, Z. Tang, *Method For Synthesizing Polyoxymethylene Dimethyl Ethers By Ionic Liquid Catalysis*, **2013**, US Patent US 8,344,183 B2.
- [106] C. Xia, H. Song, J. Chen, H. Song, Z. Li, *Method For Preparing Polyoxymethylene Dimethyl Ethers By Acetalation Reaction Of Formaldehyde With Methanol*, **2011**, US Patent US 2011/0313202 A1.
- [107] C. Xia, H. Song, J. Chen, F. Jin, M. Kang, *System And Method For Continuously Producing Polyoxymethylene Dimethyl Ethers*, **2014**, US Patent US 2014/0114092 A1.
- [108] Q. Wu, M. Wang, Y. Hao, H. Li, Y. Zhao, Q. Jiao, *RSC Adv.* **2015**, *53*, 16254–16260.
- [109] Y. Zhao, Z. Xu, H. Chen, Y. Fu, J. Shen, *J. Energy Chem.* **2013**, *22*, 833–836.
- [110] L. Lautenschütz, D. Oestreich, P. Haltenort, U. Arnold, E. Dinjus, J. Sauer, *Fuel Process. Technol.* **2017**, *165*, 27–33.
- [111] H. Y. Shang, Z. Hong, C. Li, X. Feng, Y. Han, Z. Xue, *Continuous Reaction Device for Synthesizing Polyoxymethylene Dimethyl Ethers*, **2016**, US 2016/0185902A1.
- [112] Y. Zhao, H. Wang, Y. Zhao, J. Shen, *Catal. Commun.* **2010**, *11*, 824–828.
- [113] J. Gornay, X. Sécordel, G. Tesquet, B. de Ménorval, S. Cristol, P. Fongarland, M. Capron, L. Duhamel, E. Payen, J.-L. Dubois, et al., *Green Chem.* **2010**, *12*, 1722–1725.
- [114] F. Wang, G. Zhu, Z. Li, F. Zhao, C. Xia, J. Chen, *J. Mol. Catal. A Chem.* **2015**, *408*, 228–236.

- [115] T. J. Goncalves, U. Arnold, P. N. Plessow, F. Studt, *ACS Catal.* **2017**, *7*, 3615–3621.
- [116] T. J. Goncalves, P. N. Plessow, F. Studt, *ChemCatChem* **2019**, *11*, 1949–1954.
- [117] P. Cheung, H. Liu, E. Iglesia, *J. Phys. Chem. B* **2004**, *108*, 18650–18658.
- [118] A. de Klerk, in *Fischer-Tropsch Refin.*, Wiley-VCH, **2011**, pp. 78–80.
- [119] N. Schmitz, J. Burger, E. Ströfer, H. Hasse, *Fuel* **2016**, *185*, 67–72.
- [120] A. Linzenich, K. Arning, D. Bongartz, A. Mitsos, M. Ziefle, *Appl. Energy* **2019**, *249*, 222–236.
- [121] A. O. Oyedun, A. Kumar, D. Oestreich, U. Arnold, J. Sauer, *Biofuels, Bioprod. Biorefining* **2018**, *12*, 694–710.
- [122] C. J. Baranowski, A. M. Bahmanpour, F. Héroguel, J. S. Luterbacher, O. Kröcher, *Catal. Sci. Technol.* **2019**, *9*, 366–376.
- [123] C. J. Baranowski, A. M. Bahmanpour, F. Héroguel, J. S. Luterbacher, O. Kröcher, *ChemCatChem* **2019**, *11*, 3010–3021.
- [124] C. J. Baranowski, M. Roger, A. M. Bahmanpour, O. Kröcher, *ChemSusChem* **2019**, *12*, 4421–4431.
- [125] C. J. Baranowski, T. Fovanna, M. Roger, J. McCaig, M. Signorile, A. M. Bahmanpour, D. Ferri, O. Kröcher, *Manuscr. Prep.* **2019**.
- [126] C. J. Baranowski, J. Brandon, A. M. Bahmanpour, O. Kröcher, *Manuscr. Prep.* **2019**.
- [127] J. T. Scanlon, D. E. Willis, *J. Chromatogr. Sci.* **1985**, *23*, 333–340.
- [128] D. Ferri, T. Bürgi, A. Baiker, *Helv. Chim. Acta* **2002**, *85*, 3639–3656.
- [129] D. Baurecht, U. P. Fringeli, *Rev. Sci. Instrum.* **2001**, *72*, 3782–3792.
- [130] R. M. Milton, in *Zeolite Synth.*, **1989**, pp. 1–10.
- [131] V. Blay, B. Louis, R. Miravalles, T. Yokoi, K. A. Peccatiello, M. Clough, B. Yilmaz, *ACS Catal.* **2017**, *7*, 6542–6566.
- [132] W. W. Kaeding, C. Chu, L. B. Young, S. A. Butter, *J. Catal.* **1981**, *69*, 392–398.
- [133] W. Q. Xu, Y. G. Yin, S. L. Suib, J. C. Edwards, C. L. O’Young, *J. Phys. Chem.* **1995**, *99*, 9443–9451.
- [134] J. Kärger, D. M. Ruthven, in *Handb. Zeolite Sci. Technol.*, **1992**, pp. 329–366.
- [135] J. Pérez-Ramírez, C. H. Christensen, K. Egeblad, C. H. Christensen, J. C. Groen, *Chem. Soc. Rev.* **2008**, *37*, 2530–2542.
- [136] G. Bellussi, G. Pazzuconi, C. Perego, G. Girotti, G. Terzoni, *J. Catal.* **1995**, *157*, 227–234.
- [137] C. H. Christensen, K. Johansen, E. Törnqvist, I. Schmidt, H. Topsøe, C. H. Christensen, *Catal. Today* **2007**, *128*, 117–122.
- [138] J. C. Groen, W. Zhu, S. Brouwer, S. J. Huynink, F. Kapteijn, J. A. Moulijn, J. Pérez-Ramírez, *J. Am. Chem. Soc.* **2007**, *129*, 355–360.
- [139] L. Zhao, B. Shen, J. Gao, C. Xu, *J. Catal.* **2008**, *258*, 228–234.
- [140] J. Pérez-Ramírez, S. Mitchell, D. Verboekend, M. Milina, N. L. Michels, F. Krumeich, N.

- Marti, M. Erdmann, *ChemCatChem* **2011**, *3*, 1731–1734.
- [141] X. Zhu, L. L. Lobban, R. G. Mallinson, D. E. Resasco, *J. Catal.* **2010**, *271*, 88–98.
- [142] K. Cheng, J. Kang, S. Huang, Z. You, Q. Zhang, J. Ding, W. Hua, Y. Lou, W. Deng, Y. Wang, *ACS Catal.* **2012**, *2*, 441–449.
- [143] C. J. Baranowski, A. M. Bahmanpour, O. Kröcher, *Appl. Catal. B Environ.* **2017**, 407–420.
- [144] Z. Xue, H. Shang, Z. Zhang, C. Xiong, C. Lu, G. An, *Energy & Fuels* **2016**, *31*, 279–286.
- [145] H. Matsuura, H. Murata, *J. Raman Spectrosc.* **1982**, *12*, 144–148.
- [146] V. Venkatesan, K. Sundararajan, K. Sankaran, K. S. Viswanathan, *Spectrochim. Acta - Part A Mol. Biomol. Spectrosc.* **2002**, *58*, 467–478.
- [147] D. Verboekend, S. Mitchell, M. Milina, J. C. Groen, P. Javier, **2011**, 14193–14203.
- [148] W. Ding, G. D. Meitzner, E. Iglesia, *J. Catal.* **2002**, *206*, 14–22.
- [149] A. Ghorbanpour, A. Gumidyala, L. C. Grabow, S. P. Crossley, J. D. Rimer, *ACS Nano* **2015**, *9*, 4006–4016.
- [150] M. Thommes, K. Kaneko, A. V. Neimark, J. P. Olivier, F. Rodriguez-Reinoso, J. Rouquerol, K. S. W. Sing, *Pure Appl. Chem.* **2015**, *87*, 1051–1069.
- [151] Z. Wang, Y. Jiang, O. Lafon, J. Trébosc, K. Duk Kim, C. Stampfl, A. Baiker, J. P. Amoureux, J. Huang, *Nat. Commun.* **2016**, *7*, 1–5.
- [152] F. Deng, Y. Du, C. Ye, J. Wang, T. Ding, H. Li, *J. Phys. Chem.* **1995**, *99*, 15208–15214.
- [153] Z. Yu, S. Li, Q. Wang, A. Zheng, X. Jun, L. Chen, F. Deng, *J. Phys. Chem. C* **2011**, *115*, 22320–22327.
- [154] P. Sazama, B. Wichterlova, J. Dedecek, Z. Tvaruzkova, Z. Musilova, L. Palumbo, S. Sklenak, O. Gonsiorova, *Microporous Mesoporous Mater.* **2011**, *143*, 87–96.
- [155] W. Song, J. F. Woodworth, V. H. Grassian, S. C. Larsen, *Langmuir* **2005**, *21*, 7009–7014.
- [156] J. Casanovas, F. Illas, G. Pacchioni, *Chem. Phys. Lett.* **2000**, *326*, 523–529.
- [157] D. Verboekend, A. M. Chabaneix, K. Thomas, J.-P. Gilson, J. Pérez-Ramírez, *CrystEngComm* **2011**, *13*, 3408–3416.
- [158] T. Barzetti, E. Selli, D. Moscotti, L. Forni, *J. Chem. Soc. Faraday Trans.* **1996**, *92*, 1401.
- [159] K. Góra-marek, K. Tarach, M. Choi, *J. Phys. Chem. C* **2014**, *118*, 12266–12274.
- [160] R. Bartolomeu, R. Bértolo, S. Casale, A. Fernandes, C. Henriques, P. Da Costa, F. Ribeiro, *Microporous Mesoporous Mater.* **2013**, *169*, 137–147.
- [161] C. Fernandez, I. Stan, J. P. Gilson, K. Thomas, A. Vicente, A. Bonilla, J. Pérez-Ramírez, *Chem. - A Eur. J.* **2010**, *16*, 6224–6233.
- [162] F. Schüth, K. S. W. Sing, J. Weitkamp, *Handbook of Porous Solids*, Wiley, **2002**.
- [163] V. R. Choudhary, V. S. Nayak, T. V Choudhary, *Ind. Eng. Chem. Res.* **1997**, *36*, 1812–1818.
- [164] K. Hackbarth, P. Haltenort, U. Arnold, *Chem. Ing. Tech* **2018**, *90*, 1520–1528.
- [165] J. Qi, Y. Hu, S. Jiang, W. Ma, Z. Yang, Y. Wang, *Fuel* **2019**, *245*, 521–527.

- [166] J. Guilera, E. Ramírez, C. Fité, M. Iborra, J. Tejero, *Appl. Catal. A, Gen.* **2013**, *467*, 301–309.
- [167] H. H. Murray, *Appl. Clay Sci.* **1991**, *5*, 379–395.
- [168] H. H. Murray, *Appl. Clay Sci.* **2000**, *17*, 207–221.
- [169] Z. Ding, J. T. Klopogge, R. L. Frost, *J. Porous Mater.* **2001**, *8*, 273–293.
- [170] A. M. Bahmanpour, F. Héroguel, C. J. Baranowski, J. S. Luterbacher, O. Kröcher, *Appl. Catal. A Gen.* **2018**, *560*, 165–170.
- [171] F. Uddin, *Metall. Mater. Trans. A Phys. Metall. Mater. Sci.* **2008**, *39*, 2804–2814.
- [172] J. T. Klopogge, *J. Porous Mater.* **1998**, *5*, 5–41.
- [173] Y. Masui, J. Wang, K. Teramura, T. Kogure, T. Tanaka, M. Onaka, *Microporous Mesoporous Mater.* **2014**, *198*, 129–138.
- [174] S. Shinde, C. Rode, *Catal. Commun.* **2017**, *88*, 77–80.
- [175] J. Wang, Y. Masui, K. Watanabe, M. Onaka, *Adv. Synth. Catal.* **2009**, *351*, 553–557.
- [176] J. Wang, Y. Masui, M. Onaka, *Tetrahedron Lett.* **2010**, *51*, 3300–3303.
- [177] J. Wang, Y. Masui, M. Onaka, *European J. Org. Chem.* **2010**, 1763–1771.
- [178] J. Wang, Y. Masui, M. Onaka, *ACS Catal.* **2011**, *1*, 446–454.
- [179] J. Wang, J. Ren, X. Liu, J. Xi, Q. Xia, Y. Zu, G. Lu, Y. Wang, *Green Chem.* **2012**, *14*, 2506–2512.
- [180] J. Wang, Y. Masui, M. Onaka, *Appl. Catal. B Environ.* **2011**, *107*, 135–139.
- [181] H. Li, J. Ren, L. Zhong, R. Sun, L. Liang, *Bioresour. Technol.* **2015**, *176*, 242–248.
- [182] T. Hara, M. Hatakeyama, A. Kim, N. Ichikuni, S. Shimazu, *Green Chem.* **2012**, *14*, 771–777.
- [183] K. Beloufa, N. Sahli, M. Belbachir, *J. Appl. Polym. Sci.* **2009**, *115*, 2820–2827.
- [184] S. Das, V. Jayaraman, *Prog. Mater. Sci.* **2014**, *66*, 112–255.
- [185] A. Neaman, M. Pelletier, F. Villieras, *Appl. Clay Sci.* **2003**, *22*, 153–168.
- [186] K. Bahranowski, A. Gaweł, A. Klimek, A. Michalik-Zym, B. D. Napruszewska, M. Nattich-Rak, M. Rogowska, E. M. Serwicka, *Appl. Clay Sci.* **2017**, *140*, 75–80.
- [187] L. Le Forestier, F. Muller, F. Villieras, M. Pelletier, *Appl. Clay Sci.* **2010**, *48*, 18–25.
- [188] V. K. Soni, R. K. Sharma, *ChemCatChem* **2016**, *8*, 1763–1768.
- [189] V. K. Soni, P. R. Sharma, G. Choudhary, S. Pandey, R. K. Sharma, *ACS Sustain. Chem. Eng.* **2017**, *5*, 5351–5359.
- [190] P. J. Wallis, W. P. Gates, A. F. Patti, J. L. Scott, E. Teoh, *Green Chem.* **2007**, *9*, 980–986.
- [191] J. Madejová, *Vib. Spectrosc.* **2003**, *31*, 1–10.
- [192] B. Tyagi, C. D. Chudasama, R. V. Jasra, *Spectrochim. Acta - Part A Mol. Biomol. Spectrosc.* **2006**, *64*, 273–278.

- [193] L. Yan, C. B. Roth, P. F. Low, *J. Colloid Interface Sci.* **1996**, *184*, 663–670.
- [194] S. Cadars, R. Guégan, M. N. Garaga, X. Bourrat, L. Le Forestier, F. Fayon, T. V. Huynh, T. Allier, Z. Nour, D. Massiot, *Chem. Mater.* **2012**, *24*, 4376–4389.
- [195] N. N. Binitha, S. Sugunan, *Microporous Mesoporous Mater.* **2006**, *93*, 82–89.
- [196] A. Phukan, S. J. Borah, P. Bordoloi, K. Sharma, B. J. Borah, P. P. Sarmah, D. K. Dutta, *Adv. Powder Technol.* **2017**, *28*, 1585–1592.
- [197] C. Eypert-Blaison, L. J. Michot, B. Humbert, M. Pelletier, F. Villieras, J. B. D’Espinoise de la Caillerie, *J. Phys. Chem. B* **2002**, *106*, 730–742.
- [198] D. Amalric-Popescu, F. Bozon-Verduraz, *Catal. Today* **2001**, *70*, 139–154.
- [199] R. Alvero, M. D. Alba, M. A. Castro, J. M. Trillo, *J. Phys. Chem.* **1994**, *98*, 7848–7853.
- [200] W. Jones, *Catal. Today* **1988**, *2*, 357–367.
- [201] N. J. Clayden, C. M. Dobson, A. Fern, *J. Chem. Soc. Dalt. Trans.* **1989**, 843–847.
- [202] S. Indris, M. Scheuermann, S. M. Becker, V. Šepelák, R. Kruk, J. Suffner, F. Gyger, C. Feldmann, A. S. Ulrich, H. Hahn, *J. Phys. Chem. C* **2011**, *115*, 6433–6437.
- [203] J. Chen, X. P. Wu, L. Shen, Y. Li, D. Wu, W. Ding, X. Q. Gong, M. Lin, L. Peng, *Chem. Phys. Lett.* **2016**, *643*, 126–130.
- [204] P. Ferrini, J. Dijkmans, R. De Clercq, S. Van de Vyver, M. Dusselier, P. A. Jacobs, B. F. Sels, *Coord. Chem. Rev.* **2017**, *343*, 220–255.
- [205] C. Fan, Y. Peng, Q. Zhu, L. Lin, R. Wang, A. Xu, *J. Phys. Chem. C* **2013**, *117*, 24157–24166.
- [206] Y. Yang, Y. Wang, S. Yin, *Appl. Surf. Sci.* **2017**, *420*, 399–406.
- [207] H. Wang, K. Dou, W. Y. Teoh, Y. Zhan, T. F. Hung, F. Zhang, J. Xu, R. Zhang, A. L. Rogach, *Adv. Funct. Mater.* **2013**, *23*, 4847–4853.
- [208] J.-F. Lambert, G. Poncelet, *Top. Catal.* **1997**, *4*, 43–56.
- [209] S. Ghosh, L. Manna, *Chem. Rev.* **2018**, *118*, 7804–7864.
- [210] F. Liu, T. Wang, Y. Zheng, J. Wang, *J. Catal.* **2017**, *355*, 17–25.
- [211] J. C. Vega-Vila, J. W. Harris, R. Gounder, *J. Catal.* **2016**, *344*, 108–120.
- [212] S. Bordiga, C. Lamberti, F. Bonino, A. Travert, F. Thibault-Starzyk, *Chem. Soc. Rev.* **2015**, *44*, 7262–7341.
- [213] W. Dai, C. Wang, B. Tang, G. Wu, N. Guan, Z. Xie, M. Hunger, L. Li, *ACS Catal.* **2016**, *6*, 2955–2964.
- [214] J. A. Jennings, S. Parkin, E. Munson, S. P. Delaney, J. L. Calahan, M. Isaacs, K. Hong, M. Crocker, *RSC Adv.* **2017**, *7*, 25987–25997.
- [215] P. Wolf, M. Valla, F. Núñez-Zarur, A. Comas-Vives, A. J. Rossini, C. Firth, H. Kallas, A. Lesage, L. Emsley, C. Copéret, et al., *ACS Catal.* **2016**, *6*, 4047–4063.
- [216] W. Dong, Z. Shen, B. Peng, M. Gu, X. Zhou, B. Xiang, Y. Zhang, *Sci. Rep.* **2016**, *6*, 26713.
- [217] A. Corma, F. Llopis, J. B. Monton, S. Weller, *J. Catal.* **1993**, *142*, 97–109.

- [218] J. Dijkmans, D. Gabriëls, M. Dusselier, F. de Clippel, P. Vanelderen, K. Houthoofd, A. Malfliet, Y. Pontikes, B. F. Sels, *Green Chem.* **2013**, *15*, 2777–2785.
- [219] W. N. P. van der Graaff, G. Li, B. Mezari, E. J. M. Hensen, E. A. Pidko, *ChemCatChem* **2015**, *7*, 1152–1160.
- [220] F. Liu, R. Wei, T. Wang, *Fuel Process. Technol.* **2018**, *180*, 114–121.
- [221] Y. Zheng, Q. Tang, T. Wang, J. Wang, *Chem. Eng. Sci.* **2015**, *134*, 758–766.
- [222] M. E. Davis, *Microporous Mesoporous Mater.* **1998**, *21*, 173–182.
- [223] B. M. Weckhuysen, J. Yu, *Chem. Soc. Rev.* **2015**, *44*, 7022–7024.
- [224] Y. Zhi, H. Shi, L. Mu, Y. Liu, D. Mei, D. M. Camaioni, J. A. Lercher, *J. Am. Chem. Soc.* **2015**, *137*, 15781–15794.
- [225] A. Corma, O. Marie, F. J. Ortega, *J. Catal.* **2004**, *222*, 338–347.
- [226] K. Chen, J. Damron, C. Pearson, D. Resasco, L. Zhang, J. L. White, *ACS Catal.* **2014**, *4*, 3039–3044.
- [227] A. Vjunov, M. Wang, N. Govind, T. Huthwelker, H. Shi, D. Mei, J. L. Fulton, J. A. Lercher, *Chem. Mater.* **2017**, *29*, 9030–9042.
- [228] M. Wang, N. R. Jaegers, M.-S. Lee, C. Wan, J. Z. Hu, H. Shi, D. Mei, S. D. Burton, D. M. Camaioni, O. Y. Gutiérrez, et al., *J. Am. Chem. Soc.* **2019**, *141*, 3444–3455.
- [229] S. Eckstein, P. H. Hintermeier, R. Zhao, E. Baráth, H. Shi, Y. Liu, J. A. Lercher, *Angew. Chemie Int. Ed.* **2019**, *58*, 3450–3455.
- [230] Y. Liu, A. Vjunov, H. Shi, S. Eckstein, D. M. Camaioni, D. Mei, E. Baráth, J. A. Lercher, *Nat. Commun.* **2017**, *8*, 2–9.
- [231] Y. Liu, E. Baráth, H. Shi, J. Hu, D. M. Camaioni, J. A. Lercher, *Nat. Catal.* **2018**, *1*, 141–147.
- [232] P. Müller, P. Wolf, I. Hermans, *ACS Catal.* **2016**, *6*, 2760–2769.
- [233] P. Müller, I. Hermans, *Ind. Eng. Chem. Res.* **2017**, *56*, 1123–1136.
- [234] T. Bürgi, A. Baiker, *J. Phys. Chem. B* **2002**, *106*, 10649–10658.
- [235] R. Wirz, D. Ferri, A. Baiker, *Langmuir* **2006**, *22*, 3698–3706.
- [236] M. Sakakibara, Y. Yonemura, *J. Mol. Struct.* **1980**, *66*, 333–337.
- [237] T. A. Mohamed, *J. Mol. Struct. THEOCHEM* **2005**, *713*, 179–192.
- [238] M. J. Frisch, G. W. Trucks, H. B. Schlegel, G. E. Scuseria, M. A. Robb, J. R. Cheeseman, G. Scalmani, V. Barone, G. A. Petersson, H. Nakatsuji, et al., **2016**.
- [239] A. D. Becke, *J. Chem. Phys.* **1993**, *98*, 1372–1377.
- [240] C. Lee, W. Yang, R. G. Parr, *Phys. Rev. B* **1988**, *37*, 785–789.
- [241] S. Grimme, J. Antony, S. Ehrlich, H. Krieg, *J. Chem. Phys.* **2010**, *132*, 154104.
- [242] J. Tomasi, B. Mennucci, R. Cammi, *Chem. Rev.* **2005**, *105*, 2999–3094.
- [243] R. Ditchfield, W. J. Hehre, J. A. Pople, *J. Chem. Phys.* **1971**, *54*, 724–728.
- [244] S. Eckstein, P. H. Hintermeier, M. V. Olarte, Y. Liu, E. Baráth, J. A. Lercher, *J. Catal.*

- 2017**, *352*, 329–336.
- [245] G. Skodras, G. Nenes, N. Zafeiriou, *Appl. Therm. Eng.* **2015**, *74*, 111–118.
- [246] S. Campisi, D. Ferri, A. Villa, W. Wang, D. Wang, O. Kröcher, L. Prati, *J. Phys. Chem. C* **2016**, *120*, 14027–14033.
- [247] J. K. Wilmshurst, *Can. J. Chem.* **1958**, *36*, 285–289.
- [248] M. Kobayashi, R. Iwamoto, H. Tadokoro, *J. Chem. Phys.* **1966**, *44*, 922–933.
- [249] C. Mondelli, D. Ferri, J. D. Grunwaldt, F. Krumeich, S. Mangold, R. Psaro, A. Baiker, *J. Catal.* **2007**, *252*, 77–87.
- [250] N. S. Gould, B. Xu, *J. Catal.* **2018**, *358*, 80–88.
- [251] M. Ouda, F. Mantoi, K. Hesterwerth, E. Bargiacchi, H. Klein, R. J. White, *React. Chem. Eng.* **2018**, *3*, 676–695.
- [252] A. M. Bahmanpour, A. Hoadley, A. Tanksale, *Rev. Chem. Eng.* **2014**, *30*, 583–604.
- [253] S. Su, P. Zaza, A. Renken, *Chem. Eng. Technol.* **1994**, *17*, 34–40.
- [254] G. I. N. Waterhouse, G. A. Bowmaker, J. B. Metson, *Appl. Catal. A Gen.* **2004**, *265*, 85–101.
- [255] P. Zaza, H. Randall, R. Doepper, A. Renken, *Catal. Today* **1994**, *20*, 325–334.
- [256] R. S. Aries, *Process for Making Anhydrous Monomeric Formaldehyde*, **1960**, 2953602.
- [257] L.-P. Ren, W.-L. Dai, X.-L. Yang, J.-H. Xu, Y. Cao, H. Li, K. Fan, *Catal. Letters* **2005**, *99*, 83–87.
- [258] N. Y. Usachev, I. M. Krukovskii, S. A. Kanaev, *Pet. Chem.* **2004**, *44*, 379–394.
- [259] T. Yamamoto, A. Shimoda, T. Okuhara, M. Misono, *Chem. Lett.* **1988**, *17*, 273–276.
- [260] A. Music, J. Batista, J. Levec, *Appl. Catal. a-General* **1997**, *165*, 115–131.
- [261] M. Sagou, T. Deguchi, S. Nakamura, *Stud. Surf. Sci. Catal.* **1989**, *44*, 139–146.
- [262] M. Sagou, H. Fujii, *Process for Producing Formaldehyde*, **1988**, 4788347.
- [263] A. Meyer, A. Renken, *Chem. Eng. Technol. - CET* **1990**, *13*, 145–149.
- [264] Y. Matsumura, K. Hashimoto, S. Yoshida, *J. Catal.* **1991**, *131*, 226–233.
- [265] S. Su, M. R. Prairie, A. Renken, *Appl. Catal. a-General* **1992**, *91*, 131–142.
- [266] S. J. Su, M. R. Prairie, A. Renken, *Appl. Catal. a-General* **1993**, *95*, 131–142.
- [267] J. Sauer, G. Emig, *Chem. Eng. Technol.* **1995**, *18*, 284–291.
- [268] S. Ruf, G. Emig, *Appl. Catal. A Gen.* **1997**, *161*, L19–L24.
- [269] A. E. Palomares, G. Eder-Mirth, M. Rep, J. A. Lercher, *J. Catal.* **1998**, *180*, 56–65.
- [270] Y. Wang, M. Zhu, L. Kang, B. Dai, *Microporous Mesoporous Mater.* **2014**, *196*, 129–135.
- [271] T. C. Keller, K. Desai, S. Mitchell, J. Pérez-Ramírez, *ACS Catal.* **2015**, *5*, 5388–5396.
- [272] T. C. Keller, M. Položij, B. Puértolas, H. V. Thang, P. Nachtigall, J. Pérez-Ramírez, *J. Phys. Chem. C* **2016**, *120*, 4954–4960.

-
- [273] N. S. Poonia, A. V. Bajaj, *Chem. Rev.* **1979**, *79*, 389–445.
- [274] M. Huang, A. Adnot, S. Kaliaguine, *J. Am. Chem. Soc.* **1992**, *114*, 10005–10010.
- [275] Y. Matsumura, K. Hashimoto, H. Kobayashi, S. Yoshida, *J. Chem. Soc. Faraday Trans.* **1990**, *86*, 561–565.
- [276] D. Aronowitz, D. Naegeli, *Int. J. Chem. Kinet.* **1977**, *9*, 471–479.
- [277] N. Rendón, F. Blanc, C. Copéret, *Coord. Chem. Rev.* **2009**, *253*, 2015–2020.
- [278] J. M. Rimsza, R. E. Jones, L. J. Criscenti, *J. Colloid Interface Sci.* **2018**, *516*, 128–137.
- [279] K. S. Walton, M. B. Abney, M. Douglas LeVan, *Microporous Mesoporous Mater.* **2006**, *91*, 78–84.
- [280] I. A. Weinstock, *Chem. Rev.* **1998**, *98*, 113–170.
- [281] H. Han, M. Liu, X. Nie, F. Ding, Y. Wang, J. Li, X. Guo, C. Song, *Microporous Mesoporous Mater.* **2016**, *234*, 61–72.
- [282] L. Kang, K. Han, *Microporous Mesoporous Mater.* **2010**, *127*, 90–95.

Appendices

Appendix A

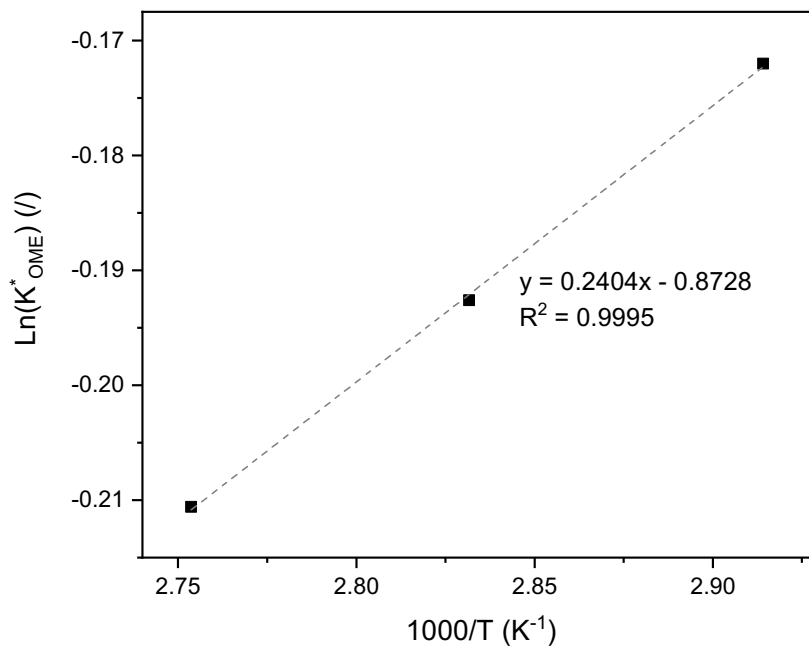


Figure A8-1. van 't Hoff plot of the experimental values of K^*_{OME} . The model is indicated by a dashed line. The OME synthesis process was performed with an OME_1/TRI ratio of 3.3 and 0.5 wt % of catalyst. Reaction was stopped after 90, 180 and 360 min respectively for the synthesis at 90, 80 and 70 °C.

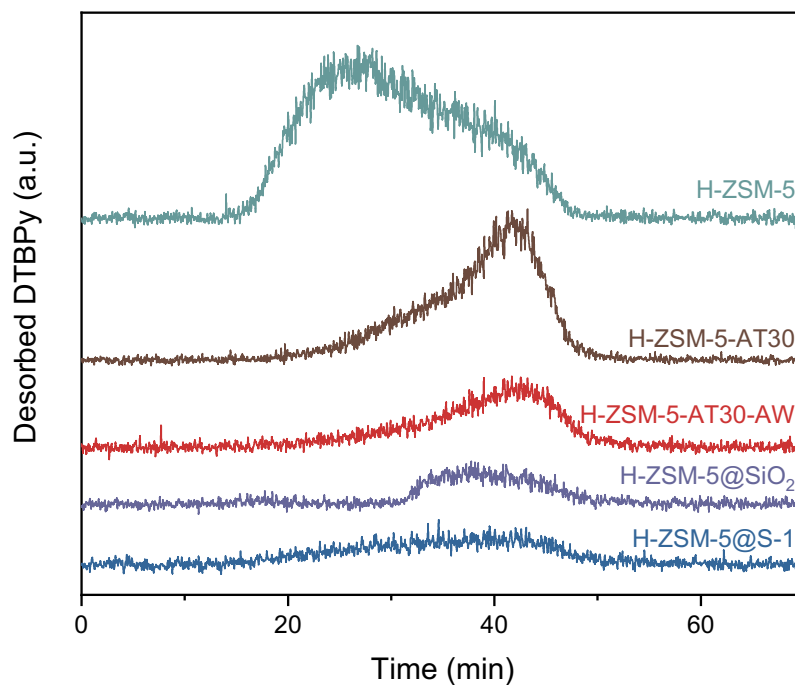


Figure A8-2. DTBPy-TPD for untreated, mesoporous and passivated zeolites.

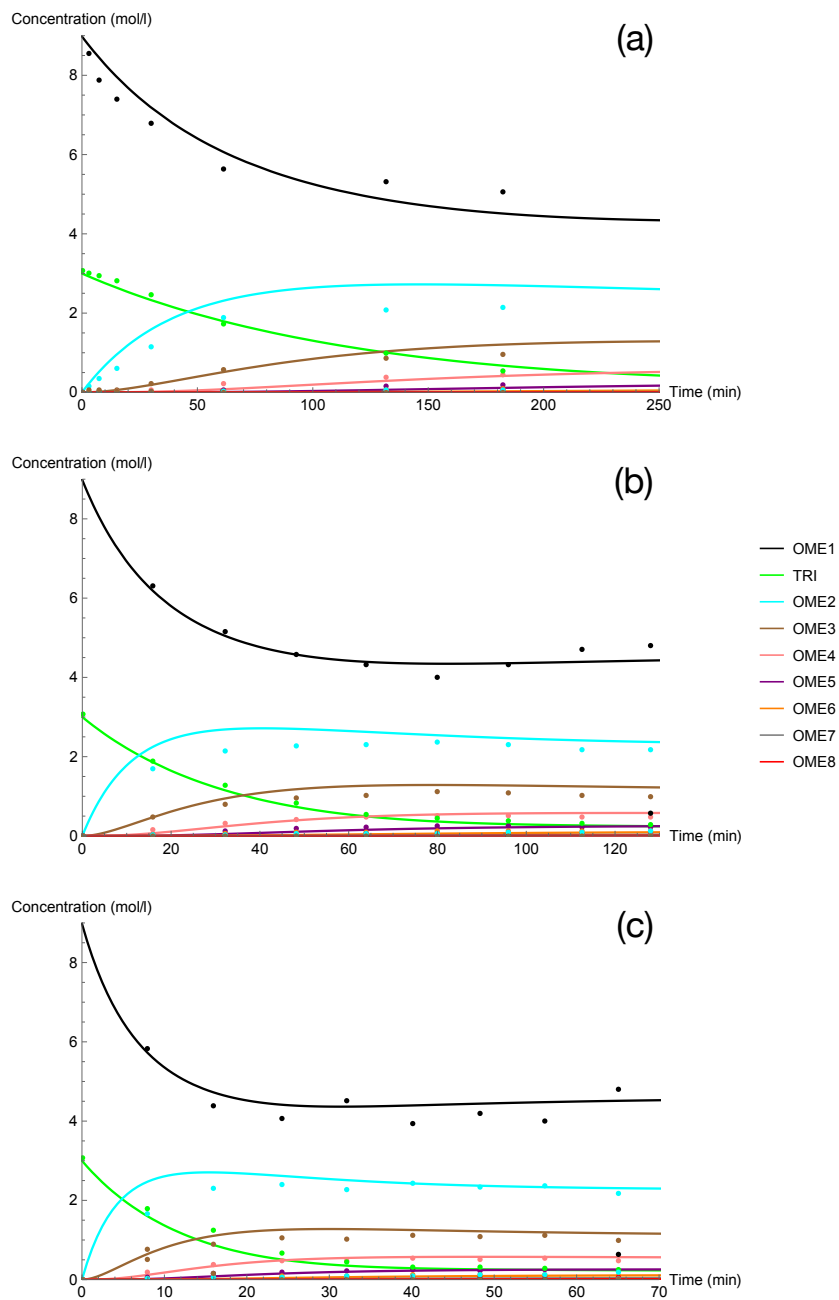


Figure A8-3. Concentration of the various components vs. time (OME₁/TRI: 3.3; 0.5 wt % H-ZSM-5) for experiments (a) K1 at 70 °C, (b) K2 at 80 °C and (c) K3 at 90 °C. The model output is given by the solid lines.

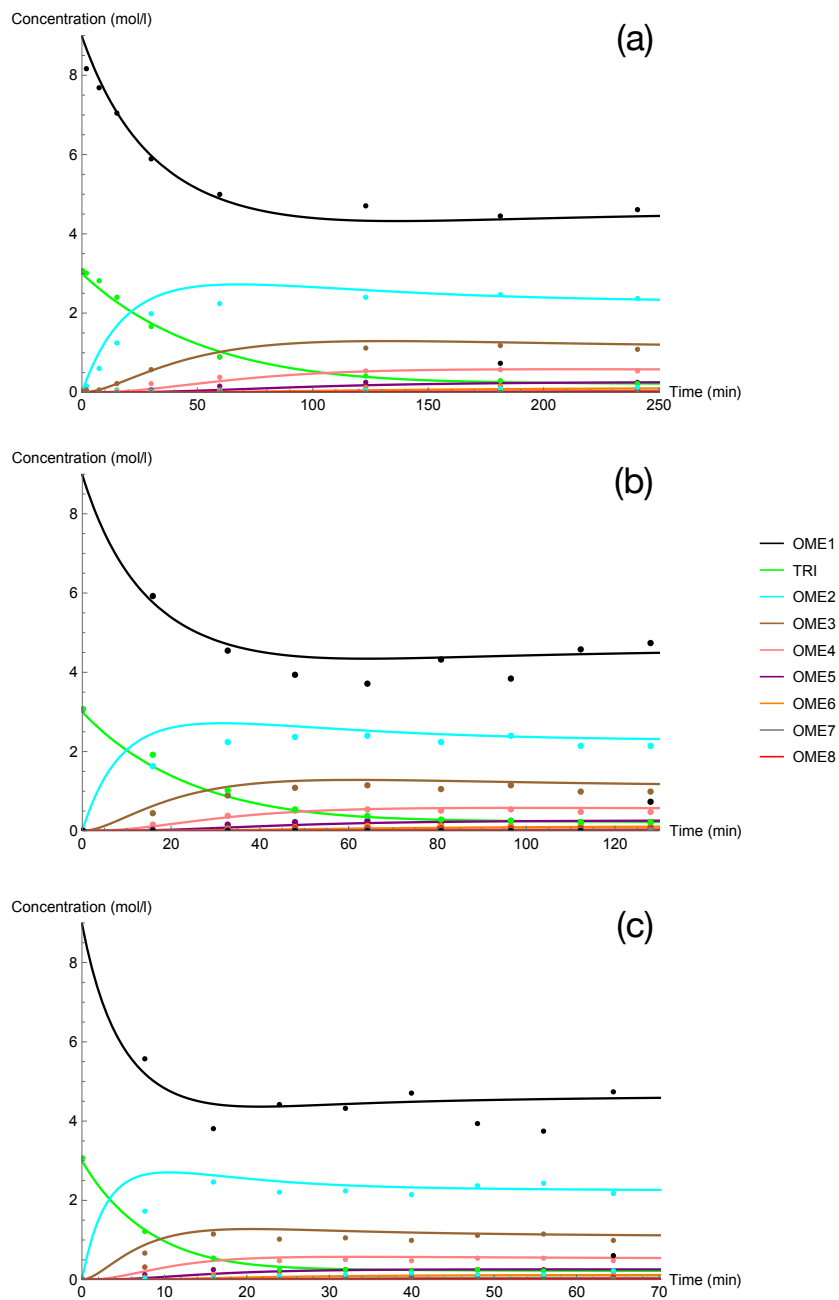


Figure A8-4. Concentration of the various components vs. time (OME_i/TRI: 3.3; 0.5 wt % H-ZSM-5-AT30_{0.4M}-AW) for experiments (a) K4 at 70 °C, (b) K5 at 80 °C and (c) K6 at 90 °C. The model output is given by the solid lines.

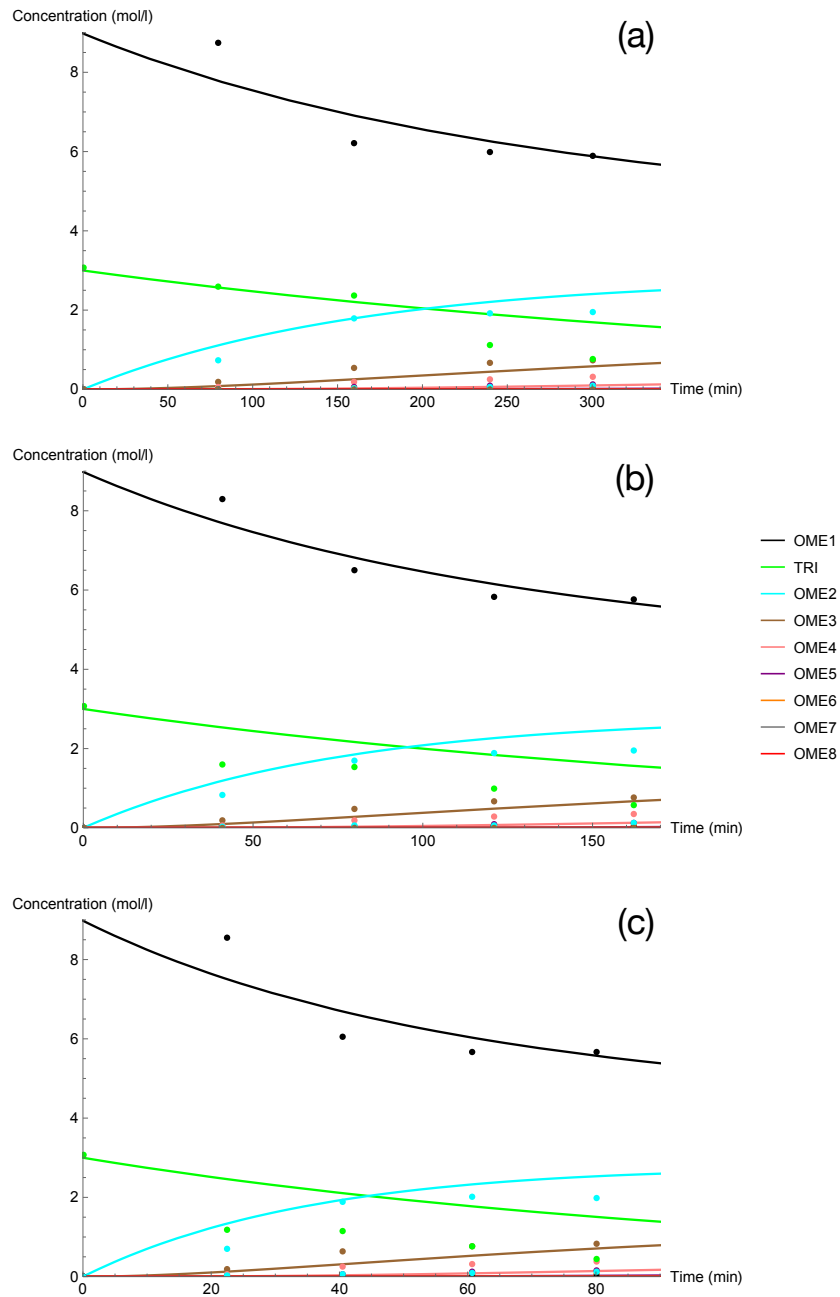


Figure A8-5. Concentration of the various components vs. time (OME₁/TRI: 3.3; 0.5 wt % H-ZSM-5@S-1) for experiments (a) K7 at 70 °C, (b) K8 at 80 °C and (c) K9 at 90 °C. The model output is given by the solid lines.

Appendix B

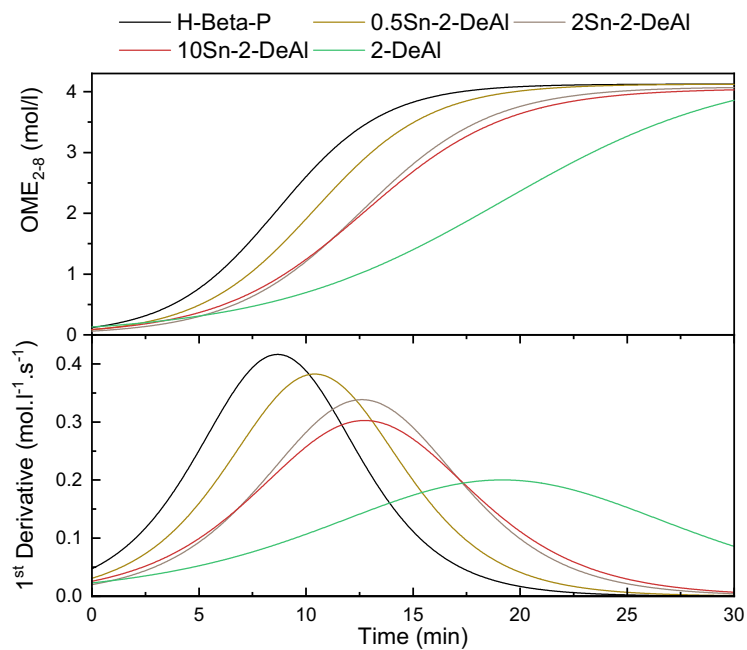


Figure B8-6. (top) Curve fitting of the OME₂₋₈ concentration vs. time using the Boltzmann function during OME synthesis from TRI and OME₁ (T = 30 °C, 0.5 wt % catalyst, molar ratio OME₁:TRI = 3.3). (bottom) 1st derivative of the Boltzmann fitting functions vs. time.

Appendix C

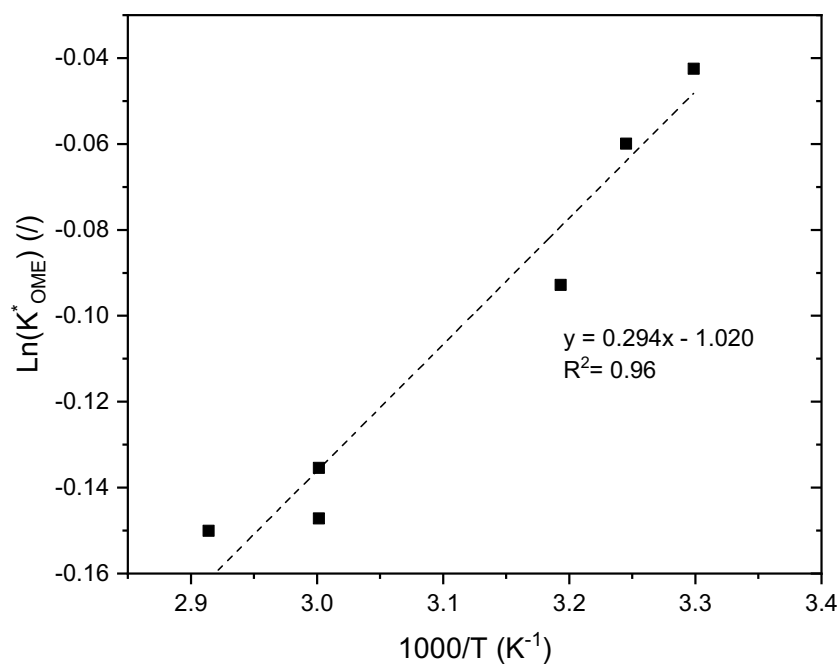


Figure C8-7. Van 't Hoff plot of the experimental values of K^*_{OME} . The model is indicated by a dashed line. The OME synthesis process was performed with an OME₁/TRI ratio of 3.3 and 0.5 wt % of catalyst.

DFT calculation aimed at supporting experimental evidences from both the kinetic and the ATR-IR study. Preliminary, the relative stability of the two most stable isomers of both OME₁ and TRI was evaluated. The structure of the adopted molecular models is reported in Figure C8-8.

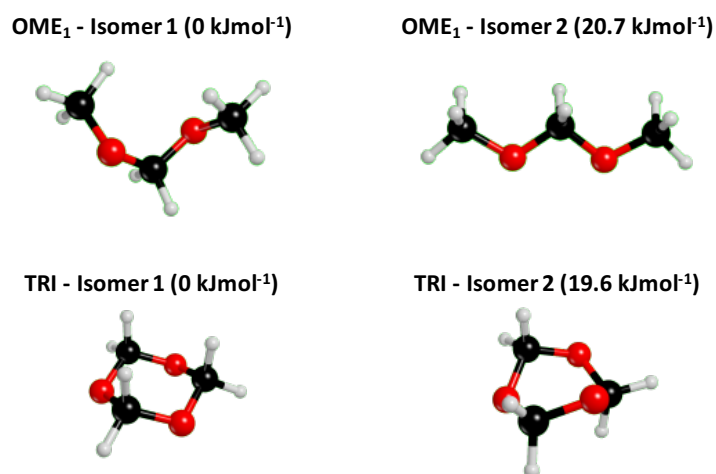


Figure C8-8. Molecular models of the most stable isomers of OME₁ and TRI adopted in the B3LYP-D3/CBS simulations. The relative stability (ΔG) of the isomers for each molecule is reported in brackets.

We further simulated the adsorption of OME₁, TRI and water over a minimal BAS model: the optimized adduct structures are shown in Figure C8-9. We report here only the results

concerning the adducts of the most stable isomers of both OME_1 and TRI over BAS, since the adsorption does not significantly alter the isomers relative stability.

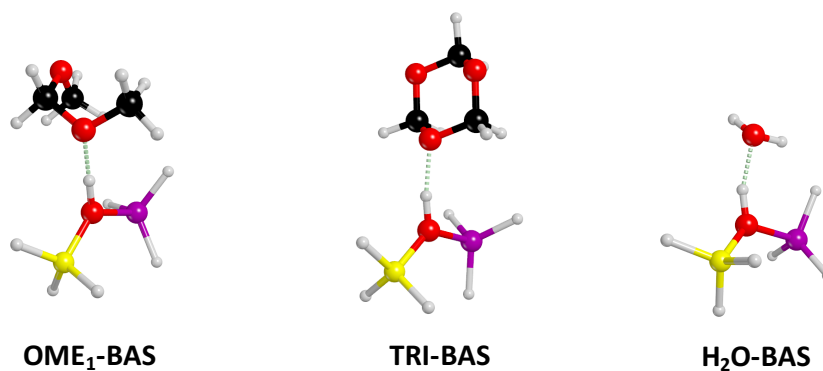


Figure C8-9. Molecular models of the OME_1 , TRI and H_2O adducts with BAS, as adopted in the B3LYP-D3/CBS simulations.

In order to compute accurate electronic energies, a CBS extrapolation strategy was adopted. We performed single point calculations at the B3LYP-D3/6-31+G(d,p) relaxed geometry by exploiting the same Hamiltonian, but adopting the Dunning aug-cc-pVnZ basis sets (with $n=2,3,4$, here indicating the maximum angular momentum L of functions included in the basis). The B3LYP/CBS electronic energies were obtained by linear extrapolation at $n=0$ for the single point energies vs n^{-3} , as exemplified for OME_1 (isomer 1) in Figure C8-10.

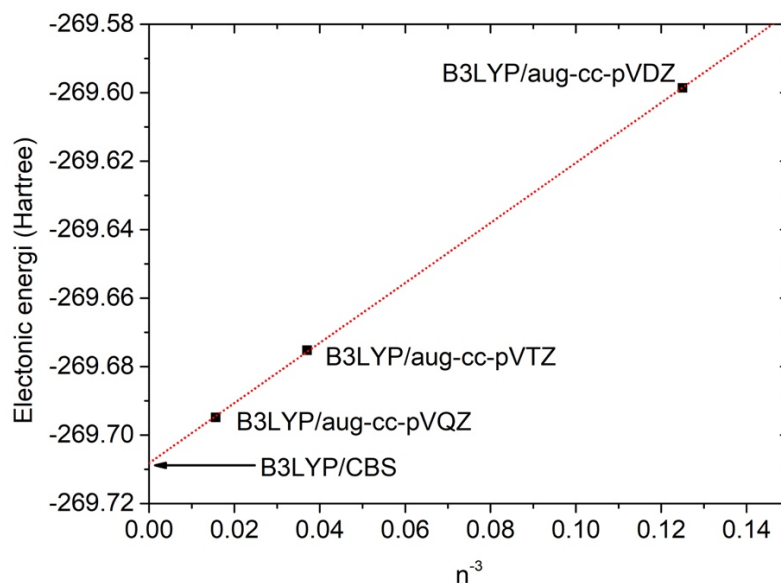


Figure C8-10. CBS extrapolation for OME_1 (isomer 1).

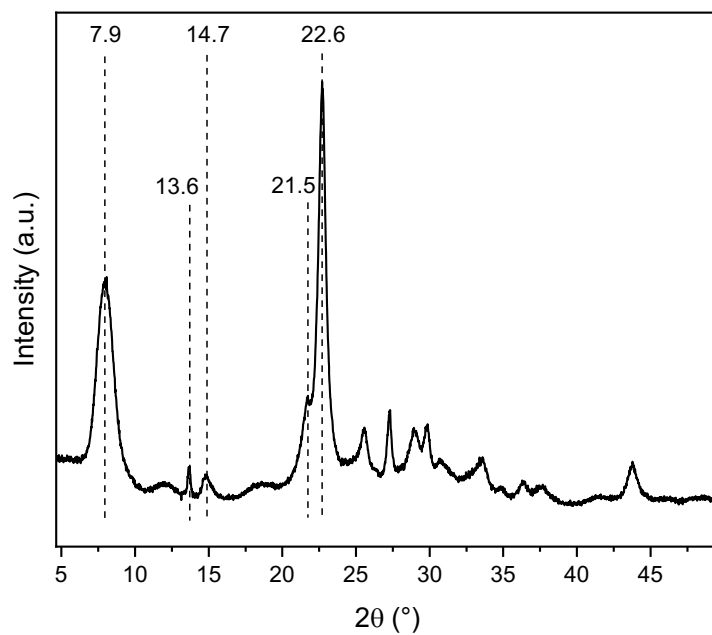


Figure C8-11. XRD pattern of zeolite H-Beta.

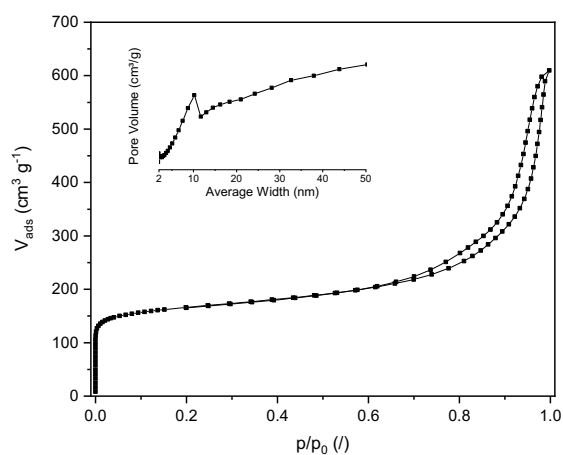
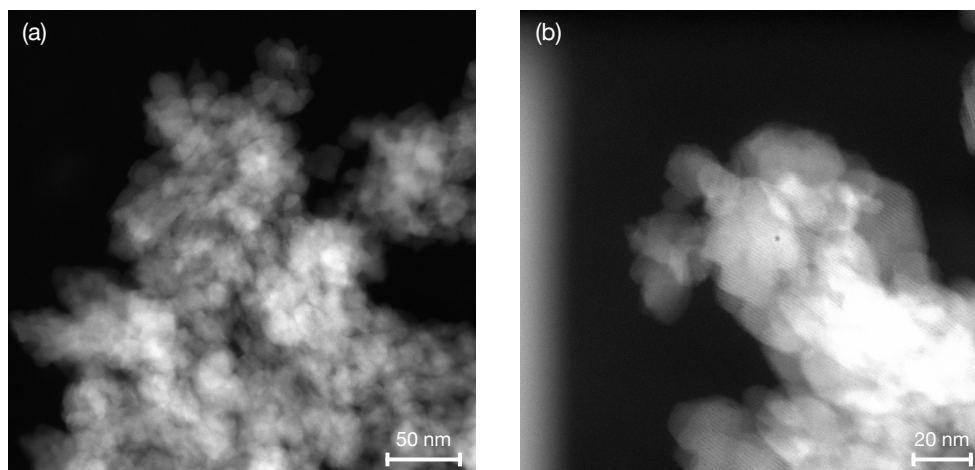
Figure C8-12. N₂ physisorption of zeolite H-Beta, (inset) BJH distribution plot.

Figure C8-13. STEM images of zeolite H-Beta.

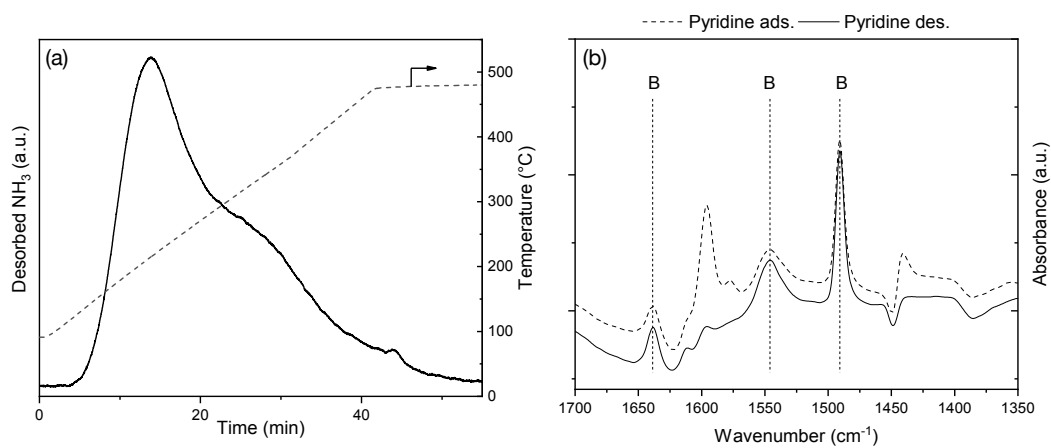


Figure C8-14. Characterization of the acidity of zeolite H-Beta by (a) NH_3 -TPD and (b) pyridine adsorption (dash line) and desorption (continuous line) in cyclohexane by ATR-IR spectroscopy (B indicates pyridine bonded to Brønsted acid sites).

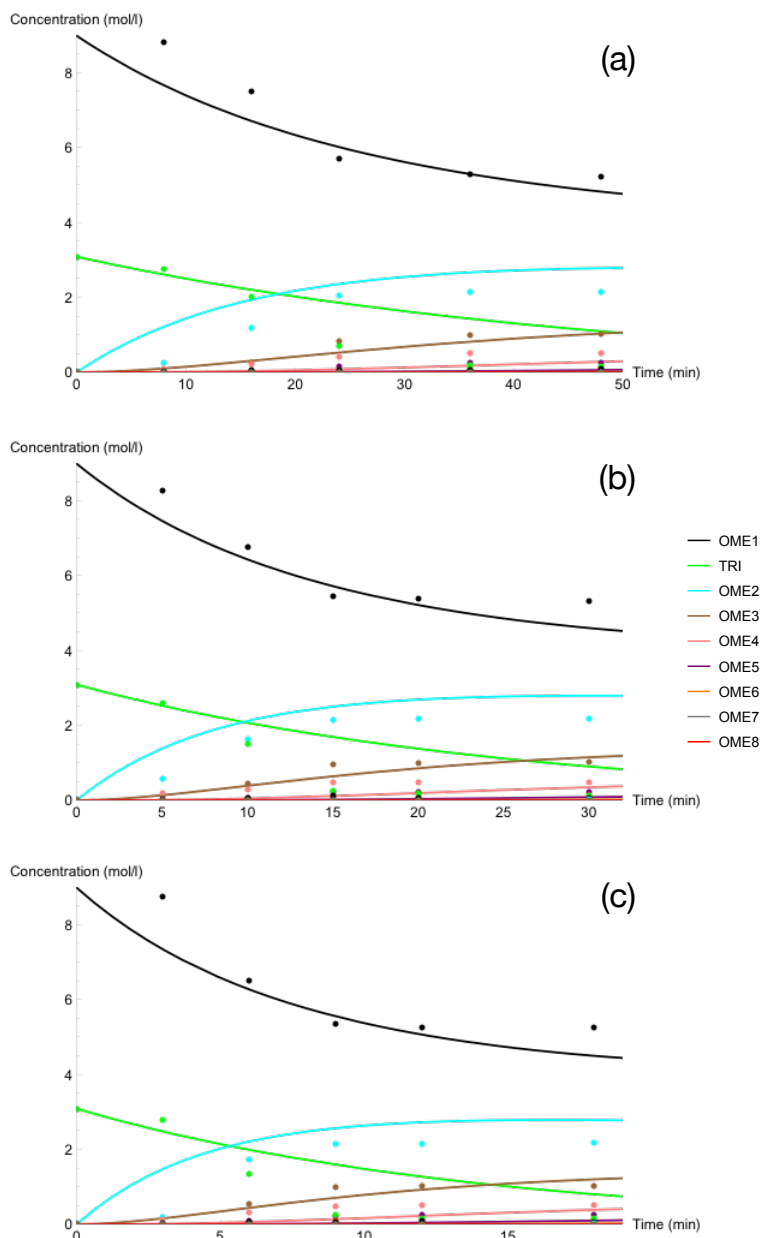


Figure C8-15. Concentration of the various components vs. time (OME₁/TRI: 3.3; 0.5 wt % H-Beta) for experiments with OME₁-0.03-H₂O (a) K1 at 25 °C, (b) K2 at 30 °C and (c) K3 at 35 °C. The model output is given by the solid lines.

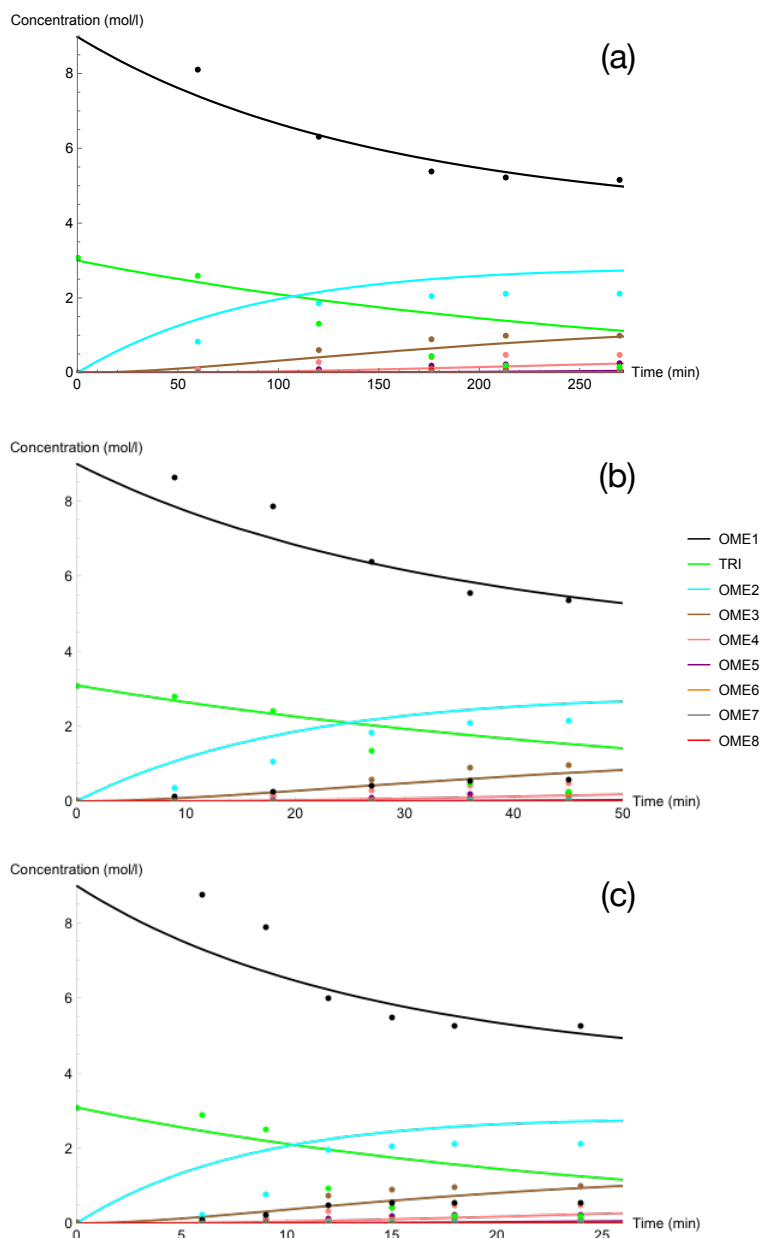


Figure C8-16. Concentration of the various components vs. time (OME₁/TRI: 3.3; 0.5 wt % H-Beta) for experiments with OME₁-0.21-H₂O (a) K4 at 40 °C, (b) K5 at 50 °C and (c) K6 at 60 °C. The model output is given by the solid lines.

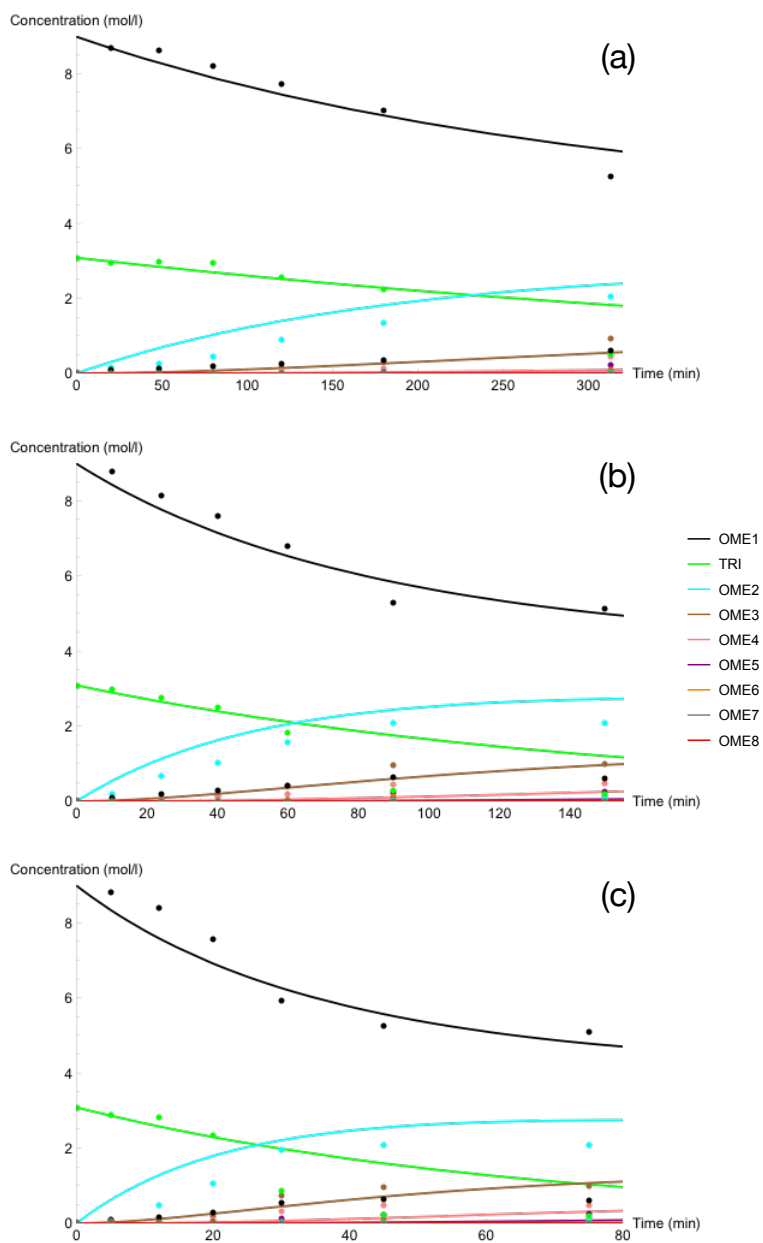


Figure C8-17. Concentration of the various components vs. time (OME₁/TRI: 3.3; 0.5 wt % H-Beta) for experiments with OME₁-0.44-H₂O (a) K7 at 50 °C, (b) K8 at 60 °C and (c) K9 at 70 °C. The model output is given by the solid lines.

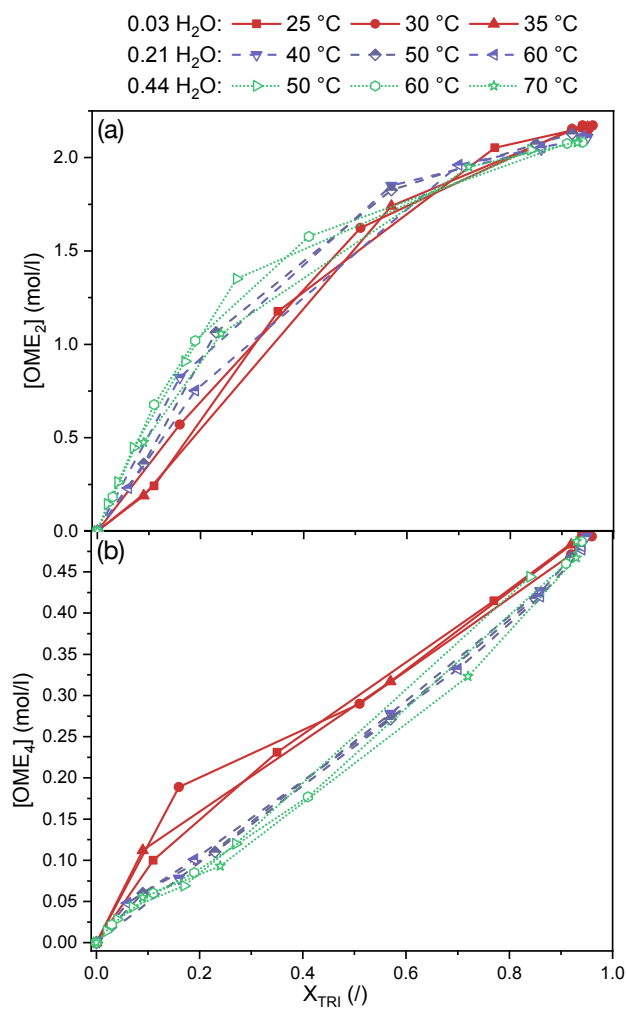


Figure C8-18. Synthesis of OME using various water concentrations in OME₁ with (a) OME₂ concentration and (b) OME₄ concentration, as a function of TRI conversion X_{TRI} .

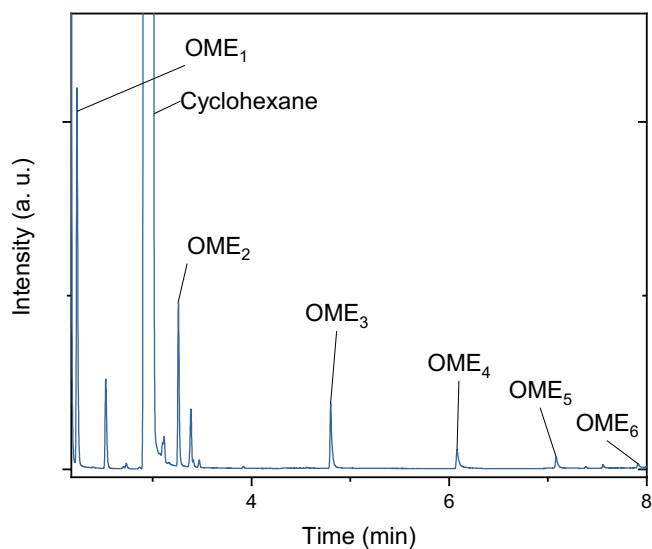


Figure C8-19. Chromatogram after 5 min of reaction of 10 mM OME₁ and TRI in cyclohexane (10 wt % H-Beta and T = 25 °C).

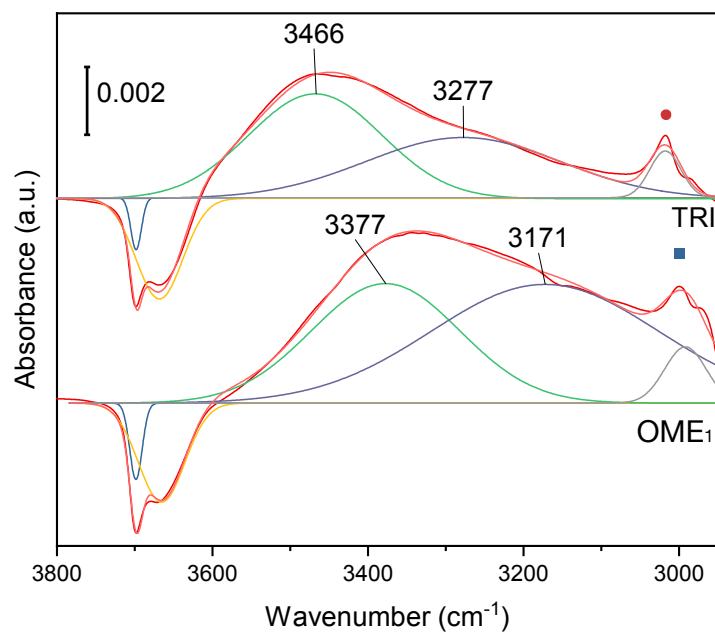


Figure C8-20. Deconvolution of the phase-domain spectra (290°) of TRI vs. neat and OME₁ vs. neat. The circle and the square indicate the peaks related to TRI and OME₁ in solution, respectively.

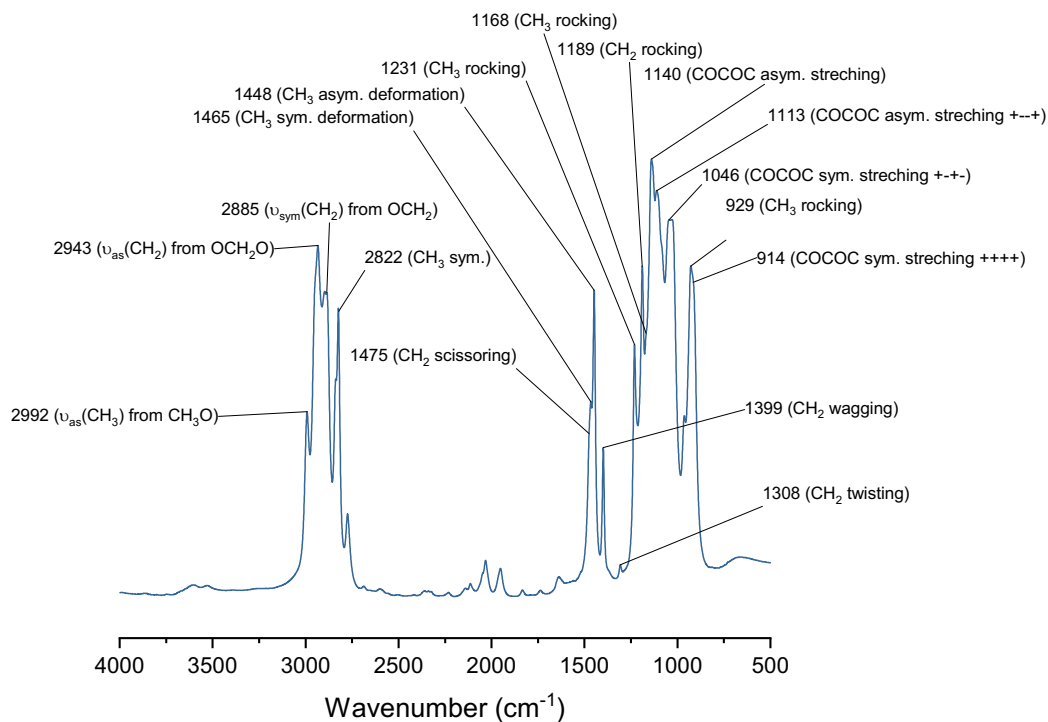


Figure C8-21. ATR-FTIR reference spectrum of OME₁.

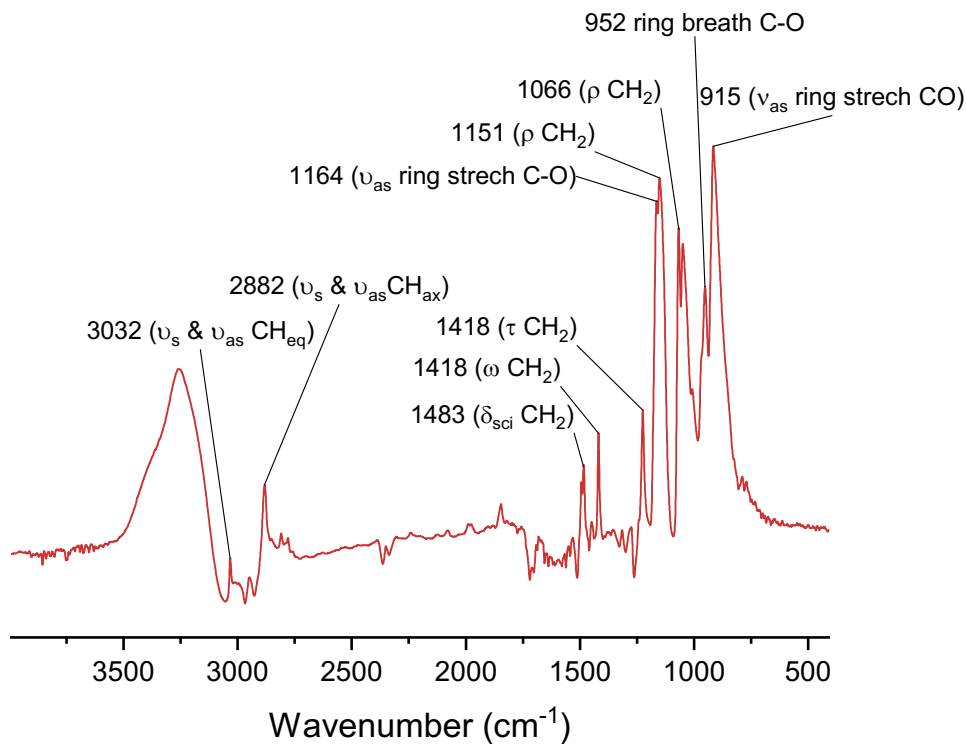


Figure C8-22. ATR-FTIR reference spectrum of TRI.

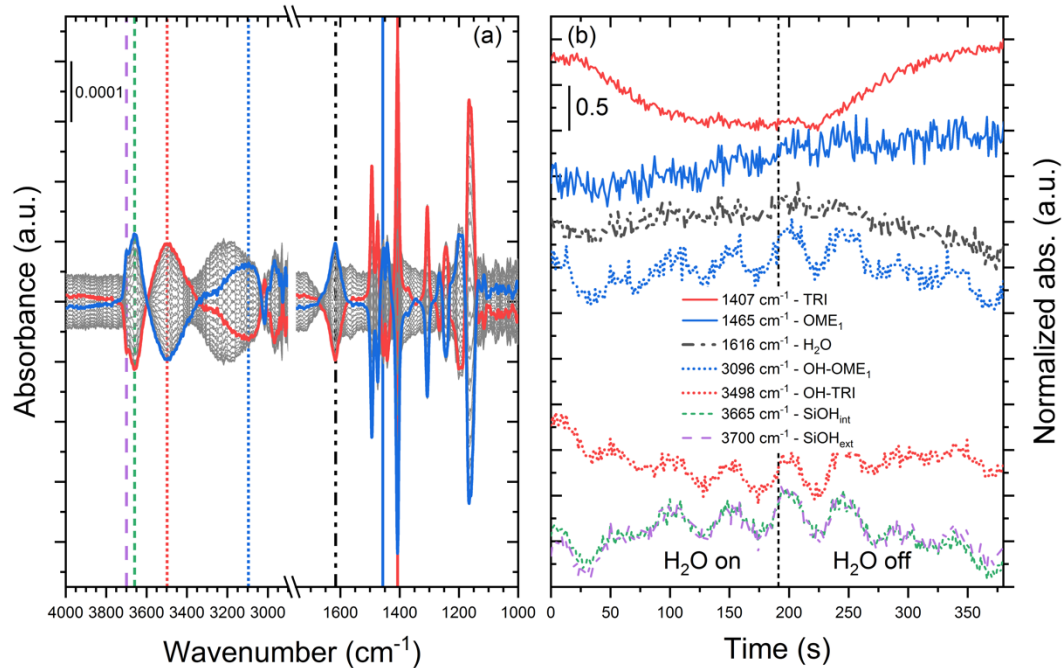


Figure C8-23. ATR-IR spectra of $\text{OME}_1 + \text{TRI}$ vs. $\text{OME}_1 + \text{TRI} + \text{H}_2\text{O}$ in the (a) phase-domain and (b) time-domain. Selected vibrational bands in the time-domain are displayed vertically in the phase-domain with the corresponding line pattern and colour.

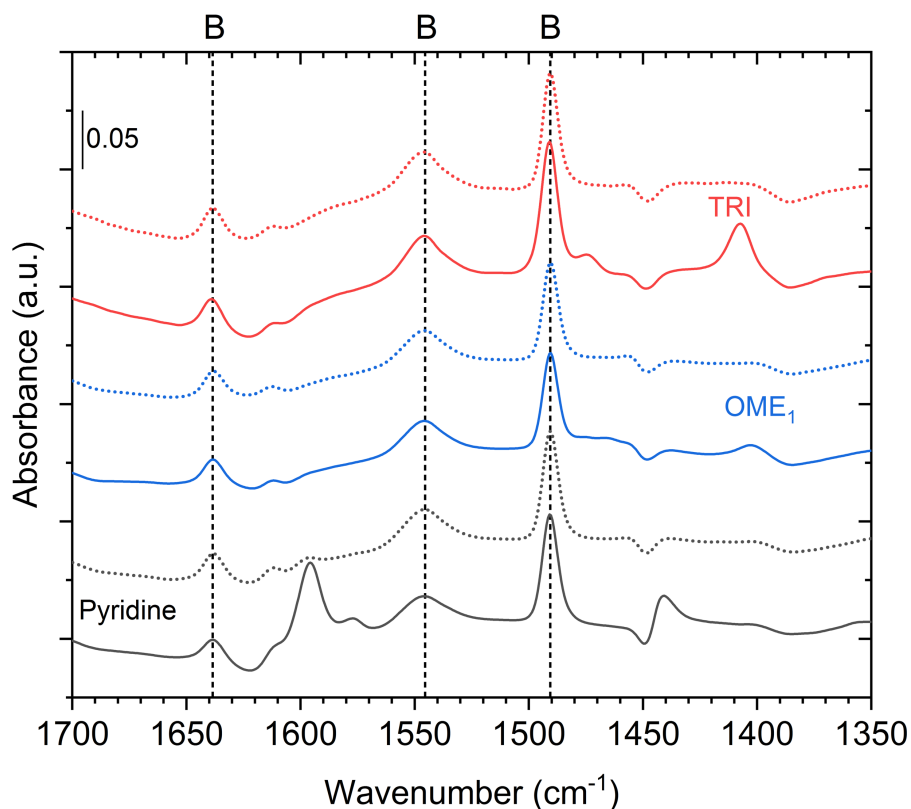


Figure C8-24. Adsorption (plain line) and desorption (dashed line) of pyridine (black), followed by adsorption-desorption of OME_1 (blue) and TRI (red) on H-Beta in cyclohexane.

List of publications

Peer-reviewed papers

C.J. Baranowski, J. Brandon, A.M. Bahmanpour, O. Kröcher, Alkali metal grafting on silica for methanol catalytic dehydrogenation. *Manuscript in preparation*.

C.J. Baranowski, T. Fovanna, M. Roger, J. McCaig, M. Signorile, A.M. Bahmanpour, D. Ferri, O. Kröcher, Water inhibition of oxymethylene dimethyl ether synthesis over an H-BEA zeolite: a combined kinetic and in situ ATR-IR study. *Manuscript in preparation*.

C.J. Baranowski, M. Roger, A.M. Bahmanpour, O. Kröcher, Nature of the synergy between Brønsted and Lewis acid sites in Sn-Beta zeolites for polyoxymethylene dimethyl ethers synthesis. *ChemSusChem* **2019**, cssc.201901814.

A.M. Bahmanpour, F. Héroguel, M. Kılıç, C.J. Baranowski, L. Artiglia, U. Röthlisberger, J.S. Luterbacher, O. Kröcher, Cu–Al Spinel as a Highly Active and Stable Catalyst for the Reverse Water Gas Shift Reaction. *ACS Catal.* **2019**, 9 (7), 6243–6251.

C.J. Baranowski, A.M. Bahmanpour, F. Héroguel, J.S. Luterbacher, O. Kröcher, Insights into the Nature of the Active Sites of Tin-Montmorillonite for the Synthesis of Polyoxymethylene Dimethyl Ethers (OME). *ChemCatChem* **2019**, 11 (13), 3010–3021.

C.J. Baranowski, A.M. Bahmanpour, F. Héroguel, J.S. Luterbacher, O. Kröcher, Prominent role of mesopore surface area and external acid sites for the synthesis of polyoxymethylene dimethyl ethers (OME) on a hierarchical H-ZSM-5 zeolite. *Catal. Sci. Technol.* **2019**, 9 (2), 366–376.

A.M. Bahmanpour, F. Héroguel, C.J. Baranowski, J.S. Luterbacher, O. Kröcher, O. (2018) Selective synthesis of dimethyl ether on eco-friendly K10 montmorillonite clay. *Appl. Catal. A Gen.* **2018**, 560, 165–170.

C.J. Baranowski, A.M. Bahmanpour, O. Kröcher, Catalytic synthesis of polyoxymethylene dimethyl ethers (OME): A review. *Appl. Catal. B Environ.* **2017**, 217, 407–420.

Talks

Nature of the synergy between Brønsted and Lewis acid sites in Sn-Beta zeolites for oxymethylene dimethyl ethers synthesis, SCS fall meeting, Zurich, Switzerland, September 19th **2019**.

Mesoporosity and external acidity for oxymethylene dimethyl ethers synthesis on a hierarchical H-ZSM-5 zeolite, European congress on catalysis Europacat, Aachen, Germany, August 18-23 **2019**.

Posters

Oxymethylene dimethyl ethers as a sustainable alternative to Diesel: advances on heterogeneous catalysis for large-scale production, SCCER Biosweet annual conference, Luzern, Switzerland, September 3th **2019**.

Investigation of the catalytic performance of tin-montmorillonite (Sn-Mont) for the synthesis of polyoxymethylene dimethyl ethers (OME), SCS fall meeting, Lausanne, Switzerland, September 7th **2018**. Awarded the best poster in Catalysis Science & Engineering (runner-up).

Synthesis of polyoxymethylene dimethyl ethers catalyzed by H-ZSM-5, H-Y and H-MOR, Catalysis fundamentals and practice summer school, Liverpool, United Kingdom, July 17-21 **2017**.

Exploring new synthesis routes for polyoxymethylene dimethyl ethers production as new diesel fuel substitute, SCS seminars on process chemistry, Freiburg, Switzerland, January 16-18 **2016**.

Cover Features

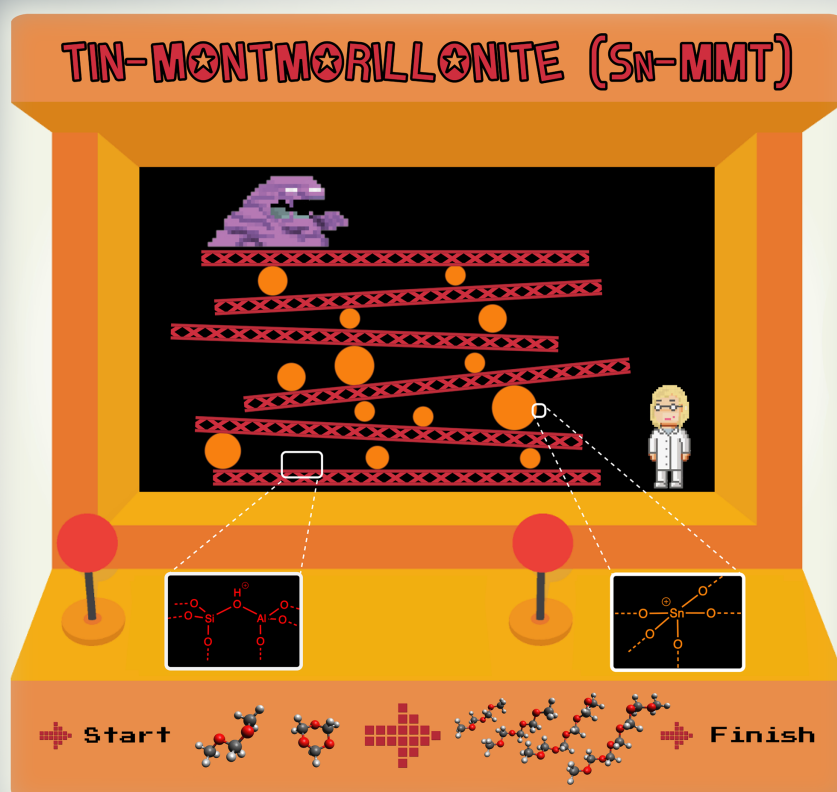
Two cover features were published in ChemCatChem and ChemSusChem based on the work that was presented in this thesis. The covers are here presented and accompanied by an explanation that links the graphics to the scientific content.

Cover feature 1

The first cover feature relates to Chapter 4 and is connected to an article published in ChemCatChem (2019, 11, 3010–3021). This cover was made using Adobe® Illustrator by Christophe Baranowski. The idea of the cover originates from a striking similarity between the structure of tin-montmorillonite and the famous video arcade game Donkey Kong, that was highlighted by Jack Brandon. Due to copyright laws, Donkey Kong and Mario were replaced by a purple monster and a scientist, respectively. This choice was motivated by the context of research on oxymethylene dimethyl ethers (OME). Scientists are working to find alternatives to fossil fuels (the purple monster), and tin-montmorillonite was found to be an efficient material to catalyze OME synthesis from trioxane and dimethoxymethane. The structure is composed of montmorillonite layers in between which SnO₂ nanocrystals are inserted. In the arcade game, the latter are barrels that are going down the structure. To symbolize the work done in our article on the nature of the two catalyst active sites, two “action” buttons were introduced: Brønsted acid sites resulting from the crystallization of SnO₂, and Lewis acid sites generated by undercoordinated Sn surface sites.

Heterogeneous & Homogeneous & Bio- & Nano-
CHEMCATCHEM
CATALYSIS

TIN-MONTMORILLONITE (Sn-MMT)



13/2019

Cover Feature:

C. J. Baranowski et al.

Insights into the Nature of the Active Sites of Tin-Montmorillonite
for the Synthesis of Polyoxymethylene Dimethyl Ethers (OME)

A Journal of



WILEY-VCH

www.chemcatchem.org

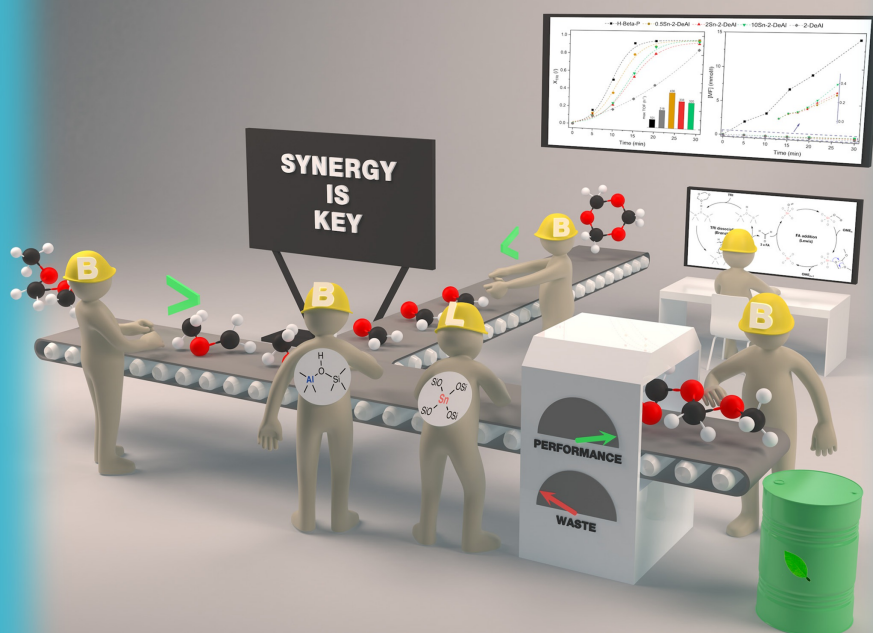
Cover feature 1

The second cover feature relates to Chapter 5 and is connected to an article published in *ChemSusChem* (**2019**, *12*, 4421–4431). The cover sketches were done by Christophe Baranowski, and the final cover illustration was made by Mahir Dzambegovic.

During the past years, the OME community has discovered many materials with various features that were able to catalyze the synthesis of OME. Their acidity was shown to be a key parameter, and a synergy between Brønsted and Lewis acid sites was also reported. In our work, we studied systematically the synthesis of OME using a series of Beta zeolites with a varying degree of Brønsted and Lewis acidity. This cover highlights the findings we reported in the article. The operators of the OME production line symbolize Brønsted or Lewis acid sites originating from bridging hydroxyl groups and tetrahedral Sn, respectively. They can be recognized by the sign “B” or “L” on their hard hats and by the scheme they carry on their back. B operators are present in each position of the factory line: trioxane decomposition, dimethoxymethane initiation, formaldehyde insertion and OME termination. The L operator is present only in the formaldehyde insertion position. When B and L operators work together, it results in an increased performance (i.e. the turnover frequency) and a decreased amount of waste (i.e. the production of methyl formate). A panel displaying “Synergy is key” is a reminder of the type of panels that are typically visible in some line production factories. The operator at the back ensures that this synergy is happening by monitoring the overall process.

CHEMISTRY & SUSTAINABILITY
CHEMSUSCHEM

ENERGY & MATERIALS



19/2019

Cover Feature:

C. J. Baranowski et al.

Nature of Synergy between Brønsted and Lewis Acid Sites in Sn–Beta Zeolites for Polyoxymethylene Dimethyl Ethers Synthesis

WILEY-VCH

www.chemsuschem.org

A Journal of



Curriculum Vitae

Name: Christophe Jean Baranowski

Date of birth: 17.10.1989

Place of birth: Brussels, Belgium

Nationality: Belgian and Polish

Employment history

Jan. 2014 – Jan. 2015 Health & Safety Specialist, Abercrombie & Fitch Co.,
Northern Europe

Nov. 2012 – Jan. 2014 Technology Consultant in the chemical and natural re-
sources industries, Accenture, Benelux

Professional education

Jan. 2016 – current PhD student in the group of catalysis for biofuels at the
Swiss Federal Institute of Technology Lausanne (EPF
Lausanne, Switzerland) under the supervision of Prof.
Dr. Oliver Kröcher

Sep. 2009 – June 2012 MSc in Chemical and Material Science Engineering at
the Ecole Polytechnique de Bruxelles (ULB, Brussels,
Belgium). Thesis on “Contribution to the development
of a solar drier” supervised by Prof. Dr. Benoit Haut.
One-year exchange at the Swiss Federal Institute of
Technology Lausanne (EPF Lausanne, Switzerland)

Sep. 2007 – June 2009

BSc in Applied Science at the Ecole Polytechnique de
Bruxelles (ULB, Brussels, Belgium).